

CHEMICAL WEAR OF CARBON-BASED REFRACTORY MATERIALS IN A SILICOMANGANESE FURNACE TAP-HOLE

by

Joalet Dalene Steenkamp

A thesis submitted in partial fulfilment of the requirements for the degree
PhD (metallurgical engineering) in the

Department of Materials Science and Metallurgical Engineering
Faculty of Engineering, Built Environment and Information Technology
University of Pretoria

November 2014

Abstract

The aim of the study presented here was to investigate the potential for chemical wear of carbon-based refractory materials in a silicomanganese furnace tap-hole. In the study, three research questions were addressed:

1. Is chemical reaction between refractory and slag or refractory and metal a potential wear mechanism?
2. Is the choice in carbon-based refractory material important from a tap-hole refractory life perspective?
3. What are the implications for the life of the tap-hole in a SiMn furnace?

To study the potential for chemical wear, thermodynamic calculations were conducted to determine the potential for the formation of SiC and SiMn at 1600°C through reduction of SiO₂ and MnO and dissolution of C (and subsequent reaction with Si) in metal. The thermodynamic calculations were based on published [1] metal and slag composition and carbon. Cup test experiments based on synthetic slag and graphite proved SiC formation conclusively, but not SiMn formation.

To study the effect of the choice in carbon-based refractory material, two types of refractory materials – carbon block and ramming paste – available commercially and industrial slag were sourced, prepared and characterised. Wettability studies proved the formation of SiC at 1588°C with slag being wetting towards refractory in an argon atmosphere and non-wetting in a CO-atmosphere. Under wetting conditions, the wetting angle of slag on carbon block was slightly higher (50°) at holding temperature compared to that of ramming paste (30°). Under non-wetting conditions the angles were 160° and 150° respectively. Cup test experiments based on industrial slag and carbon-based refractory material proved both SiC and SiMn formation at 1600°C conclusively and confirmed the wetting behaviour of slag towards refractory at larger scale.

To study the implications for the life of the tap-hole in a SiMn furnace, the tap-hole of a 48 MVA SiMn furnace was excavated and profiled. The wear predicted by thermodynamic modelling was supported by mass flow calculations.

It was concluded that chemical reaction between carbon-based refractory materials and slag and metal is one of the mechanisms responsible for wear in the tap-hole of a silicomanganese furnace.

Keywords: Tap-hole, silicomanganese, submerged arc furnace, carbon block, cold ramming paste

Declaration

I declare that the thesis, which I hereby submit for the degree PhD (metallurgical engineering) at the University of Pretoria, is my own work and has not previously been submitted by me for a degree at this or any other tertiary institution.

Dedication

Rudolph, Rudi and Esté: Thank you for sometimes letting me go to the woods and at other times being the woods that I go to. I love you with all my heart.



Figure 1: “Red forest” – Lombardy, Italy.
Source: Corrado Orio photography.

I went to the woods because I wished to live deliberately...I wanted to live deep and suck out all the marrow of life... to put to rout all that was not life... and not when I had come to die, discover that I had not lived.

From: Walden, Henry David Thoreau

Acknowledgements

Soli Deo Gloria

Professor Pistorius: Thank you for the flight.



Figure 2: “Follow me” – SiMn metal and slag flowing from launder to ladle and overflowing into a second ladle. Photographer: JD Steenkamp.

Your children are not your children.
They are the sons and daughters of Life's longing for itself.
They come through you but not from you,
And though they are with you yet they belong not to you.
You may give them your love but not your thoughts,
For they have their own thoughts.
You may house their bodies but not their souls,
For their souls dwell in the house of tomorrow, which you cannot visit, not even in your dreams.
You may strive to be like them, but seek not to make them like you.
For life goes not backward nor tarries with yesterday.
You are the bows from which your children as living arrows are sent forth.
The archer sees the mark upon the path of the infinite, and He bends you with His might that His
arrows may go swift and far.
Let your bending in the Archer's hand be for gladness;
For even as He loves the arrow that flies, so He loves also the bow that is stable.

From: The Prophet, Kahlil Gibran

Professor Tangstad: Thank you for helping me find me.



Figure 3: “Perfection” – an ant rolling a water droplet on a rough surface, an example of ideal non-wetting conditions. Photographer: Unknown.

Student’s Prayer - Umberto Maturana (Chilean biologist & philosopher)

Don’t impose on me what you know,
I want to explore the unknown
and be the source of my own discoveries.
Let the known be my liberation, not my slavery.
The world of your truth can be my limitation;
your wisdom my negation.
Don’t instruct me; let’s walk together.
Let my riches begin where yours ends.
Show me so that I can stand
on your shoulders.
Reveal yourself so that I can be
something different.
You believe that every human being
can love and create.
I understand, then, your fear
when I ask you to live according to your wisdom.
You will not know who I am
by listening to yourself.
Don’t instruct me; let me be.
Your failure is that I be identical to you.

Some people come in your life as blessings. Some come in your life as lessons – Mother Teresa

---when we learnt the lessons, they become blessings too.

THANK YOU to each and everyone who blessed my life along this journey.

Namaste

Table of Contents

CHEMICAL WEAR OF CARBON-BASED REFRACTORY MATERIALS IN A SILICOMANGANESE FURNACE TAP-HOLE	1
ABSTRACT	II
DECLARATION	II
DEDICATION	III
ACKNOWLEDGEMENTS	IV
TABLE OF CONTENTS	VIII
LIST OF TABLES	XII
LIST OF FIGURES	XVI
LIST OF EQUATIONS	XXIV
LIST OF ABBREVIATIONS	XXV
1 INTRODUCTION	1
1.1 Manganese and its compounds	1
1.2 Brief history of manganese ferroalloy production	1
1.3 Commercial grades of manganese ferroalloy and their applications	1
1.4 Industrial production of manganese ferroalloys	3
1.5 Lining designs installed in industrial-scale SAFs producing SiMn	5
1.5.1 Lining design principles	5
1.5.2 Examples of lining designs applied in SiMn production	6
1.6 The tap-hole	8
1.6.1 Tap-hole operating practice	8
1.6.2 Tap-hole maintenance practice	9
1.7 Research problem and questions	9
1.8 Overview of chapters	9

2	LITERATURE REVIEW	11
2.1	Introduction	11
2.2	Carbothermic SiMn production process	11
2.2.1	Process overview	11
2.2.2	Structure of carbon	12
2.2.3	Carbon reactivity studies	13
2.2.4	Wettability tests	14
2.3	Carbon-based refractory materials	20
2.3.1	Carbon in refractory materials	20
2.3.2	Different types of carbon-based refractory materials	21
2.3.3	Influence of thermal conductivity of carbon-based refractory materials	22
2.4	Refractory wear mechanisms	28
2.4.1	Different types of refractory wear mechanisms	28
2.4.2	Development of carbon-based refractory materials in ironmaking	29
2.4.3	Wear mechanisms in ironmaking blast furnace hearth	29
2.4.4	Role of additives in carbon-based refractory material	30
2.4.5	Refractory wear mechanisms in manganese ferroalloy furnaces	31
2.5	Studying refractory wear mechanisms	31
2.5.1	Laboratory-scale experiments	32
2.5.2	Thermodynamic calculations	33
2.6	Conclusion	34
3	POTENTIAL FOR CHEMICAL REACTION – PART A (CALCULATIONS)	35
3.1	Introduction	35
3.2	Method	35
3.3	Results	37
3.4	Discussion	38
3.5	Conclusion	48
4	POTENTIAL FOR CHEMICAL REACTION – PART B (LABORATORY EXPERIMENTS)	50
4.1	Introduction	50
4.2	Method	50
4.3	Results	56

4.4	Discussion	60
4.5	Conclusion	62
5	IMPORTANCE OF CHOICE IN REFRACTORY – PART A (CHARACTERISATION OF MATERIALS)	63
5.1	Introduction	63
5.2	Method	63
5.3	Results	66
5.4	Discussion	76
5.5	Conclusion	80
6	IMPORTANCE OF CHOICE IN REFRACTORY- PART B (WETTABILITY TESTS)	81
6.1	Introduction	81
6.2	Method	81
6.3	Results	84
6.4	Discussion	101
6.5	Conclusion	105
7	IMPORTANCE OF CHOICE IN REFRACTORY- PART C (CUP TESTS)	106
7.1	Introduction	106
7.2	Method	106
7.3	Results	108
7.4	Discussion	112
7.5	Conclusion	123
8	IMPLICATIONS FOR THE LIFE OF THE TAP-HOLE IN A SIMN FURNACE	125
8.1	Introduction	125
8.2	Background	125
8.3	Method	128

8.4	Results	128
8.5	Discussions	133
8.5.1	Potential for chemical reaction between slag or metal and refractory	133
8.5.2	Refractory consumption	138
8.6	Conclusions	140
9	FINAL CONCLUSIONS AND RECOMMENDATIONS FOR FUTURE RESEARCH	142
10	REFERENCES	145
11	APPENDIX A: SUMMARY OF WETTABILITY RESULTS	156
11.1	Synthetic slag on ramming paste matrix in Ar-gas	156
11.2	Industrial slag on ramming paste matrix in Ar-gas	159
11.3	Industrial slag on ramming paste aggregate in Ar-gas	161
11.4	Industrial slag on carbon block in Ar-gas	163
11.5	Industrial slag on ramming paste matrix in CO-gas	165
11.6	Industrial slag on ramming paste aggregate in CO-gas	167
11.7	Industrial slag on carbon block in CO-gas	169
12	APPENDIX B: DENSITY CALCULATIONS FOR LIQUID METAL PHASE	171
13	APPENDIX C: CALCULATION OF MASS TRANSFER COEFFICIENT FOR SILICA FOR LAMINAR FLOW INSIDE A CIRCULAR PIPE	173

List of Tables

TABLE 1: CATEGORIES OF MANGANESE FERROALLOYS PRODUCED INTERNATIONALLY AND THEIR TYPICAL CHEMICAL COMPOSITION (BALANCE FE) [7], [8].	2
TABLE 2: TYPICAL CHEMICAL COMPOSITION (PERCENTAGE BY MASS) AND PROCESS TEMPERATURE OF SLAG TAPPED FROM THE FURNACE DURING THE PRODUCTION OF MANGANESE FERROALLOYS [1].	4
TABLE 3: TYPICAL DISTRIBUTION OF FEED INTO A SAF PRODUCING SIMN ACCORDING TO THE ORE-BASED ROUTE OR INTEGRATED ROUTE [1], [14] (PER CENT BY MASS).	4
TABLE 4: TYPICAL COMPOSITION OF TAPPED SIMN ALLOY IN MASS PER CENT [1].	12
TABLE 5: TYPICAL COMPOSITION OF TAPPED SIMN SLAG IN MASS PER CENT [1].	12
TABLE 6: TYPICAL COMPOSITION OF OFF GAS IN PER CENT BY VOLUME [1].	12
TABLE 7: THERMAL CONDUCTIVITY OF DIFFERENT TYPES OF CARBON REFRACTORY MATERIAL AGAINST THAT OF OTHER TYPES OF REFRACTORY MATERIALS AT 1000°C.	23
TABLE 8: ASSUMED SIMN PROCESS CONDITIONS, MATERIAL PROPERTIES AND FURNACE DIMENSIONS UTILISED IN MODEL, WITH SOURCES OF DATA INDICATED.	27
TABLE 9: RESULTANT FREEZE LINING THICKNESS FOR DIFFERENT TYPES OF REFRACTORY MATERIAL CALCULATED WITH EQUATION 17 AND BASED ON THE ASSUMPTIONS IN TABLE 8.	27
TABLE 10: RESULTANT HEAT LOSS FOR DIFFERENT TYPES OF REFRACTORY MATERIAL CALCULATED WITH EQUATION 18 AND BASED ON THE ASSUMPTIONS IN TABLE 8.	28
TABLE 11: PUBLISHED [1] RELATIVE MASSES OF SLAG SPECIES (A REPEAT OF TABLE 5) AND ARGON UTILISED IN THERMODYNAMIC CALCULATIONS CONDUCTED IN FACTSAGE 6.4.	35
TABLE 12: PUBLISHED [1] METAL COMPOSITION (A REPEAT OF TABLE 4) UTILISED IN THERMODYNAMIC CALCULATIONS CONDUCTED IN FACTSAGE 6.4, AND USING THE INTERACTION PARAMETERS OF LI AND MORRIS [119].	36
TABLE 13: STANDARD REFERENCE STATES APPLIED IN THE CALCULATION OF THE ΔG° FOR EACH CHEMICAL REACTION IN FACTSAGE 6.4.	37
TABLE 14: CHEMICAL COMPOSITION OF THE SLAG PHASE (PERCENTAGE BY MASS): AS PUBLISHED [1] (A), AND AS CALCULATED FOR (B) SLAG ONLY AT EQUILIBRIUM AND (C) SLAG AT EQUILIBRIUM WITH GRAPHITE.	40
TABLE 15: CHEMICAL COMPOSITION OF THE METAL PHASE (PERCENTAGE BY MASS): AS PUBLISHED [1] (A), AND AS CALCULATED IN FACTSAGE FOR (B) METAL ONLY, (C) METAL EQUILIBRATED WITH GRAPHITE AND (D) SLAG EQUILIBRATED WITH GRAPHITE.	40
TABLE 16: CALCULATED CHEMICAL COMPOSITION OF THE GAS PHASE (VOLUME PER CENT WHEN TOTAL PRESSURE IS 1 ATMOSPHERE) FOR THE GAS FORMED WHEN SLAG EQUILIBRATED WITH GRAPHITE.	41
TABLE 17: ACTIVITY OF SLAG COMPONENTS (LIQUID REFERENCE STATE) AS FUNCTIONS OF TEMPERATURE (CALCULATED WITH FACTSAGE 6.4) FOR SLAG ANALYSIS IN TABLE 11.	41
TABLE 18: ACTIVITY OF METAL COMPONENTS AS FUNCTIONS OF TEMPERATURE (CALCULATED WITH FACTSAGE 6.4 OR USING THE MODEL BASED ON THE INTERACTION PARAMETERS OF LI AND MORRIS) FOR METAL COMPOSITION IN TABLE 12. REFERENCE STATES: GRAPHITE FOR CARBON; PURE LIQUIDS FOR ALL OTHERS.	41
TABLE 19: MOLE BALANCE FOR MN WHEN 100G OF SLAG (COMPOSITION TABLE 11) IS EQUILIBRATED WITH 100G GRAPHITE IN THE TEMPERATURE RANGE 1550°C TO 1650°C.	43
TABLE 20: MOLE BALANCE FOR SI WHEN 100G OF SLAG (COMPOSITION TABLE 11) IS EQUILIBRATED WITH 100G GRAPHITE IN THE TEMPERATURE RANGE 1550°C TO 1650°C.	43
TABLE 21: MOLE BALANCE FOR C WHEN 100G OF SLAG (COMPOSITION TABLE 11) IS EQUILIBRATED WITH 100G GRAPHITE IN THE TEMPERATURE RANGE 1550°C TO 1650°C.	43
TABLE 22: APPLICATION OF THE PHASE RULE TO FIGURE 23 AND THE CONSEQUENCES THEREOF.	44

TABLE 23: ACTIVITY OF CARBON AND SIC AT 1600°C (CALCULATED WITH FACTSAGE 6.4; SOLID REFERENCE STATES) FOR METAL EQUILIBRATED WITH SLAG WITH PUBLISHED [1] COMPOSITION (TABLE 14 (A)), AT A SLAG / METAL MASS RATIO OF 1.2.	48
TABLE 24: REACTIONS MOST LIKELY TO BE RESPONSIBLE FOR WEAR IN THE TAP-HOLE; EQUILIBRIUM CONSTANTS, K, CALCULATED WITH FACTSAGE 6.4. THE ACTIVITY DATA UTILIZED TO CALCULATE THE REACTION QUOTIENT, Q, WAS TAKEN FROM TABLE 17 AND TABLE 18. THE VALUES ARE FOR A TYPICAL TAPPING TEMPERATURE OF 1600°C.	49
TABLE 25: Q/K RATIOS AT DIFFERENT TEMPERATURES FOR REACTIONS MOST LIKELY TO BE RESPONSIBLE FOR WEAR IN THE TAP-HOLE. (EQUILIBRIUM CONSTANTS, K, CALCULATED WITH FACTSAGE 6.4; ACTIVITY DATA UTILIZED TO CALCULATE THE REACTION QUOTIENT, Q, CALCULATED WITH FACTSAGE 6.4 FOR THE SLAG, AND BOTH FACTSAGE 6.4 AND THE MODEL BY LI & MORRIS FOR METAL).	50
TABLE 26: PURE MINERAL BLEND ON WHICH SYNTHETIC SLAG WAS BASED.	51
TABLE 27: BULK CHEMICAL COMPOSITION OF SYNTHETIC SLAG SAMPLES DETERMINED BY WET CHEMISTRY METHODS (AVERAGE PERCENTAGE BY WEIGHT AND STANDARD DEVIATION OF THREE SAMPLES PER MATERIAL).	56
TABLE 28: COMPOSITION OF AMORPHOUS SLAG PHASE (I) IN SYNTHETIC SLAG – AVERAGE OF 10 EDS POINT ANALYSES.	57
TABLE 29: ANALYSIS OF METAL PHASE (WEIGHT PER CENT) OF METAL ACCUMULATION AT THE SLAG / REFRACTORY INTERFACE OF THE SAMPLE PREPARED AT 1550°C DETERMINED AS AVERAGE OF EDS POINT ANALYSIS OF 4 METAL PARTICLES AT 15 KV.	58
TABLE 30: ANALYSIS OF METAL PHASE (WEIGHT PER CENT) OF METAL ACCUMULATION AT THE SLAG / REFRACTORY INTERFACE OF THE SAMPLE PREPARED AT 1650°C DETERMINED AS AVERAGE OF EDS POINT ANALYSIS OF 3 METAL PARTICLES AT 15 KV.	59
TABLE 31: CHEMICAL COMPOSITION OF STEEL CONTAMINANT.	60
TABLE 32: SUMMARY OF THE PREDICTED POTENTIAL FOR THE REACTION PRODUCTS TO FORM AND THE PRESENCE OF ACTUAL REACTION PRODUCTS FORMED.	61
TABLE 33: RESULTS OF ANF CALCULATIONS TO DETERMINE THE AMOUNT OF IODOFORM TO BE ADDED TO RESIN TO IMPROVE CONTRAST BETWEEN RESIN AND CARBON WITHOUT NEGATIVELY INFLUENCING CONTRAST BETWEEN RESIN AND INORGANIC PHASES PRESENT IN THE REFRACTORY SAMPLES.	65
TABLE 34: BULK CHEMICAL COMPOSITION OF AS-RECEIVED INDUSTRIAL SLAG SAMPLES DETERMINED BY WET CHEMISTRY METHODS (AVERAGE PERCENTAGE BY WEIGHT AND STANDARD DEVIATION OF THREE SAMPLES PER MATERIAL).	66
TABLE 35: NORMALISED ELEMENTAL ANALYSIS OF SLAG PHASES (WEIGHT PER CENT) DETERMINED AS AVERAGE OF FIVE EDS POINT ANALYSIS PER PHASE AT 15 KV.	68
TABLE 36: COMPOSITION OF SLAG PHASES SIMPLIFIED TO FIVE COMPONENT SYSTEM AND NORMALISED (WEIGHT PER CENT) – BASED ON EDS ANALYSIS IN TABLE 35.	68
TABLE 37: ANALYSIS OF METAL PHASES (WEIGHT PER CENT) DETERMINED AS AVERAGE OF EIGHT EDS POINT ANALYSIS FOR THE LARGE PARTICLES – SEE FIGURE 46 – AND FIVE FOR SMALL PARTICLES – SEE FIGURE 42 – AT 15 KV.	69
TABLE 38: BULK CHEMICAL COMPOSITION OF THE REFRACTORY MATERIAL.	70
TABLE 39: BULK CHEMICAL COMPOSITION OF THE ASH PHASE PREPARED BY COMBUSTING THE REFRACTORY MATERIAL AT 815°C IN AIR.	70
TABLE 40: CRYSTALITE SIZE L_c AND INTER PLANAR DISTANCE (D_{002}) OF THE REFRACTORY MATERIAL AND COMPONENTS DERIVED FROM XRD.	73
TABLE 41: TOTAL POROSITY PER REFRACTORY SAMPLE DETERMINED BY XRT.	74
TABLE 42: CHEMICAL COMPOSITION (PERCENTAGE BY MASS) OF THE CARBON BLOCK AND PRE-FIRED RAMMING PASTE UTILIZED TO CALCULATE THE EQUILIBRIUM PHASE DISTRIBUTION OF BOTH. THE	

COMPOSITIONS WERE DERIVED FROM THE PROXIMATE AND ASH ANALYSES IN TABLE 38 AND TABLE 39 AND ADJUSTED FOR SI AND SiO₂ CONTENTS BASED ON XRD ANALYSES IN FIGURE 50 AND FIGURE 52. ... 78

TABLE 43: EXPERIMENTAL CONDITIONS OF WETTABILITY TESTS. 81

TABLE 44: REPEATABILITY OF WETTING ANGLE MEASUREMENTS ON LEFT-HAND AND RIGHT-HAND SIDE ON TIME SERIES OF 20 CONSECUTIVE IMAGES AND 10 REPEATS OF A SINGLE IMAGE TAKEN UNDER WETTING AND NON-WETTING CONDITIONS. THE DATASET WAS TAKEN FROM THE EXPERIMENT CONDUCTED WITH SYNTHETIC SLAG ON RAMMING PASTE MATRIX SUBSTRATE IN AN ARGON ATMOSPHERE. THE HOLDING TEMPERATURE WAS 1588°C. 85

TABLE 45: SERIES OF RECORDED IMAGES AS A FUNCTION OF TEMPERATURE AND TIME FOR THE SYNTHETIC SLAG ON RAMMING PASTE MATRIX SUBSTRATE IN AN ARGON ATMOSPHERE WHEN THE HEATING RATE WAS 300°C. THE HOLDING TEMPERATURE WAS 1588°C. 88

TABLE 46: SERIES OF RECORDED IMAGES AS A FUNCTION OF TEMPERATURE AND TIME FOR THE SYNTHETIC SLAG ON RAMMING PASTE MATRIX SUBSTRATE IN AN ARGON ATMOSPHERE. THE HOLDING TEMPERATURE WAS 1588°C. 89

TABLE 47: REPEATABILITY OF VOLUME RATIO ON TIME SERIES OF 20 CONSECUTIVE IMAGES AND 10 REPEATS OF A SINGLE IMAGE TAKEN UNDER WETTING AND NON-WETTING CONDITIONS. THE DATASET WAS TAKEN FROM THE EXPERIMENT CONDUCTED WITH SYNTHETIC SLAG ON RAMMING PASTE MATRIX SUBSTRATE IN AN ARGON ATMOSPHERE. THE HOLDING TEMPERATURE WAS 1588°C. 91

TABLE 48: DEPENDENCY OF WETTING ANGLE ON CHANGE IN VOLUME CAUSED BY GAS FORMATION AT 15 MINUTES INTO THE HOLDING PERIOD FOR THE SYNTHETIC SLAG ON RAMMING PASTE MATRIX SUBSTRATE IN AN ARGON ATMOSPHERE. THE HOLDING TEMPERATURE WAS 1588°C. IMAGES WERE TAKEN 10 SECONDS APART. 92

TABLE 49: SUMMARY OF THE MAXIMUM DEPTH – MEASURED IN FIGURE 78 TO FIGURE 80 – TO WHICH INDUSTRIAL SLAG INFILTRATED INTO THE REFRACTORY SAMPLES. THE HOLDING TEMPERATURE WAS 1592°C AND ATMOSPHERE ARGON GAS. 97

TABLE 50: CALCULATED EQUILIBRIUM CONTACT ANGLE (θ_c) FOR SLAG ON CARBON BLOCK BASED ON PUBLISHED [48], [63] WETTABILITY DATA FOR SLAGS ON DIFFERENT SUBSTRATES AND THE CARBON BLOCK PHASE DISTRIBUTION ESTIMATED FROM TABLE 38. 102

TABLE 51: PUBLISHED [48], [63] COMPOSITIONS OF SLAGS UTILIZED TO MEASURE WETTABILITY OF GRAPHITE AND CORUNDUM (A) AND SIC (B). 102

TABLE 52: SECTIONED CUP TEST SAMPLES WHERE (A) INDUSTRIAL SIMN SLAG WAS HELD FOR 4 HOURS IN CUPS MADE OF (B) INDUSTRIAL GRADE RAMMING PASTE, RAMMED INTO (C) GRAPHITE CRUCIBLES AND THEN PREBAKED, OR (D) CARBON BLOCK AT THREE DIFFERENT HOLDING TEMPERATURES. TO ENSURE SLAG REMAIN IN PLACE DURING CUTTING, CUPS WERE FILLED WITH (E) RESIN WHICH WAS ALLOWED TO CURE PRIOR TO SECTIONING. 108

TABLE 53: MAXIMUM DEPTH OF INFILTRATION (MM) OF INDUSTRIAL SLAG INTO REFRACTORY AS MEASURED ON STITCHED LOM IMAGES. 109

TABLE 54: DEFINITION OF VARIABLES APPLIED IN EQUATION 30 AND VALUES APPLIED IN CALCULATIONS. ... 118

TABLE 55: TERMINAL VELOCITY (U_T) AND SETTLING DISTANCE AFTER 4 HOURS (ΔZ) FOR DIFFERENT METAL DROPLET DIAMETERS (D_{DROPLET}) IN SLAG AT 1600°C. SETTLING DISTANCE WAS DERIVED FROM TERMINAL VELOCITY ESTIMATED WITH THE HADAMARD-RYBCZYNSKI EXPRESSION (EQUATION 30) AND VARIABLES DEFINED IN TABLE 54. 118

TABLE 56: COMPOSITION OF METAL DROPLETS (PERCENTAGE BY MASS; CARBON NOT ANALYZED) IN RAMMING PASTE IN CONTACT WITH INDUSTRIAL SLAG AT 1600°C FOR 4 HOURS. TYPES OF METAL DROPLET WERE IDENTIFIED IN FIGURE 101. COMPOSITION BASED ON SEM-EDS POINT ANALYSIS CONDUCTED AT 10 KV ON TEN DROPLETS EACH PER CATEGORY EXCEPT FOR THE TWO LARGE DROPLETS (A AND B). CA WAS UTILIZED AS SLAG-INDICATOR AND ALL ANALYSIS CONTAINING MORE THAN 1%CA WERE DELETED FROM DATASET. ANALYSIS PER DROPLET (PERCENTAGE BY MASS) WAS NORMALISED

AND THE AVERAGES AND STANDARD DEVIATIONS CALCULATED. NORMALISED COMPOSITION PER DROPLET WAS CONVERTED TO NUMBER OF MOLES IN 100G AND SI:MN RATIO CALCULATED. AVERAGE AND 95% CONFIDENCE LIMITS OF SI:MN RATIO PER DROPLET CATEGORY WERE CALCULATED.	122
TABLE 57: DEFINITION OF VARIABLES APPLIED IN EQUATION 31 AND VALUES APPLIED IN CALCULATIONS. ...	123
TABLE 58: COMPOSITION AND THERMAL CONDUCTIVITY OF REFRACTORY MATERIALS AS OBTAINED FROM SUPPLIER DATASHEETS EXCEPT WHERE INDICATED DIFFERENTLY.....	126
TABLE 59: AVERAGE AND STANDARD DEVIATION OF AS-RECEIVED SLAG ANALYSES AND SLAG COMPOSITION CORRECTED FOR METAL INCLUSIONS.....	128
TABLE 60: AS-RECEIVED METAL COMPOSITION.	128
TABLE 61: MATERIAL COMPOSITIONS APPLIED IN FREE ENERGY MINIMIZATION CALCULATIONS WHERE SLAG IS REACTED WITH EITHER C- OR SIC-BASED REFRACTORY MATERIAL (MASS PERCENTAGES).	134
TABLE 62: MATERIAL COMPOSITIONS (MASS PERCENTAGES) APPLIED IN FREE ENERGY MINIMIZATION CALCULATIONS WHERE METAL IS REACTED WITH EITHER C- OR SIC-BASED REFRACTORY MATERIAL.....	134
TABLE 63: ACTUAL MASS OF C AND SIC REFRACTORY WORN AS CALCULATED FROM THE WEAR PROFILE IN FIGURE 104.	139
TABLE 64: TOTAL AMOUNT OF SLAG TAPPED THROUGH THE TAP-HOLE ESTIMATED FROM ACTUAL PRODUCTION FIGURES.	139
TABLE 65: CALCULATION OF MASS TRANSFER COEFFICIENT FOR SILICA FOR LAMINAR FLOW INSIDE A CIRCULAR PIPE.	140
TABLE 66: SYNTHETIC SLAG ON RAMMING PASTE MATRIX SUBSTRATE IN AN ARGON ATMOSPHERE HELD AT 1588°C.....	156
TABLE 67: INDUSTRIAL SLAG ON RAMMING PASTE MATRIX SUBSTRATE IN AN ARGON ATMOSPHERE HELD AT 1588°C.....	159
TABLE 68: INDUSTRIAL SLAG ON RAMMING PASTE AGGREGATE SUBSTRATE IN AN ARGON ATMOSPHERE HELD AT 1588°C.....	161
TABLE 69: INDUSTRIAL SLAG ON CARBON BLOCK SUBSTRATE IN AN ARGON ATMOSPHERE HELD AT 1588°C. 163	
TABLE 70: INDUSTRIAL SLAG ON RAMMING PASTE MATRIX SUBSTRATE IN A CO-GAS ATMOSPHERE HELD AT 1588°C.....	165
TABLE 71: INDUSTRIAL SLAG ON RAMMING PASTE AGGREGATE SUBSTRATE IN A CO-GAS ATMOSPHERE HELD AT 1588°C.....	167
TABLE 72: INDUSTRIAL SLAG ON CARBON BLOCK SUBSTRATE IN A CO-GAS ATMOSPHERE HELD AT 1588°C... 169	
TABLE 73: METAL COMPOSITION APPLIED IN CALCULATION OF DENSITY OF METAL (P_{METAL}).....	171
TABLE 74: DEFINITION OF VARIABLES APPLIED IN EQUATION 35 AND DENSITIES CALCULATED AT 1600°C.	172
TABLE 75: DENSITY OF THE 3-COMPONENT METAL.....	172
TABLE 76: DENSITY OF LIQUID FE-C ALLOYS AS A FUNCTION OF CARBON CONTENT CALCULATED ACCORDING TO EQUATION 36.	172
TABLE 77: CALCULATING THE CONCENTRATION OF SiO_2 IN THE SLAG.	173

List of Figures

FIGURE 1: “RED FOREST” – LOMBARDY, ITALY. SOURCE: CORRADO ORIO PHOTOGRAPHY.	III
FIGURE 2: “FOLLOW ME” – SIMN METAL AND SLAG FLOWING FROM LAUNDER TO LADLE AND OVERFLOWING INTO A SECOND LADLE. PHOTOGRAPHER: JD STEENKAMP.	V
FIGURE 3: “PERFECTION” – AN ANT ROLLING A WATER DROPLET ON A ROUGH SURFACE, AN EXAMPLE OF IDEAL NON-WETTING CONDITIONS. PHOTOGRAPHER: UNKNOWN.	VI
FIGURE 4: WORLD REAL UNIT CONSUMPTION OF MANGANESE FERROALLOYS, 2001 – 2010 [10]–[12].	2
FIGURE 5: PRODUCTION METHODS FOR HCFEMN AND SIMN ALLOY. THREE DISTINCT PROCESSES ARE IN OPERATION ONE PRODUCING HCFEMN, THE OTHER SIMN AND THE THIRD HAVING HCFEMN PRODUCTION INTEGRATED WITH SIMN PRODUCTION (INDICATED BY DOTTED LINE).	3
FIGURE 6: EXAMPLE OF AN OPEN FURNACE UTILIZED TO PRODUCE SIMN BEING FED THROUGH A FEED CHUTE IN THE ROOF [16].	5
FIGURE 7: STEADY STATE HEAT TRANSFER PRINCIPLES ON WHICH A) INSULATING AND B) CONDUCTIVE LINING DESIGNS ARE BASED.	6
FIGURE 8: INSULATING LINING INSTALLED FOR SIMN AND HCFEMN PRODUCTION, NO COOLING [17].	7
FIGURE 9: (A) CONDUCTIVE LINING INSTALLED FOR HCFEMN PRODUCTION, WITH FORCED AIR COOLING ON THE HEARTH AND THIN FILM COOLING ON THE SIDE WALLS WITH (B) THE TAP-HOLE DESIGN [23].	8
FIGURE 10: LAYOUT OF A SAF UTILIZED IN THE PRODUCTION OF SIMN [32].	11
FIGURE 11: HEXAGONAL ARRANGEMENT OF CARBON IN GRAPHITE [36].	13
FIGURE 12: INTERMOLECULAR FORCES ACTING ON MOLECULE AT SURFACE OF LIQUID VS. INTERMOLECULAR FORCES ACTING ON MOLECULE WITHIN A LIQUID AFTER KOTZ AND PURCELL [49].	15
FIGURE 13: SURFACE TENSION FORCES ON A LIQUID IN A CAPILLARY TUBE WHERE (A) IS THE CAPILLARY ACTION IN ELEVATION AND (B) THE CAPILLARY ACTION IN DEPRESSION AFTER [50].	15
FIGURE 14: SCHEMATIC OF FORCES AT EQUILIBRIUM - RESPECTIVE SURFACE TENSIONS AND WEIGHT - AND THEIR RELATION TO THE CONTACT ANGLE WITH (A) NON-WETTING LIQUID – SESSILE DROP – RESTING ON A FLAT, HORIZONTAL SOLID SURFACE, (B) WETTING LIQUID – SESSILE DROP – RESTING ON A FLAT, HORIZONTAL SOLID SURFACE AND (C) WETTING LIQUID ON VERTICAL SOLID SURFACE AFTER [52] – A,B – AND [50] – C.	16
FIGURE 15: SCHEMATIC ILLUSTRATION OF A SOLID CYLINDER MELTING TO FORM A SESSILE DROP WITH AN INITIAL CONTACT ANGLE OF 120° AND SPREADING OVER THE SUBSTRATE WITH TIME TO ACHIEVE FINAL EQUILIBRIUM OF 30° [56].	19
FIGURE 16: CONCEPTUAL REFRACTORY LAYOUT OF THE LINING OF A SAF BASED ON THE CONDUCTIVE DESIGN PRINCIPLE – SCHEMATIC AFTER MATYAS ET AL [31].	23
FIGURE 17: DEFINITION OF MODEL PARAMETERS.	25
FIGURE 18: ELECTRICAL ANALOGUE OF THE CONCEPTUAL FURNACE SLAG LINE DESIGN IN FIGURE 17.	26
FIGURE 19: EQUILIBRIUM PHASE DISTRIBUTION OF UNREACTED (A) SLAG AND (B) METAL AS A FUNCTION OF TEMPERATURE. THE SLAG COMPOSITION WAS GIVEN IN TABLE 11 AND METAL COMPOSITION IN TABLE 12.	37
FIGURE 20: EQUILIBRIUM PHASE DISTRIBUTION OF SLAG WITH COMPOSITION IN TABLE 11.	38
FIGURE 21: EQUILIBRIUM PHASE DISTRIBUTION AS A FUNCTION OF TEMPERATURE, WHEN REACTING GRAPHITE (REPRESENTING REFRACTORY) WITH AN EQUAL MASS OF (A) SLAG AND (B) METAL. SLAG COMPOSITION AS IN TABLE 11; METAL COMPOSITION AS IN TABLE 12.	38
FIGURE 22: (A) EQUILIBRIUM PHASE DISTRIBUTION AS A FUNCTION OF TEMPERATURE (REPEAT OF FIGURE 21A), WHEN REACTING GRAPHITE (REPRESENTING REFRACTORY) WITH AN EQUAL MASS OF SLAG (COMPOSITION AS IN TABLE 11). (B) GRAPHICAL REPRESENTATIONS OF POTENTIAL EQUILIBRIUM PHASES AND PARTICIPATING COMPONENTS PER PHASE WHEN SLAG EQUILIBRATES WITH GRAPHITE IN THE TEMPERATURE RANGE 1550°C TO 1650°C.	39

FIGURE 23: CALCULATED CARBON SOLUBILITY IN MN-FE-SI-C ALLOYS WITH A FIXED MN:FE RATIO OF 6.8 AT 1500°C – 1650°C. 44

FIGURE 24: CALCULATED CARBON SOLUBILITY IN MN-FE-SI-C ALLOYS WITH DIFFERENT MN:FE RATIOS AT 1500°C – 1650°C. APART FROM THE DATA FROM OLSEN ET AL [1] THE DATA WAS CALCULATED IN FACTSAGE 6.4 AS PART OF THIS STUDY. CROSSES INDICATE THE PUBLISHED [1] METAL COMPOSITION (PURPLE) AND EQUILIBRIUM METAL COMPOSITIONS CALCULATED AT 1600°C FOR METAL ONLY (GREY), METAL IN CONTACT WITH GRAPHITE (BLACK) AND METAL PRODUCED WHEN SLAG IS IN CONTACT WITH GRAPHITE (GREEN) - FOR THE ANALYSES REFER TO TABLE 15. 45

FIGURE 25. CALCULATED CARBON SOLUBILITY IN MN-FE-SI-C ALLOYS WITH A FIXED MN:FE RATIO OF 6.8 AT 1500°C – 1650°C. THE PURPLE CROSS INDICATES THE PUBLISHED [1] METAL COMPOSITION - REFER TO TABLE 15 FOR ANALYSIS. THE BLUE CROSS IS FOR METAL CONTAINING 17.5%SI AND 1.5%C AND THE YELLOW CROSS FOR METAL CONTAINING 17.5%SI AND 1.7%C. 46

FIGURE 26: CALCULATED CARBON SOLUBILITY IN MN-FE-SI-C ALLOYS WITH A FIXED MN:FE RATIO OF 5.1 AT 1600°C AS CALCULATED IN FACTSAGE 6.4 AND AS RECONSTRUCTED FROM OLSEN ET AL [1]. THE PURPLE CROSS INDICATES THE PUBLISHED [1] METAL COMPOSITION - REFER TO TABLE 15 FOR ANALYSIS. 47

FIGURE 27: (A) EQUILIBRIUM PHASE DISTRIBUTION AS A FUNCTION OF TEMPERATURE (REPEAT OF FIGURE 21 B), WHEN REACTING GRAPHITE (REPRESENTING REFRACTORY) WITH AN EQUAL MASS OF METAL (COMPOSITION AS IN TABLE 12). (B) GRAPHICAL REPRESENTATIONS OF POTENTIAL EQUILIBRIUM PHASES AND PARTICIPATING COMPONENTS PER PHASE WHEN METAL EQUILIBRATES WITH GRAPHITE IN THE TEMPERATURE RANGE 1550°C TO 1650°C. 48

FIGURE 28: EXPERIMENTAL SETUP FOR THE PREPARATION OF THE SYNTHETIC SLAG SAMPLE AT MINTEK WITH (A) THE '50KG' INDUCTION FURNACE, (B) THE BLEND OF RAW MATERIALS, (C) THE GRAPHITE CRUCIBLE / SUSCEPTOR, (D) REFRACTORY SAND, (E) GRAPHITE THERMOCOUPLE SHEATH IMMERSSED IN THE SLAG, (F) ALUMINA THERMOCOUPLE SHEATH, (G) TYPE R THERMOCOUPLE EXTENSION WIRE AND (H) MINERAL WOOL COVER. 51

FIGURE 29: DIMENSIONS OF THE GRAPHITE CRUCIBLE UTILIZED TO PREPARE THE SYNTHETIC SLAG. 52

FIGURE 30: EQUILIBRIUM PHASE DISTRIBUTION OF SYNTHETIC SLAG BASED ON PURE MINERAL BLEND IN TABLE 26. 52

FIGURE 31: SYNTHETIC SLAG BEING PREPARED AT MINTEK BEING (A) CAST FROM THE INDUCTION FURNACE INTO A GRAPHITE SLAG POT AND (B) ALLOWED TO COOL IN THE SLAG POT. 52

FIGURE 32: EXPERIMENTAL SETUP FOR PURE COMPONENT EXPERIMENTS. 54

FIGURE 33: DESIGN OF CRUCIBLES UTILISED IN CUP TEST EXPERIMENTS WITH (A) GRAPHITE CRUCIBLE – A IN FIGURE 32 – AND (B) GRAPHITE SUSCEPTOR WITH LID – G AND H IN FIGURE 32. ALL MEASUREMENTS IN MM. 54

FIGURE 34: (A) EQUILIBRIUM PHASE DISTRIBUTION OF SYNTHETIC SLAG BASED ON THE BULK CHEMICAL COMPOSITION, AS CALCULATED WITH FACTSAGE 6.4. (B) SEM BSE IMAGE OF SYNTHETIC SLAG (SCALE BAR 20 MM) WITH (I) AMORPHOUS SLAG PHASE ONLY. 57

FIGURE 35: X-RAY DIFFRACTION PATTERN OF SYNTHETIC SLAG (NO SI-STANDARD). 57

FIGURE 36: SEM BSE MICROGRAPH OF METAL ACCUMULATION AT THE SLAG / REFRACTORY INTERFACE OF THE SAMPLE PREPARED AT 1550°C. THE SAMPLE BOTTOM AND SIDEWALLS MAGNIFIED 300 TIMES (SCALE BAR 100 MM) IN (A) AND 1800 TIMES (SCALE BAR 10 MM) IN (B). THE PHASES PRESENT WERE (I) SLAG, (II) METAL AND (III) GRAPHITE. 58

FIGURE 37: SEM BSE MICROGRAPH OF METAL ACCUMULATION AT THE SLAG / REFRACTORY INTERFACE OF THE SAMPLE PREPARED AT 1650°C. THE SAMPLE BOTTOM AND SIDEWALLS MAGNIFIED 300 TIMES (SCALE BAR 100 MM) IN (A) AND 1800 TIMES (SCALE BAR 10 MM) IN (B). THE PHASES PRESENT WERE (I) SLAG, (II) METAL, (III) GRAPHITE AND (IV) SIC. NOTE THAT THE SIC DID NOT FORM A PROTECTIVE LAYER AT THE SLAG / REFRACTORY INTERFACE BUT DETACHED FROM THE GRAPHITE. 59

FIGURE 38: SEM BSE MICROGRAPH OF METAL ACCUMULATION AT THE SLAG / REFRACTORY INTERFACE OF THE SAMPLE PREPARED AT 1650°C (SCALE BAR 10 MM; ENLARGED VIEW OF FIGURE 37). THE PHASES PRESENT WERE (I) SLAG, (II) METAL, (III) GRAPHITE AND (IV) SIC. NOTE THAT THE SIC DID NOT FORM AS A PROTECTIVE LAYER AT THE SLAG / REFRACTORY INTERFACE, BUT DETACHED UPON FORMATION. 59

FIGURE 39: MODELLED (SIC SYNTHETIC) VS. MEASURED (SIC 1 – SIC 5) EDS SPECTRA AT 15 KV OF THE SIC PHASE IDENTIFIED IN FIGURE 37. THE SAMPLE WAS COATED WITH PLATINUM. 60

FIGURE 40: EQUILIBRIUM PHASE DISTRIBUTION AS FUNCTIONS OF TEMPERATURE WHEN SYNTHETIC SLAG (COMPOSITION IN TABLE 28) EQUILIBRATES WITH GRAPHITE, AND (A) NO STEEL CONTAMINANT ADDED, (B) 0.5G STEEL CONTAMINANT ADDED AND (C) 5.0G STEEL CONTAMINANT ADDED. 61

FIGURE 41: SCHEMATIC DRAWING SHOWING THE MAIN MICROSTRUCTURAL FEATURES OF CARBON BLOCK AND RAMMING PASTE: LARGE AND SMALL CARBON-BASED AGGREGATE, BINDER PHASE, AIR GAPS AND MATRIX. 64

FIGURE 42: SEM BSE IMAGE OF AS-RECEIVED INDUSTRIAL SLAG WITH (A) AMORPHOUS SLAG PHASE, (B) SIC PHASE, (C) METAL PHASE AND (D) MNS. SCALE BAR INDICATES 20 MM. 66

FIGURE 43: SEM BSE IMAGE OF AS-RECEIVED INDUSTRIAL SLAG WITH (A) AMORPHOUS SLAG PHASE AND (B) SECONDARY SLAG PHASE. SCALE BAR INDICATES 100 MM. 67

FIGURE 44: SEM BSE IMAGE OF AS-RECEIVED INDUSTRIAL SLAG WITH (A) AMORPHOUS SLAG PHASE CONTAINING FINELY DISPERSED SIMN METAL AND MNS DROPLETS – SEE FIGURE 42 – , (B) LARGE METAL PARTICLES, (C) SIC AND (D) AMORPHOUS SLAG PHASE CONTAINING SECONDARY SLAG PHASE – SEE FIGURE 43. SCALE BAR INDICATES 500 MM. 67

FIGURE 45: SPECTRA OF EDS POINT ANALYSIS OF 5 DIFFERENT SIC PARTICLES COMPARED AGAINST THE SIMULATED SPECTRA FOR SIC AT THE SAME CONDITIONS (POINT ANALYSIS, 15 KV). 68

FIGURE 46: SEM BSE IMAGE OF AS-RECEIVED INDUSTRIAL SLAG WITH LARGE METAL PARTICLES (MARKED “A”) OF WHICH THE AVERAGE CHEMICAL COMPOSITION IS REPORTED IN TABLE 37. SCALE BAR INDICATES 100 MM. 69

FIGURE 47: XRD PATTERN OF THE SLAG SAMPLE WITH MARKERS INDICATING THE SIGNIFICANT PEAKS FOR CRYSTALLINE PHASES IDENTIFIED. 70

FIGURE 48: SEM BACKSCATTERED ELECTRON IMAGE OF (I) CARBON BLOCK AND (II) PRE-FIRED RAMMING PASTE MOUNTED IN RESIN CONTAINING 5% IODOFORM WITH (A) CARBON AGGREGATE AND (B) MATRIX. SCALE BAR INDICATES 200 MM. 71

FIGURE 49: SEM BSE IMAGE OF (I) CARBON BLOCK AND (II) PRE-FIRED RAMMING PASTE MOUNTED IN RESIN CONTAINING 5% IODOFORM WITH (A) CARBON AGGREGATE, (B) CORUNDUM, (C) SIC, (D) IODOFORM IMPREGNATED RESIN AND (E) (SI, AL, K, NA, FE)-CONTAINING MINERALS. SCALE BAR INDICATES 20 MM. 71

FIGURE 50: XRD PATTERN OF THE RAMMING PASTE REFRACTORY SAMPLE WITH MARKERS INDICATING THE SIGNIFICANT PEAKS FOR PHASES IDENTIFIED. FOR IDENTIFICATION OF THE HIGH INTENSITY PEAK SEE FIGURE 51. 72

FIGURE 51: XRD PATTERN OF THE RAMMING PASTE REFRACTORY SAMPLE WITH MARKERS IDENTIFYING THE HIGH INTENSITY PEAK. 72

FIGURE 52: XRD PATTERN OF THE CARBON BLOCK REFRACTORY SAMPLE WITH MARKERS INDICATING THE SIGNIFICANT PEAKS FOR PHASES IDENTIFIED. FOR IDENTIFICATION OF THE HIGH INTENSITY PEAK SEE FIGURE 53. 73

FIGURE 53: XRD PATTERN OF THE CARBON BLOCK REFRACTORY SAMPLE WITH MARKERS IDENTIFYING THE HIGH INTENSITY PEAK. 73

FIGURE 54: PORE SIZE DISTRIBUTION OF THREE SAMPLES OF RAMMING PASTE AGGREGATE AND AN EXAMPLE OF XRT MICROGRAPHS DEFINING THE VOLUME OF MATERIAL ON WHICH ONE OF THE MEASUREMENTS WERE BASED. 74

FIGURE 55: PORE SIZE DISTRIBUTION OF THREE SAMPLES OF PRE-FIRED RAMMING PASTE MATRIX AND AN EXAMPLE OF XRT MICROGRAPHS DEFINING THE VOLUME OF MATERIAL ON WHICH ONE OF THE MEASUREMENTS WERE BASED.	74
FIGURE 56: PORE SIZE DISTRIBUTION OF THREE SAMPLES OF CARBON BLOCK AND AN EXAMPLE OF XRT MICROGRAPHS DEFINING THE VOLUME OF MATERIAL ON WHICH ONE OF THE MEASUREMENTS WERE BASED.....	75
FIGURE 57: MICROGRAPHS OBTAINED FOR PRE-FIRED RAMMING PASTE WITH (I) XRT IMAGES AND (II) SEM BSE IMAGE AT 10KV OF (A) AGGREGATE AND (B) MATRIX; FOR CARBON BLOCK WITH (III) XRT IMAGE AND (IV) SEM BSE IMAGE AT 15KV. SCALE BAR INDICATES 200 MM IN (II) AND 200 MM IN (IV).	75
FIGURE 58: QUATERNARY OXIDE PHASE DIAGRAM FOR THE 20%AL ₂ O ₃ – CAO – MGO – SIO ₂ SLAG SYSTEM ([125]) WITH THE COMPOSITION OF THE SECONDARY SLAG PHASE (SIMPLIFIED TO 20%AL ₂ O ₃ – 10%MGO – 45%SIO ₂ – 25%CAO) INDICATED AS A RED DOT.....	76
FIGURE 59: EQUILIBRIUM PHASE DISTRIBUTION (PERCENTAGE BY MASS) OF (I) THE AMORPHOUS SLAG PHASE AND (II) THE SECONDARY SLAG PHASE BASED ON THE BULK CHEMICAL COMPOSITION; CALCULATED WITH FACTSAGE 6.4. IN (III) THE PREDICTED EQUILIBRIUM PHASES ARE SHOWN FOR THE COMPOSITION OF THE SECONDARY SLAG PHASE, IF ANORTHITE FORMATION IS SUPPRESSED.	77
FIGURE 60: EQUILIBRIUM PHASE DISTRIBUTION (PERCENTAGE BY MASS) OF (A) THE CARBON BLOCK AND (B) THE PRE-FIRED RAMMING PASTE BASED ON THE CHEMICAL COMPOSITIONS IN TABLE 42; CALCULATED WITH FACTSAGE 6.4.....	79
FIGURE 61: EQUILIBRIUM PHASE DISTRIBUTION WHEN REACTING 100G INDUSTRIAL SLAG WITH 100G OF (A) CARBON BLOCK AND (B) 100G PREBAKED RAMMING PASTE AT DIFFERENT TEMPERATURES. (SLAG COMPOSITION AS GIVEN IN TABLE 34 AND REFRACTORY COMPOSITIONS AS IN TABLE 42).....	79
FIGURE 62: SKETCH OF THE WETTABILITY FURNACE AND EXPERIMENTAL SETUP [39].	81
FIGURE 63: RESULTS OF TEMPERATURE VALIDATION EXPERIMENT INDICATING OFFSET OF PYROMETER MEASUREMENT 14°C BELOW AND OF TYPE-C THERMOCOUPLE 47°C ABOVE MELTING POINT OF PURE IRON (1535°C).	83
FIGURE 64: SKETCH OF SAMPLE PREPARATION FOR WETTING EXPERIMENTS ANALYSIS (AFTER CIFTJA ET AL., 2010).	83
FIGURE 65: WETTING ANGLE – θ – OF SYNTHETIC SLAG ON RAMMING PASTE MATRIX SUBSTRATE IN AN ARGON ATMOSPHERE AS MEASURED IN (A) NON-WETTING CONDITIONS AND (B) WETTING CONDITIONS.	84
FIGURE 66: WETTING ANGLE – θ – OF SYNTHETIC SLAG ON RAMMING PASTE MATRIX SUBSTRATE IN AN ARGON ATMOSPHERE AS A FUNCTION OF TIME AND TEMPERATURE. THE HOLDING TEMPERATURE WAS 1588°C.....	85
FIGURE 67: COMPARISON BETWEEN WETTING ANGLES OF TWO DUPLICATE TESTS. THE STANDARD DEVIATION BOUNDARIES ARE BASED ON THE LARGEST VALUE OF STANDARD DEVIATION (θ) CALCULATED UNDER WETTING CONDITIONS – SEE TABLE 44.	86
FIGURE 68: BALLING (MELTING) TEMPERATURES OF SYNTHETIC SLAG ON DIFFERENT SUBSTRATES IN ARGON PLOTTED ON THE EQUILIBRIUM PHASE DISTRIBUTION OF SYNTHETIC SLAG (PERCENTAGE BY MASS) BASED ON THE CHEMICAL COMPOSITIONS IN TABLE 27 DETERMINED IN FACTSAGE 6.4.	86
FIGURE 69: WETTING ANGLE – θ – OF SYNTHETIC SLAG ON RAMMING PASTE MATRIX SUBSTRATE IN AN ARGON ATMOSPHERE AS A FUNCTION OF TIME AND TEMPERATURE. OPEN SYMBOLS REPRESENT IMAGES IN TABLE 46 TAKEN DURING HEAT-UP PHASE AND RED SYMBOLS IMAGES TAKEN AT HOLDING TEMPERATURE AT 5 MINUTE INTERVALS. THE HOLDING TEMPERATURE WAS 1588°C.....	90
FIGURE 70: DEFINITIONS OF PARAMETERS APPLIED IN VOLUME CALCULATIONS OF DROPLETS UNDER (A) WETTING AND (B) NON-WETTING CONDITIONS.	91

FIGURE 71: V_x/V_{REF} OF IMAGES IN TABLE 46 (NUMERICAL VALUES) SUPERIMPOSED ON THE MEASURED CONTACT ANGLES (AS PLOTTED IN FIGURE 69), FOR THE SYNTHETIC SLAG ON A RAMMING PASTE MATRIX SUBSTRATE IN AN ARGON ATMOSPHERE WITH THE HOLDING TEMPERATURE AT 1588°C. 92

FIGURE 72: CALCULATED VOLUME RATIO (V_x/V_{REF}) OF SYNTHETIC SLAG ON RAMMING PASTE MATRIX SUBSTRATE IN AN ARGON ATMOSPHERE AT 5, 15 AND 25 MINUTES INTO THE HOLDING PERIOD. CALCULATIONS WERE DONE AT 1 SECOND INTERVALS FOR 30 SECONDS AT EACH HOLDING PERIOD. RED LINES REPRESENT CALCULATED AVERAGE VOLUME RATIO OVER EACH 30 SECOND TIME PERIOD. THE HOLDING TEMPERATURE WAS 1588°C. 93

FIGURE 73: SEM BSE MICROGRAPH AND EDS ELEMENTAL MAPS FOR SI, CA AND AL DETERMINED AT 15KV FOR SYNTHETIC SLAG ON RAMMING PASTE MATRIX SUBSTRATE IN AN ARGON ATMOSPHERE WITH (A) REFRACTORY AGGREGATE, (B) REACTION PRODUCT AND (C) REFRACTORY MATRIX INFILTRATED BY SLAG. THE HOLDING TEMPERATURE WAS 1588°C. 94

FIGURE 74: MEASURED EDS SPECTRUM (15KV) OF SI-RICH LAYER IN FIGURE 73. THE SI-RICH LAYER FORMED AT THE INTERFACE BETWEEN SYNTHETIC SLAG AND AN AGGREGATE PARTICLE PRESENT IN THE RAMMING PASTE MATRIX. THE EXPERIMENT WAS CONDUCTED WITH SYNTHETIC SLAG ON RAMMING PASTE MATRIX SUBSTRATE IN AN ARGON ATMOSPHERE. THE HOLDING TEMPERATURE WAS 1588°C. 94

FIGURE 75: WETTING ANGLE – θ – AS FUNCTIONS OF TIME, FOR INDUSTRIAL SLAG ON DIFFERENT SUBSTRATES (CARBON BLOCK, RAMMING PASTE AGGREGATE AND RAMMING PASTE MATRIX SUBSTRATES) IN EITHER AR OR CO ATMOSPHERES. THE HOLDING TEMPERATURE WAS 1588°C. 95

FIGURE 76: RANGE OF BALLING (MELTING) TEMPERATURES OF INDUSTRIAL SLAG FOR WETTABILITY TESTS CONDUCTED IN ARGON GAS ON DIFFERENT TYPES OF REFRACTORY SUBSTRATES PLOT, SUPERIMPOSED ON THE EQUILIBRIUM PHASE DISTRIBUTION OF INDUSTRIAL SLAG (PERCENTAGE BY MASS), CALCULATED FOR THE CHEMICAL COMPOSITIONS IN TABLE 34 USING FACTSAGE 6.4. THE BALLING TEMPERATURE OF THE SLAG IN CO-GAS (NOT INDICATED ON GRAPH) RANGED BETWEEN 1563°C AND 1576°C. 96

FIGURE 77: CALCULATED VOLUME RATIO OF INDUSTRIAL SLAG DROPLET ON RAMMING PASTE MATRIX SUBSTRATE IN (A) AN AR-GAS ATMOSPHERE AND (B) A CO-GAS ATMOSPHERE AT 5, 15 AND 25 MINUTES INTO THE HOLDING PERIOD. CALCULATIONS WERE DONE AT 1 SECOND INTERVALS FOR 30 SECONDS AT EACH HOLDING PERIOD. RED LINES REPRESENT CALCULATED AVERAGE VOLUME RATIO OVER EACH 30-SECOND PERIODS. 96

FIGURE 78: STITCHED (A) LOM AND (B) SEM BSE MICROGRAPHS OF (I) CARBON BLOCK EXPOSED TO (II) INDUSTRIAL SLAG AT 1592°C IN AN ARGON ATMOSPHERE WITH (III) INFILTRATION OF THE SLAG INTO THE CARBON BLOCK. SCALE BARS INDICATE 1MM ON (A) AND 100 MM ON (B). MAXIMUM INFILTRATION DEPTH REPORTED IN TABLE 49 INDICATED BY YELLOW LINE ON (B). 98

FIGURE 79: STITCHED (A) LOM AND (B) SEM BSE MICROGRAPHS OF (I) RAMMING PASTE AGGREGATE EXPOSED TO (II) INDUSTRIAL SLAG AT 1592°C IN AN ARGON ATMOSPHERE WITH INFILTRATION OF SLAG INTO THE (III) RAMMING PASTE AGGREGATE AND (IV) RAMMING PASTE MATRIX. SCALE BARS INDICATE 1MM ON (A) AND 100 MM ON (B). MAXIMUM INFILTRATION DEPTH REPORTED IN TABLE 49 INDICATED BY YELLOW LINE ON (B). 99

FIGURE 80: STITCHED (A) LOM AND (B) SEM BSE MICROGRAPHS OF (I) RAMMING PASTE MATRIX EXPOSED TO (II) INDUSTRIAL SLAG AT 1592°C IN AN ARGON ATMOSPHERE WITH (III) METAL DROPLETS AND (IV) INFILTRATION OF SLAG INTO THE RAMMING PASTE MATRIX. SCALE BARS INDICATE 1MM IN (A) AND 100 MM IN (B). MAXIMUM INFILTRATION DEPTH REPORTED IN TABLE 49 INDICATED BY YELLOW LINE IN (B). 100

FIGURE 81: MEASURED EDS SPECTRA (AREA ANALYSIS AT 5KV) OF POWDERED INDUSTRIAL SLAG (SLAG02) AND INDUSTRIAL SLAG BALL FORMED IN WETTABILITY STUDY PERFORMED IN CO-GAS (BALL02). NOTE THE MUCH LARGER C PEAK IN THE LATTER CASE. 103

FIGURE 82: CORRELATION BETWEEN WETTING ANGLE AND MAXIMUM INFILTRATION DEPTH AS MEASURED BY (A) CIFTJA ET AL [47] FOR MOLTEN SOLAR GRADE SILICON ON DIFFERENT GRADES OF GRAPHITE AND (B)

FOR THE STUDY PRESENTED HERE FOR INDUSTRIAL SLAG ON COMMERCIAL REFRACTORIES IN AR-GAS ATMOSPHERE 15 MINUTES INTO THE HOLDING TIME AT 1588°C. IN (B) SOLID DIAMOND REPRESENTS RAMMING PASTE AGGREGATE, SOLID TRIANGLE REPRESENTS RAMMING PASTE MATRIX AND OPEN CIRCLE REPRESENTS CARBON BLOCK. FOR INFILTRATION DEPTHS IN (B) REFER TO TABLE 49 AND FOR WETTING ANGLES TO FIGURE 75. 104

FIGURE 83: CORRELATION BETWEEN MAXIMUM INFILTRATION DEPTH - FIGURE 75 - AND (A) TOTAL POROSITY - TABLE 41 -, (B) AVERAGE OPEN EQUIVALENT PORE SIZE - FIGURE 54 TO FIGURE 56 - AND (C) FINAL VOLUME RATIO. SOLID DIAMOND REPRESENTS RAMMING PASTE AGGREGATE, SOLID TRIANGLE REPRESENTS RAMMING PASTE MATRIX AND OPEN CIRCLE REPRESENTS CARBON BLOCK. DATA PRESENTED FOR WETTING ANGLE AT 15 MINUTES INTO THE HOLDING TIME AT 1588°C FOR INDUSTRIAL SLAG ON COMMERCIAL REFRACTORIES IN AR-GAS ATMOSPHERE. 104

FIGURE 84: EXPERIMENTAL APPARATUS UTILISED IN CUP TESTS. 106

FIGURE 85: DESIGN OF CRUCIBLES UTILISED IN CUP TEST EXPERIMENTS WITH (A) CARBON BLOCK CRUCIBLE AND (B) RAMMING PASTE CRUCIBLE WITH GRAPHITE SHELL - ALL MEASUREMENTS IN MM. 107

FIGURE 86: SECTIONED (A) CARBON BLOCK CRUCIBLE EXPOSED TO (B) INDUSTRIAL SLAG AT (I) 1500°C AND (II) 1600°C FOR 4 HOURS IN AN ARGON ATMOSPHERE. THE CAVITY WAS FILLED WITH (C) RESIN AFTER COOLING TO KEEP SLAG INTACT DURING CUTTING. WETTING ANGLES WERE MEASURED AS DESCRIBED IN CHAPTER 6. 109

FIGURE 87: STITCHED LOM-IMAGE OF CARBON BLOCK REACTED WITH INDUSTRIAL SIMN SLAG AT 1600°C FOR 4 HOURS. THE RED LINE IS THE BOUNDARY INDICATING THE EXTENT OF INFILTRATION OF SLAG INTO THE REFRACTORY WITH (A) SLAG, (B) REACTION ZONE, (C) AGGREGATE AND (D) UNREACTED REFRACTORY. YELLOW ARROW INDICATES DEPTH OF INFILTRATION. SCALE BAR INDICATES 2MM. 110

FIGURE 88: (I) LOM AND (II) SEM BSE IMAGE OF RAMMING PASTE IN CONTACT WITH INDUSTRIAL SLAG AT 1600°C FOR 4 HOURS WITH (A) SLAG, (B) REACTION ZONE, (C) AGGREGATE AND (D) UNREACTED REFRACTORY. YELLOW LINES INDICATE DEPTHS OF INFILTRATION. THE POSITION OF (II) IS INDICATED IN THE RECTANGLE IN (I). SCALE BARS INDICATE (I) 1MM AND (II) 100 MICRON. 110

FIGURE 89: SEM BACKSCATTERED ELECTRON IMAGE OF SLAG-REFRACTORY INTERFACE FOR CARBON BLOCK EXPOSED TO INDUSTRIAL SLAG AT 1600°C FOR 4 HOURS IN A CRUCIBLE TEST WITH (A) AGGREGATE, (B) MATRIX, (C) SIC, (D) SLAG AND (E) METAL. SCALE BAR INDICATE 15 MICRON. 111

FIGURE 90: SEM BACKSCATTERED ELECTRON IMAGE OF RAMMING PASTE EXPOSED TO INDUSTRIAL SLAG AT 1600°C FOR 4 HOURS IN A CRUCIBLE TEST WITH (A) AGGREGATE, (B) REMNANTS OF MATRIX, (C) SIC, (D) SLAG, (E) METAL AND (F) REACTION ZONES. SCALE BAR INDICATE 10 MICRON. 111

FIGURE 91: CORRELATION BETWEEN MAXIMUM INFILTRATION DEPTH - TABLE 53 - AND (A) TOTAL POROSITY - TABLE 41 - AND (B) AVERAGE OPEN EQUIVALENT PORE SIZE - FIGURE 54 TO FIGURE 56. SOLID CIRCLE REPRESENTS RAMMING PASTE AND OPEN CIRCLE REPRESENTS CARBON BLOCK. TOTAL POROSITY OF RAMMING PASTE BASED ON VOLUME AVERAGE OF AGGREGATE AND MATRIX AND PORE SIZE ON WEIGHTED AVERAGE. MASS RATIO OF 20/80 MATRIX/AGGREGATE AND BULK DENSITY OF 1.8 G/CM³ WAS ASSUMED. 113

FIGURE 92: HIGH RESOLUTION XRD PATTERNS – DERIVED FROM FIGURE 51 AND FIGURE 53 – OF THE RAMMING PASTE AND CARBON BLOCK REFRACTORY SAMPLES AT THE GRAPHITE PEAK. 113

FIGURE 93: SEM BSE OF RAMMING PASTE EXPOSED TO INDUSTRIAL SLAG AT 1600°C FOR FOUR HOURS. MICROGRAPHS WERE TAKEN FROM THE SIDE OF THE CRUCIBLE AND INDICATE THE PRESENCE OF BOTH SIC AND SIMN REACTION PRODUCTS. SCALE BAR INDICATE 100 MICRON. 114

FIGURE 94: SEM BSE OF CARBON BLOCK EXPOSED TO INDUSTRIAL SLAG AT 1600°C FOR FOUR HOURS. SCALE BAR INDICATE 20 MICRON. 115

FIGURE 95: COLLAGE OF SEM BSE MICROGRAPHS INDICATING THE PRESENCE OF SMALL METAL DROPLETS (BRIGHT SPOTS), SMALLER THAN 25 MICRON, BOTH ON THE SIDE OF THE CRUCIBLE AND AT THE BOTTOM FOR THE CUP TEST WHERE RAMMING PASTE EXPOSED TO INDUSTRIAL SLAG AT 1600°C FOR FOUR

HOURS. THE AREA IN THE RED RECTANGLE IN ENLARGED IN FIGURE 96. SCALE BAR INDICATES 100 MICRON.	116
FIGURE 96: SEM BSE MICROGRAPHS INDICATING THE PRESENCE OF SMALL METAL DROPLETS (BRIGHT SPOTS) CONCENTRATED NEAR THE RAMMING PASTE REFRACTORY AS OPPOSED TO THE BULK OF THE INDUSTRIAL SLAG ON THE SIDEWALL OF THE CRUCIBLE FOR THE CUP TEST WHERE RAMMING PASTE EXPOSED TO INDUSTRIAL SLAG AT 1600°C FOR FOUR HOURS. SCALE BAR INDICATES 100 MICRON.	117
FIGURE 97: SEM BSE MICROGRAPHS INDICATING THE PRESENCE OF SIC (DARK GREY PHASE) CONCENTRATED IN THE SLAG:REFRACTORY REACTION ZONE BOTH ON THE (A) SIDE AND AT THE (B) BOTTOM OF THE CRUCIBLE FOR RAMMING PASTE EXPOSED TO INDUSTRIAL SLAG AT 1600°C FOR FOUR HOURS. SCALE BAR INDICATES 100 MICRON.	117
FIGURE 98: SEM BSE IMAGES OF RAMMING PASTE AFTER CONTACT WITH INDUSTRIAL SLAG AT 1600°C FOR 4 HOURS (REGION SHOWN IS SLAG NEAR THE LOWER INTERFACE WITH THE REFRACTORY) INDICATING DIAMETERS OF SEVERAL METAL DROPLETS; 300 TIMES MAGNIFICATION. THE NUMBERS ON THE MICROGRAPH INDICATE THE APPARENT METAL DROPLET DIAMETERS IN MICRON. SCALE BAR INDICATES 100 MICRON.	119
FIGURE 99: SEM BSE IMAGES OF RAMMING PASTE AFTER CONTACT WITH INDUSTRIAL SLAG AT 1600°C FOR 4 HOURS (REGION SHOWN IS SLAG NEAR THE LOWER INTERFACE WITH THE REFRACTORY) INDICATING DIAMETERS OF SEVERAL METAL DROPLETS; 2500 TIMES MAGNIFICATION. THE NUMBERS ON THE MICROGRAPH INDICATE THE APPARENT METAL DROPLET DIAMETERS IN MICRON. SCALE BAR INDICATES 10 MICRON.	119
FIGURE 100: TWO SECTIONS IN THE SEM BSE MICROGRAPH FROM FIGURE 96 INDICATING THE AREAS ON WHICH IMAGE ANALYSES WERE CONDUCTED TO QUANTIFY THE PRESENCE OF SMALL METAL DROPLETS (BRIGHT SPOTS) (A) CONCENTRATED NEAR THE REFRACTORY AS OPPOSED TO THE (B) BULK OF THE SLAG. SCALE BAR INDICATES 100 MICRON.	120
FIGURE 101: SEM BSE IMAGES OF FOR RAMMING PASTE AFTER CONTACT WITH INDUSTRIAL SLAG AT 1600°C FOR 4 HOURS, SHOWING METAL DROPLETS SIZE CATEGORIES: (A,B) LARGE, (C) APPARENT DIAMETER OF 5 – 10 MICRON IN SLAG, (D) APPARENT DIAMETER OF 5 – 10 MICRON AT INTERFACE BETWEEN SLAG AND REACTION ZONE AND (E) ALONG RIM OF AGGREGATE PARTICLE. ALSO INDICATED IS (F) SIC. SCALE BARS INDICATE (I) 100 MICRON AND (II) 10 MICRON.	121
FIGURE 102: SIMN LINING DESIGN – DRAWING TO SCALE.	126
FIGURE 103: TAP-HOLE AREA OF SIMN FURNACE WITH (A) THERMAL IMAGE AND (B) VISIBLE-LIGHT PHOTOGRAPH OF SECTION OF STEEL SHELL ON WHICH THERMAL IMAGE WAS BASED. THE MAXIMUM TEMPERATURE OF 480°C (INDICATED) WAS MEASURED AT THE TAP-HOLE ITSELF.	127
FIGURE 104: REFRACTORY DESIGN DRAWING WITH RED LINE INDICATING THE REFRACTORY HOT FACE AS DETERMINED DURING EXCAVATION – DRAWING TO SCALE.	129
FIGURE 105: VIEW OF TAP-HOLE REGION WITH (A) SUPER DUTY FIRE-CLAY BRICKS, (B) HIGH GRADE CARBON RAMMING, (C) SIC BRICKS, (D) SLAG WITH BURDEN AND / OR COKE BED MATERIAL, (E) MIXED MATERIAL CONTAINING METAL AND (F) TAP CLAY MUSHROOM. (A) INDICATES THE WORN TAP-HOLE FILLED WITH A SLAG-AND-COKED BED TOP LAYER AND (MAINLY METAL BOTTOM LAYER AND (B) THE WORN CHANNEL 500 WIDE AND PARTIALLY FILLED WITH SLAG WITH COKE BED. THE TAP-HOLE (FIGURE 109) IS TO THE LEFT OF (E) AND LOWER (D).	130
FIGURE 106: CLOSER VIEW OF TAP-HOLE B WITH (A) SUPER DUTY FIRE-CLAY BRICKS, (B) HIGH GRADE CARBON RAMMING, (C) SIC BRICKS, (D) SLAG WITH BURDEN AND / OR COKE BED MATERIAL, (E) MIXED MATERIAL CONTAINING METAL AND (F) TAP CLAY MUSHROOM.	130
FIGURE 107: CLOSER VIEW OF ZONES IN FRONT OF TAP-HOLE B WITH (B) HIGH GRADE CARBON RAMMING, (C) SIC BRICKS, (D) SLAG WITH BURDEN AND / OR COKE BED MATERIAL, (E) MIXED MATERIAL CONTAINING METAL AND (F) TAP CLAY MUSHROOM.	131

FIGURE 108: GOING INTO TAP-HOLE B WITH (C) SIC BRICKS, (D) SLAG WITH BURDEN AND / OR COKE BED MATERIAL, (E) MIXED MATERIAL CONTAINING METAL AND (F) TAP CLAY MUSHROOM INFILTRATED WITH SLAG.	131
FIGURE 109: TAP-HOLE B WITH (C) SIC BRICKS, (D) SLAG WITH BURDEN AND / OR COKE BED MATERIAL AND (E) MIXED MATERIAL CONTAINING METAL.	132
FIGURE 110: TAP-HOLE B PUT INTO PERSPECTIVE. THE OPERATING PERSONNEL ARE STANDING ON (G) THE STEEL SHELL / FIRECLAY CASTABLE OF THE FURNACE HEARTH SAMPLING THE METAL LAYER AT THE INTERFACE BETWEEN THE (I) HIGH GRADE CARBON RAMMING AND (J) BURDEN. ALSO NOTE THE (H) FIVE LAYERS OF SUPER DUTY FIRECLAY BRICKS IN THE HEARTH.	132
FIGURE 111: EQUILIBRIUM PHASE DISTRIBUTION OF INDUSTRIAL SLAG BASED ON COMPOSITIONS IN TABLE 61 WITH SOLID LINES PRESENTING SLAG CORRECTED FOR METAL ENTRAINMENT AND DOTTED LINES NOT.	134
FIGURE 112: PREDICTED (A) PHASE DISTRIBUTION OF AS-RECEIVED METAL AND (B) CHEMICAL COMPOSITION OF LIQUID METAL PHASE AS A FUNCTION OF TEMPERATURE.	135
FIGURE 113: CALCULATED CARBON SOLUBILITY IN MN-SI-FE ALLOYS WITH FIXED MN:FE RATIO OF 4.5 AT 1500–1700°C. THE BLACK CROSS INDICATES THE COMPOSITION OF THE ALLOY GIVEN IN TABLE 62.	135
FIGURE 114: PREDICTED PHASE DISTRIBUTION OF 100G SLAG REACTED WITH 100G OF (A) SIC- AND (B) C-BASED REFRACTORY MATERIAL AS A FUNCTION OF TEMPERATURE. SOLID LINES REPRESENT THE BORDERS FOR PHASE DISTRIBUTION CALCULATED FROM THE AS-RECEIVED SLAG ANALYSIS AND DOTTED LINES CALCULATED FROM THE CORRECTED SLAG ANALYSIS.	136
FIGURE 115: PREDICTED CHEMICAL COMPOSITION OF (A) SLAG, (B) METAL AND (C) GAS PHASES THAT FORM WHEN REACTING 100G SLAG WITH 100G OF SIC- (GREY SYMBOLS) OR C- (BLACK SYMBOLS) BASED REFRACTORY MATERIAL AS FUNCTIONS OF TEMPERATURE.	137
FIGURE 116: CALCULATED EQUILIBRIUM CONSUMPTION OF (A) CARBON AND (B) SIC THROUGH REACTION WITH EITHER SLAG OR METAL, WHERE THE MASS OF SLAG OR METAL IS EQUAL TO THAT OF THE REFRACTORY. EQUILIBRIUM CALCULATIONS WERE CONDUCTED WITH FACTSAGE.	138
FIGURE 117: MOLAR VOLUME OF (A) FESI-ALLOY MEASURED AT 1450°C AND (B) SIMN-ALLOY MEASURED AT 1550°C, WITH IDEAL RELATIONSHIP SHOWN.	171

List of Equations

EQUATION 1: DEFINITION OF B_5	3
EQUATION 2: SCHERRER'S EQUATION	13
EQUATION 3: YOUNG'S EQUATION	16
EQUATION 4: DUPRE'S EQUATION	17
EQUATION 5: WENZEL'S EQUATION.....	17
EQUATION 6: AKSAY'S EQUATION.....	18
EQUATION 7: CASSIE-BAXTER LAW	18
EQUATION 8: CONTACT ANGLE FROM SPHERICAL CAP DATA.....	20
EQUATION 9: FOURIER'S LAW	24
EQUATION 10: NEWTON'S LAW	24
EQUATION 11: FOURIER'S LAW APPLIED TO THE RADIAL DISTANCE IN A CYLINDER.....	25
EQUATION 12: OHM'S LAW	25
EQUATION 13: CONDUCTIVE RESISTANCE	26
EQUATION 14: CONVECTIVE RESISTANCE	26
EQUATION 15: HEAT TRANSFER RATE TO LINING BY CONVECTION.....	26
EQUATION 16: HEAT TRANSFER RATE THROUGH THE LINING	27
EQUATION 17: FREEZE LINING RESISTANCE	27
EQUATION 18: HEAT TRANSFER RATE THROUGH AN INSULATING LINING.....	28
EQUATION 19: CHANGE IN GIBBS' FUNCTION #1.....	33
EQUATION 20: CHANGE IN GIBBS' FUNCTION #2.....	33
EQUATION 21: REACTION QUOTIENT.....	33
EQUATION 22: ACTIVITY	34
EQUATION 23: PHASE RULE [120]	44
EQUATION 24: TOTAL POROSITY (P_T)	65
EQUATION 25: EQUIVALENT PORE SIZE (EPS)	65
EQUATION 26: AVERAGE ATOMIC NUMBER (ANF)	65
EQUATION 27: VOLUME OF THE SPHERICAL CAP [126]	90
EQUATION 28: FORMATION OF SIC THROUGH SiO_2 REDUCTION	93
EQUATION 29: DEPOSITION OF CARBON FROM CO-GAS [69].....	103
EQUATION 30: HADAMARD-RYBCZYNSKI EXPRESSION [131].....	118
EQUATION 31: ANDERSON-HASLER EXPRESSION [134]	123
EQUATION 32: REFRACTORY CONSUMPTION CALCULATION #1.....	138
EQUATION 33: REFRACTORY CONSUMPTION CALCULATION #2.....	138
EQUATION 34: SLAG AVAILABLE FOR REACTION PER TON OF SLAG TAPPED.	139
EQUATION 35: DENSITY OF PURE LIQUID METAL AS A FUNCTION OF TEMPERATURE (P(T)) [142], [143]	171
EQUATION 36: DENSITY OF LIQUID FE-C ALLOYS AS A FUNCTION OF CARBON CONTENT AND TEMPERATURE [144].....	172
EQUATION 37: FLUX CALCULATION.....	173
EQUATION 38: RATE OF SiO_2 TRANSFER THROUGH BOUNDARY LAYER (KG/H).....	173
EQUATION 39: AMOUNT OF SLAG AVAILABLE FOR TAP PER TON OF SLAG TAPPED.	174

List of Abbreviations

BSE	Back-scattered electron
EDS	Energy dispersive spectroscopy
EMPA	Electron microprobe analysis
FEGSEM	Field Emission Gun Scanning Electron Microscope
FeMn	Ferromanganese
FeSi	Ferrosilicon
HCFeMn	High carbon ferromanganese
ICP	Inductively couple plasma
KMnO ₄	Potassium permanganate
LCSiMn	Low carbon silicomanganese
LOM	Light optical microscope
MCFeMn	Medium carbon ferromanganese
MIP	Mercury intrusion porosimetry
MnCl ₂	Manganous chloride
MnO	Manganous oxide
MnO ₂	Manganese dioxide
MnS	Manganese sulphide
MnSO ₄	Manganese sulphate
SAF	Submerged arc furnace
SE	Secondary electron
SEM	Scanning electron microscope
SiC	Silicon carbide
SiMn	Silicomanganese
SiO ₂	Silicon dioxide
tpa	Tonnes per annum
XRD	X-ray diffraction
XRF	X-ray fluorescence
XRT	X-ray tomography

1 Introduction

1.1 Manganese and its compounds

Manganese is the 12th most abundant element in the Earth's crust, with an average concentration of 0.1 per cent. It is the 4th most abundant metal in commercial use. In nature, manganese is found in the form of oxides, carbonates, and silicates [1-3]. Manganese was recognized and isolated as a separate chemical element in 1774 by Carl Wilhelm Scheele and Johan Gottlieb Gahn [2]. The Spartans, in ancient Greece, utilized manganese in their steel weapons to give superior strength. The Romans and Egyptians utilized manganese compounds to remove or add colour to their glass during glassmaking [1], as is still done today [3]. The Chinese utilized it in glazes to give their pottery an aubergine colour [4]. The first commercial use of manganese during the industrial revolution was as the laboratory reagent, KMnO_4 , which was produced for the first time by Johann Glauber in 1659 [5]. MnO_2 was utilized in the manufacture of chlorine in the mid-18th century [2].

1.2 Brief history of manganese ferroalloy production

As commodity, large scale consumption of manganese started when Sir Henry Bessemer introduced manganese as deoxidizing agent in the eponymous steelmaking process he developed in 1855. He added spiegeleisen after the oxygen blow to remove oxygen from the steel and add manganese and carbon. This was done as pig iron (produced in blast furnaces) contained high levels (10-20 per cent) of manganese. The idea was patented by Robert Mushet. In 1866 Siemens patented the use of ferromanganese in steelmaking to control the levels of sulphur and phosphorus. This paved the way not only for modern steelmaking, but also for the modern production of manganese ferroalloys [1].

Commercial production of ferromanganese containing 65 per cent Mn, started in France in 1875, using blast furnace technology [6]. From 1890 ferromanganese could also be produced by SAF [6], but for the first half of the 20th century all ferromanganese was produced in blast furnaces [1]. Blast furnaces use 4-6 times as much coke per ton of ferromanganese as do SAFs, so due to the high cost and scarcity of coke, and the relative high capital investment required to build a blast furnace, electric arc furnaces started to replace blast furnace technology in the second half of the 20th century. By 2005 approximately three-quarters of the world production was by SAF and the remainder by blast furnace [1].

1.3 Commercial grades of manganese ferroalloy and their applications

Manganese ferroalloys produced commercially can be divided into the following four categories [1], which are listed together with their typical chemical compositions in the Table 1: HCFeMn, refined ferromanganese (MCFeMn), SiMn and LCSiMn [7], [8].

Table 1: Categories of manganese ferroalloys produced internationally and their typical chemical composition (balance Fe) [7], [8].

	Mn (%)	Si (%)	C _{max} (%)	P _{max} (%)	S _{max} (%)
HCFeMn – grade A and B	74.0 – 82.0	1.2	7.5	0.35	0.050
MCFeMn – grade A to D	80.0 – 85.0	0.35 – 1.5	1.5	0.30	0.020
LCFeMn – grade A and B	80.0 – 90.0	2.0 – 7.0	0.75	0.30	0.020
SiMn – grade A	65.0 – 68.0	18.5 – 21.0	1.5	0.20	0.040
SiMn – grade B	65.0 – 68.0	16.0 – 18.5	2.0	0.20	0.040
SiMn – grade C	65.0 – 68.0	12.5 – 16.0	3.0	0.20	0.040

Ninety per cent of the manganese ferroalloys produced is utilized in steelmaking [1] where manganese is added to steel in order to:

- Deoxidize the steel i.e. remove oxygen from the steel as MnO, although silicon and aluminium are stronger deoxidizers. Silicon deoxidizes steel and manganese enhances the effect of silicon deoxidation by forming stable manganese silicates and aluminates [1].
- React with sulphur to form MnS instead of FeS. At hot rolling temperatures of 900°C to 1100°C steel becomes brittle due to the formation of liquid FeS on grain boundaries. The phenomenon is referred to as ‘hot shortness’. MnS remains solid at hot rolling temperatures [9].
- Influence the strength, toughness and hardness of the steel [1].

The graph in Figure 4 reflects the world’s real unit consumption of manganese ferroalloys in kilograms per metric ton of steel from 2001 – 2010 [10].

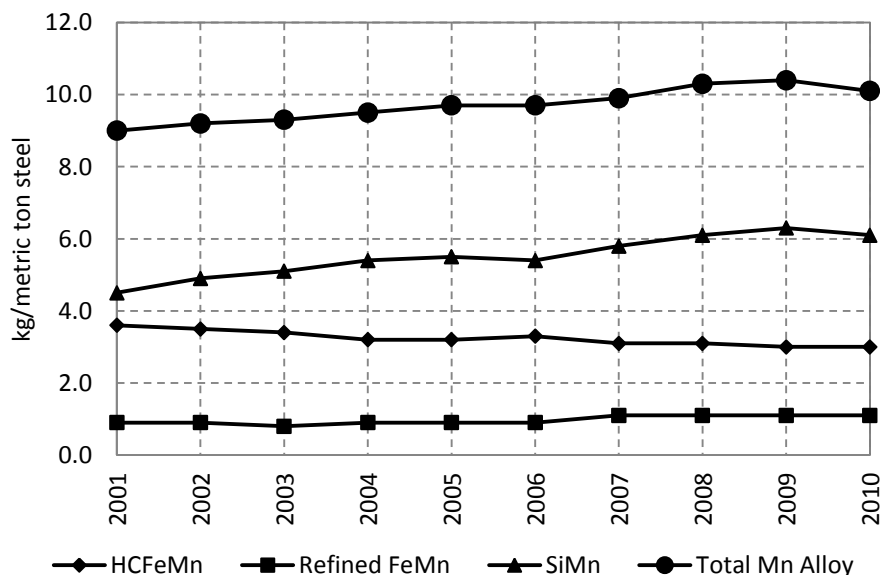


Figure 4: World real unit consumption of manganese ferroalloys, 2001 – 2010 [10]–[12].

For the five years 2006 – 2010, manganese ferroalloy consumption was in the order of 10 kg Mn per ton of steel. It is said that SiMn is preferred over HCFeMn and FeSi as an additive in steelmaking, as a cleaner steel is produced more readily due to the formation of liquid manganese silicates as opposed to solid SiO₂ [1]. The trend is reflected in Figure 4 in the rise in consumption of SiMn and decrease in

consumption of HCFeMn over the 10 year period investigated (2001 – 2010). The refined grades, refined FeMn and LCFeSi, are utilized in steels with low carbon specifications [1].

Other applications of manganese include:

- *Electrolytic manganese metal* utilized primarily in alloys of aluminium and copper where it improves the corrosion resistance of aluminium [1].
- $KMnO_4$ utilized as disinfectant, deodorant and as bleaching and analytical reagent [2];
- $MnSO_4$ utilized as fertiliser, especially in citrus production, and as reducing agent in the manufacture of paint and varnish driers [2];
- MnO utilized as raw material in the production of manganous salts, additive in fertilizers and reagent in textile printing [2];
- $MnCl_2$ utilized as catalyst in the chlorination of organic compounds and as an additive to animal feed [2]; and
- MnO_2 utilized in dry cell batteries, as chemical oxidant in organic synthesis and as raw material in the production of chemical grade manganous oxide [2].

1.4 Industrial production of manganese ferroalloys

To produce manganese ferroalloys, a carbothermic reduction process is followed in which manganese-bearing minerals are reduced by solid carbon reductants producing alloy, slag and off-gas [1], [13]. From a slag chemistry perspective, three distinct processes are in operation one producing HCFeMn, the other SiMn and the third having HCFeMn production integrated with SiMn production (Figure 5).

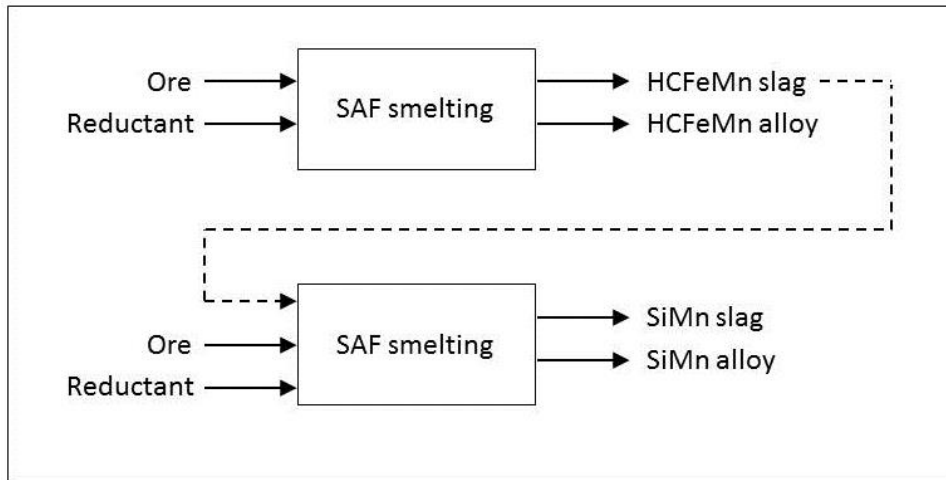


Figure 5: Production methods for HCFeMn and SiMn alloy. Three distinct processes are in operation one producing HCFeMn, the other SiMn and the third having HCFeMn production integrated with SiMn production (indicated by dotted line).

The typical slag compositions and tapping temperatures are summarized in Table 2 [1] with B_5 defined in Equation 1. The most significant differences between the two processes producing HCFeMn are the MnO content (40% vs. 15%) and the B_5 (1.7 vs. 1.2).

Equation 1: Definition of B_5

$$B_5 = \frac{CaO + MgO + MnO}{Al_2O_3 + SiO_2}$$

Table 2: Typical chemical composition (percentage by mass) and process temperature of slag tapped from the furnace during the production of manganese ferroalloys [1].

	SiO ₂	Al ₂ O ₃	MnO	MgO	CaO	B ₅	Process temperature
HCFeMn	24	21	15	5	35	1.2	1400 – 1450°C
HCFeMn (integrated)	24	13	40	6	17	1.7	1400 – 450°C
SiMn	45	16	9	9	21	0.6	1500 – 1600°C

In the integrated process the slag to metal mass ratio for SiMn production is typically 1.2 and the tap temperature 1600°C. In the other SiMn production process the slag to metal ratio is typically 0.8 and tapping temperature 1350°C – 1450°C [14]. The temperature range reported by Gous et al [14] is significantly lower than the calculated process temperature of 1600°C required for SiMn production. A temperature of 1600°C is required to produce SiMn containing 17.0% Si in equilibrium with slag with SiO₂-activity of 0.2 [1]. SiO₂-activity of 0.2 is typical for slag from SiMn production. Furthermore a difference between tapping temperature and process temperature of 50 – 100°C is typical of plant operations [1]. The likely reason for the temperatures reported by Gous et al [14] being too low is the presence of fume generated during tapping and/or calibration of the pyrometers [15].

In Table 3 the typical distribution of feed into a SAF producing SiMn according to the ore-based route is compared to that of the integrated route. Apart from the price of ore, the two other main cost drivers for the production of manganese ferroalloys, are the price of reductant and the price of electricity [1].

Table 3: Typical distribution of feed into a SAF producing SiMn according to the ore-based route or integrated route [1], [14] (per cent by mass).

		Ore-based	Integrated route
Reductant	Coal	25	-
	Coke	-	11
Primary Si-source	Quartz	14	13
	Si-metal sculls	-	4
Primary Mn-Source	HCFeMn slag	-	40
	Lumpy ore	36	12
	Metal fines - SiMn	2	-
	Metal fines - HCFeMn	-	7
	Ore briquettes	6	-
	Sintered ore	18	-
Other	Dolomite	-	3
	Remelts	-	11
Total		100	100

SAFs utilized for the production of SiMn are typically circular with three Söderberg electrodes in an equilateral arrangement. The furnaces can be open, semi-open or closed, depending on the environmental regulations of each specific country. The furnaces can be stationary or rotating. Typically production furnaces carry loads of 15 – 45 MW, and at this size the furnaces are always stationary. In southern Africa the installed capacities range from 6 MVA to 81 MVA (estimated as 4.4 MW and 50 MW) [16].

The SAF designs can be open (see Figure 6), closed or semi-closed. A closed furnace has a sealed roof with no or very little air ingress and the furnace off-gases are therefore not combusted. The roof of an open furnace is not sealed and furnace off-gas is combusted on top of the furnace bed. A semi-open furnace is similar to an open furnace, but with doors installed between the furnace rim and roof to reduce air ingress and heat losses. The conversion between HCFeMn and SiMn production is fairly easy from a furnace design perspective [17], although optimal operating performance will be achieved only in a custom-designed furnace.



Figure 6: Example of an open furnace utilized to produce SiMn being fed through a feed chute in the roof [16].

1.5 Lining designs installed in industrial-scale SAFs producing SiMn

1.5.1 Lining design principles

When designing a furnace lining, two design principles could be followed [17]–[20]:

1. Design a lining to minimize energy losses from the furnace (insulating lining or external insulation); or
2. Design a lining to protect the hot face of the refractory from chemical wear by freezing a layer of refractory material onto the hot face of the lining (conductive lining or self-forming insulation).

The steady state heat transfer principles of each type of lining are illustrated in Figure 7 [19], [21], [22].

In an insulating lining, heat is transferred from the liquid process materials to the furnace shell through the principles of convection (curved arrows) and conduction (straight arrows). The steel shell is primarily protected by layers of refractory material with a high resistance to heat flux (q_1) in the form of low thermal conductivity. The high resistance to heat flux prevents heat from reaching the steel shell. Although the refractory is in direct contact with liquid slag it can be protected to some extent against slag attack by ensuring that the slag is saturated in components present in the hot face refractory. In an insulating lining design the refractory installation is permanent. A combination of blocks, bricks and monolithic materials is utilized in the design and for manganese

ferroalloys the materials typically consist of MgO , Al_2O_3 or SiO_2 with a layer of carbon-based material on the hot face. The refractory is contained by a steel shell which could be cooled by water or air or not cooled at all [17].

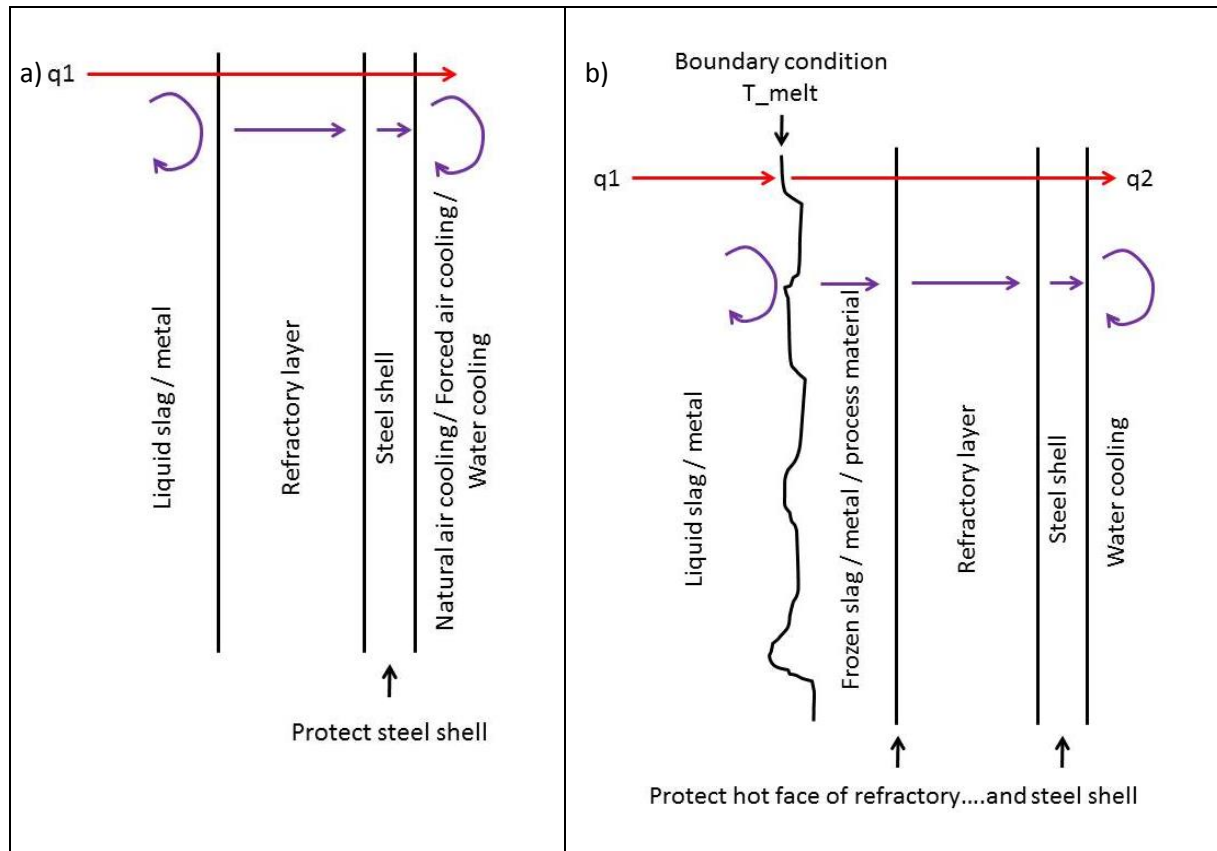


Figure 7: Steady state heat transfer principles on which a) insulating and b) conductive lining designs are based.

In a conductive lining, furnace conditions are manipulated to ensure that a layer of slag, metal or raw materials or combinations thereof are frozen onto the hot face of the refractory. From a heat transfer perspective the frozen layer of process materials forms a boundary condition: Its melting point does not change (or remains fairly constant). As long as the layer of material is present on the refractory hot face, the heat flux to the steel shell (q_2) will equal that of the heat flux from the process (q_1) i.e. $q_1 = q_2$. This layer of process material therefore not only protects the steel shell from high temperatures (as is the case for the insulating lining), but also reduces the hot face temperature of the refractory thereby protecting it from alkali or slag attack. In a conductive lining design some parts of the refractory installation is permanent and others sacrificial. In manganese ferroalloys these designs are based on combinations of carbon and graphite materials which require a sacrificial material on the hot face under the oxidizing conditions that prevail during furnace start-up. Typically MgO or Al_2O_3 materials are utilized as sacrificial lining material. The refractory is contained by a steel shell cooled by water in the upper sections and air in the hearth area [19], [23].

In the next section an application of both types of lining design philosophies are discussed.

1.5.2 Examples of lining designs applied in SiMn production

The first example is that of a lining designed according to the insulating design principle (Figure 8) discussed in a paper by Brun [17]. The lining was installed in 1968 in a furnace in Norway and lasted

until 1970. No form of sidewall cooling was installed. It is an example of an insulating lining installed with the intention to produce both SiMn and HCFeMn [17].

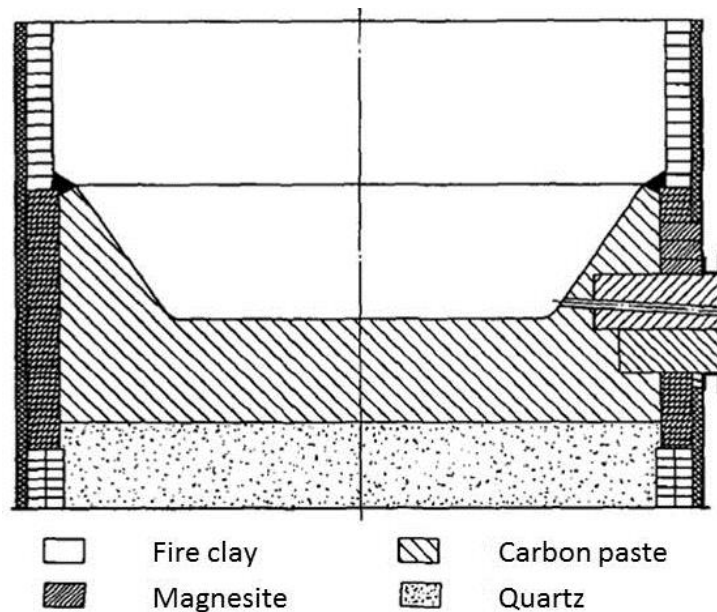


Figure 8: Insulating lining installed for SiMn and HCFeMn production, no cooling [17].

The hearth consisted of a quartz layer with carbon paste tamped on top. Sidewalls in the lower hearth area consisted of a steel shell with a thin layer of electrode paste (75 – 80% calcined anthracite a 15 – 20% tar binder) followed by a double layer of fireclay brick. The hot face of the fireclay brick was in contact with the quartz. Sidewalls in the upper hearth area consisted of a steel shell with a thin layer of electrode paste followed by a single layer of magnesia brick. The hot face of the magnesia brick was in contact with quartz or tamped carbon. The electrode paste was installed to allow for slag to freeze when breaking through the tamped carbon paste. Sidewalls in the bath area consisted of a steel shell with a thin layer of electrode paste followed by a single layer of magnesia brick. The hot face of the magnesia brick was in contact with the tamped carbon. Sidewalls in the freeboard area consisted of a steel shell with a thin layer of electrode paste followed by a single layer of fireclay brick.

The tap-hole refractory material was not stated specifically, but based on discussions of another design in the paper by Brun [17], it is assumed that the tap-hole consisted of carbon blocks with permanent hole surrounded by magnesia.

The second example is that of a lining designed according to the conductive design principle (Figure 9). Although the case under investigation was that of a lining installed in a furnace producing HCFeMn, the supplier of the technology claims that the design is installed in SiMn production furnaces as well. In this conductive lining the furnace hearth was cooled by blowing air over the surface of the steel shell. The sidewalls were cooled by thin film water cooling [23].

The lining (Figure 9) in the hearth consisted of the steel shell, covered by a levelling castable, covered by a ceramic brick, then graphite blocks, then a thick layer of carbon blocks and then again a layer of carbon bricks [23]. For the whole length of the side wall the steel shell was in contact with a graphite tile layer. In the various zones of the side wall – hearth, bath and free board – the subsequent material layers differed. In the lower hearth area the graphite tile was in contact with carbon rammable. In the middle hearth area the graphite tile was covered by carbon brick followed by a layer of carbon rammable. In the bath area the graphite tile was in contact with carbon brick

and a sacrificial ceramic brick. In the free board area the graphite tile was covered by a ceramic brick only.

The tap-hole consisted of a carbon tap-block with graphite sleeve and carbon mickey – see Figure 9 (b).

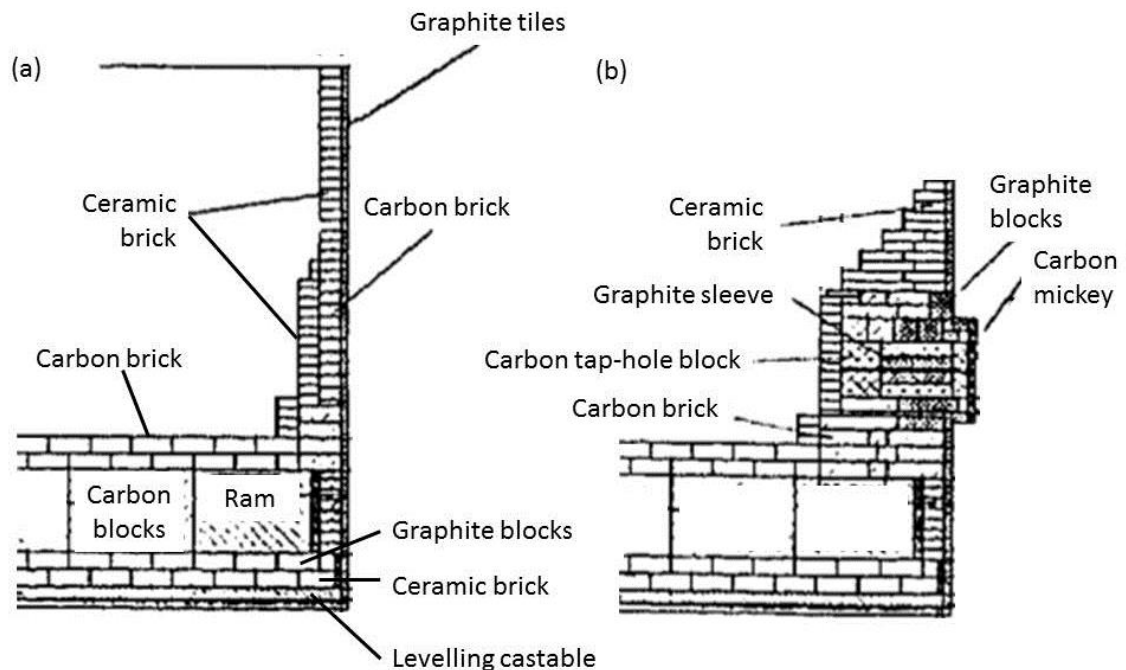


Figure 9: (a) Conductive lining installed for HCFEMn production, with forced air cooling on the hearth and thin film cooling on the side walls with (b) the tap-hole design [23].

In summary, tapblocks in SiMn production typically consist of carbon-based material with no specific cooling of the tapblocks as is typically done in the production of platinum group metals or ferronickel [24], [25].

1.6 The tap-hole

In SiMn production slag and metal are tapped intermittently from the smelter either through a single tap-hole or two bi-level tap-holes. Small-scale (6MVA) to medium-scale (48MVA) smelters will typically have two, single level tap-holes where metal and slag are tapped from the same tap-hole. Large-scale (75 – 81MVA) smelters will typically have four bi-level tap-holes, where slag is tapped from two higher level tap-holes and metal from two lower level tap-holes.

1.6.1 Tap-hole operating practice

For small-scale (6MVA) to medium-scale (48MVA) smelters taps will be alternated between the two tap-holes (if this tap is through tap-hole #1 the next tap will be through tap-hole #2). For large-scale (75 – 81MVA) smelters slag taps are alternated between slag tap-holes and metal taps between metal tap-holes [26]. For a medium-scale smelter the tap duration is typically 20 minutes and varies between 20 and 40 minutes. The tap-to-tap time is typically 2 hours (10 – 11 taps per 24 hours). The slag tapping temperature is typically 1600°C. The tap-hole is typically closed with ceramic clay after a tap to prevent liquid metal and slag from leaking from the furnace between taps. To open the tap-hole, a specialized drill is utilized and to close it, a mudgun with tap-hole clay. Should it be required, oxygen lancing is utilized to open the tap-hole when impossible to open with a drill. Oxygen lancing

is to be avoided as much as possible as the lancing process is fairly uncontrolled and could lead to excessive damage to refractory [24].

The purpose of reconstructive tap-hole clay is not only to plug the tap-hole at the end of the tap, but also to reconstruct the sidewall by forming a ‘mushroom’ of clay protecting the sidewall from slag and metal wear [27]–[29].

1.6.2 Tap-hole maintenance practice

For the tap-holes on a typical medium-scale smelter two types of maintenance practices exist: Scheduled maintenance and breakdown maintenance. Scheduled maintenance consists of tap-hole repair conducted with electrode paste. The electrode paste is heated in an oven and plugged into the tap-hole using a mudgun. The tap-hole/mudgun interface is also repaired to ensure proper connection between the mudgun and the tap-hole when plugging the tap-hole with clay. Once the tap-hole is repaired, the electrode paste is left to cure by heating it with an external heat source AND by tapping *two* taps through the other tap-hole. Breakdown maintenance is practiced in the case of a burn-through. A large section of damaged refractory, metal and slag is removed to a depth of 70 – 75 cm (preferably within the boundaries provided by the copper coolers) until undamaged refractory is reached where the cold ramming paste could tie-in. The area is boxed in and the cold ramming paste is rammed into position and cured. A tap-hole is then drilled through the paste using the tapping drill i.e. no spacer is utilised to form a tap-hole during ramming [30].

1.7 Research problem and questions

A commercial producer of SiMn – producing SiMn using the integrated process – found that tap-holes built from cold ramming paste during breakdown maintenance wore at a higher rate than the tapblock installed with the initial lining. In both instances the refractory materials were carbon-based. The producer wanted to obtain a better understanding of the cause of wear [30]. The goal of the study presented here was to determine to what extent chemical reaction between slag and refractory materials could be responsible for the wear observed. To reach the goal, the following research questions were addressed in the thesis:

Question 1: When exposing carbon-based refractory material (ramming paste and carbon block) to SiMn slag or metal in the tap-hole, is chemical reaction between refractory and slag or refractory and metal a potential wear mechanism?

Question 2: Is the choice in carbon-based refractory material important from a tap-hole refractory life perspective?

Question 3: Having obtained answers to Question 1 and Question 2, what are the implications for the life of the tap-hole in a SiMn furnace?

1.8 Overview of chapters

The three research questions are addressed in the following chapters:

Chapter 2: A review of literature was conducted to obtain a better understanding of carbothermic SiMn reduction process, carbon-based refractory materials in general, wear mechanisms applicable to refractory materials and ways in which these wear mechanisms are studied. The chapter concludes with a review of the first research question.

Chapter 3: Thermodynamic calculations were conducted as a first test of the argument that chemical reaction between refractory and slag or refractory and metal is a potential wear mechanism for

carbon-based refractory material in the tap-hole. The chapter concludes with a statement on the requirement for experimental validation of these thermodynamic calculations.

Chapter 4: Laboratory scale tests were conducted to support the results of the thermodynamic calculations conducted in Chapter 3. Synthetic SiMn slag and pure graphite were used as materials and an induction furnace as heat source. The chapter concludes with an introduction to the second research question which will be addressed in Chapter 5, Chapter 6 and Chapter 7 through further laboratory-scale experiments based on industrial SiMn slag and two commercial grades of refractory material: Carbon block and ramming paste.

Chapter 5: Preparation and characterisation of the industrial SiMn slag and two commercial grades of refractory material are discussed and thermodynamic calculations repeated based on the chemical analysis obtained. The chapter concludes with a review of the second research question in terms of the results obtained for the industrial SiMn slag and two commercial grades of refractory material, and introduces the first set of laboratory-scale experiments: Wettability tests.

Chapter 6: Wettability tests were conducted in which the wettability of the two commercial grades of refractory material by industrial (and in some instances synthetic) SiMn slag in both Ar-gas and CO-gas atmospheres at 1592°C were quantified. The chapter concludes with a review of both first and second research questions and an introduction to the second set of laboratory-scale experiments: Cup tests.

Chapter 7: Cup tests were conducted in which the potential for chemical reaction between, and infiltration by, industrial SiMn slag and the two commercial grades of refractory material were investigated at 1400°C, 1500°C and 1600°C. The chapter concludes with a review of both first and second research questions and an introduction to the third research question to be addressed in Chapter 8 through the presentation of results of the excavation of the tap-hole of a 48 MVA SiMn furnace.

Chapter 8: The excavation of the tap-hole of a 48 MVA SiMn furnace was reported and observations interpreted through thermodynamic and mass transfer calculations.

Chapter 9: In the final chapter, the three research questions and their arguments are reviewed; conclusions and recommendations for further investigations made.

2 Literature review

2.1 Introduction

Chapter 1 introduced SiMn as alloy and SAF as the technology applied in the production of SiMn. Carbon-based refractory materials were introduced as tap-hole refractory material as was the need for improved understanding of tap-hole wear. Chapter 1 concluded by stating the purpose of the study (to determine to what extent chemical reaction between slag and refractory materials would be responsible for tap-hole refractory wear) and introducing three research questions.

Chapter 2 reports on the literature study conducted to obtain a better understanding of carbothermic SiMn reduction process, carbon-based refractory materials in general, wear mechanisms applicable to refractory materials and ways in which these wear mechanisms are studied. The chapter concludes with a review of the first research question and an introduction to Chapter 3.

2.2 Carbothermic SiMn production process

2.2.1 Process overview

Figure 10 contains a typical cross-section of a SAF utilized to produce SiMn. Ore containing manganese and silicon oxides (Table 3) and carbon-based reductant are fed from the top of the furnace. The electrode tips are submerged in a burden of material and energy is transferred from the electrodes to the process through micro-arcing across a coke bed that floats on top of the molten metal bath [31].

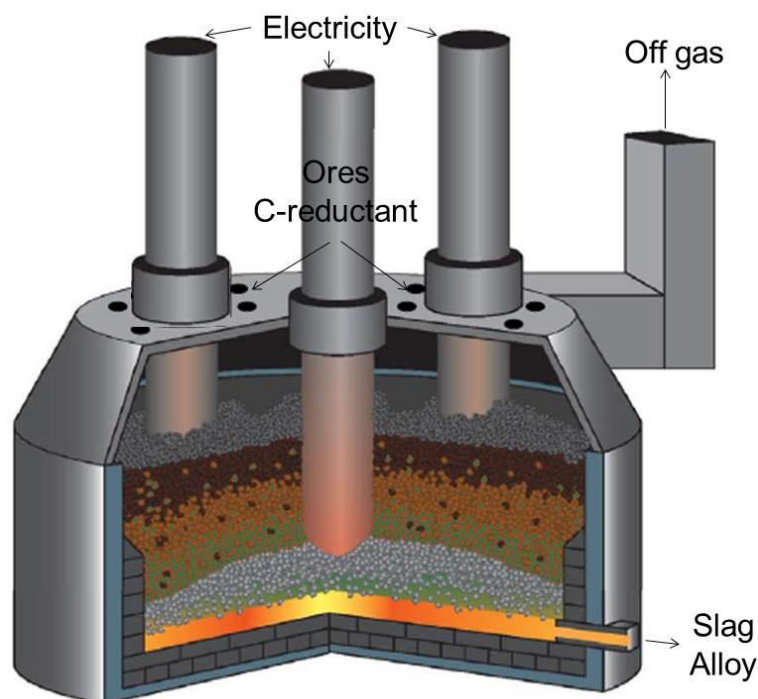


Figure 10: Layout of a SAF utilized in the production of SiMn [32].

The SiMn production process in a SAF can be divided into the following four zones with typical temperature ranges indicated in brackets [1]:

1. *Zone 1*: Drying, calcination and heating (25°C – 192°C) with the potential chemical reactions including low temperature reduction of MnO₂ to Mn₂O₃.
2. *Zone 2*: Gas reduction (192°C – 730°C) with the potential chemical reactions including the gas reduction of Mn₂O₃ and Fe₂O₃, decomposition of dolomite, precipitation of soot and reversal of alkali reduction.
3. *Zone 3*: Direct reduction (730°C – 1100°C) with the potential chemical reactions including the gas reduction of Mn₃O₄ and Fe₃O₄ with the Boudouard reaction (C + CO₂ ⇌ 2CO) running simultaneously.
4. *Zone 4*: Smelt reduction (1100°C – 1650°C) with the potential chemical reactions including melting of iron, dissolution of MnO and SiO₂ into the slag with partial reduction to form liquid metal, dissolution of carbon into the metal and reduction of K₂CO₃ to K(g). The metal, slag and carbon are said to approach chemical equilibrium at these temperatures

Slag and metal are tapped typically at 1600°C. In the tables below the typical compositions of alloy (Table 4), slag (Table 5) and off-gas (Table 6) are stated [1].

Table 4: Typical composition of tapped SiMn alloy in mass per cent [1].

%Mn	%Si	%C	%Fe
68	20	2	10

Table 5: Typical composition of tapped SiMn slag in mass per cent [1].

%MnO	%SiO ₂	%Al ₂ O ₃	%CaO	%MgO	%FeO
9	45	16	21	9	0

Table 6: Typical composition of off gas in per cent by volume [1].

%H ₂	%CO	%CO ₂	%N ₂	%O ₂
4.1	68.7	12.6	14.2	0.4

2.2.2 Structure of carbon

In nature elemental carbon is found in the form of diamonds, graphite and coal. Graphite and coal are utilized in refractory applications [33], [34]. For carbon-based refractory materials the ideal graphite or coal deposit should produce material with a low inorganic material content at a high yield [33].

The distinction between graphite and coal is made based on the differences in their crystal structure [33]. Carbon atoms in graphite are located in a hexagonal arrangement - Figure 11. Each carbon atom in graphite is linked by three covalent bonds within an aromatic layer in two dimensions. However the linkage between different aromatic layers is governed by the Van der Waals force. The linkage in this dimension is so weak that it could be easily broken by an external force [33], [35].

Carbon atoms in coal are located in a three-dimensional (3-D) network bonding the carbon atoms in coal in a highly complex structure (considered amorphous [33]) compared to that in graphite. The lamellae in coals containing up to 85% carbon are connected by crosslinks and are randomly orientated. The only way to free carbon atoms from coal is to break the 3-D connection formed by the strong bonds [35].

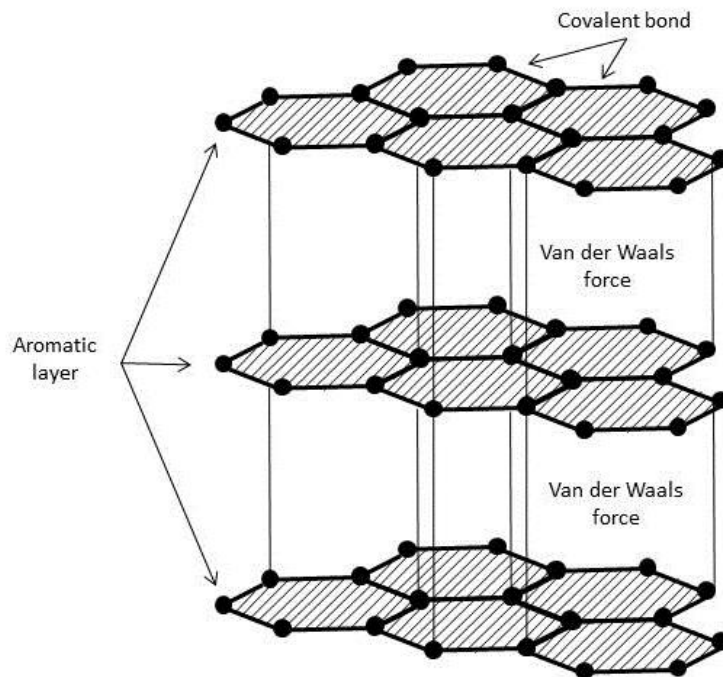


Figure 11: Hexagonal arrangement of carbon in graphite [36].

A measure of the degree of crystallinity of the coal is the average thickness of the stacks of aromatic layers (crystallites) [37]; this average thickness (L_c) can be measured by using the peak broadening effect in XRD measurements [38]. The size of L_c can be defined by an XRD technique by use of Scherrer's equation (Equation 2), where L_c is the dimension of the stack of parallel layers normal to the layer (in angstroms), λ is the wavelength of the incident X-ray (in angstroms), B is the angular width at half-maximum intensity of the [002] peak (in radians) and θ_B is the Bragg angle of the [002] peak (in degrees).

Equation 2: Scherrer's equation

$$L_c = (0.9 \lambda) / (B \cos \theta_B)$$

Although coal is generally recognized as non-crystalline it is considered to have some carbon atoms arranged in small clusters resembling the graphite structure i.e. it will report an L_c value [35]. One of the main differences between the graphite and coal structures is in their crystallite size and, therefore, the degree of ordering in carbon atom arrangement.

2.2.3 Carbon reactivity studies

Given that chemical reaction between carbon-based refractory and slag is the focus of this study, the main results of previous work on such reactions are briefly summarised.

Safarian and co-workers [39], [40] studied the reactivity of MnO-bearing slags towards different types of graphite. They found that slag reactivity of graphite is mainly dependent on temperature and graphite properties are in the lower order of importance. In another study, Safarian and co-workers [41] found that the MnO reduction rate from HCFemn slag is higher for charcoal than for cokes, in general, and that the reduction rate for industrial cokes is higher than it is for the cokes produced from single coals. In contrast studies on the kinetics of FeO and MnO reduction from HCFemn slag found that reduction by coke is faster than by charcoal and much faster than by

graphite [42]–[44]. Sun and co-workers [44] also found that an increase in the ‘ash’ (non-carbonaceous material) content of the substrate resulted in a reduction in the contact angle between MnO-bearing slags and coke.

Sahajwalla and co-workers [35], [45], [46] studied the dissolution rate of different carbonaceous materials in iron-based hot metal. They found that the more crystalline coals or chars exhibited more rapid dissolution because the complex three-dimensional bonds in poorly ordered coal are more difficult to break.

CO₂- and SiO₂-reactivity tests on the other hand indicate that more crystalline carbonaceous materials exhibits lower reactivity with gas species [37].

In the CO₂-reactivity test the carbonaceous material (typically blast furnace coke) in a packed bed containing 200 g of 20 mm-diameter particles is exposed to flowing CO₂ at 1100°C for 2 hours. After reaction the percentage mass lost (by the Boudouard reaction) is quoted as the ‘coke reactivity index’ (CRI). The extent of size degradation is quantified as the percentage of the remaining coke (after reaction and tumbling) which is larger than 10 mm and is quoted as the ‘coke strength after reaction’ (CSR). The CRI and CSR values are generally inversely related, indicating that the loss of strength in this test is a direct result of reaction [37].

In the SiO₂-reactivity test the carbonaceous material reacts with SiO₂-gas at 1650°C. When a carbonaceous reductant reacts with SiO₂, solid silicon carbide and CO-gas form. This silicon carbide eventually blocks the reaction surface. The rapidity of the onset of surface blockage can be used as an indication of reactivity with respect to SiO₂ where the onset of blockage is indicated by a decrease in the concentration of CO in the off-gas [38].

2.2.4 Wettability tests

In their studies on the reactivity of slag on carbonaceous substrates, Safarian and co-workers [43] and Sun and co-workers [44] made extensive use of the sessile drop technique. The sessile drop technique is one of the techniques available to wettability studies [47], [48]. Wettability studies are based on capillary action of a liquid on a solid substrate in a gaseous atmosphere and the material property applicable is surface tension.

Surface tension (γ) is the energy required to break through the surface of a droplet of liquid or disrupt it and spread it out as a film. To put it differently: Surface tension is the measure of the ‘toughness’ of the ‘skin’ of a liquid [49]. On a molecular level surface tension is described qualitatively as when liquid behaves as though it has a ‘skin’ because of a net inward force of attraction on the molecules on the surface – see Figure 12. The liquid molecules at the surface experience a large attractive, intermolecular¹ force from liquid molecules below the surface layer and weak attractive, intermolecular force from gas molecules. The liquid molecules below the surface layer interact with all the liquid molecules around them. The net inward force of attraction (cohesive force) on the molecules on the surface is the surface tension. The surface tension causes the surface to contract. In the absence of other forces, the liquid would form a sphere as this shape minimizes surface area. Quantitatively surface tension is expressed as a force in the surface plane per unit length with SI units of N.m⁻¹ [49]–[52]. Interfacial tension is generally taken to refer to the related surface tension between two condensed phases.

¹ Intermolecular forces between molecules: Dipole-dipole, ion-dipole, Van der Waals; Intramolecular forces within a molecule: Ionic, covalent, metallic.

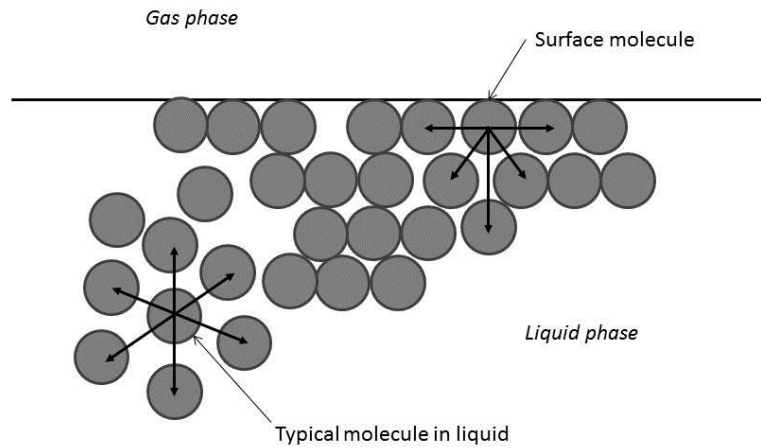


Figure 12: Intermolecular forces acting on molecule at surface of liquid vs. intermolecular forces acting on molecule within a liquid after Kotz and Purcell [49].

Capillary action is related to surface tension [49].

Capillarity is defined as the elevation or depression of a liquid in a narrow solid tube where *capillary* stems from the tubes being ‘hairlike’ [50] – see Figure 13.

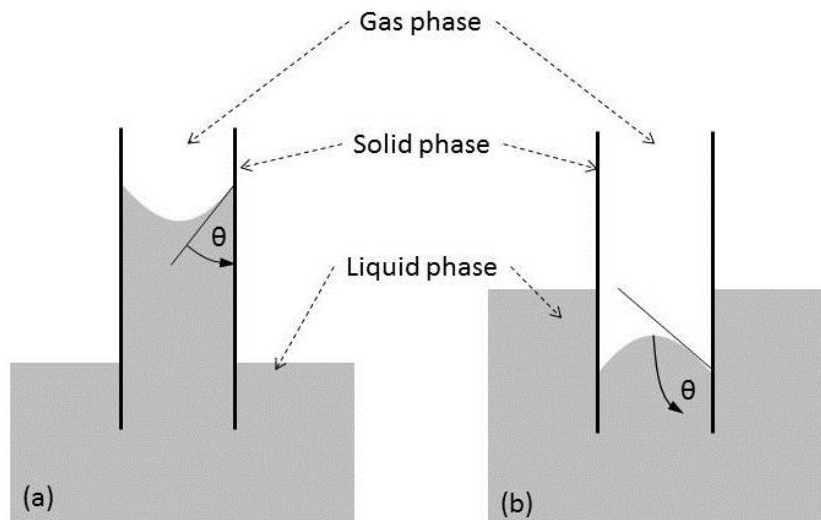


Figure 13: Surface tension forces on a liquid in a capillary tube where (a) is the capillary action in elevation and (b) the capillary action in depression after [50].

During capillary action in elevation, a liquid surface rises in a solid tube without an external differential pressure applied. For example, polar molecules in the liquid would be attracted by the adhesive force caused by polar molecules in the solid. The adhesive force between the two different substances compete with the cohesive force within the liquid and the force of gravity causing a change in level until equilibrium is reached [49].

During capillary action in depression the liquid surface is depressed in the solid tube [50].

Equilibrium is described by the contact angle, θ , an angle formed at the solid-liquid-gas interface. For capillary action in elevation $\theta < 90^\circ$ (wetting) and for capillary action in depression $\theta > 90^\circ$ (non-wetting).

The open porosity in refractory material can be seen as narrow solid tubes. If the liquid process material (metal or slag) were to wet the refractory, the result would be capillary action in elevation. An increase in the capillary action in elevation would cause an increase in the infiltration depth of the liquid process material into the refractory and an increase in the liquid / solid interfacial area.

When dissolution of refractory into the liquid or chemical reaction between the refractory and the liquid are applicable wear mechanisms, increasing the liquid / solid interfacial area would increase the refractory wear rate [53].

In wettability tests the contact angle, θ , forms at the solid (S) – liquid (L) – gas (G) interface where equilibrium is reached between the surface tensions at the solid / gas interface (γ_{SG}), liquid / solid interface (γ_{LS}) and liquid / gas interface (γ_{LG}) and gravitational force expressed as weight (w) – see Figure 14. The surface forces tends to minimise the free surface energy by forming a sphere and the gravitational forces by flattening the drop [50], [52].

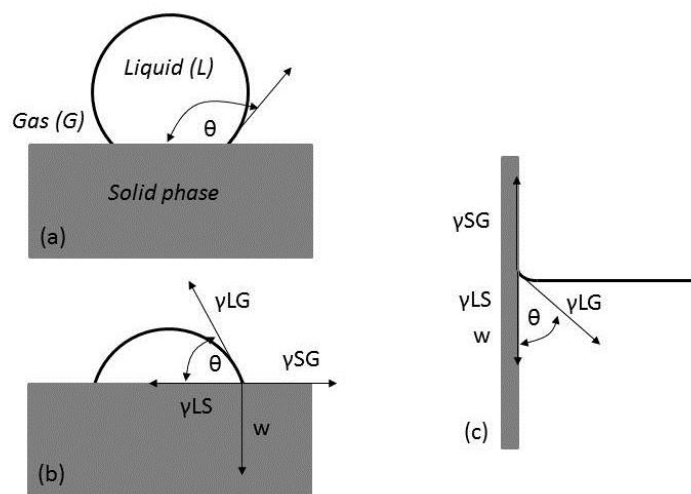


Figure 14: Schematic of forces at equilibrium - respective surface tensions and weight - and their relation to the contact angle with (a) non-wetting liquid – sessile drop – resting on a flat, horizontal solid surface, (b) wetting liquid – sessile drop – resting on a flat, horizontal solid surface and (c) wetting liquid on vertical solid surface after [52] – a,b – and [50] – c.

In non-reactive systems where mechanical equilibrium exists between a flat, undeformable, perfectly smooth and chemically homogeneous solid surface in contact with a non-reactive liquid in the presence of a vapour phase, Young's equation [54] - Equation 3 - describes the relation between the contact angle and the respective interfacial tensions.

Equation 3: Young's equation

$$(\gamma_{SG} - \gamma_{LS}) = \gamma_{LG} \cos\theta$$

When the contact angle is less than 90° the liquid wets the solid surface with complete wetting occurring at $\theta = 0^\circ$. When the contact angle is more than 90° the liquid behaves non-wetting towards the solid surface. The transition angle therefore is $\theta = 90^\circ$ [50], [52], [53].

In non-reactive systems where mechanical equilibrium exists, the work of adhesion (W_a) is defined as the energy required to separate two contacting phases and was described by the Dupre equation [53], [55] – see Equation 4.

Equation 4: Dupre's equation

$$W_a = \gamma_{LG} (1 + \cos\theta)$$

When studying a liquid (in a gas atmosphere) in isolation, the two principal parameters affecting the magnitude of surface tension are chemical composition of the phases and temperature [52]:

1. As the surface tension of a liquid depends on the relative strength of the intermolecular forces acting on the liquid surface, the chemistry of the liquid – which determines the intermolecular forces – is of importance. Components that preferentially adsorb on the surface – surface active components – can significantly lower the surface tension of the liquid. Surface active components in liquid iron include S and O [52].
2. Usually the surface tension of liquid decreases with an increase in temperature [50], [52]; exceptions include:
 - a. Slag melts with high levels of SiO₂ where a rise in temperature cause the complex molecular structures to dissociate, increase the number of unsatisfied molecular bonds at the surface and therefore increases the surface energy.
 - b. Surface active components in molten iron i.e. O and S which desorb from the surface layer as the temperature increases and therefore the surface energy increases.

Marangoni (convective) flow is induced at the free surface of a liquid when a surface tension gradient exists along this surface. The relative strength of the flow is a function of the surface tension gradient and the viscosity of the liquid. The surface tension gradient could either be caused by a temperature or a chemical gradient at the surface. The resultant Marangoni flow is known as thermocapillary or diffusocapillary respectively [52].

When studying a liquid in contact with a solid, factors affecting wettability – additional to the factors affecting the magnitude of surface tension of a liquid phase – are intermolecular bonding (dispersion forces), surface topography and porosity [53]:

1. Dispersion forces are weak attraction forces acting between atoms or molecules – the intermolecular forces referred to in the definition of surface tension. These forces are dominant in controlling the bond strength between a liquid in contact with a solid substrate when no chemical interactions occur. Dispersion forces display a weak dependence on temperature compared to chemical forces.
2. Surface topography plays a role in practical situations where the surface is not perfectly smooth as assumed in the derivation of the Young's equation (Equation 3) [53]. Surface roughness affects wetting as follows: (a) the actual surface area is increased and (b) the triple line (contact point between solid / liquid / gas) is pinned by the sharp edges [56]. The Wenzel equation [57] - Equation 5 - gives a simple relation for the observed (apparent) contact angle θ_R on a rough surface and the angle θ_s found on a perfectly smooth surface of the same solid. R (the surface roughness factor) ≥ 1 and is defined as the ratio of the true surface area to the geometric area based on the assumption of a smooth surface. The equation predicts that the observed contact angle for wetting systems will decrease with increase in R.

Equation 5: Wenzel's equation

$$\cos \theta_R = R \cos \theta_s$$

3. Porosity of the solid medium plays a significant role in wetting systems, but not in non-wetting systems. A significant decrease in contact angle was observed experimentally for an increase in

porosity of 10% in a wetting system whilst porosity up to 35% were insignificant for non-wetting systems [53].

In reactive systems the decrease in the free energy of the system drives the movement of the wetting line. The relationship between the interfacial free energy (ΔG), the interfacial tension (γ_i) between the three surface areas (solid / gas, liquid / gas, solid / liquid) and the changes in surface area (dA_i) at the interfaces caused by the movement of the wetting line was developed by Aksay and co-workers [55], [58] – see Equation 6:

Equation 6: Aksay's equation

$$\Delta G = \int_{SL} \gamma_{SL} dA_{SL} + \int_{SG} \gamma_{SG} dA_{SG} + \int_{LG} \gamma_{LG} dA_{LG}$$

From the equation above, wetting will proceed when ΔG is negative and proceed until mechanical equilibrium is reached, i.e. when ΔG is zero. ΔG is therefore the mechanical driving force for wetting.

In reactive systems intermolecular bonding (chemical forces) apply either when surface-active components adsorb at the liquid / solid interface or when a chemical reaction occurs between the liquid and solid. Initially the system will be in a non-equilibrium state [53], [59].

When adsorption is the chemical action that occurs, the rate of diffusion of surface active species to the interface will determine the time to reach equilibrium. Diffusion is dependent on temperature. When only chemical adsorption occurs, γ_{LS} is said to decrease with time in a monotonic manner, decreasing θ . Throughout the period of spreading, measurements of θ would yield non-equilibrium values.

When chemical reactions occur between the liquid and solid, mass transfer across the two-phase interface occurs to produce new solutions and / or compounds. With strong reactions, γ_{LS} (and therefore θ) is said to go through a minimum before recovering to the final equilibrium value. Reaction kinetics will determine the time to reach equilibrium and is therefore strongly dependent on the temperature of the system. The final contact equilibrium angle will depend on the equilibrium composition of the liquid and metal which will differ from that of the starting material.

The equilibrium contact angle, θ_c , for a liquid on a solid substrate of heterogeneous composition can be predicted from the wetting angles of the individual components included in the substrate, θ_i , and the volume fraction of each component, X_i , using the particular version of the Cassie-Baxter law – an analogue for the Wenzel equation (Equation 5) for rough surfaces – as defined in Equation 7 [57].

Equation 7: Cassie-Baxter law

$$\cos \theta_c = -1 + \sum [X_i (\cos \theta_i + 1)]$$

The sessile drop technique, in various variations, is applied in 90% of wettability studies at high temperatures [56]. Another technique also applied is the wetting balance technique in which the forces acting on a solid moving into and out of a liquid bath are continuously monitored during an immersion-emersion cycle. For more details on the method, the reader is referred to [56]. As the sessile drop technique was applied in this study it will be discussed in more detail, based on the schematic illustration in Figure 15.

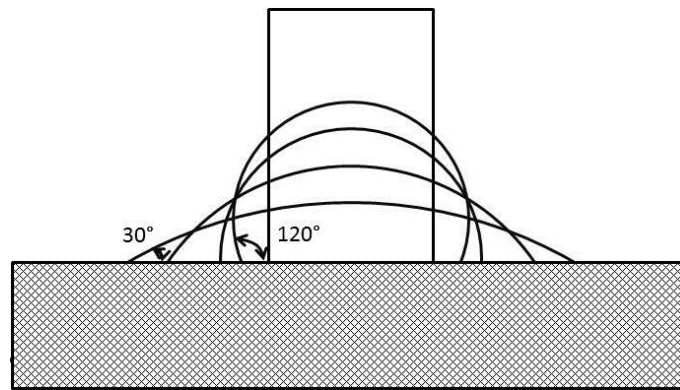


Figure 15: Schematic illustration of a solid cylinder melting to form a sessile drop with an initial contact angle of 120° and spreading over the substrate with time to achieve final equilibrium of 30° [56].

The sessile drop technique can be applied to both inert and reactive systems. It consists essentially of permitting a drop of liquid – 0.005 to 5 ml in volume – to spread over a horizontal solid substrate until an equilibrium configuration is reached or the experiment terminated. One example is that of a solid cylinder melting to form a sessile drop with an initial contact angle of 120° and spreading over the substrate with time to achieve final equilibrium of 30° as indicated in Figure 15. This method is considered the classic form of the sessile drop technique. When measuring the contact angle, θ , small drops (with volume typically 0.01ml and spherical diameter 2mm) are used for which the profiles are approximated by spherical caps [56].

When conducting a sessile drop experiment at high temperatures, the following five criteria have to be met [56]:

1. Characterisation of materials in terms of composition – specifically surface active components – surface roughness (in terms of roughness amplitude and asperity slope) and heterogeneity.
2. Flat horizontal surface with a tilt less than 1 – 2° which means that the liquid remains stable (does not roll off substrate) upon melting.
3. Test chamber to control atmosphere either through flushing with a controlled gas composition or through pulling a vacuum and subsequently back-flushing with gas.
4. Facility to heat the sample to a predetermined temperature and rate. Typically electrical resistance heating elements are utilized which should be placed outside the test chamber to prevent contamination through evaporation or desorption from their hot surfaces. Furthermore, the melting of the liquid should be achieved in times that are short compared to those allowed for subsequent spreading. This is true in particular when using liquids with wide melting ranges. Heating rates should be fast through the temperature range to minimise premature wetting of a substrate through the liquid phase from a partially molten drop.
5. Means of measuring the geometry and size of the sessile drop, often by recording images through still or video camera in which case alignment of the camera and sample is important.

Information that can be derived from the sessile drop technique includes contact angles (θ), liquid surface energies and liquid density [56]:

1. *Contact angles* (θ) formed at the solid-liquid-gas interface (Figure 13).
 - a. Test for consistency in contact angle measurements, θ , by measuring:
 - i. θ on left hand and right hand sides of drop profile and compare; and
 - ii. Height (H) and radius of substrate contact area (R) to calculate θ from spherical cap relationships based on Equation 8; compare with measured angles:

Equation 8: Contact angle from spherical cap data

$$\tan (\theta_{\text{calc}}/2) = H/R$$

- b. Verify consistency in changes in geometry and dimensional characteristics during course of experiment where:
 - i. A decrease in contact angle and drop height is mirrored by increase in radius of contact area. If not, liquid has been lost by infiltration of substrate or evaporation.
 - ii. An increase in contact angle not mirrored by decrease in radius indicates pinning of advancing liquid front triple line.
 - c. For reactive systems, heating rates and temperature hold times should be controlled well and it is important not only to record changes in contact angle with time but also drop base radii.
 - d. For reactive systems, θ is not the overall equilibrium wetting angle as the liquid phase composition changes continuously, but the contact angle that is close to but slightly different from equilibrium.
 - e. The error in contact angle measurements is typically 3°.
 - f. The smallest variations between measurements were $\pm 5^\circ$ for Au on a monocrystalline Al_2O_3 substrate (nonwetting) and for a wetting case $\pm 5^\circ$ (Si on a SiC single crystal). Measurements are very sensitive to surface roughness and oxygen partial pressure of the gaseous atmosphere with non-wetting systems being more sensitive to variations than wetting.
2. *Liquid surface energies* which can be determined in cases where droplet size is several grams – for details refer to [56].
 3. *Liquid density* which can be determined when the initial mass is known and no significant loss in mass occurred due to evaporation. If care is taken measurements have accuracy better than 1%.

2.3 Carbon-based refractory materials

2.3.1 Carbon in refractory materials

As *enabling* materials, refractories enabled the utilization of heat to make materials since the Bronze Age [18]. In the production of metals through high temperature processing, refractories are the materials that maintain sufficient physical and chemical stability at high temperatures to be utilized for structural purposes [33]. Refractories are the materials utilized to build the structures that contain pyrometallurgical processes.

Refractory materials are mainly based on 6 oxides – SiO_2 , Al_2O_3 , MgO, CaO, Cr_2O_3 and ZrO_2 – and carbon or combinations thereof [33], [60]. In refractory applications carbon is utilized either as additive giving the refractory material specific properties or as main component participating in the formation of the structure of the refractory component [61].

An example of carbon utilized as additive is found in fired carbon-containing magnesia bricks (<2%C) [18], [61]. First the fired magnesia brick is formed by preparing a blend of magnesia materials, mixing it with a binder (added to allow low temperature forming), shaping and firing to form a brick with a ceramic bond [62]. To produce carbon-containing magnesia bricks, the fired magnesia bricks are impregnated with pitch under vacuum and subsequently fired to fill pores with a carbon structure [61].

An example of carbon utilized as main component (in this example the binder phase) is found in carbon-bonded magnesia bricks (<7%C) [18], [61]. To form carbon-bonded magnesia bricks magnesia aggregate is mixed with pitch binder and subsequently shaped and fired.

In both of these applications carbon improves the corrosion resistance of the magnesia bricks to slag by reducing slag infiltration depths from the cm range to the mm range [61]. Carbon is able to do this due to its non-wetting nature towards slags [63].

In carbon-based refractory material carbon-based aggregate is mixed with carbon-based binder and subsequently shaped and fired [33], [34]. In some applications, inorganic additives i.e. SiC or Al₂O₃ are added for specific property improvements [33], [34], [64], [65].

2.3.2 Different types of carbon-based refractory materials

In carbon-based refractory materials the carbon aggregate consists of a blend that could include natural occurring graphite but mostly forms of coal that has been processed i.e. calcined anthracite, calcined coal, calcined graphite, petroleum coke, carbon black and artificial graphite [33], [34]. Distinctions are made between gas calcined and electrically calcined materials [66]–[68]. To form a specific type of refractory, different types of aggregate materials are selected based on their specific properties, mixed with a binder, shaped and fired. The binder material can be coal tar pitch (a by-product from coke ovens), petroleum pitch or resin [33], [34], [64], [69]. The material mixture, shaping and firing methods and firing temperature determine the type of carbon-based refractory material produced. As an example calcined anthracite is selected for its good resistance to molten iron (“resistance” refers to low dissolution rate compared to graphite [35]) and artificial graphite for its high thermal conductivity [64], [70].

Cold ramming paste typically consists of electrically calcined anthracite as aggregate and coal tar pitch as binder which carbonizes at 500°C but should be baked at 950°C after installation [71]. Due to the nature of the calcination process with temperatures in the reactor ranging between 1200°C and 3000°C, the electrically calcined anthracite contains 30 – 40% graphite where the calcination temperature of gas calcined anthracite at 1200°C is too low for graphite formation [71].

No industry standard classifies the different grades of carbon-based refractory materials available, unlike oxide-based refractories. Therefore the classification, description and application of carbon-based refractory materials are manufacturer specific [72]. The different types of carbon refractory material utilized in manganese ferroalloy furnace linings are electrode paste, carbon paste, carbon bricks and blocks, micropore carbon bricks, graphite bricks and blocks, semi-graphite bricks and semi-graphitized bricks.

Electrode paste [17], [23] is a monolithic (unshaped) refractory material that was utilized in earlier SAF lining designs. Electrode paste typically consists of 75-80% coke or calcined anthracite aggregate and 15-20% coal tar pitch binder [17], [73].

Carbon paste [17], [74] is also a monolithic refractory material. One material consisted of 84% calcined anthracite aggregate with 16% tar binder [20]. Another of 75 – 80% coke or calcined anthracite aggregate and 15 – 20% coal tar pitch binder [71]. A third of 50 – 70% anthracite and 15 – 25% graphite aggregate with a combination of 6 – 12% resin and 2 – 7% tar as binder phase and 1 – 5% Al₂O₃ as additive [74].

Carbon bricks and blocks [23], [72] have as aggregate calcined anthracite, calcined coal, petroleum coke or carbon black and as binder petroleum pitch or coal tar. Material is shaped by extrusion or press moulding and baked at 800 – 1400°C to carbonise the binder [23], [72], [75]. Baking can take

place in a conventional furnace or in special furnace with hydraulic ram and electrical current passing through (hot pressing) [23], [76]. To reduce the porosity of carbon bricks or blocks, the fired material is impregnated with binder material and refired [34], [72], [77]. Hot pressing is said to result in a brick that is 100 times less permeable by gaseous alkalis or zinc and with a significantly higher thermal conductivity than conventional carbon block [72].

Micropore carbon bricks [34], [66] have artificial graphite, electrical calcined graphite or gas calcined graphite as aggregate and petroleum pitch, coal tar or resin as binder. Fujihara et al [78] found that by replacing the coal tar pitch binder with a resin binder, the resistance of the carbon-based refractory to dissolution in iron was increased. To strengthen the bond matrix, generate microporosity or improve wear resistance properties, metallic Si, SiC, Al₂O₃, Ti or TiO₂ is added [34], [66]. It is especially the addition of metallic Si that produces the so-called micropore or super-micropore carbon bricks [34]. In micropore carbon bricks 95-98% of the pores are below 1µm [34].

Graphite bricks and blocks (and tiles) [23], [34], [66] are formed following the steps for carbon bricks followed by an additional graphitizing step at 2400 – 3000°C. As with carbon bricks, the porosity of graphite bricks is reduced by multiple impregnation with binder material and refiring cycles [72].

Semi-graphite bricks [23] have artificial graphite as aggregate and petroleum pitch or coal tar as binder. Material is shaped by extrusion or moulding and baked at 800 – 1400°C to carbonise the binder [23], [72]. Baking can take place in a conventional furnace or in a special furnace with hydraulic ram and electrical current passing through (hot pressing) [23]. Porosity is reduced by multiple impregnation with binder material and refiring cycles [72].

Semi-graphitized bricks [23], [72] are formed by following the steps for carbon bricks, with an additional firing step at 1600 – 2200°C. The temperature range is high enough for some changes in the crystal structure of the carbon to occur (changing physical and chemical properties) but below the graphitization temperature [72]. Because both aggregate and binder phases are heat treated, semi-graphitized bricks have higher thermal conductivity and resistance to chemical attack (alkali or oxidation) than both carbon and semi-graphite bricks. The reason being that in carbon block, alkali and zinc attack the binder phase first and semi-graphitized binder has a higher resistance to attack [72].

2.3.3 Influence of thermal conductivity of carbon-based refractory materials

One of the main parameters influenced by the differences in baking temperatures is the thermal conductivity of the carbon-based refractory materials formed [72]. Table 7 summarises the thermal conductivity of different types of carbon-based refractory materials at 1000°C as well as some of the other types of refractory materials.

Table 7: Thermal conductivity of different types of carbon refractory material against that of other types of refractory materials at 1000°C.

	k [W/mK] at 1000°C	Reference
Carbon paste	7 – 11	[71], [74]
Carbon bricks (conventional)	6 – 17	[34], [72]
Carbon bricks (hot pressed)	19	[72]
Micropore carbon bricks	6 – 12	[34]
Graphite bricks	35 – 80	[34], [72]
Semi-graphite bricks (conventional)	15 – 32	[34], [72]
Semi-graphite bricks (hot pressed)	32	[72]
Semi-graphitized bricks	32	[72]
Fireclay	1.1 – 1.5	[79]
Insulating fireclay	0.3 – 0.5	[79]
Magnesia bricks	2.2 – 4.2	[79]
MgO-C (20%)	14	[79]
Corundum bricks (98% Al ₂ O ₃)	2.4 – 4	[79]
High alumina bricks (60% Al ₂ O ₃)	1.4 – 1.7	[79]
Insulating high alumina (95% Al ₂ O ₃)	1.2	[79]
Insulating high alumina (60-75% Al ₂ O ₃)	0.5 – 7.5	[79]
SiC with oxide bond	5	[79]
SiC with Si ₃ N ₄ sialon bond	8	[79]

To put the thermal conductivities listed in Table 7 in perspective, one has to revisit the lining design principles discussed in 1.5.1. The impact of differences in thermal conductivity of the refractory materials is illustrated through a one-dimensional radial heat transfer model for a circular SAF depicted in Figure 16. The refractory layout was based on the conductive design principle (defined in Figure 7b). The system consisted of a water-cooled steel shell lined with refractory material. Onto the refractory material a layer of frozen slag had formed. The layer of frozen slag remained in contact with liquid slag.

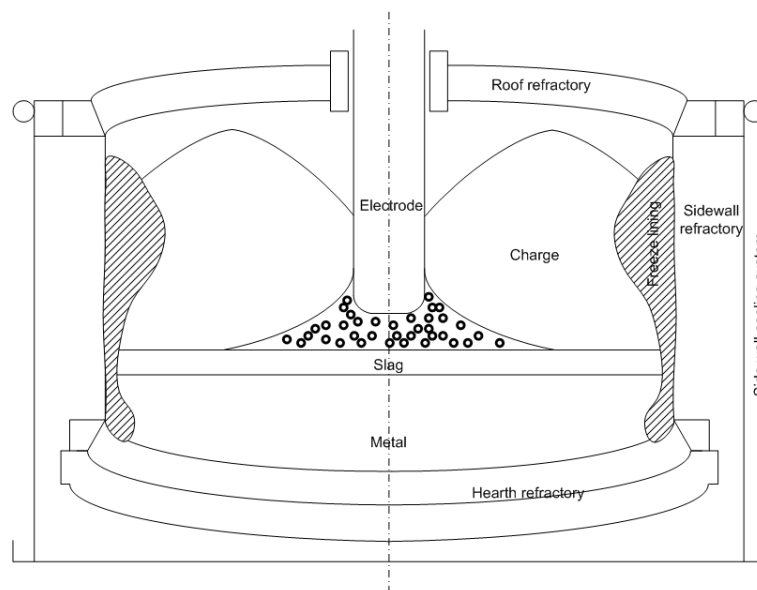


Figure 16: Conceptual refractory layout of the lining of a SAF based on the conductive design principle – schematic after Matyas et al [31].

The heat transfer model parameters were defined for the multi-layer cylindrical system in Figure 17.

It was assumed that for this system temperature was only a function of the radial distance and independent of the axial distance. The system was therefore classified as one-dimensional [21].

The only space coordinate to be classified was the radius, r . In Figure 17, r is defined for each layer as well as the notation identifying the temperature associated with each position.

It was further assumed that the system had reached steady state conditions and the thickness of the freeze lining therefore remained constant.

As a final assumption the heat transfer mechanisms for the system were limited to convection and conduction. Heat was transferred by conduction through the freeze-lining, the refractory material and the steel shell. From the slag layer to the freeze-lining, and from the steel shell to the water, heat was transferred through convection.

For conduction heat transfer, in a radial direction, Fourier's law applies (Equation 9) [21]:

Equation 9: Fourier's law

$$q = -kA \frac{dT}{dr}$$

In Equation 9, q is the heat transfer rate (W); k is the thermal conductivity (W/mK); A is the area of heat flow (m^2); and dT/dr is the temperature gradient (K/m).

For convection heat transfer, Newton's law of cooling applies (Equation 10) [21]:

Equation 10: Newton's law

$$q = hA(T_w - T_\infty)$$

In Equation 10, h is the convection heat transfer coefficient (W/m²K); T_w is the temperature at the solid/liquid interface and T_∞ is the temperature of the bulk of the liquid.

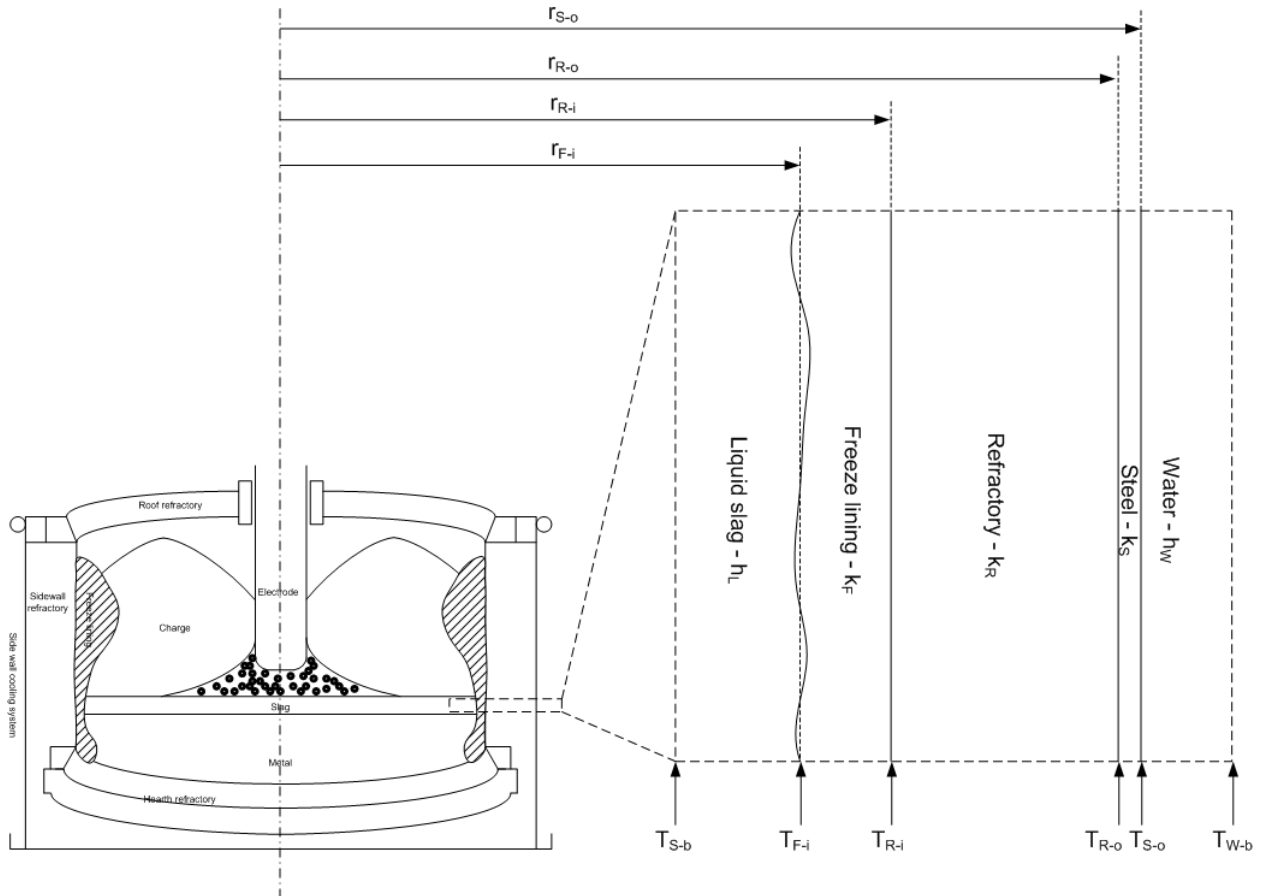


Figure 17: Definition of model parameters.

Integration of Equation 9 over a radial distance from r_i to r_o yields the heat transfer rate as a function of the temperature difference across this radial distance in a cylinder (Equation 11).

Equation 11: Fourier's law applied to the radial distance in a cylinder

$$q = \frac{2\pi k(T_i - T_o)}{\ln(r_o/r_i)}$$

An analogy utilized to solve heat transfer problems, is that of Ohm's law in electric-circuit theory (Equation 12) [19], [80]:

Equation 12: Ohm's law

$$I = \frac{V}{R}$$

In Equation 12, I is current, V is potential and R is resistance.

When comparing Equation 11 to Equation 12, it can be seen that q is analogous to I , $T_i - T_o$ to V and $2\pi k/\ln(r_o/r_i)$ to $1/R$. Voermann et al [81] and Verscheure et al [80] demonstrated that once the freeze lining has been established, the heat transfer rate through the furnace wall is determined by convective heat transfer from the liquid slag to the hot face of the freeze lining under steady state conditions. The hot face temperature of the freeze lining becomes a boundary condition for the

system. Heat transferred from the hot liquid slag in the furnace to the cooling water for the design in Figure 17 can therefore be expressed as the electrical analogue in Figure 18.

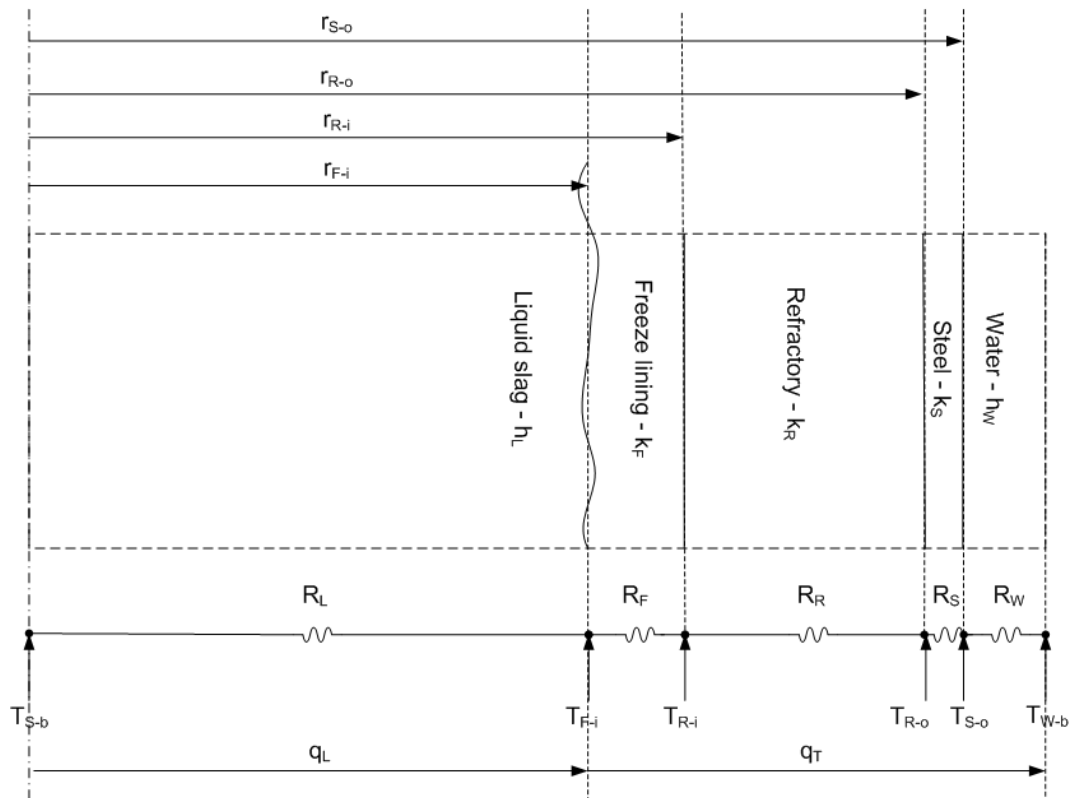


Figure 18: Electrical analogue of the conceptual furnace slag line design in Figure 17.

Each of the conduction resistances (R_S , R_R and R_F) is given by Equation 13 (which is derived from Equation 11); the two convection resistances are given by Equation 14 (from Equation 10); these expressions are for a unit length of the cylindrical furnace wall.

Equation 13: Conductive resistance

$$R_{cond} = \frac{\ln(r_o/r_i)}{2\pi k}$$

Equation 14: Convective resistance

$$R_{conv} = \frac{1}{2\pi r h}$$

From Figure 18, at steady state the heat transfer rate from the hot liquid slag to the hot face of the freeze lining (q_L ; Equation 15) equals the heat transfer rate from the hot face of the freeze lining to the cooling water (q_T ; Equation 16).

Equation 15: Heat transfer rate to lining by convection

$$q_L = \frac{(T_{S-b} - T_{F-i})}{R_L}$$

Equation 16: Heat transfer rate through the lining

$$q_T = \frac{(T_{F-i} - T_{W-b})}{R_F + R_R + R_S + R_W}$$

Based on these equations, the required freeze lining resistance is calculated in Equation 17.

Equation 17: Freeze lining resistance

$$R_F = \frac{1}{2h_L \pi r_{F-i}} \left[\frac{(T_{F-i} - T_{W-b})}{(T_{S-b} - T_{F-i})} \right] - (R_R + R_S + R_W)$$

From an initial estimate of the freeze lining resistance, the freeze lining thickness was calculated from Equation 17. An iterative procedure was followed, because the (unknown) thickness of the freeze lining affects the slag / freeze contact area and hence the heat transfer rate from the furnace. The assumed process conditions, material properties and furnace dimensions in Table 8 were utilised in these calculations.

Table 8: Assumed SiMn process conditions, material properties and furnace dimensions utilised in model, with sources of data indicated.

Symbol	Value	Units	Reference
T_{W-b}	303	K	Estimate
T_{F-i}	1573	K	Estimate based on Muller and Steenkamp [82]
T_{S-b}	1923	K	Estimate based on Olsen et al [1]
h_W	2000	$Wm^{-2}K^{-1}$	Estimate based on Welty et al [83]
k_S	45	$Wm^{-1}K^{-1}$	Estimate based on Welty et al [83]
k_R	Varied	$Wm^{-1}K^{-1}$	Table 7
k_F	2	$Wm^{-1}K^{-1}$	Estimate based on Steenkamp et al [84]
h_L	75	$Wm^{-2}K^{-1}$	Estimate based on Duncanson and Toth [19]
r_{S-o}	5.83	m	Estimate
r_{R-o}	5.8	m	Estimate based on Brun [17]
r_{R-i}	5.5	m	Estimate based on Brun [17]

As the main aim of a conductive lining design is to protect the hot face of the refractory from chemical wear by freezing a layer of refractory material onto the hot face of the lining, the effect of thermal conductivity (k_R) of different types of refractory material on freeze lining thickness are summarised in Table 9. As the thermal conductivity of the refractory material decreases, the thickness of the freeze lining decreases until no freeze lining forms. The thermal conductivity where the freeze lining disappears (for the assumptions stated in Table 8) is $6.1785 Wm^{-1}K^{-1}$.

Table 9: Resultant freeze lining thickness for different types of refractory material calculated with Equation 17 and based on the assumptions in Table 8.

$k_R [Wm^{-1}K^{-1}]$	Typical material	Freeze lining thickness [mm]
80	Graphite	88
10	Carbon paste, bricks or micropore carbon	37
5	SiC	0
2	Magnesia	0
1	Insulating material	0

For refractory layout based on the insulating design principle (defined in Figure 7a), no freeze lining exists. Only one heat transfer equation applies (q , Equation 18). Again each of the conduction resistances (R_S and R_R) is given by Equation 13 and the two convection resistances (R_L and R_W) by Equation 14.

Equation 18: Heat transfer rate through an insulating lining

$$q = \frac{(T_{S-b} - T_{W-b})}{R_L + R_R + R_S + R_W}$$

As the main aim of an insulating design is to minimize heat losses from the furnace, the effect of thermal conductivity (k_R) of different types of refractory material on heat lost are summarised in Table 10.

Table 10: Resultant heat loss for different types of refractory material calculated with Equation 18 and based on the assumptions in Table 8.

k_R [$\text{Wm}^{-1}\text{K}^{-1}$]	Typical material	Q [W]
80	Graphite	3 095 236
10	Carbon paste, bricks or micropore carbon	1 282 665
5	SiC	768 405
2	Magnesia	348 832
1	Insulating material	182 630

For a typical furnace height of 6m [17], the heat loss for a lining design based on the insulating principle will be 18.6MW for $80 \text{ Wm}^{-1}\text{K}^{-1}$, 7.7MW for $10 \text{ Wm}^{-1}\text{K}^{-1}$ and 1.1MW for $1 \text{ Wm}^{-1}\text{K}^{-1}$.

Heat losses calculated for a lining design based on the conductive principle is 0.89 MW for $80 \text{ Wm}^{-1}\text{K}^{-1}$ and 0.91 MW for $6.1785 \text{ Wm}^{-1}\text{K}^{-1}$. These heat losses results in typical heat loss of 5.4 MW for a furnace 6m high.

The typical operating load for a SAF defined in Table 8 is 27 MW [17] and the SiMn process typically requires 3 MW/ton SiMn produced [1]. Heat lost to the environment reduces the heat available to the process and increases the cost of production.

Irrespective of the type of material, these calculations illustrate that carbon-based refractory materials are heat conductors rather than insulators – see 1.5.1 [72]. Therefore, to protect these linings from chemical attack, proper cooling to below critical attack temperature is required [72]. The importance of the cooling system (water, air or oil [85]) and contact between the conductive refractory and water cooling system cannot be overemphasised [72], [86], [87].

2.4 Refractory wear mechanisms

2.4.1 Different types of refractory wear mechanisms

Refractory wear mechanisms reported in literature for SAFs producing manganese ferroalloys were densification, spalling, erosion and corrosion.

Densification (infiltration) is caused by slag / metal infiltrating pores and / or reacting with refractory [88].

Spalling is caused by thermal stress caused by a high thermal gradient across a single refractory body [88] as when refractory material on the hot face fractures and breaks away due to densification and / or thermal stress [89].

Erosion (abrasion) is caused by slag, metal and solid material abrading refractory [19], [88].

Corrosion (chemical wear) is caused when the system is not at equilibrium. Slag, metal or a flux will dissolve the refractory components it is not saturated with and / or chemically react with them [88]. Corrosion always begins with the interaction of some minor (binder phase) or major (aggregate) constituents of the refractories with the liquid slag or metal [69].

When investigating the potential for densification, corrosion or erosion as potential wear mechanisms, knowing whether or not the slag or metal is fully liquid at the prevailing temperature is important [69] as is the chemical composition of the liquid phase.

2.4.2 Development of carbon-based refractory materials in ironmaking

As more than 60% of all refractory materials are utilized in the iron and steel industry [18] development of refractory materials is mainly driven by applications in this industry [33], [90]. This is also the case for carbon-based refractory materials where developments are mainly driven by their application in the blast furnace hearth [70]. It seems that even in ancient times (the advent of the Iron Age was 2000BC), carbon-based refractory materials were utilized in the form of fine charcoal mixed with clays in Europe, Japan and China [90]. During the Industrial Revolution (18th and 19th century AC), the graphite crucible (presumably for blast furnace iron-making which commenced in 1709) was introduced in 1834 and carbon block in 1863 [90].

Nitta et al [70] gave an overview of the development of carbon blocks for blast furnace hearths at Nippon Steel where carbon blocks have been utilized in blast furnace hearths since 1951 [90] replacing fireclay bricks [91]. In the USA carbon-based refractories have been utilized in the hearth since 1944 [92].

In Japan, stave cooling of blast furnaces utilized for iron making was introduced in 1967. The intervention resulted in the hearth becoming the most critical part of the furnace determining the life of the lining and driving the development of high durability carbon blocks [90] (also reported elsewhere [93]). These developments extended the life of blast furnace linings from 5 years producing 2 million tons of iron (fireclay brick hearth) to 10 years producing 30 million tons of iron (carbon block hearth) [91] with actual refractory life of 15 years and predicted life of 25 years reported by others [94].

Initial developments were aimed at preventing penetration of molten iron into the blocks and to improve their corrosion resistance and thermal conductivity [70], [75]. Recent developments aimed at achieving higher corrosion resistance by actively producing a protective layer at the surface of the carbon block through contact with molten iron and slag [19], [75], [95].

In some hearth designs, a ceramic pad is installed on top of the carbon-based refractory material in order to protect the material against wear [87]. Another technique utilized to protect the hearth refractory is the addition of titanium-bearing ores (typically ilmenite) to the burden or through the tuyeres to form a protective layer of titanium carbonitride on the furnace hearth [87].

2.4.3 Wear mechanisms in ironmaking blast furnace hearth

The mechanisms reported for the wear of carbon brick linings in the hearth floor and hearth sidewall of blast furnaces producing iron are corrosion, densification, thermal stress related and erosion.

Corrosion is caused by different chemical reactions including:

1. Attack by slag [72].
2. Oxidation of carbon by water vapour at temperatures above 400°C [33], [34], [72], [77].
3. Attack by metallic zinc and zinc oxide [77] which preferentially attacks the binder phase [87].
4. Alkali (K and Na) attack causing the brick to crack [72], [96], with preferential attack on the binder phase at temperatures above 870°C [87].
5. Dissolution of carbon in pig iron [33], [70], [72], [77] at temperatures above 1100°C [87] with graphite having a higher dissolution rate [72], [78]. It was found that the binder phase may dissolve preferentially to the aggregate and once the binder phase dissolved, the aggregate particles were carried away by molten iron [77], [78].

Densification is caused by infiltration of molten iron into pores [65], [70], [78].

Erosion is caused by liquid metal [65], [72].

Thermal stresses (which could potentially result in spalling) are attributed to:

1. Thermal stresses in the lining caused by incorrect compensation for differential thermal expansion [33], [65], [87].
2. Temperature related wear includes large thermal loads; abrupt temperature fluctuations; thermal shock and thermomechanical stresses [86], [87].
3. Seepage of liquid pig iron and slag into the refractories [86], [92].
4. CO-degradation where carbon is deposited in the brick (or joints between bricks) at temperatures below 1000°C due to the Boudouard reaction where CO decompose to CO₂ and C [72]. Iron (in the refractory) acts as catalyst for the reaction [69]. The wear mechanism is not limited to carbon-based refractories but is observed in any CO-gas environment; an example in hearth linings consisting of fireclay bricks reported by Van Vlack [97]. For this reason very low iron contents of carbon-based refractories are required [72].

Embrittlement of material on the hot side of the brick and subsequent loss of cooling capacity is a wear pattern reported by several authors [65], [70], [78], [98]. Fujihara et al [78] attributed the formation of the brittle layer to a combination of infiltration of molten iron into pores with preferential dissolution of the binder phase into the iron, zinc and alkali attack and thermal stresses created due to the restriction of thermal expansion.

2.4.4 Role of additives in carbon-based refractory material

The development of carbon-based refractory materials was driven by the need to address the wear mechanisms described in section 2.4.3. Selection of aggregate or binder materials and differences in production methods were described in section 2.3.2. The role of additives is discussed here in more details.

Si, SiC, Al, Al₂O₃, Ti and TiO₂ are typically added to carbon refractories to strengthen the bond matrix, to generate micro-porosity and improve wear resistance properties [34].

In carbon-based ramming paste, Si is added to the matrix to react with carbon from the binder or aggregate to produce a SiC binder phase *in situ* [99]. In carbon block, Si is added to form Si-O-N whiskers in the pores during baking, reducing pore size and creating microporosity [64]. Chen et al [100] found that the amount of SiC increased with increase in temperature when baking carbon block containing metallic silicon (8% by mass) in the temperature range 1000°C – 1600°C with temperature of formation having a significant effect on the morphology of the SiC formed and

subsequently, total porosity and density. Addition of multi-walled carbon nanotubes (up to 5% by mass) in combination with metallic silicon (8% by mass) increased thermal conductivity and reduced porosity by forming SiC [101].

SiC is added as finely dispersed material to increase the packing density of the refractory (decreasing porosity) and to increase resistance of the blocks to abrasive wear [65], [77]. SiC is also added to increase thermal conductivity [87].

SiO₂ is added to create preferential sites for alkali attack to occur under controlled conditions [72], [87] resulting in less damage due to the swelling associated with alkali attack of inorganic components [33], [96].

Al₂O₃ is added for its resistance to acid slag [64], [75] and to increase the resistance of the binder phase to dissolution into iron by strengthening the bond matrix [75], [77], [78].

Ti is added to increase the viscosity of molten iron by forming TiN and TiC at the refractory / slag interface [64], [75]. When TiC formation led to micro-crack formation in the refractory, TiC rather than Ti was added [64], [75].

Al is added to form Al₄C₃ and AlN to increase thermal conductivity and reduce the mean diameter of open pores [102], [103] and, when added with SiO₂, result in total conversion of SiO₂ to SiC [65].

2.4.5 Refractory wear mechanisms in manganese ferroalloy furnaces

In SAFs producing manganese ferroalloys, examples were found of *densification* where alkali attack of alumina brick resulted in subsequent volume increase [17] and where metal penetrated open pores [66]. Examples of *corrosion* found were alkali attack of carbon tamping paste [17], oxidation by water leakages [66], metal attack of carbon refractory [66] and slag attack of carbon paste and tar dolomite brick [17].

2.5 Studying refractory wear mechanisms

To obtain an idea of the wear mechanisms involved, ideally samples of refractory material that has been in service in the furnace should be investigated. These samples would have experienced the history of the lining in all its complexity [36]. The samples are obtained during the furnace dig out and the investigation that follows is referred to as the “post mortem” after the medical examination of cadavers [36], [90]. Sugita [64] attributes the first investigation of this kind to a study conducted by Le Chatelier in 1917 on refractory materials from an open hearth furnace roof. Van Vlack reported on a study conducted on refractory samples obtained from a blast furnace utilized for iron-making [97].

When samples from the actual furnace are not available, laboratory-scale experiments are conducted to simulate specific conditions in a furnace and investigate the refractory wear mechanisms [36], [79]. Limitations of these tests are that the true service conditions cannot be simulated and the validity of statements made about the performance of the material is limited to the range of test conditions applied [36], [69], [79]. These techniques are therefore most suitable for product comparisons rather than predicting actual performance in a furnace, but as Chesters [36] said when discussing the merits of selecting a suitable refractory material for a specific application based on laboratory tests “...the assessor is likely to be right 8 or 9 times out of 10. This is preferable to guessing...”

2.5.1 Laboratory-scale experiments

Baxendale [104] defines three functional areas of laboratory tests available to study refractory materials: characterisation (datasheet properties), service-related properties and design data. For the current investigation the laboratory test methods of interest were limited to those applied to refractory characterisation and simulation of chemical wear, more specifically with regards to refractory resistance to slag [36], [104].

Refractory characterisation tests available include chemical analysis, mineralogical analysis, microscopic examination, bulk density and apparent porosity, true density and true porosity and pore size distribution [104].

Chemical analysis qualifies and quantifies the bulk chemical composition of the refractory materials [36], [104]. The most commonly utilized method is X-ray fluorescence (XRF) [79], [104]. The technique is based on the phenomenon that each element fluoresces characteristically when exposed to X-rays [104], [105]. The technique is not viable for elements low in the periodic table (fluorine downwards) for which other techniques i.e. wet chemistry and inductively coupled plasma (ICP) analysis could be applied [104], [105]. In coal analysis, the ultimate [106] analysis technique is applied to obtain bulk chemistry. In the ultimate analysis the bulk carbon, sulphur, nitrogen and hydrogen contents of the samples are determined experimentally [107], [108] and the oxygen content calculated by difference.

Mineralogical analysis qualifies and quantifies the bulk phase chemistry of the refractory materials [36], [104]. The most commonly utilized method is X-ray diffraction (XRD) applied in combination with the Rietveld technique [79], [104]. The technique is based on the diffraction of incident X-rays along crystallographic planes and is described by Bragg's formulation of X-ray diffraction [104], [109]. In coal analysis, the proximate [110] analysis technique is applied. In the proximate analysis the inherent moisture [111], volatile matter [112] and ash [113] contents are determined experimentally and fixed carbon content calculated by difference. *Inherent moisture* is the percentage loss in weight of 1 gram of air-dried sample after drying to a constant weight at 105°C (typically for 90 minutes). *Volatile matter* is determined by the percentage loss in weight of 1 gram of sample heated for 7 minutes at 900°C in the absence of air, less the percentage inherent moisture. *Ash* is determined by the percentage weight remaining of 1 gram of slowly heated coal after complete combustion in a ventilated muffle furnace at 815°C. The heating schedule is from room temperature to 500°C in 60 min, held at 500°C for 30 min, then raised to 815°C over a period of 30 min and held there for 60 min. The *fixed carbon content* is calculated by difference to 100%.

Microscopic examination is conducted to obtain an improved understanding of the microstructural properties of a sample [104]. It includes the study of polished sections using hand lenses, reflected light microscopes, optical microscopes or a scanning electron microscopes (SEM) [79], [104]. The resolution of an optical microscope is typically larger than 0.5 μm (5.0×10^{-5} cm) and of a SEM in the range 20 – 30 \AA ($2.0 - 3.0 \times 10^{-7}$ cm). A SEM could therefore be utilised to study mineral structures not visible through optical microscopy [36]. When energy dispersive X-ray spectroscopy (EDS) is added to the SEM investigation, the chemistry of specific particles and therefore their mineralogy could be determined from polished sections [79].

Bulk density is the ratio of the mass of the refractory material to its bulk volume. *Apparent porosity* is the ratio of the volume of the open pores of the refractory material to the bulk volume. The Archimedean evacuation method is applied to determine both [104]. *True density* is the ratio of the mass of the refractory material to its true volume. *True porosity* is the ratio of the total volume of open and sealed pores to the bulk volume. The pycnometer method is applied to determine both

[104]. *Pore size distribution* gives an indication of the size distribution of the open pores and is determined by mercury intrusion porosimetry [104].

Tests for chemical wear are often described as static or dynamic in nature [104], [114]. The *crucible (cup) test* [36], [104], [115], [116] is an example of a static test that is commonly applied. According to DIN specification (1065) a 44mm diameter hole is drilled 35mm deep into a block of refractory 80 x 80 mm by 65mm high; filled with 50g slag and heated to a given temperature for a stated time. When the sample is cooled down, it is sectioned and the extent of the reaction with slag is determined. Additional work required includes microscopy of polished sections of the slag / refractory interface. The *rotating finger test* [104], [114] is an example of a dynamic test in which a finger of refractory material is rotated in a stationary liquid bath.

To support actual plant trials and laboratory tests, fundamental studies based on thermodynamics (phase diagrams [90] or calculations using software i.e. FACTSage [100], [102], [117]) are conducted.

2.5.2 Thermodynamic calculations

In thermodynamics the change in Gibbs function can be utilized as a criterion to determine whether or not a chemical reaction can occur. The equations applied in Chapter 3 were derived from first principles [118] and summarised below.

For the general reaction $aA + bB \rightleftharpoons dD + eE$ involving solutions (i.e. non-standard conditions) the change in Gibbs' function (ΔG) is given by Equation 19 or Equation 20.

Equation 19: Change in Gibbs' function #1

$$\Delta G = \Sigma \Delta G_{products} - \Sigma \Delta G_{reagents} = dG_D + eG_e - aG_A - bG_B$$

Equation 20: Change in Gibbs' function #2

$$\Delta G = RT \ln\left(\frac{Q}{K}\right)$$

Where Q is referred to as the reaction quotient which for a reaction at equilibrium ($\Delta G = 0$) becomes K, the equilibrium constant. Q is defined in Equation 21 with a_i the activity of the species participating in the reaction.

Equation 21: Reaction quotient

$$Q = \frac{a_D^d \times a_E^e}{a_A^a \times a_B^b}$$

From Equation 20, when:

- $Q/K = 1$, $\Delta G = 0$ the reaction is at equilibrium
- $Q/K < 1$, $\Delta G < 0$ and driving force for the forward reaction does exist
- $Q/K > 1$, $\Delta G > 0$ and driving force for the forward reaction does not exist

In order to apply Equation 19 or Equation 20 to a specific chemical reaction, the standard states which will be adopted in the calculations have to be selected and the activities of the species relative to these standard states, have to be obtained ([68]). For gases behaving ideally, $a_i = P_i$ (the partial

pressure of the gas). For liquid and solid states a_i is related to the concentration according to Equation 22 ([68]):

Equation 22: Activity

$$a_i = \gamma_i N_i$$

In Equation 22 concentration is expressed as mol fraction (N_i) and γ_i is the activity coefficient. For the SiMn system under investigation, activity data for slag was derived from FACTSage and for the alloy from either FACTSage [117] or the interaction parameters derived by Li & Morris [119].

2.6 Conclusion

The first research question posed was: *when exposing carbon-based refractory material (ramming paste and carbon block) to SiMn slag or metal in the tap-hole, is chemical reaction between refractory and slag or refractory and metal a potential wear mechanism?*

Carbon block and ramming paste are two of several types of carbon-based refractory materials for which both aggregate and binder phase are carbonaceous. The main driver for the development of carbon-based refractories is the application in blast furnaces utilized for iron-making and associated wear mechanisms. Wear mechanisms include thermal stress related wear, densification, erosion or corrosion (chemical reaction). Chemical reactions include slag attack and dissolution of carbon into iron. Developments included the optimisation of the selection of aggregate material such as anthracite or graphite; selection of binder phase such as resin or coal tar; manufacturing processes and addition of inorganic additives such as Al_2O_3 or Si. Developments were primarily aimed at changing the material porosity either through changing the manufacturing process or by adding inorganic additives.

In SiMn production, chemical reaction between refractory and slag is one of the potential wear mechanisms applicable to the carbon-based refractory materials. Industrial examples of slag and metal attack of carbon refractories were reported [17] implying that the slag, metal and carbon refractories were not at chemical equilibrium. From a process perspective slag, metal and carbon were said to be at chemical equilibrium inside the furnace at process temperatures of 1650°C [1] implying that slag, metal and carbon refractories should be at chemical equilibrium in the tap-hole. To clarify these contradicting statements and improve the understanding of the potential for chemical reaction between refractory and slag or refractory and metal, Chapter 3 reports on the theoretical equilibrium for the system studied through thermodynamic calculations, one of the methods available to study refractory wear mechanisms.

3 Potential for chemical reaction – Part A (calculations)

3.1 Introduction

In Chapter 2 the SiMn production process and carbon-based refractory materials were discussed. From literature on slag, metal and carbon interactions it was concluded that slag, metal and carbon in the SAF are at chemical equilibrium and therefore slag, metal and carbon refractories in the tap-hole should also be at chemical equilibrium. However, literature on refractory wear in SiMn furnaces stated that it is not the case.

To obtain a better understanding of chemical equilibrium in the tap-hole, thermodynamic calculations were conducted with FACTSage 6.4. Chapter 3 reports on the results, concludes with a review of the first research question and an introduction to Chapter 4.

3.2 Method

To obtain a first understanding of the system under investigation, the equilibrium phase distributions of slag and of metal were calculated as functions of temperature at 1 atmosphere pressure. The Equilib model in FACTSage 6.4 was applied.

The slag calculations were based on the published [1] chemical composition stated in Table 11. To enable the calculation to converge, a small amount of argon was included in the calculation to allow formation of a small fraction of trivalent manganese in the slag. The FToxid and FACTPS databases were selected. The temperature range and intervals were specified as 1550°C – 1650°C at 25°C intervals. Default gas, liquids and solids were selected as pure species. Duplicates were suppressed with data from the FToxid database having preference to that of the FACTPS database. As solution species liquid slag (SLAGA) was selected with possible two-phase immiscibility and all other solution species as potential phases, except for the spinel and monoxide options for which ASpinel and AMonoxide only were selected. Normal equilibrium was calculated. The results reported were the mass of each phase present and the mass of each component per phase, all as functions of temperature.

Table 11: Published [1] relative masses of slag species (a repeat of Table 5) and argon utilised in thermodynamic calculations conducted in FACTSage 6.4.

MnO	SiO ₂	CaO	MgO	Al ₂ O ₃	Ar
9	45	21	9	16	0.00001

To calculate the liquidus temperature of the slag, the same method was applied except for the temperature range selected as 1000 – 1550°C at 25°C intervals and transitions and normal equilibrium calculated. Activities of slag components were found with FactSage, using liquid reference states in all cases.

For the metal calculations the chemical composition stated in Table 12 was utilised. For the metal calculations the FSstel and FACTPS databases were selected. The temperature range and intervals were specified as 1550 – 1650°C at 25°C intervals. Default gas, liquids and solids were selected as pure species. Duplicates were suppressed with data from the FSstel database having preference to that of the FACTPS database. As solution species liquid metal (LIQU) was selected with possible two-phase immiscibility and all other solution species as potential stable phases excluding diamond.

Normal equilibrium was calculated. The results reported were the mass of each phase present and the mass of each component per phase, all as functions of temperature.

Table 12: Published [1] metal composition (a repeat of Table 4) utilised in thermodynamic calculations conducted in FACTSage 6.4, and using the interaction parameters of Li and Morris [119].

Mn	Si	Fe	C
68	20	10	2

Activity data for metal components were calculated in FACTSage, and also utilising the interaction parameters of Li and Morris [119].

The equilibrium phase distribution of the reaction products upon equilibration of equal masses (100g, in the calculations) of slag or metal with refractory was calculated as a function of temperature (1550 – 1650°C at 25°C intervals), using the Equilib module in FACTSage 6.4. In these preliminary calculations, the refractory was assumed to be 100% graphite, with no ash-forming components or additives.

In these calculations, the total pressure was taken to be 1 atm. This means that gas could only form as stable product if the sum of the partial pressures of gas species would equal 1 atm. This is seen as reasonable, since reaction between slag and refractory could practically only proceed if CO (or CO-rich) bubbles could nucleate (with an internal pressure slightly higher than 1 atm).

For the refractory / slag interaction the FToxid, FSstel and FACTPS databases were selected. The composition of the slag stated in Table 11 was applied. The calculation converged without the addition of any argon. Default gas, liquids and solids were selected as pure species. Duplicates were suppressed with data from the FToxid database having first priority followed by FSstel and then the FACTPS databases. As solution species, liquid slag (SLAGA) and liquid metal (LIQU) were selected as possible phases with possible 2-phase immiscibility. Normal equilibrium was calculated.

For the refractory / metal interaction the FSstel and FACTPS databases were selected. The composition of the metal was as stated in Table 12. Default gas, liquids and solids were selected as pure species. Duplicates were suppressed with data from the FSstel database having priority over the FACTPS database. Liquid metal (LIQU) was selected as possible phase with 2-phase immiscibility. Normal equilibrium was calculated.

To calculate the carbon solubility as a function of Si-content and temperature at a fixed Mn:Fe ratio, the Equilib model in FACTSage 6.4 was applied. The FSstel and FACTPS databases were selected. Equilibrium calculations were conducted for metal with a Mn:Fe ratio of 6.8; the chemical composition of the metal was manipulated as follows:

- Mn: 6.8g
- Fe: 1g
- Si: Specified variable ranging between 0.0 and 4.0g
- C: Calculated variable (for saturation)

The equilibrium conditions specified were:

- Temperature: From 1500 to 1650°C at 50°C intervals
- Pressure: 1 atmosphere

Default solids were selected as pure species. Duplicates were suppressed with data from the FSstel database having preference to that of the FACTPS database. As solution species liquid metal (LIQU) was selected and all other solutions as dormant (metastable) phases.

A similar procedure was followed for metal with a Mn:Fe ratio of 5.1 except that the temperature was fixed at 1600°C (for comparison with literature data).

The equilibrium constant, K , for each balanced reaction was calculated at 1600°C using the Reaction module of FACTSage 6.4. The FACTPS database was selected. The standard reference state for each component is listed in Table 13.

Table 13: Standard reference states applied in the calculation of the ΔG° for each chemical reaction in FACTSage 6.4.

Component	MnO	SiO ₂	C	Mn	Si	CO	SiC
Reference state	Liquid	Liquid	Solid-1 graphite	Liquid	Liquid	Gas	Solid-1

The reaction quotient, Q , was either calculated from activity data generated in FACTSage 6.4 for the composition of slag (Table 11) and of metal (Table 12) or from activity data for metal components based on the interaction parameters of Li and Morris [119].

3.3 Results

The equilibrium phase distribution as a function of temperature is shown for slag only (Figure 19a), for metal only (Figure 19b), for slag and carbon (Figure 21a) and for metal and carbon (Figure 21b) in the temperature range 1550 to 1650°C. Figure 20 contains the equilibrium phase distribution of the slag in the temperature range 1000 to 1550°C.

The chemical compositions of the different phases as a function of temperature (1550°C – 1650°C) are indicated for the slag phase in Table 14, metal phase in Table 15 and gas phase in Table 16.

The activities of components as a function of temperature are indicated for the slag phase in Table 17 and metal phase in Table 18.

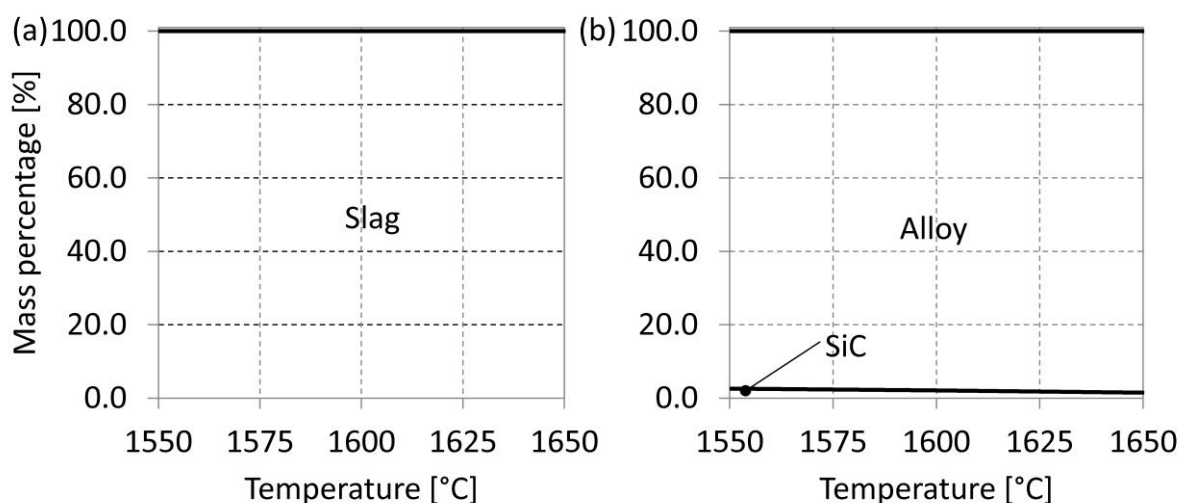


Figure 19: Equilibrium phase distribution of unreacted (a) slag and (b) metal as a function of temperature. The slag composition was given in Table 11 and metal composition in Table 12.

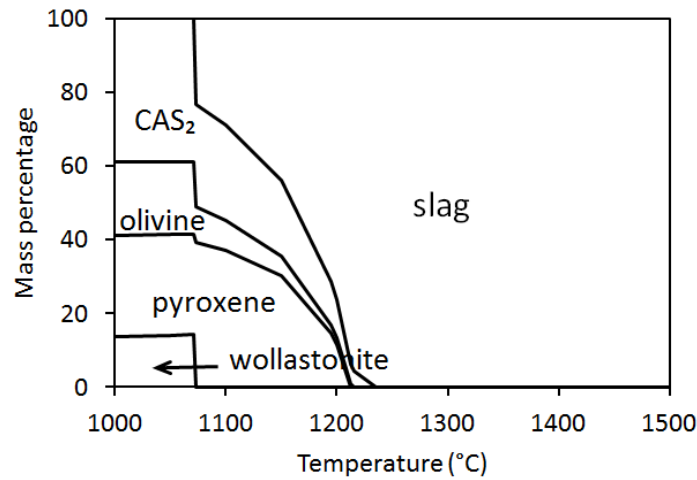


Figure 20: Equilibrium phase distribution of slag with composition in Table 11.

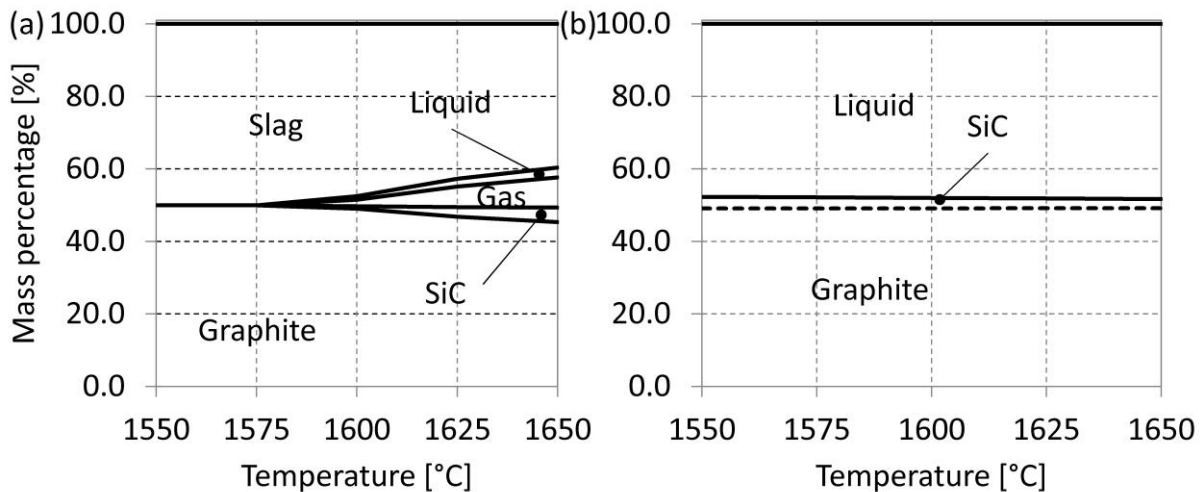


Figure 21: Equilibrium phase distribution as a function of temperature, when reacting graphite (representing refractory) with an equal mass of (a) slag and (b) metal. Slag composition as in Table 11; metal composition as in Table 12.

3.4 Discussion

Based on the published [1] slag composition, the slag is fully liquid in the temperature range under investigation (Figure 19a). The calculated liquidus temperature of the slag is 1235°C with anorthite (CaSi_2) the primary phase (Figure 20).

Slag will react with graphite to form solid SiC, liquid metal and a gas phase (Figure 22a). Except for MgO at higher temperature, the only slag components participating in the reduction reactions are MnO and SiO_2 . For the slag with initial composition stated in Table 11 both MnO and SiO_2 contents of the equilibrated slag decrease with increase in temperature (Table 14c). Reduction of MnO to Mn reporting to the metal phase would commence at 1593°C and to the gas phase at 1600°C. The Mn reporting to both metal phase (Table 15d) and gas phase (Table 16)) increases with an increase in temperature. These changes are illustrated by the mole balance for Mn reported in Table 19.

Reduction of SiO_2 to Si reporting to the metal phase (Table 15d) would commence at 1593°C. Reduction of SiO_2 to SiO in the gas phase (Table 16) and the formation of solid SiC would commence at 1600°C. These changes are illustrated by the mole balance for Mn reported in Table 20.

Upon formation of the metal phase (starting at 1593°C), C would report to the gas phase as CO (Table 16) and dissolve into the metal phase that formed (Table 15d). Upon the formation of the SiC phase (starting at 1600°C), C would also report to the SiC phase. These changes are illustrated by the mole balance for Mn reported in Table 21. In Figure 22b, the predicted equilibrium phases and participating components are summarised for the slag / graphite reaction.

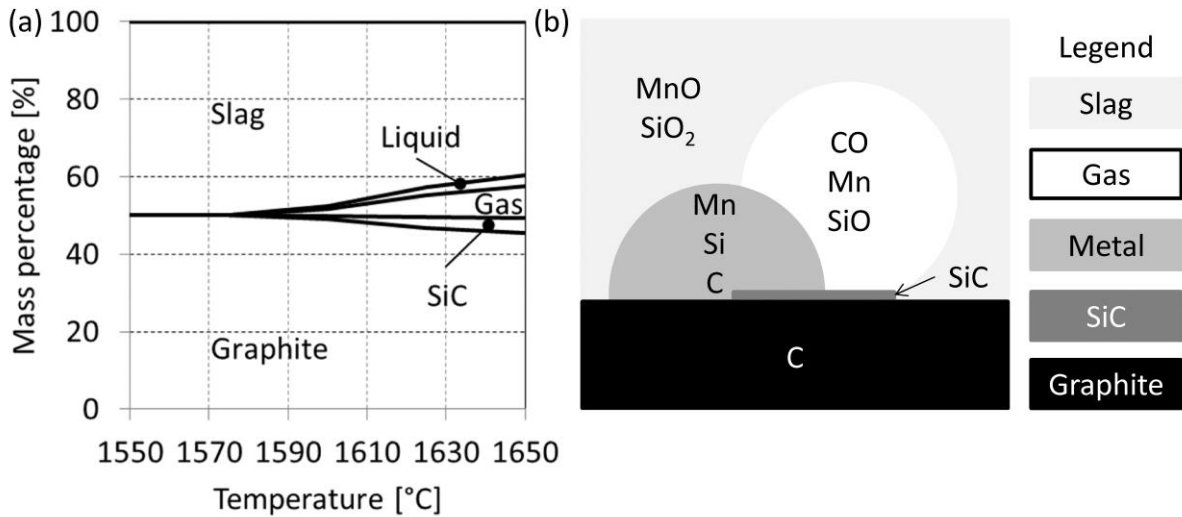


Figure 22: (a) Equilibrium phase distribution as a function of temperature (repeat of Figure 21a), when reacting graphite (representing refractory) with an equal mass of slag (composition as in Table 11). (b) Graphical representations of potential equilibrium phases and participating components per phase when slag equilibrates with graphite in the temperature range 1550°C to 1650°C.

Table 14: Chemical composition of the slag phase (percentage by mass): As published [1] (a), and as calculated for (b) slag only at equilibrium and (c) slag at equilibrium with graphite.

T (°C)	%MnO			%SiO ₂			%Al ₂ O ₃			%CaO			%MgO		
	a	b	c	a	b	c	a	b	c	a	b	c	a	b	c
1550	9.0	9.0	9.0	45.0	45.0	45.0	16.0	16.0	16.0	21.0	21.0	21.0	9.0	9.0	9.0
1575	9.0	9.0	9.0	45.0	45.0	45.0	16.0	16.0	16.0	21.0	21.0	21.0	9.0	9.0	9.0
1600	9.0	9.0	7.2	45.0	45.0	44.4	16.0	16.0	16.8	21.0	21.0	22.1	9.0	9.0	9.5
1625	9.0	9.0	4.9	45.0	45.0	41.3	16.0	16.0	18.7	21.0	21.0	24.6	9.0	9.0	10.5
1650	9.0	9.0	3.3	45.0	45.0	38.7	16.0	16.0	20.2	21.0	21.0	26.5	9.0	9.0	11.3

Table 15: Chemical composition of the metal phase (percentage by mass): As published [1] (a), and as calculated in FACTSage for (b) metal only, (c) metal equilibrated with graphite and (d) slag equilibrated with graphite.

T (°C)	%Fe				%C				%Mn				%Si			
	a	b	c	d	a	b	c	d	a	b	c	d	a	b	c	d
1550	10.0	10.3	10.5	0.0	2.0	1.2	1.9	2.2	68.0	69.9	71.3	81.1	20.0	18.6	16.3	16.8
1575	10.0	10.2	10.5	0.0	2.0	1.3	2.0	2.3	68.0	69.7	71.1	81.1	20.0	18.8	16.4	16.7
1600	10.0	10.2	10.4	0.0	2.0	1.4	2.1	2.0	68.0	69.5	70.9	79.8	20.0	18.9	16.6	18.1
1625	10.0	10.2	10.4	0.0	2.0	1.5	2.2	2.1	68.0	69.3	70.7	79.6	20.0	19.1	16.8	18.3
1650	10.0	10.2	10.4	0.0	2.0	1.6	2.2	2.1	68.0	69.1	70.4	79.3	20.0	19.2	17.0	18.6

Table 16: Calculated chemical composition of the gas phase (volume per cent when total pressure is 1 atmosphere) for the gas formed when slag equilibrated with graphite.

T(°C)	CO	Mg	SiO	Mn
1550	No gas			
1575	No gas			
1600	98.0%	0.1%	0.7%	1.2%
1625	97.6%	0.2%	0.8%	1.5%
1650	97.0%	0.4%	0.8%	1.8%

Table 17: Activity of slag components (liquid reference state) as functions of temperature (calculated with FACTSage 6.4) for slag analysis in Table 11.

T [°C]	SiO ₂	MnO	Al ₂ O ₃	CaO	MgO
1550	0.214	0.021	0.00663	0.000516	0.00942
1575	0.212	0.022	0.00663	0.000588	0.00957
1600	0.211	0.023	0.00663	0.000667	0.00972
1625	0.209	0.025	0.00662	0.000754	0.00986
1650	0.208	0.026	0.00661	0.000851	0.01000

Table 18: Activity of metal components as functions of temperature (calculated with FACTSage 6.4 or using the model based on the interaction parameters of Li and Morris) for metal composition in Table 12. Reference states: Graphite for carbon; pure liquids for all others.

T(°C)	FACTSage 6.4				Li & Morris		
	aMn_FS	aSi_FS	aC_FS	aFe_FS	aMn_LM	aSi_LM	aC_LM
1550	0.202	0.042	0.757	0.03	0.172	0.031	0.685
1575	0.199	0.046	0.765	0.03	0.175	0.032	0.628
1600	0.197	0.051	0.773	0.03	0.178	0.033	0.576
1625	0.195	0.056	0.781	0.03	0.18	0.034	0.53

1650	0.193	0.061	0.790	0.03	0.183	0.035	0.489
------	-------	-------	-------	------	-------	-------	-------

Table 19: Mole balance for Mn when 100g of slag (composition Table 11) is equilibrated with 100g graphite in the temperature range 1550°C to 1650°C.

T(°C)	IN	OUT			
		GAS	Metal	Slag	Total
1550	0.127	0.000	0.000	0.127	0.127
1575	0.127	0.000	0.000	0.127	0.127
1593	0.127	0.000	0.016	0.742	0.127
1600	0.127	0.002	0.029	0.096	0.127
1625	0.127	0.006	0.062	0.059	0.127
1650	0.127	0.010	0.080	0.037	0.127

Table 20: Mole balance for Si when 100g of slag (composition Table 11) is equilibrated with 100g graphite in the temperature range 1550°C to 1650°C.

T(°C)	IN	OUT				
		GAS	Metal	Slag	SiC	Total
1550	0.749	0.000	0.000	0.749	0.000	0.749
1575	0.749	0.000	0.000	0.749	0.000	0.749
1593	0.749	0.000	0.007	0.742	0.000	0.749
1600	0.749	0.001	0.013	0.701	0.034	0.749
1625	0.749	0.003	0.028	0.586	0.132	0.749
1650	0.749	0.005	0.036	0.510	0.198	0.749

Table 21: Mole balance for C when 100g of slag (composition Table 11) is equilibrated with 100g graphite in the temperature range 1550°C to 1650°C.

T(°C)	IN	OUT				
		GAS	Metal	C	SiC	TOTAL
1550	8.326	0.000	0.000	8.326	0.000	8.326
1575	8.326	0.000	0.000	8.326	0.000	8.326
1593	8.326	0.031	0.002	8.162	0.034	8.326
1600	8.326	0.125	0.003	8.163	0.034	8.326
1625	8.326	0.392	0.007	7.795	0.132	8.326
1650	8.326	0.565	0.010	7.553	0.198	8.326

Based on the published [1] metal composition, the metal is saturated in SiC, and as temperature increases the solubility of SiC increases (Figure 19b). This is in agreement with the saturation phase expected for metal containing more than 16-18% Si published by Olsen et al [1].

In Figure 23 the saturation lines calculated in FACTSage for a Mn:Fe ratio of 6.8 at 1500, 1550, 1600 and 1650°C are shown. The points of double saturation, where metal is saturated in both C and SiC, the zones of single saturation, where metal is saturated in either C or SiC, and the zone where metal is unsaturated in C and SiC, are indicated.

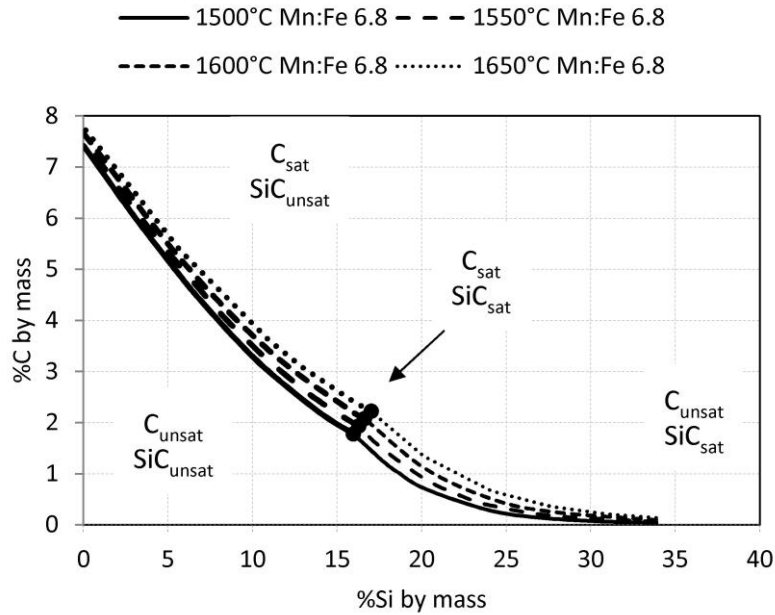


Figure 23: Calculated carbon solubility in Mn-Fe-Si-C alloys with a fixed Mn:Fe ratio of 6.8 at 1500°C – 1650°C.

The phase rule can be utilized to analyse the multi-phase system presented in Figure 23 – see results in Table 22. The phase rule is defined in Equation 23 ([120]):

Equation 23: Phase rule [120]

$$F = C - P + 2 - R$$

Where:

- F: Degrees of freedom.
- C: Number of components; in Figure 23 it is 3: Si, C, Mn:Fe ratio (fixed).
- P: Number of phases; in Figure 23 it could be liquid metal, graphite and SiC.
- R: Number of restrictions such as fixed temperature and pressure; the lines in Figure 23 are for conditions that are isothermal (1500°C, 1550°C, 1600°C or 1650°C) and isobaric (1 atmosphere pressure), hence $R = 2$.

Table 22: Application of the phase rule to Figure 23 and the consequences thereof.

Condition	C	P	R	F	Comment
Double saturation	3	3	2	0	No degree of freedom; for each temperature there is only one metal composition where double saturation occurs
Single saturation	3	2	2	1	One degree of freedom which means that for a fixed temperature and Mn:Fe ratio, either the Si or the C content could vary while maintaining saturation (of graphite or SiC) in the liquid metal.
No saturation	3	1	2	2	Two degrees of freedom which means that for a fixed Mn:Fe ratio temperature, the Si and the C content could be varied independently with only liquid metal present.

In Figure 24 the saturation lines calculated in FACTSage at 1600°C for a Mn:Fe ratio of 5.1, 6.8 and Mn only were constructed together with data redrawn from Olsen et al [1] for HCFEMn with a Mn:Fe ratio of 5.1 at 1600°C.

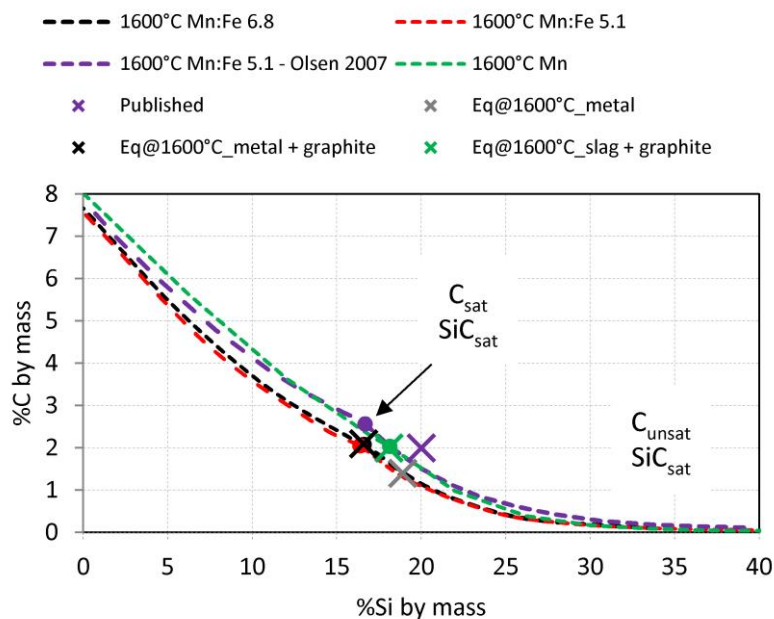


Figure 24: Calculated carbon solubility in Mn-Fe-Si-C alloys with different Mn:Fe ratios at 1500°C – 1650°C. Apart from the data from Olsen et al [1] the data was calculated in FACTSage 6.4 as part of this study. Crosses indicate the published [1] metal composition (purple) and equilibrium metal compositions calculated at 1600°C for metal only (grey), metal in contact with graphite (black) and metal produced when slag is in contact with graphite (green) - for the analyses refer to Table 15.

Also indicated in Figure 24 are the published [1] metal composition and the equilibrium metal compositions calculated at 1600°C for metal only, metal in contact with graphite and metal produced when slag is in contact with graphite. For the different metal compositions refer to Table 15.

In Figure 24 the published [1] metal analysis (purple cross) is not at equilibrium at 1600°C. The apparent supersaturation with silicon and carbon might be attributed to a number of causes, including the ones discussed below.

Possibility 1: the carbon content of the metal composition might be incorrect. Olsen et al [1] also reported metal compositions with 67%Mn, 17.5%Si and 1.5%C or 1.7%C, the difference being iron. Metal compositions with lower carbon contents approach the equilibrium lines for 1550°C (1.5%C) and 1600°C (1.7%C) with the metal potentially saturated in SiC but still not in C – refer to Figure 25.

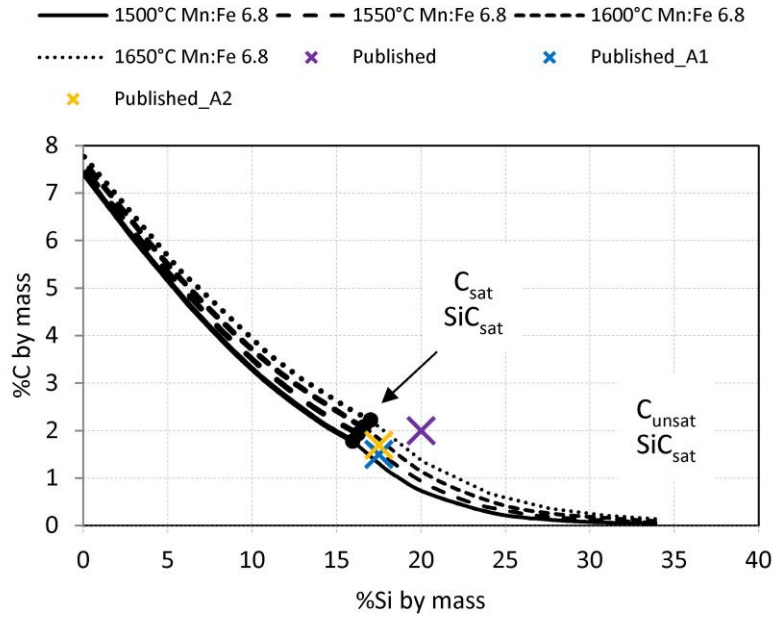


Figure 25. Calculated carbon solubility in Mn-Fe-Si-C alloys with a fixed Mn:Fe ratio of 6.8 at 1500°C – 1650°C. The purple cross indicates the published [1] metal composition - refer to Table 15 for analysis. The blue cross is for metal containing 17.5%Si and 1.5%C and the yellow cross for metal containing 17.5%Si and 1.7%C.

Possibility 2: The solution models might not apply to ferroalloys as the database (FSstel) was developed for steelmaking. In Figure 26 there is a 20% offset in carbon content for dual saturation and only 2% for silicon when comparing the carbon solubility lines calculated in FACTSage to those published by Olsen et al [1]. In both instances though the published [1] metal composition would be unsaturated in C and saturated in SiC.

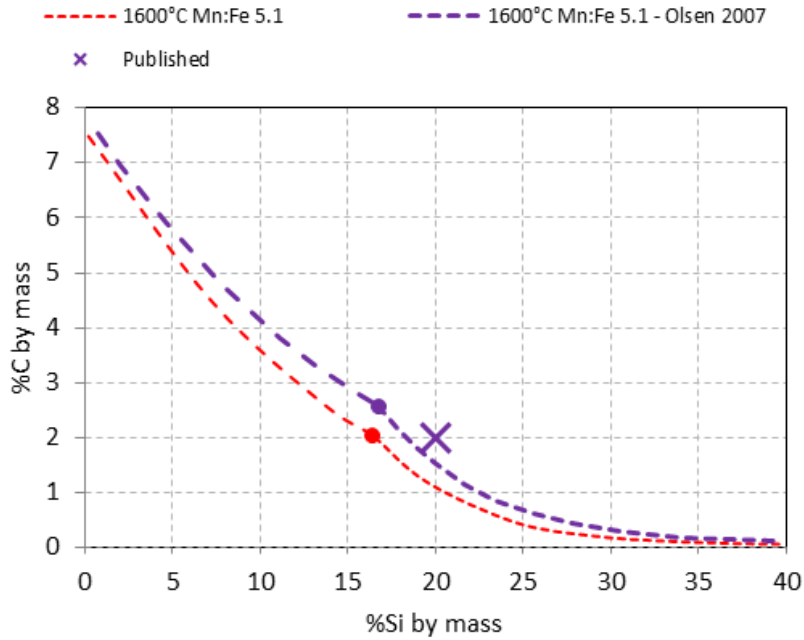


Figure 26: Calculated carbon solubility in Mn-Fe-Si-C alloys with a fixed Mn:Fe ratio of 5.1 at 1600°C as calculated in FACTSage 6.4 and as reconstructed from Olsen et al [1]. The purple cross indicates the published [1] metal composition - refer to Table 15 for analysis.

Possibility 3: The tapped metal temperature might be even higher than 1650°C with the metal being quenched during sampling. At higher temperatures, the published [1] metal composition will approach levels of unsaturation in both SiC and C. Quenching would prevent the SiC from precipitating from the sample during cooling and therefore result in metal with a higher carbon analysis.

Possibility 4: Upon sampling the metal might contain entrained SiC (and / or carbon) resulting in metal analysis indicating higher silicon or carbon contents.

Irrespective of the reasons for the higher carbon content of published [1] metal analysis (purple cross in Figure 24), the equilibrated metal is clearly only saturated in SiC and not in C. By implication this means that the metal tapped from the furnace is only saturated in SiC and not in C. This fact is illustrated in Figure 24 by the data point calculated for metal at 1600°C (grey cross) and confirmed by calculated carbon activity of the metal in the temperature range 1500 – 1650°C ranging between 0.76 and 0.79 (FACTSage 6.4) or 0.69 and 0.49 (Li & Morris).

Therefore, when metal with the published [1] metal analysis (Table 12) is brought into contact with graphite at constant temperature and pressure, it will drive to the dual saturation point by dissolving carbon and precipitating SiC to adjust the metal composition in terms of C and Si along the C-solubility line. In Figure 24 this will be from the grey cross to black cross along the black dotted lines. The concept is illustrated conceptually in Figure 27.

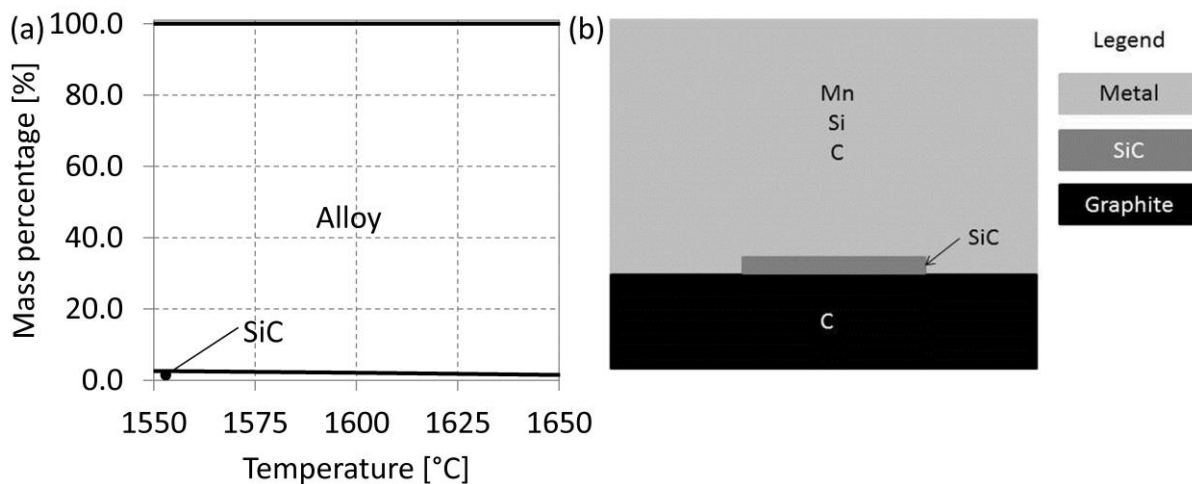


Figure 27: (a) Equilibrium phase distribution as a function of temperature (repeat of Figure 21 b), when reacting graphite (representing refractory) with an equal mass of metal (composition as in Table 12). (b) Graphical representations of potential equilibrium phases and participating components per phase when metal equilibrates with graphite in the temperature range 1550°C to 1650°C.

It is expected that metal produced in the coke bed would be saturated in both carbon and SiC, similar to the calculation for initially SiC-saturated metal equilibrated with carbon. One of the potential reasons for metal not being saturated in carbon after being tapped from the furnace could be that during tapping the metal is separated from the carbon source (coke bed) and is in contact with slag that might not be fully equilibrated with carbon. Further reaction of slag with metal could result in metal not being saturated in C and potentially not in SiC – see Table 23.

In Table 23, the a_c and a_{SiC} are reported as an indication of the potential of carbon dissolution and SiC formation. In reality SiC is a compound which does not exist as a dissolved component in metal. A SiC activity less than 1 indicates that the metal is not saturated with SiC.

Table 23: Activity of carbon and SiC at 1600°C (calculated with FACTSage 6.4; solid reference states) for metal equilibrated with slag with published [1] composition (Table 14 (a)), at a slag / metal mass ratio of 1.2.

	a_c	a_{SiC}
Published [1] slag	0.88	0.81

Another reason could potentially be the effect of lancing, but lancing does not form part of this study.

3.5 Conclusion

The first research question posed was: *When exposing carbon-based refractory material (ramming paste and carbon block) to SiMn slag or metal in the tap-hole, is chemical reaction between refractory and slag or refractory and metal a potential wear mechanism?*

Thermodynamic calculations indicated that the reactions most likely responsible for wear in the tap-hole are the reduction of SiO₂ to produce SiC or alloyed Si and MnO producing alloyed Mn – see Table 24 – and the dissolution of carbon in metal up to the point of dual saturation – in both carbon

and SiC. Depending on the model applied in calculating the activities of the metal components, the production of both SiC and alloyed Si and alloyed Mn should be possible at 1600°C ([119]) or SiC and alloyed Mn should form, but not alloyed Si ([117]). In addition, the metal – formed either by the slag reactions or present as tapped metal – would be saturated in SiC but not in C, and would therefore tend to dissolve carbon and further precipitate SiC to reduce the Si content until dual saturation is reached (Figure 24).

Table 24: Reactions most likely to be responsible for wear in the tap-hole; equilibrium constants, K, calculated with FACTSage 6.4. The activity data utilized to calculate the reaction quotient, Q, was taken from Table 17 and Table 18. The values are for a typical tapping temperature of 1600°C.

Reaction	K	$K^i_{1600^\circ\text{C}}$	FACTSage _{1600°C}	Q/K	Li & Morris _{1600°C}	Q/K
$\text{SiO}_2 + 3\text{C} \rightleftharpoons \text{SiC} + 2\text{CO}$	$1/a_{\text{SiO}_2}$	5.1	$a_{\text{SiO}_2} = 0.211$	0.9	-	-
$\text{SiO}_2 + 2\text{C} \rightleftharpoons \text{Si} + 2\text{CO}$	$a_{\text{Si}}/a_{\text{SiO}_2}$	0.2	$a_{\text{Si}} = 0.051$	1.2	$a_{\text{Si}} = 0.033$	0.8
$\text{MnO} + \text{C} \rightleftharpoons \text{Mn} + \text{CO}$	$a_{\text{Mn}}/a_{\text{MnO}}$	13	$a_{\text{MnO}} = 0.023$ $a_{\text{Mn}} = 0.197$	0.7	$a_{\text{Mn}} = 0.178$	0.6

ⁱ The reference condition for SiO₂, MnO, Si and Mn were the liquid phase, for SiC the solid phase, for C solid graphite and for CO the pure gas at 1 atm.

To validate the predictions and clarify the potential for formation of Mn or SiMn, laboratory scale experiments were conducted. The experiments were based on a synthetic, five component slag as source of SiO₂ and MnO and pure graphite as source of carbon. Chapter 4 reports on these experiments.

4 Potential for chemical reaction – Part B (laboratory experiments)

4.1 Introduction

As reported in Chapter 3, thermodynamic calculations indicated that the slag reactions most likely responsible for wear in the tap-hole are the reduction of SiO_2 to produce SiC and potentially alloyed Si, and of MnO to produce alloyed Mn (Table 24). The metal reactions would also result in the dissolution of carbon in the metal to reach the point of dual saturation (in both carbon and SiC - Figure 24).

Two models of activity data are available for the calculation of activities in the metal system: A model by Li and Morris [119] and the Equilib model in FACTSage [117] based on the FSstel database. According to the model by Li and Morris, the production of both alloyed Si and alloyed Mn is possible at 1600°C (Table 24). According to FACTSage, SiC and alloyed Mn should form, but not alloyed Si.

To test the predictions and clarify the potential for formation of Mn or SiMn laboratory scale experiments were conducted. Chapter 4 reports the results, and concludes with a review of the first research question and an introduction to Chapter 5.

4.2 Method

In Table 25 the results of the thermodynamic calculations are summarised. At 1550°C none of the reactions should be possible and at 1650°C all reactions could occur ($Q/K < 1$; $\Delta G < 0$) and in addition, the metal formed in the slag reactions would tend to dissolve carbon and produce SiC until dual saturation in both C and SiC is reached.

Table 25: Q/K ratios at different temperatures for reactions most likely to be responsible for wear in the tap-hole. (Equilibrium constants, K, calculated with FACTSage 6.4; activity data utilized to calculate the reaction quotient, Q, calculated with FACTSage 6.4 for the slag, and both FACTSage 6.4 and the model by Li & Morris for metal).

Reaction	1550°C		1600°C		1650°C	
	Q _{FACTSage} /K	Q _{Li & Morris} /K	Q _{FACTSage} /K	Q _{Li & Morris} /K	Q _{FACTSage} /K	Q _{Li & Morris} /K
$\text{SiO}_2 + 3\text{C} \rightleftharpoons \text{SiC} + 2\text{CO}$	2.4	-	0.9	-	0.3	-
$\text{SiO}_2 + 2\text{C} \rightleftharpoons \text{Si} + 2\text{CO}$	3.3	2.5	1.2	0.8	0.3	0.3
$\text{MnO} + \text{C} \rightleftharpoons \text{Mn} + \text{CO}$	1.2	1.0	0.7	0.6	0.4	0.4

It was therefore decided to conduct the experiments in which pure graphite crucibles were exposed to a synthetic, five component slag at 1550°C or 1650°C. Based on previous experiments – some of them conducted by Mølneås [116] – 4 hours was selected as a suitable duration and it was decided to conduct experiments in an argon atmosphere. The synthetic slag was prepared by melting pure minerals sourced from Sigma Aldrich as listed in Table 26.

The minerals were weighed and mixed by hand. The mixture was homogenised by splitting into 10 sub-samples using a 3-way splitter and recombining the sub-samples into one sample. The homogenisation step was repeated three times. The minerals were melted in a '50kg' induction furnace at Mintek – see Figure 28. A custom-made graphite crucible (acting at the same time as the susceptor) was ordered from Graftech – see dimensions in Figure 29. A protective atmosphere was

created by covering the crucible with a mineral wool blanket and blowing argon through a pipe with the outlet placed below the surface.

The melting temperature for the slag was calculated in FACTSage 6.4 as 1217°C - Figure 30 - using the method described in paragraph 3.2 and the chemical composition in Table 26. For control purposes the target temperature was selected at 100°C above the melting temperature of the slag. Temperature was measured with a type R thermocouple placed below the slag surface and protected by both an alumina and a graphite sheath. The temperature was controlled by manually changing the power input to the furnace. After melting, the slag was poured into a graphite slag pot and allowed to solidify and cool - Figure 31.

Table 26: Pure mineral blend on which synthetic slag was based.

Component	Mass [kg]	% Mass	Grade
MnO	0.9	10.6	Manganese (II) oxide -60 mesh 99% pure
SiO ₂	3.8	44.7	Quartz powder +230 mesh
Al ₂ O ₃	1.3	15.3	Aluminium oxide extra pure
CaO	2.1	24.7	Calcium oxide fine powder extra pure
MgO	0.4	4.7	Magnesium oxide light extra pure
Total	8.5	100	



Figure 28: Experimental setup for the preparation of the synthetic slag sample at Mintek with (a) the '50kg' induction furnace, (b) the blend of raw materials, (c) the graphite crucible / susceptor, (d) refractory sand, (e) graphite thermocouple sheath immersed in the slag, (f) alumina thermocouple sheath, (g) type R thermocouple extension wire and (h) mineral wool cover.

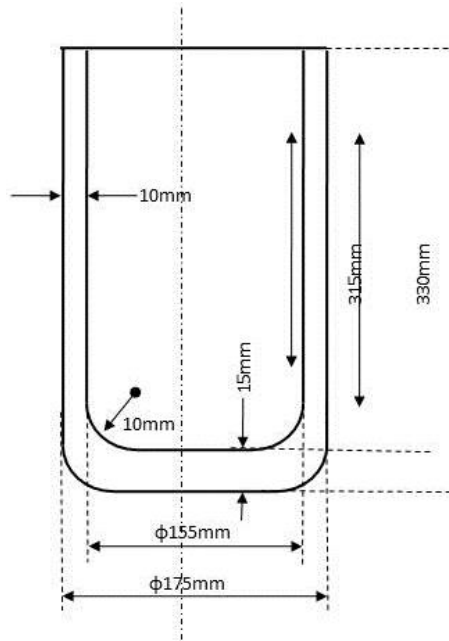


Figure 29: Dimensions of the graphite crucible utilized to prepare the synthetic slag.

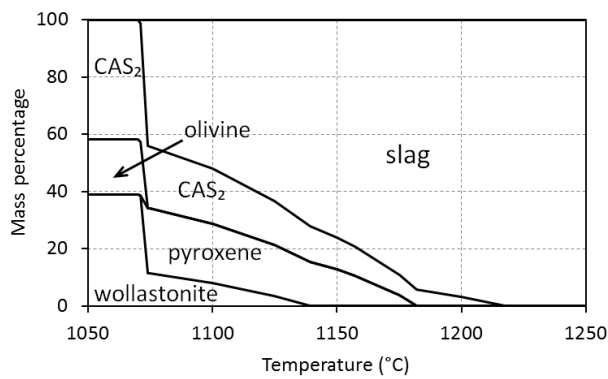


Figure 30: Equilibrium phase distribution of synthetic slag based on pure mineral blend in Table 26.

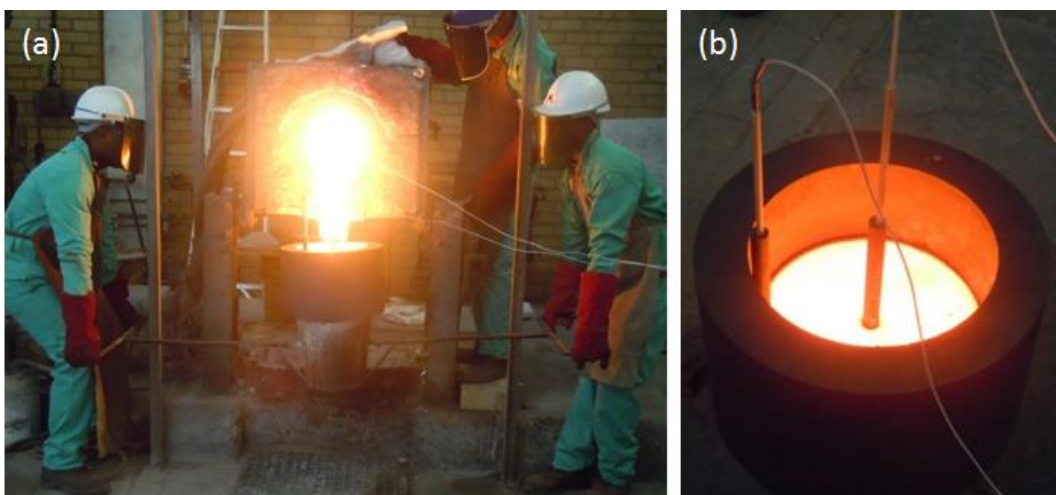


Figure 31: Synthetic slag being prepared at Mintek being (a) cast from the induction furnace into a graphite slag pot and (b) allowed to cool in the slag pot.

Once cooled, the slag was manually broken out of the slag pot using a hammer and chisel. The crushed slag was milled with stainless steel balls in a Normand Electrical ball mill, pulverised in a tungsten carbide sample holder in a swing mill and sieved to $-425\mu\text{m}$. The sieved sample was split into sub-samples and subsequently into sub-sub samples using a 10-way rotary splitter.

One of the representative, sub-sub samples of slag was characterised as follows:

1. Bulk chemical composition was determined by wet chemical methods at an in-house laboratory at a South African producer of SiMn with ISO 9001:2000 accreditation:
 - ICP: FeO, CaO, MgO, Al_2O_3
 - Gravimetry: SiO_2
 - Titration: MnO
2. Bulk phases were determined by XRD. The relative phase amounts (weight %) were estimated using the Rietveld method. When quantifying the amorphous content of the slag, twenty per cent Si was added (as a standard).
3. Compositions of specific phases were determined by:
 - Preparing polished sections and sputter coating these with gold
 - Microanalysis with FEGSEM-EDS at 15 kV (point analyses)

The following instruments were utilized for analytical purposes:

- XRD: PANalytical X'Pert Pro powder diffractometer with X'Celerator detector and variable divergence- and receiving slits with Mn filtered Fe- $\text{K}\alpha$ radiation. Phases were identified with X'Pert Highscore plus software.
- FEGSEM EDS: ZEISS LEO 1525 FEGSEM with EDS conducted with an Oxford INCA Energy System.

A schematic of the experimental setup for reaction of the slag is indicated in Figure 32 and of the crucible design in Figure 33. The design, procurement, installation and commissioning of the experimental setup (including the high frequency induction power supply) formed part of the scope of the study.

Power was supplied by an Ambrell Ecoheat ES high frequency induction power supply. Temperature was measured with type B and R thermocouples wired through a four bore alumina sleeve (M) allowing for the hot junctions to be positioned at the same level. The type B thermocouple was utilized for control with readings logged manually. The type R thermocouple was utilized as the reference thermocouple with temperature readings logged automatically. The temperature was controlled by manually changing the voltage set point on the induction furnace control panel. Due to the aggressive nature of the slag towards the alumina, measurement of the temperature in the slag itself was not possible.

Bubble alumina was added to the graphite susceptor for two reasons: 1) to support the small graphite crucible filled with slag and 2) to act as heat sink ensuring that the temperature measured by the thermocouple represents the temperature of the slag.

In each experiment a small graphite crucible was filled with a 5g representative synthetic slag sample. The crucible was placed in a graphite susceptor with graphite lid supported by bubble alumina (J). The graphite lid (G) had two 10mm ports - inlets for the alumina thermocouple sheath (C) and alumina sleeve (D) utilized to blow 99.998% argon gas onto the surface of the lid – and five 6mm ventilation holes (F) for gasses formed to escape. The induction coil was cast in coil grout (I). The graphite susceptor was supported by bubble alumina. The top of the graphite susceptor was aligned with the top of the induction coil grout.

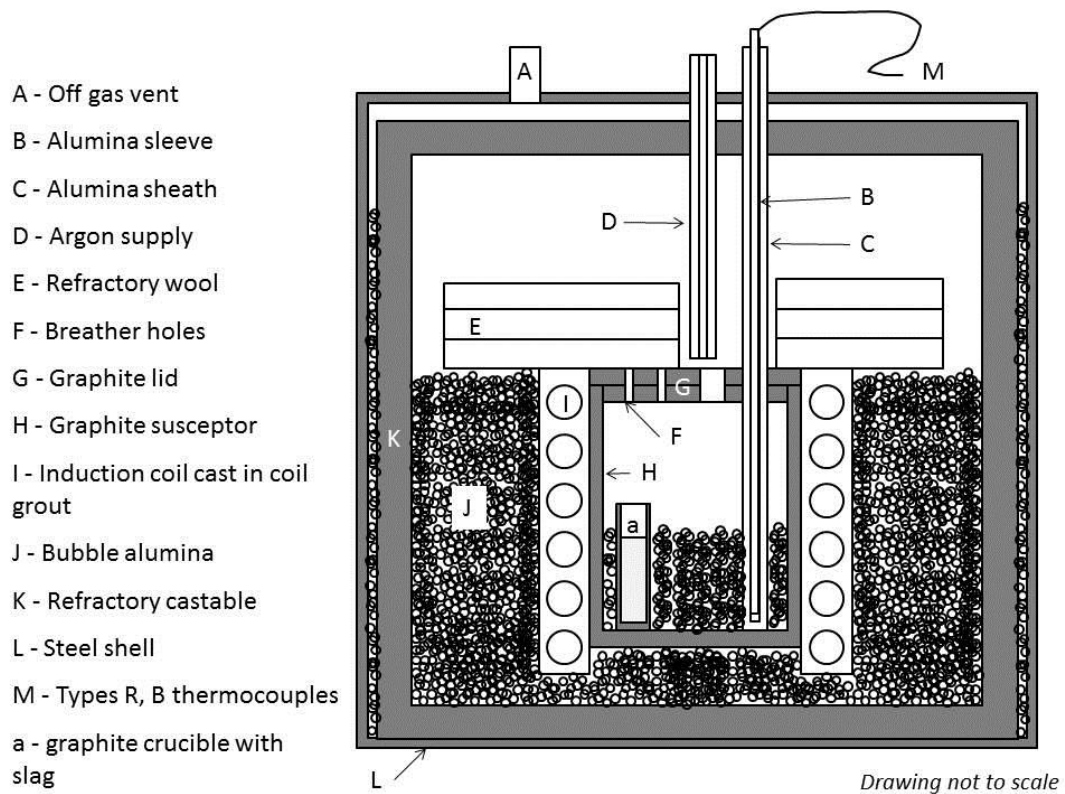


Figure 32: Experimental setup for pure component experiments.

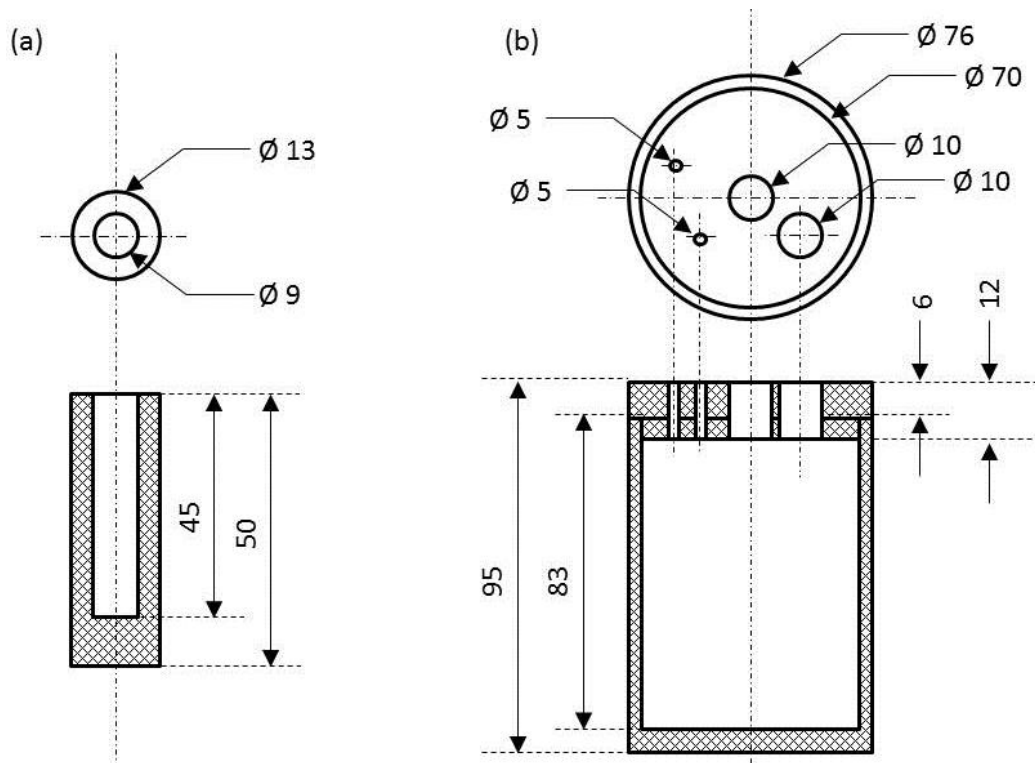


Figure 33: Design of crucibles utilised in cup test experiments with (a) graphite crucible – a in Figure 32 – and (b) graphite susceptor with lid – G and H in Figure 32. All measurements in mm.

To control the atmosphere, the experimental setup was contained in a stainless steel shell – L – with stainless steel lid. The lid had inlet ports for the thermocouple sheath and argon supply and an outlet port for the off gases (A). Joints were sealed using gaskets cut from high temperature silicone and high temperature O-rings.

To improve insulation a precast refractory cylinder – K – and refractory lid were positioned in the steel shell. The gaps between the steel shell and refractory cylinder and between the refractory cylinder and induction coil were filled with bubble alumina. The susceptor lid was covered by three layers of 30mm thick, high temperature refractory blanket – E – (Rath Altra Mat 80) with openings for the thermocouple sheath and argon sleeve.

The experimental procedure was as follows:

1. Prepare crucible (a)
 - a. Weigh slag
 - b. Fill small graphite crucible
2. Assemble large graphite crucible
3. Assemble thermocouple: type R + type B in a four-bore alumina sleeve
4. Assemble furnace
 - a. Replace contaminated alumina bubbles
 - b. Install crucible surrounded by alumina bubbles
 - c. Install 3 layers of kaowool
 - d. Install refractory lid
 - e. Install alumina thermocouple sheath
 - f. Install alumina thermocouple sleeve: first allow the thermocouple hot junction to touch the bottom of the sleeve and then pull it up + 10mm. Hold in place mechanically.
 - g. Install argon
 - h. Install lid
 - i. Tighten all screws
 - j. Install off gas
5. Run test
 - a. Run water
 - b. Flush chamber with argon for 20 min at a high flow rate (1.552 litres/minute)
 - c. Reduce argon flow rate (0.517 litres/minute)
 - d. Power on
 - e. Heat to 1550°C or 1650°C by manually adjusting the target voltage set-point (145V or 150V respectively).
 - f. Hold for 4 hours at temperature by manually adjusting the voltage set point. During the holding period the control temperature readings ranged between the set-point $\pm 5^\circ\text{C}$.
6. End test
 - a. Switch off power
 - b. Switch off argon
 - c. Keep water running
7. Open furnace immediately after ending test (top of crucible turned black within minutes)
 - a. Remove off gas
 - b. Remove thermocouple sleeve
 - c. Remove thermocouple sheath
 - d. Remove argon
 - e. Loosen all screws

- f. Remove lid
- g. Remove refractory lid
- h. Remove 3 layers of kaowool
8. Allow furnace to cool overnight
9. Remove samples
10. Label samples

Once the samples were removed a post mortem investigation was conducted as follows:

1. Cut samples
 - a. Cast samples in epoxy
 - b. Slice samples lengthwise
 - c. Cut off top section not of interest and discard
2. Prepare polished sections
 - a. Lay samples face down in sample holder
 - b. Fill with resin
 - c. Draw vacuum
 - d. Allow to set in drying oven at 50°C overnight
 - e. Grind
 - f. Polish
 - g. Clean
 - h. Keep in desiccator
3. Study polished sections
 - a. Light optical microscope (LOM)
 - b. FEGSEM – samples coated with Au or Pt

Equilibrium phase distribution of the slag as a function of temperature, the equilibrium constants of the slag reactions with carbon and activities of participating components were calculated with FACTSage 6.4. These calculations were based on the actual bulk chemical analysis of the slag (Table 27).

4.3 Results

The bulk chemical composition of the slag is given in Table 27.

Table 27: Bulk chemical composition of synthetic slag samples determined by wet chemistry methods (average percentage by weight and standard deviation of three samples per material).

	MnO	SiO ₂	CaO	MgO	Al ₂ O ₃
Average	11.3	44.3	23.8	5.2	15.5
StDev	0.3	0.2	0.1	0.1	0.1

The predicted phase distribution is shown in Figure 34a and an SEM BSE image of the synthetic slag in Figure 34b. The average and standard deviation of 10 SEM EDS analyses of the amorphous slag phase is given in Table 28. As expected, the EDS analyses are similar to the bulk slag composition.

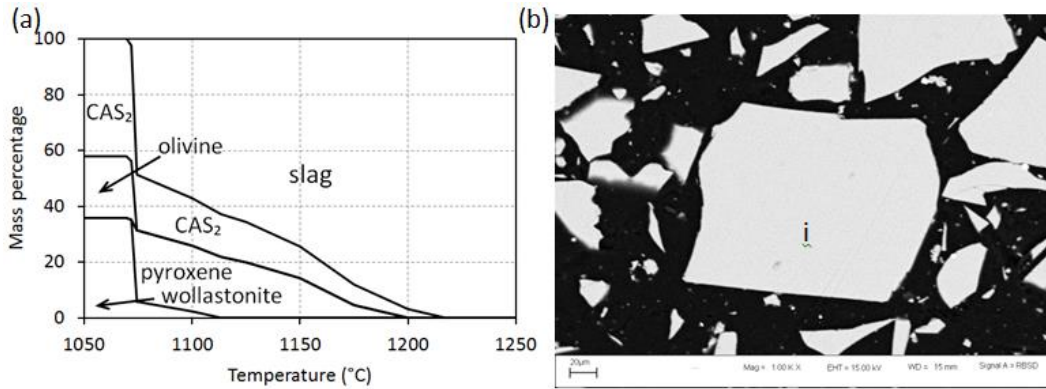


Figure 34: (a) Equilibrium phase distribution of synthetic slag based on the bulk chemical composition, as calculated with FACTSage 6.4. (b) SEM BSE image of synthetic slag (scale bar 20 μm) with (i) amorphous slag phase only.

Table 28: Composition of amorphous slag phase (i) in synthetic slag – average of 10 EDS point analyses.

	MnO	SiO ₂	CaO	MgO	Al ₂ O ₃
Average	10	47	22	5	16
StDev	0.2	0.3	0.2	0.1	0.1

The XRD results confirmed the fact that only amorphous (glass) phase was present in the synthetic slag - Figure 35.

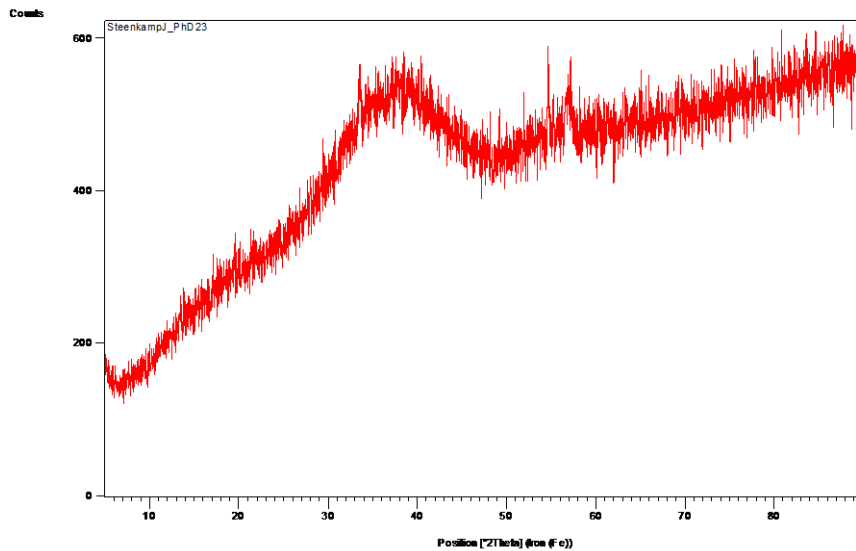


Figure 35: X-ray diffraction pattern of synthetic slag (no Si-standard).

SEM BSE micrographs and SEM EDS results for the experiment conducted at 1550°C are reported in

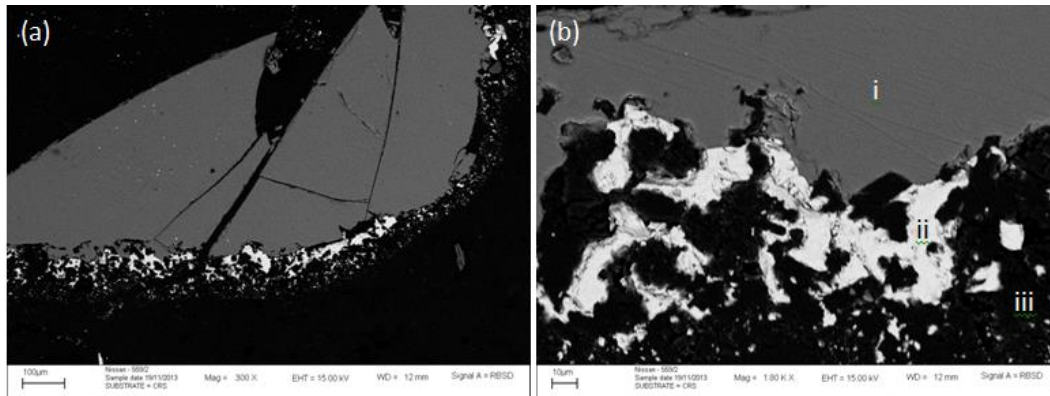


Figure 36 and Table 29 respectively. The standard deviations of both silicon and manganese are high and a larger sample size will improve the results, but the analysis as is was considered suitable for the study.

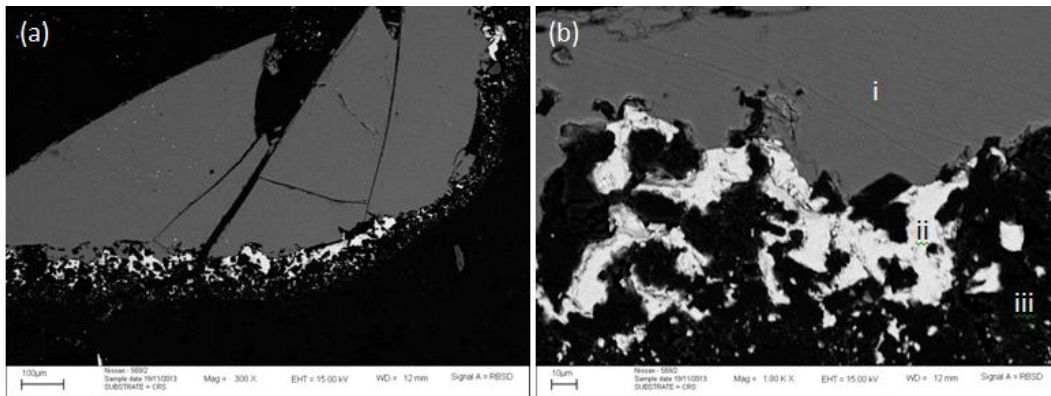


Figure 36: SEM BSE micrograph of metal accumulation at the slag / refractory interface of the sample prepared at 1550°C. The sample bottom and sidewalls magnified 300 times (scale bar 100 μm) in (a) and 1800 times (scale bar 10 μm) in (b). The phases present were (i) slag, (ii) metal and (iii) graphite.

Table 29: Analysis of metal phase (weight per cent) of metal accumulation at the slag / refractory interface of the sample prepared at 1550°C determined as average of EDS point analysis of 4 metal particles at 15 kV.

	Weight per cent [%]				
	Si	Mn	Fe	Cr	Ni
Average	15.6	63.1	17.4	2.5	1.4
StDev	5.7	6.3	0.3	0.4	0.7

SEM BSE micrographs and SEM EDS results for the experiment conducted at 1650°C are reported in Figure 37, Figure 38 and Table 30 respectively. The modelled and measured EDS spectra for the SiC phase (found in the reacted sample) are presented in Figure 39.

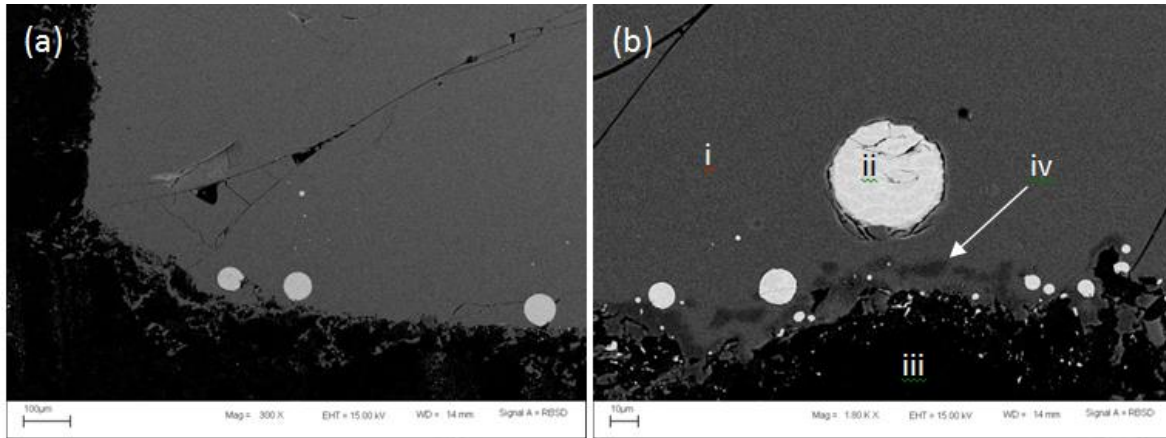


Figure 37: SEM BSE micrograph of metal accumulation at the slag / refractory interface of the sample prepared at 1650°C. The sample bottom and sidewalls magnified 300 times (scale bar 100 µm) in (a) and 1800 times (scale bar 10 µm) in (b). The phases present were (i) slag, (ii) metal, (iii) graphite and (iv) SiC. Note that the SiC did not form a protective layer at the slag / refractory interface but detached from the graphite.

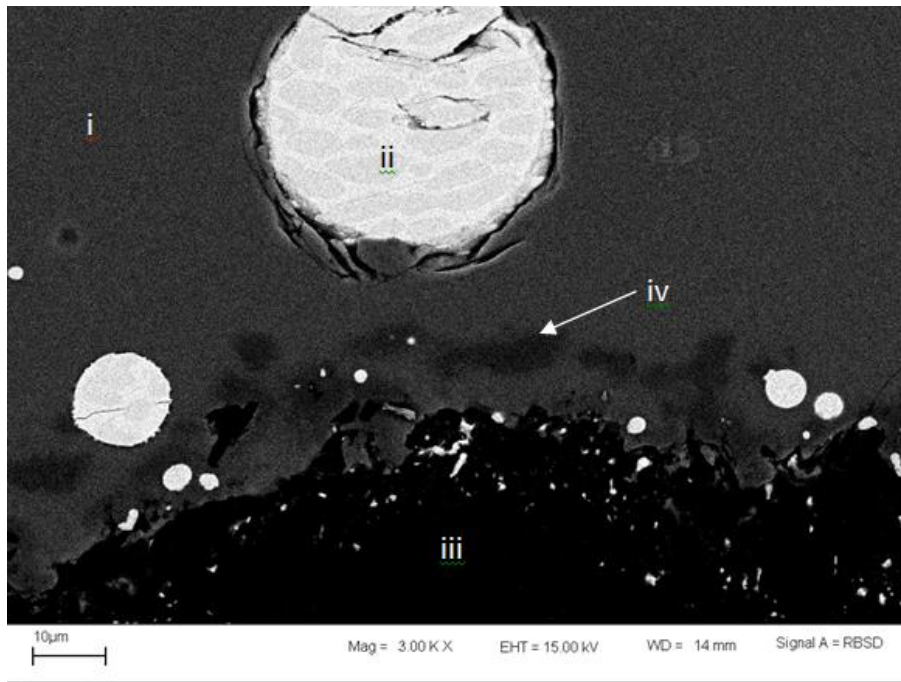


Figure 38: SEM BSE micrograph of metal accumulation at the slag / refractory interface of the sample prepared at 1650°C (scale bar 10 µm; enlarged view of Figure 37). The phases present were (i) slag, (ii) metal, (iii) graphite and (iv) SiC. Note that the SiC did not form as a protective layer at the slag / refractory interface, but detached upon formation.

Table 30: Analysis of metal phase (weight per cent) of metal accumulation at the slag / refractory interface of the sample prepared at 1650°C determined as average of EDS point analysis of 3 metal particles at 15 kV.

	Weight per cent [%]				
	Si	Mn	Fe	Cr	Ni
Average	20.2	71.4	6.8	1.1	0.7

StDev	4.5	5.0	0.6	0.1	0.2
-------	-----	-----	-----	-----	-----

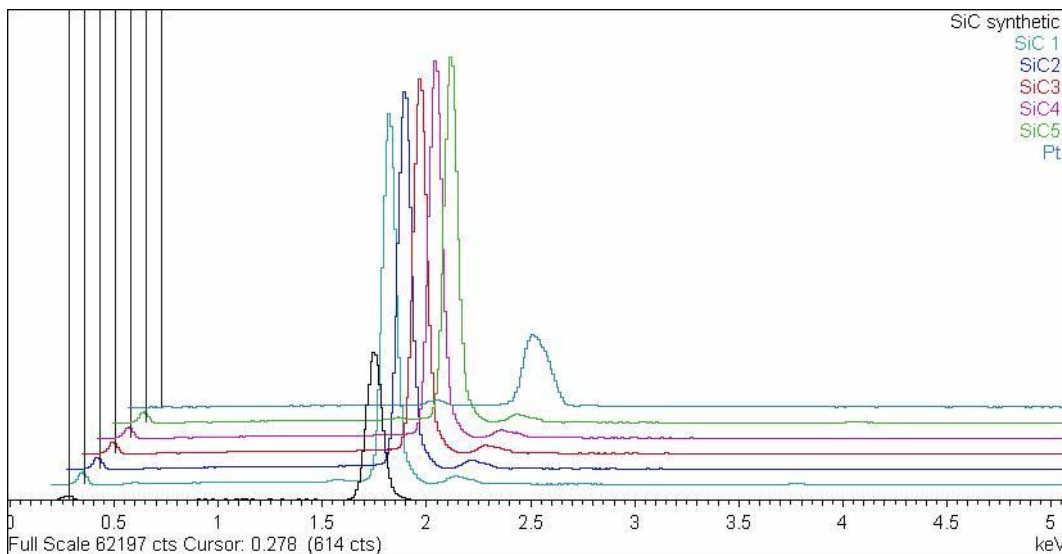


Figure 39: Modelled (SiC synthetic) vs. measured (SiC 1 – SiC 5) EDS spectra at 15 kV of the SiC phase identified in Figure 37. The sample was coated with platinum.

4.4 Discussion

According to the bulk chemical composition of the synthetic slag, the planned slag composition was reached. EDS analysis indicated the composition of the amorphous slag phase to be slightly lower in CaO and higher in SiO₂ but if this were due to undissolved material, their contents were below the detection limit (1 – 2%) of the XRD.

Metal phases containing Si and Mn formed in both experiments (1550°C and 1650°C) and SiC formed in the high temperature experiment but not in the low temperature experiment. The SiC that formed did not form a solid layer – a potentially protective *in situ* refractory material [18] – at the slag / refractory interface, but detached from the interface. Some of the SiC particles were attached to metal droplets but whether these SiC particles formed during slag / refractory interaction or metal / refractory interaction (reaching the point of SiC saturation) remains unanswered.

The metal phases were contaminated by Fe-Cr-Ni, most probably originating from the balls utilized to mill the slag. To estimate the effect of the contamination on the potential for the reduction reactions to occur, additional thermodynamic calculations were conducted in FACTSage 6.4. The calculations were based on 100g slag with composition in Table 29, 100g graphite and 0.5 g and 5.0 g of steel contaminant with composition in Table 31 (estimated from metal analyses in Table 29 and Table 30).

Table 31: Chemical composition of steel contaminant.

Weight per cent [%]				
Si	Mn	Fe	Cr	Ni
0	0	81.7	11.7	6.6

Calculations were conducted in the Equilib module with the FToxid, FSstel and FACTPS databases selected. As pure species gases, liquids and solids were selected. As solution species only liquid metal (LIQU) and liquid slag (SLAGA) were selected. Results were presented in Figure 40.

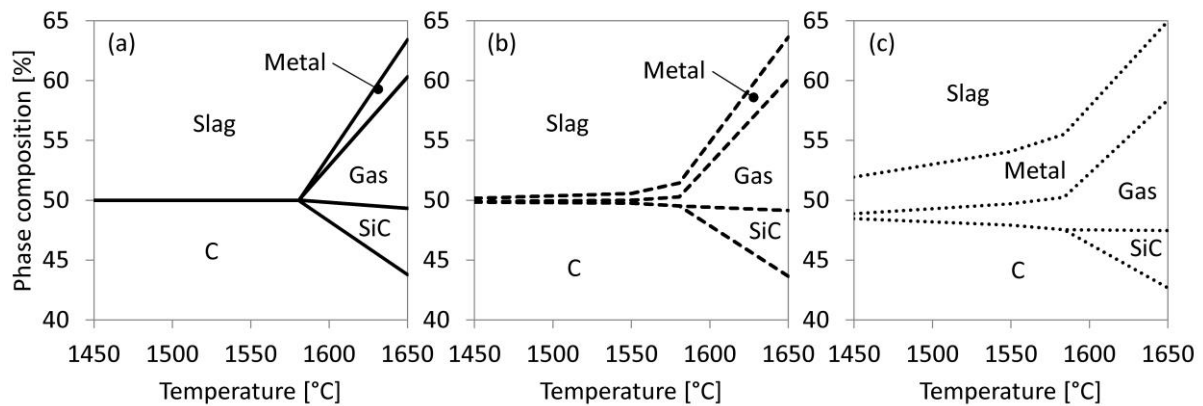


Figure 40: Equilibrium phase distribution as functions of temperature when synthetic slag (composition in Table 28) equilibrates with graphite, and (a) no steel contaminant added, (b) 0.5g steel contaminant added and (c) 5.0g steel contaminant added.

From the results in Figure 40a and Figure 40b although the presence of 0.5g steel contaminant would allow for the reduction of Mn to occur at temperatures even lower than 1450°C, the effect on the extent of formation of Mn, Si and SiC is insignificant.

From the results in Figure 40a and Figure 40b although the presence of 0.5g steel contaminant would allow for the reduction of Mn to occur at temperatures even lower than 1450°C, the effect on the extent of formation of Mn, Si and SiC is insignificant.

Similarly, the presence of 5g steel contaminant would have allowed for the reduction of both Mn and Si to occur at temperatures even lower than 1450°C. The temperature at which SiC can form is raised slightly (1581°C – 1584°C) and the amount of SiC formed at 1650°C reduces slightly from 11.1g to 9.8g.

Table 32 contains a summary of the predicted potential for the reaction products to form and whether or not these products were observed in either of the experiments.

Table 32: Summary of the predicted potential for the reaction products to form and the presence of actual reaction products formed.

Reaction	1550°C		1650°C	
	Prediction	Actual	Prediction	Actual
$\text{SiO}_2 + 3\text{C} \rightleftharpoons \text{SiC} + 2\text{CO}$	No	No	Yes	Yes
$\text{SiO}_2 + 2\text{C} \rightleftharpoons \text{Si} + 2\text{CO}$	No	Yes	Yes	Yes
$\text{MnO} + \text{C} \rightleftharpoons \text{Mn} + \text{CO}$	No	Yes	Yes	Yes

4.5 Conclusion

The first research question was: *When exposing carbon-based refractory material (ramming paste and carbon block) to SiMn slag or metal in the tap-hole, is chemical reaction between refractory and slag or refractory and metal a potential wear mechanism?*

Based on the work conducted in Chapter 3 and Chapter 4, this question can be answered as follows:

Chemical reaction between carbon-based refractory material and slag (and metal) is possible at tapping temperatures. The reduction of SiO_2 in the slag by carbon in the refractory to form SiC as reaction product was demonstrated, but formation of Si and Mn could not be proven conclusively due to the presence of steel contaminants in the synthetic slag.

Since chemical reaction between refractory and slag was proven to be a potential wear mechanism, the second research question was raised - *Is the choice in carbon-based refractory material important from a tap-hole refractory life perspective?*

In order to answer the question, further experimental work was required. The first step was to source, prepare and characterise industrial grade carbon-based refractory material and industrial SiMn slag as described in Chapter 5.

5 Importance of choice in refractory – Part A (characterisation of materials)

5.1 Introduction

In Chapter 3 and Chapter 4, the potential for chemical reaction between refractory and slag or refractory and metal as wear mechanism in the tap-hole was investigated. The formation of SiC as reaction product was demonstrated conclusively but not the formation of metal.

To study the impact that the choice in carbon-based refractory material would have on tap-hole refractory life, commercially available carbon block and carbon-based cold ramming paste and industrial slag from a SAF based on the integrated process were sourced, prepared and characterised. Chapter 5 reports on the results and concludes with a review of the second research question and an introduction to Chapter 6.

5.2 Method

Industrial slag was supplied by an international SiMn producer that produces HCFeMn and SiMn according to the integrated process. At the plant the slag is tapped into ladles and then cast onto slag beds. Once cooled the slag is collected by front end loader. The sample utilized in the experiments was collected by hand from the slag bed.

The as-received slag was milled with stainless steel balls in a Normand Electrical ball mill, pulverised in a tungsten carbide sample holder in a swing mill and sieved to $-425\mu\text{m}$. The sieved sample was split into sub-samples and subsequently into sub-sub samples using a 10-way rotary splitter.

The bulk chemical composition of three representative samples was determined by wet chemistry methods. The composition of phases and phase distribution were determined by X-ray diffraction, SEM (scanning electron microscopy) and FEGSEM (field emission gun scanning electron microscopy) with EDS (energy dispersive spectroscopy) at 15 kV as area analysis.

Two different types of refractory materials were utilized in the slag / refractory interaction experiments:

1. Carbon block
2. Cold ramming paste

Both materials consisted of carbon-based aggregate and a matrix consisting of a carbon-based binder with inorganic additives added intentionally to the binder phase of the carbon block. In the text, the combination of small carbon-based aggregate and binder phase is referred to as 'matrix'. In Figure 41 these main microstructural phases were presented schematically.

A large, unused carbon block sample (not previously installed in a SAF) was received from the project sponsor. No history of the sample was provided. Cold ramming paste samples were supplied by the material supplier both in granular form - as usually supplied to clients as a rammable - and rammed and fired on pilot scale under controlled conditions (950°C) that simulate plant installation. After firing samples (50mm diameter, 50mm height) were core-drilled from the pre-fired ramming paste.

Refractory material samples received were analysed using proximate analysis techniques to determine the inherent moisture, ash and volatile matter and calculating the fixed carbon content by difference. Refractory material samples received were also analysed using ultimate analysis techniques which measures the bulk carbon, sulphur, nitrogen and hydrogen contents of the

samples and then calculate the oxygen content by difference. As a bulk analysis technique, the organic and inorganic components (associated with the ‘ash’ phase after combustion) of the refractory are included in the ultimate analysis.

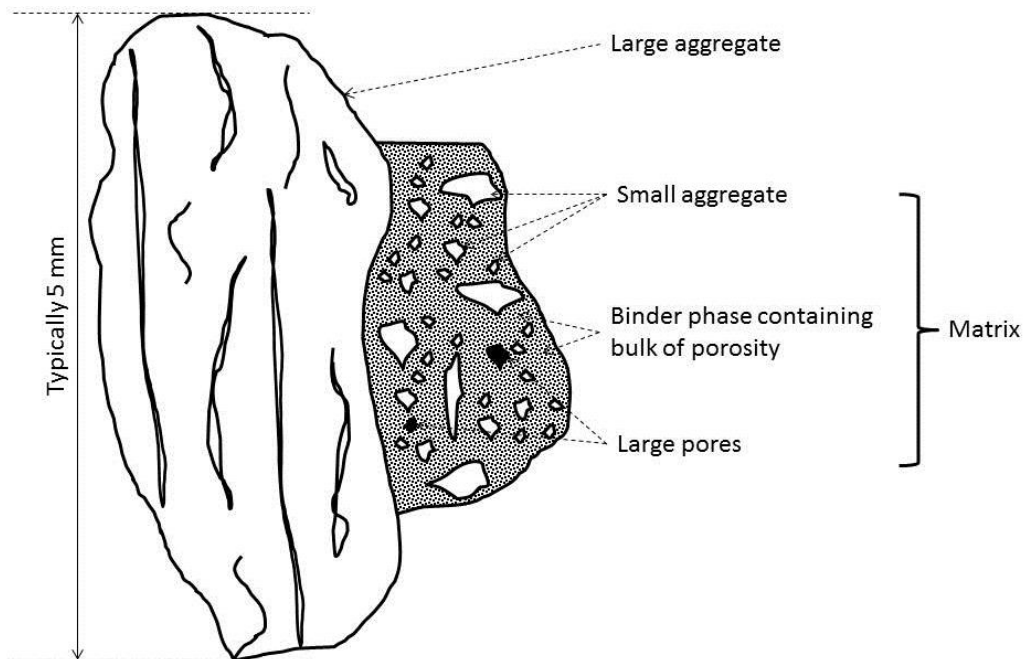


Figure 41: Schematic drawing showing the main microstructural features of carbon block and ramming paste: Large and small carbon-based aggregate, binder phase, air gaps and matrix.

The chemical composition of the ash phase was determined by ICP. As-received materials were submitted for XRD (X-ray diffraction). The relative phase amounts (weight %) were estimated using the Rietveld method and L_c (graphite crystallite size) calculated [38].

The porosity of 3 samples each of carbon block, ramming paste aggregate and ramming paste matrix were determined by X-ray tomography. One of the prebaked ramming paste samples was sliced to 3mm thickness from which samples of the aggregate and matrix were broken by hand.

For X-ray tomography, the Nikon XTH 225 ST micro-focus system at the MIXRAD facility situated at the South African Nuclear Energy Corporation (NECSA) was utilized. Scans were conducted at 100 kV and 100 μ A and a 0.25 mm Cu filter was applied to obtain better transmission and X-ray characteristics to minimize artifacts. The number of projections was 1000 with an exposure of 25 frames per projection which resulted in scan times of approximately an hour. These scanning parameters resulted in volume elements with dimensions ranging from 6.2 – 7.3 μ m which constitute a spatial resolution ranging from 238.3 – 405.2 μ m³.

Each dataset generated was analysed using VGStudio software associated with the instrument [121]. To calculate the porosity of a material type, a rectangular volume was selected from within the scanned sample. The volume of this triangle was known (V_T). The volume of each pore in the material (V_p) was determined by differences in grey-scale between the air in the pores and the different material types in the sample. The grey-scale intensity associated with a material type was a function of the density of the material. The total porosity (P_T) was then calculated from this data – Equation 24.

Equation 24: Total porosity (P_T)

$$P_T = \sum V_p / V_T \times 100$$

To obtain an idea of the pore size distribution the assumption was made that each pore volume was cubic in shape and the equivalent pore size (EPS) defined as the length of one of the sides of the cube – Equation 25. The results were presented as the cumulative pore volume as a function of EPS.

Equation 25: Equivalent pore size (EPS)

$$EPS = V_p^{1/3}$$

For microscopy, polished sections were prepared of the carbon block, the granular ramming paste and the pre-fired ramming paste. These were studied using FEGSEM EDS. The samples were mounted in Struers EpoFix with 6% iodoform (CHI_3) added in powdered form to improve contrast between pores filled with resin and carbon materials in the refractory [122], [123]. To calculate the amount of iodoform to be added, the method of calculating the average atomic number (ANF) per phase described by Straszheim et al [123] was utilised. The ANF for a specific phase is the sum of the product of the mass fraction of each element and its atomic number – see Equation 26.

Equation 26: Average atomic number (ANF)

$$ANF = \sum_{i=1}^n (\text{mass fraction})_i \times (\text{atomic number})_i$$

In selecting the amount of iodoform to be added, care had to be taken to increase the average atomic number (ANF) of the resin to more than that of the carbon, but less than that of the mineral phases identified by XRD (corundum – Al_2O_3 , moissanite – SiC , and quartz – SiO_2). The results obtained for a 6% CHI_3 sample are presented in Table 33.

Table 33: Results of ANF calculations to determine the amount of iodoform to be added to resin to improve contrast between resin and carbon without negatively influencing contrast between resin and inorganic phases present in the refractory samples.

Elements	H	C	O	Al	Si	I							
Atomic mass	1	12	16	27	28	127							
Atomic number	1	6	8	13	14	53							
Material	Composition (atomic ratios)						Composition (mass fraction)						ANF
	H	C	O	Al	Si	I	H	C	O	Al	Si	I	
Carbon	0	1	0	0	0	0	0	1.0	0	0	0	0	6.0
Epoxy	-	-	-	-	-	-	0.1	0.7	0.2	0	0	0	6.0
CHI_3	1	1	0	0	0	3	0	0	0	0	0	1.0	51.4
Al_2O_3	0	0	3	2	0	0	0	0	0.5	0.5	0	0	10.6
SiO_2	0	0	2	0	1	0	0	0	0.5	0	0.5	0	10.8
Si	0	0	0	0	1	0	0	0	0	0	1.0	0	14.0
SiC	0	1	0	0	1	0	0	0.3	0	0	0.7	0	11.6
6% CHI_3 -Epoxy							0.1	0.7	0.2	0.0		0.1	8.8

The preparation procedure was as follows:

- 1) Place sample in sample holder.
- 2) Add resin to measuring cup.

- 3) Weigh iodoform.
- 4) Add iodoform to resin and stir gently for 1 minute. Small gas bubbles associated with the powder cause the liquid to appear cloudy.
- 5) Add hardener.
- 6) Place sample in sample holder in a vacuum chamber and position cup containing iodoform resin in tilting unit.
- 7) Draw vacuum just to the point where resin starts to form bubbles. Close the valve to maintain vacuum at this specific pressure. Do not continue to draw vacuum deeper.
- 8) Cast resin onto sample.
- 9) Immediately break vacuum and remove sample.
- 10) Allow resin to set overnight at room temperature.

5.3 Results

The bulk chemical composition of the as-received industrial slag is given in Table 34.

Table 34: Bulk chemical composition of as-received industrial slag samples determined by wet chemistry methods (average percentage by weight and standard deviation of three samples per material).

	MnO	FeO	SiO ₂	CaO	MgO	Al ₂ O ₃	Total
Average	7.5	0.1	45.3	23.5	7.1	16.5	100.0
StDev	0.2	0.1	0.5	0.4	0.02	0.1	

SEM BSE images of the as-received industrial slag are presented in Figure 42 to Figure 44.

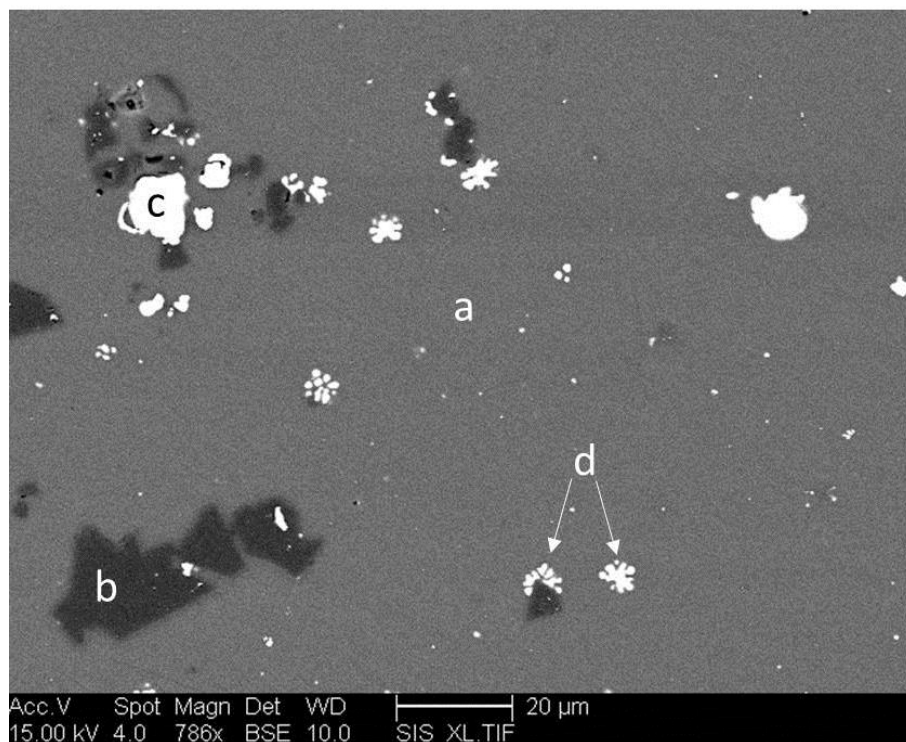


Figure 42: SEM BSE image of as-received industrial slag with (a) amorphous slag phase, (b) SiC phase, (c) metal phase and (d) MnS. Scale bar indicates 20 μm.

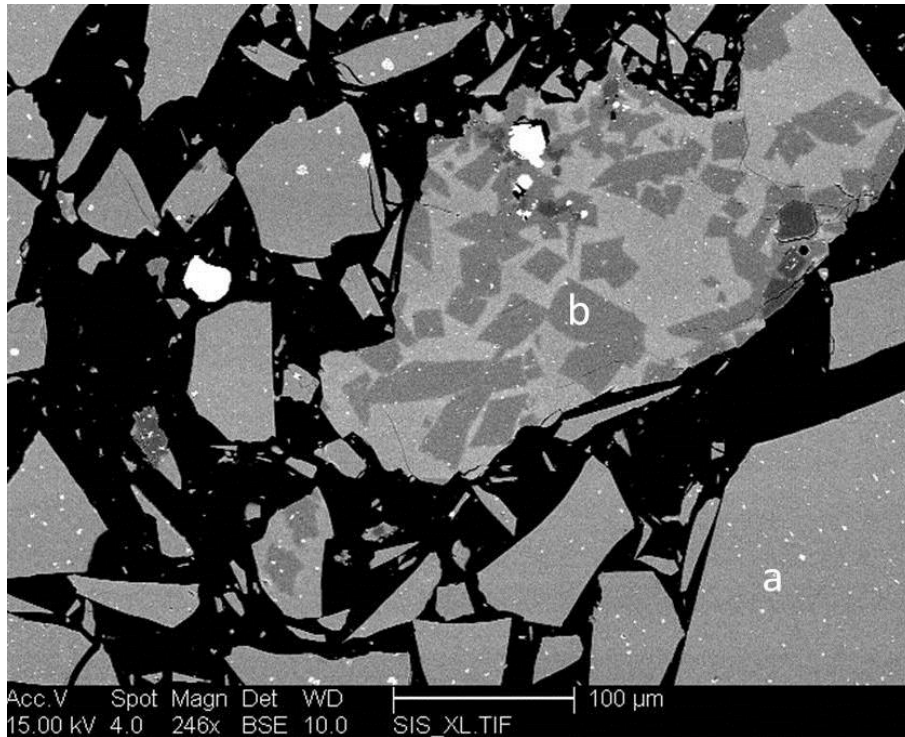


Figure 43: SEM BSE image of as-received industrial slag with (a) amorphous slag phase and (b) secondary slag phase. Scale bar indicates 100 μm.

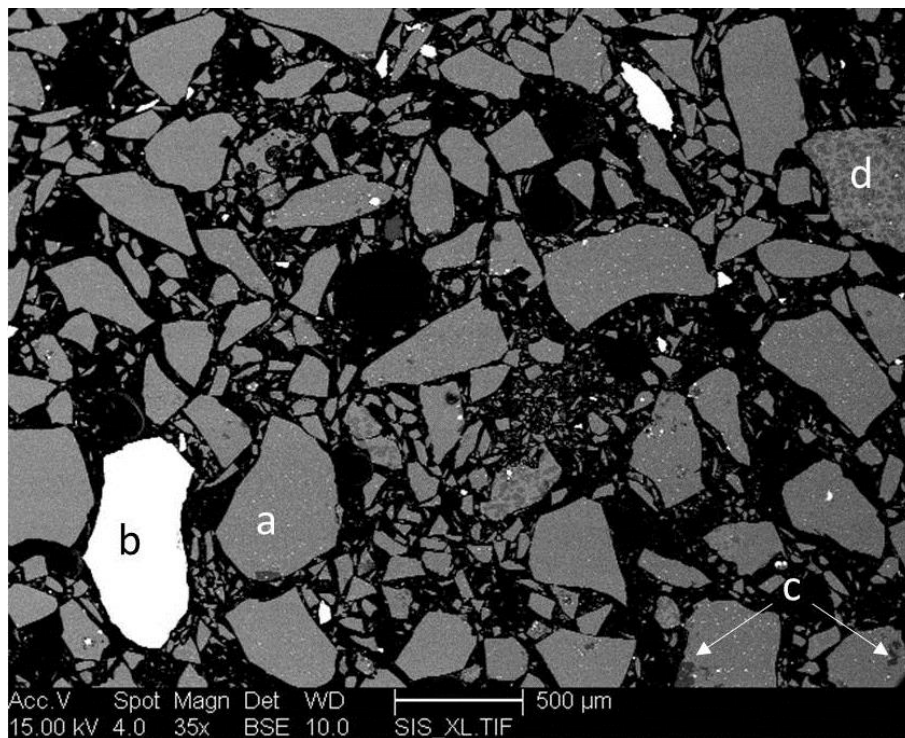


Figure 44: SEM BSE image of as-received industrial slag with (a) amorphous slag phase containing finely dispersed SiMn metal and MnS droplets – see Figure 42 – , (b) large metal particles, (c) SiC and (d) amorphous slag phase containing secondary slag phase – see Figure 43. Scale bar indicates 500 μm.

The modelled and measured EDS spectra for the SiC phase present in the as-received industrial slag as identified in Figure 42 are presented in Figure 45; the measured EDS spectra correspond to that expected for pure SiC.

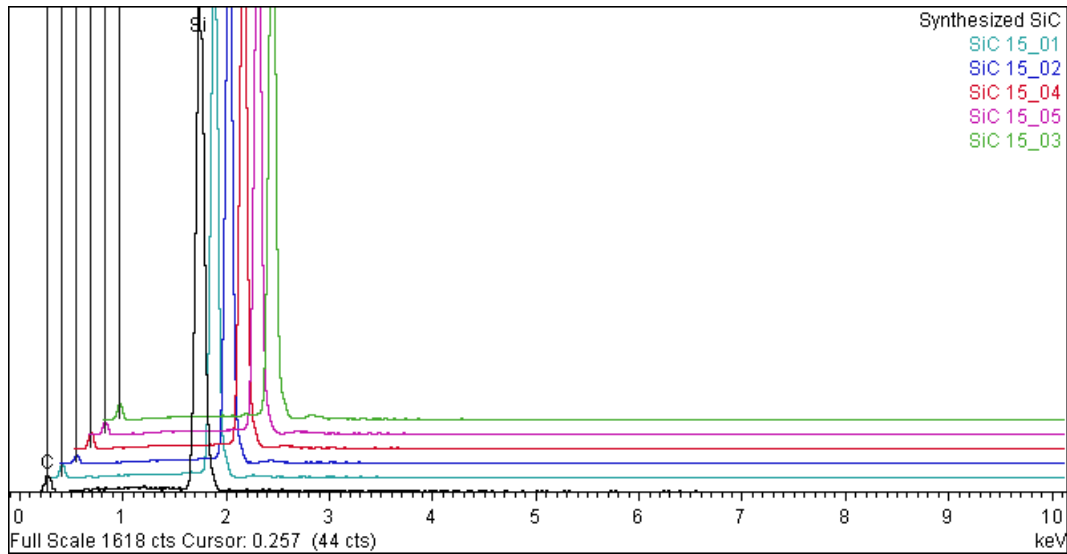


Figure 45: Spectra of EDS point analysis of 5 different SiC particles compared against the simulated spectra for SiC at the same conditions (point analysis, 15 kV).

The normalised composition of the amorphous slag and secondary slag phase – Figure 43 – as determined by SEM EDS is presented in Table 35 and simplified to a five component system in Table 36.

Table 35: Normalised elemental analysis of slag phases (weight per cent) determined as average of five EDS point analysis per phase at 15 kV.

	Na	Mg	Al	Si	S	K	Ca	Mn	Ba	Total
Amorphous slag phase	0.1	7.7	16.5	38.2	0.5	1.1	32.3	2.1	1.6	100.0
Stdev	0.2	0.2	0.3	0.5	0.1	0.1	0.6	0.3	0.2	
Secondary slag phase	-	12.5	17.9	37.8	0.5	-	28.3	3.1	-	100.0
Stdev	-	12.8	18.1	37.9	0.2	-	0.3	0.4	-	

Table 36: Composition of slag phases simplified to five component system and normalised (weight per cent) – based on EDS analysis in Table 35.

	MgO	Al ₂ O ₃	SiO ₂	CaO	MnO	Total
Amorphous slag phase	7	18	47	26	2	100
Secondary slag phase	11	21	47	18	2	100

The normalised composition of the metal phase – identified in Figure 42 and Figure 46 – as determined by SEM EDS is presented in Table 37.

Table 37: Analysis of metal phases (weight per cent) determined as average of eight EDS point analysis for the large particles – see Figure 46 – and five for small particles – see Figure 42 – at 15 kV.

	Mass per cent			Moles			
	Si	Mn	Fe	Si	Mn	Fe	Mn:Si
Large	37.4	58.8	3.9	1.33	1.07	0.07	1.24
Stdev	0.4	0.5	0.5	0.01	0.01	0.01	0.02
Small	19.3	78.5	2.2	0.69	1.43	0.04	0.49
Stdev	3.8	4.0	1.2	0.14	0.07	0.02	0.12

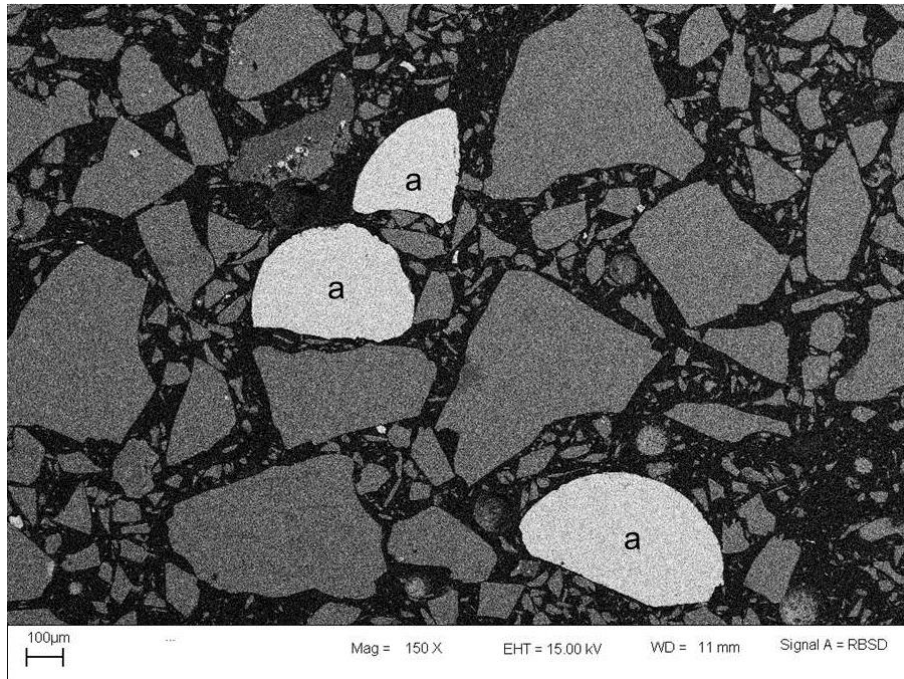


Figure 46: SEM BSE image of as-received industrial slag with large metal particles (marked “a”) of which the average chemical composition is reported in Table 37. Scale bar indicates 100 μm.

The XRD pattern of the as-received industrial slag is presented in Figure 47. Markers in Figure 47 indicate the significant peaks for phases considered based on SEM BSE microscopy and EDS analysis and confirmed by matching their predicted diffraction pattern in terms of positions and peak intensities [109]. Phases considered, but which did not match, were Anorthite, Mn_3Si and Ferrite.

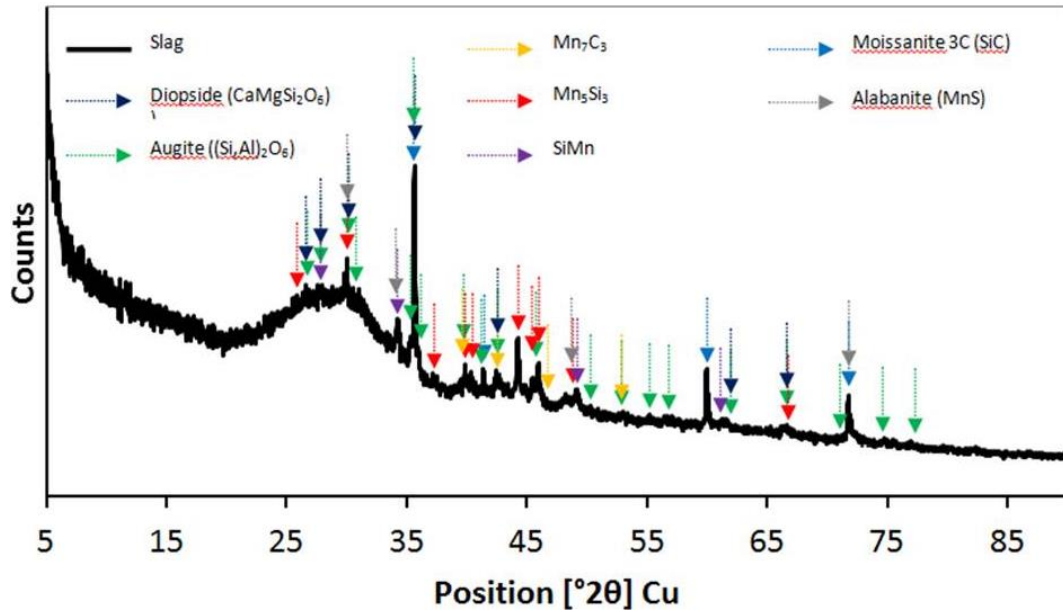


Figure 47: XRD pattern of the slag sample with markers indicating the significant peaks for crystalline phases identified.

The composition of the refractory material is presented in Table 38 and the bulk composition of the ash phase (combustion product that formed when combusting the refractory material at 815°C in air) in Table 39.

Table 38: Bulk chemical composition of the refractory material.

	Dry basis			Air-dried	
	Ash	Vols	Fix-C	Moisture	Total S
Carbon block	22.7	0.2	77.0	0.1	0.12
Pre-fired ramming paste	6.3	1	92.6	0.1	0.25

Table 39: Bulk chemical composition of the ash phase prepared by combusting the refractory material at 815°C in air.

	SiO ₂	Al ₂ O ₃	TiO ₂	CaO	MgO	FeO	Total
Carbon block	58.2	38.5	0.2	0.4	0.2	2.5	100
Pre-fired ramming paste	56.9	31.3	1.5	1.3	1.2	7.8	100

The SEM BSE images of the refractory material are presented in Figure 48 and Figure 49 at higher magnification.

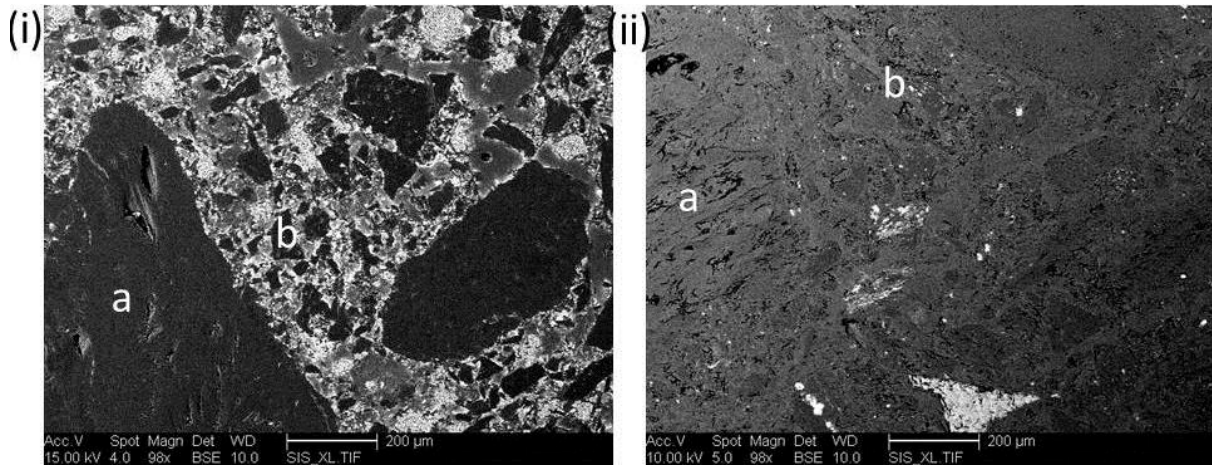


Figure 48: SEM backscattered electron image of (i) carbon block and (ii) pre-fired ramming paste mounted in resin containing 5% iodoform with (a) carbon aggregate and (b) matrix. Scale bar indicates 200 µm.

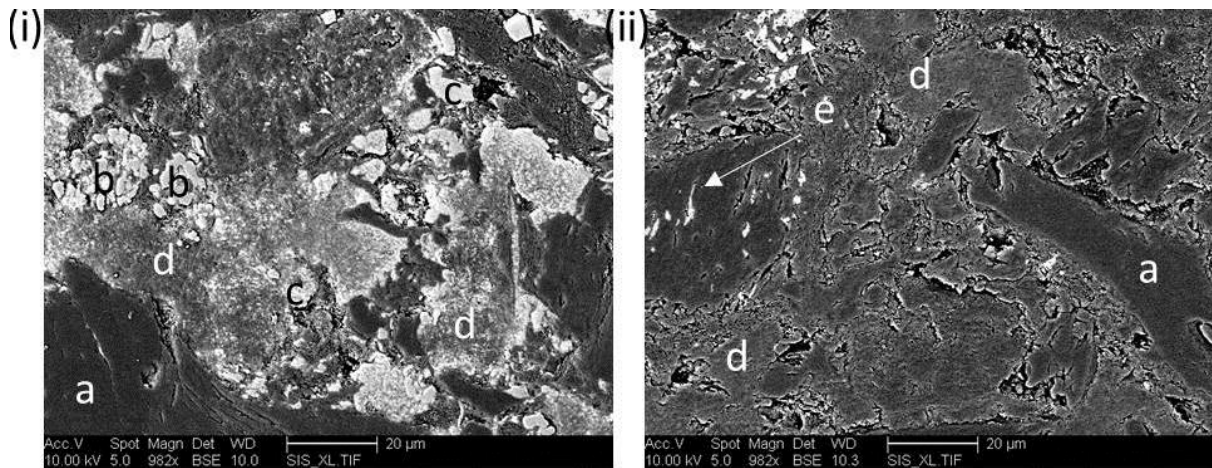


Figure 49: SEM BSE image of (i) carbon block and (ii) pre-fired ramming paste mounted in resin containing 5% iodoform with (a) carbon aggregate, (b) corundum, (c) SiC, (d) iodoform impregnated resin and (e) (Si, Al, K, Na, Fe)-containing minerals. Scale bar indicates 20 µm.

The XRD pattern of the pre-fired ramming paste is presented in Figure 50 and Figure 51. Markers indicate the significant peaks for phases considered based on SEM BSE microscopy and EDS analysis and confirmed by matching their predicted diffraction pattern in terms of positions and peak intensities [109]. Phases considered but which did not match were corundum, moissanite 3C, TiC, ferrite and Al_4C_3 .

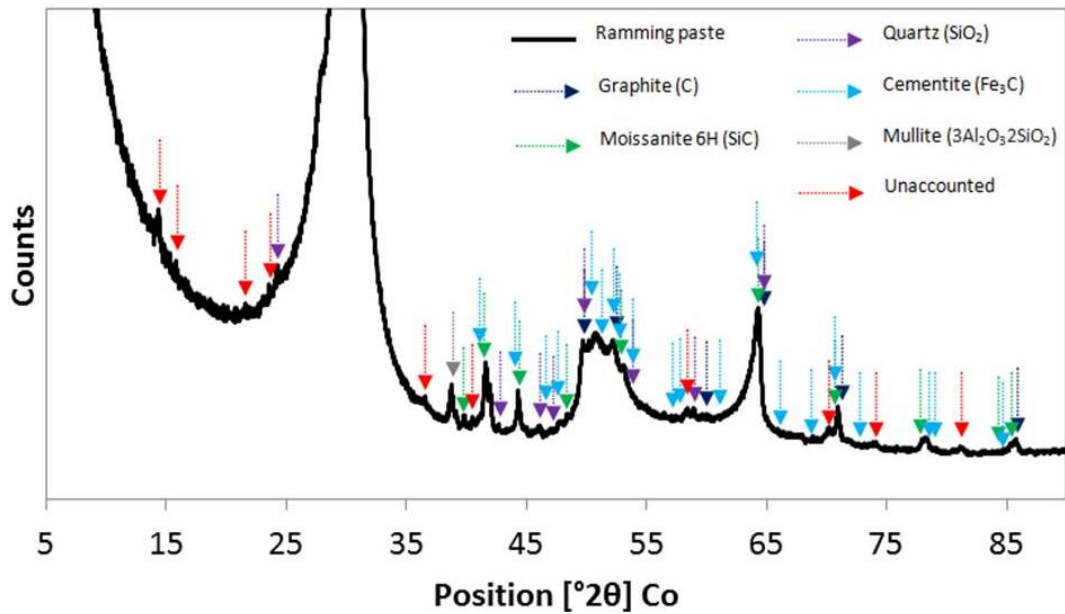


Figure 50: XRD pattern of the ramming paste refractory sample with markers indicating the significant peaks for phases identified. For identification of the high intensity peak see Figure 51.

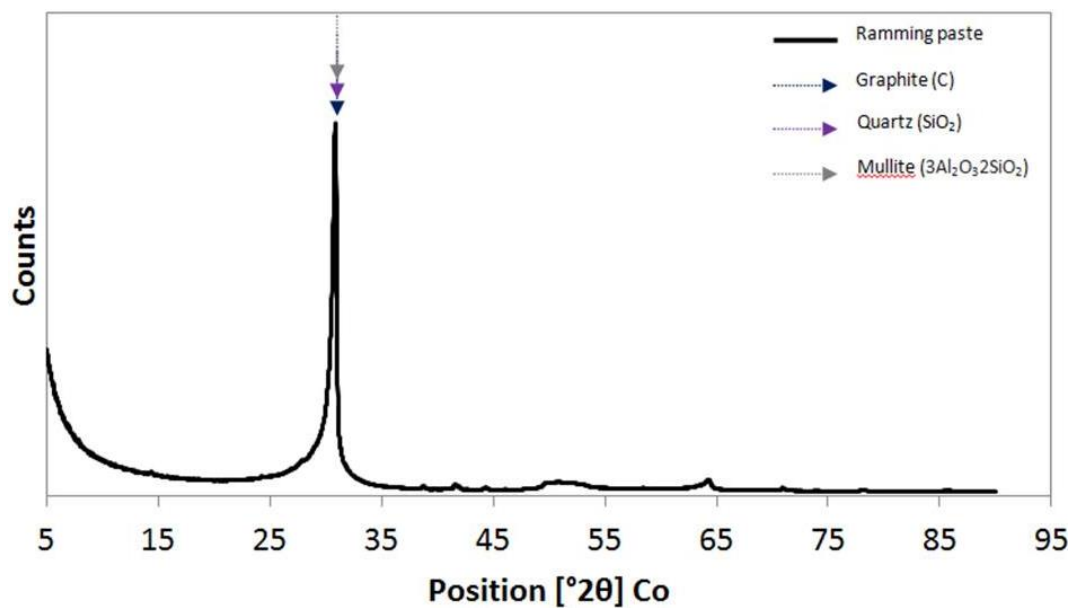


Figure 51: XRD pattern of the ramming paste refractory sample with markers identifying the high intensity peak.

The XRD pattern of the carbon block is presented in Figure 52 and Figure 53. Markers indicate the significant peaks for phases considered based on SEM BSE microscopy and EDS analysis and confirmed by matching their predicted diffraction pattern in terms of positions and peak intensities [109]. Phases considered but which did not match were silicon, moissanite 6H and quartz.

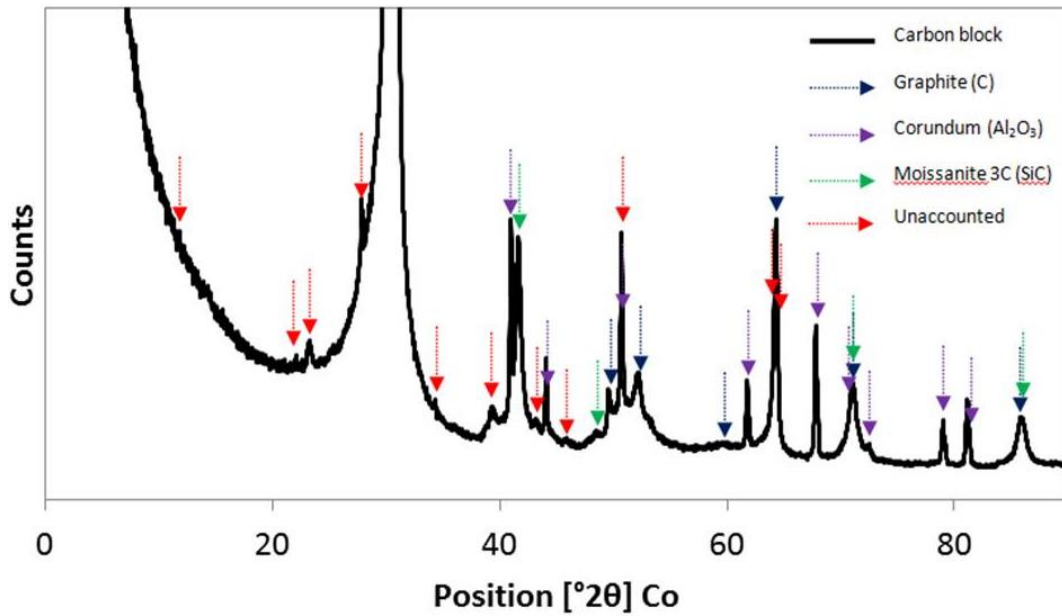


Figure 52: XRD pattern of the carbon block refractory sample with markers indicating the significant peaks for phases identified. For identification of the high intensity peak see Figure 53.

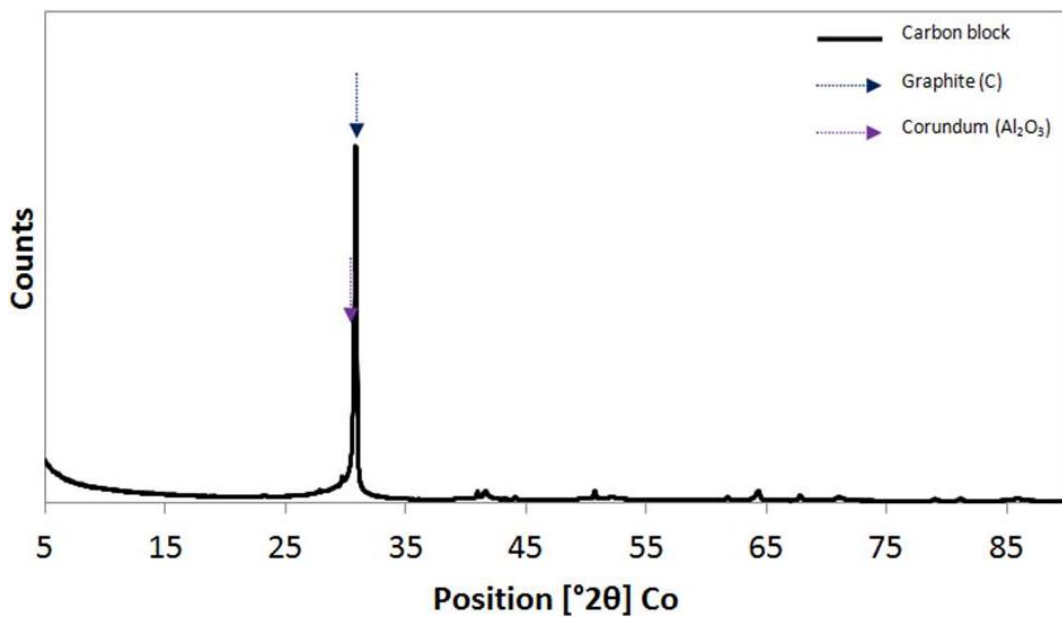


Figure 53: XRD pattern of the carbon block refractory sample with markers identifying the high intensity peak.

In Table 40 the crystallite size and inter planar distance of the refractory materials derived from the XRD results in Figure 51 and Figure 53 are presented.

Table 40: Crystallite size L_c and inter planar distance (d_{002}) of the refractory material and components derived from XRD.

	L_c [Å]	d_{002} [Å]
Carbon block	430	3.4
Pre-fired ramming paste	201	3.4

The data produced by XRT was manipulated to calculate the total porosity – presented in Table 41 – and cumulative porosity as a function of equivalent pore size is presented in Figure 54 to Figure 56 together with examples of the micrographs generated by XRT. XRT measures the porosity in terms of volume. The equivalent pore size was derived from the measured volume. Round symbols indicate the size of largest pore or series of connected pores i.e. is indicative of open porosity. Full lines indicate the size of the small pores and are indicative of closed porosity. Dashed lines indicate which round symbol is associated with which set of small pores.

Table 41: Total porosity per refractory sample determined by XRT.

	Ramming paste matrix	Ramming paste aggregate	Carbon block
a	26.1	13.7	7.6
b	17.7	20.4	11.2
c	22.7	17.2	13.8
Average	22.2	17.1	10.9

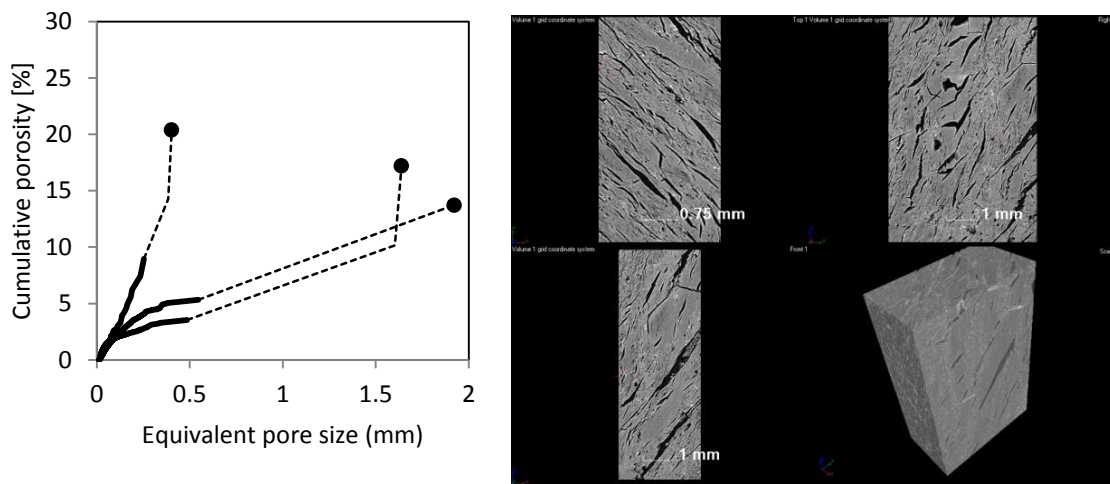


Figure 54: Pore size distribution of three samples of ramming paste aggregate and an example of XRT micrographs defining the volume of material on which one of the measurements were based.

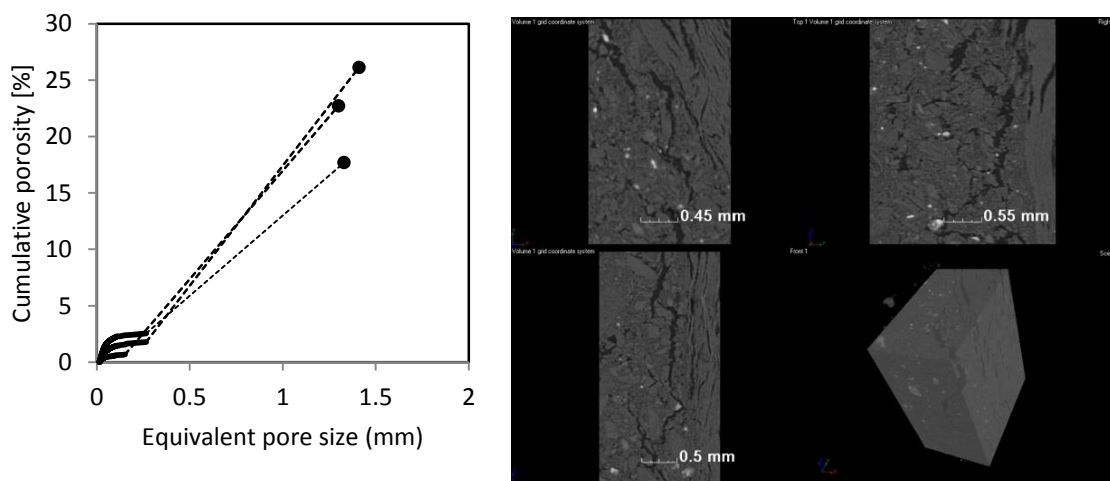


Figure 55: Pore size distribution of three samples of pre-fired ramming paste matrix and an example of XRT micrographs defining the volume of material on which one of the measurements were based.

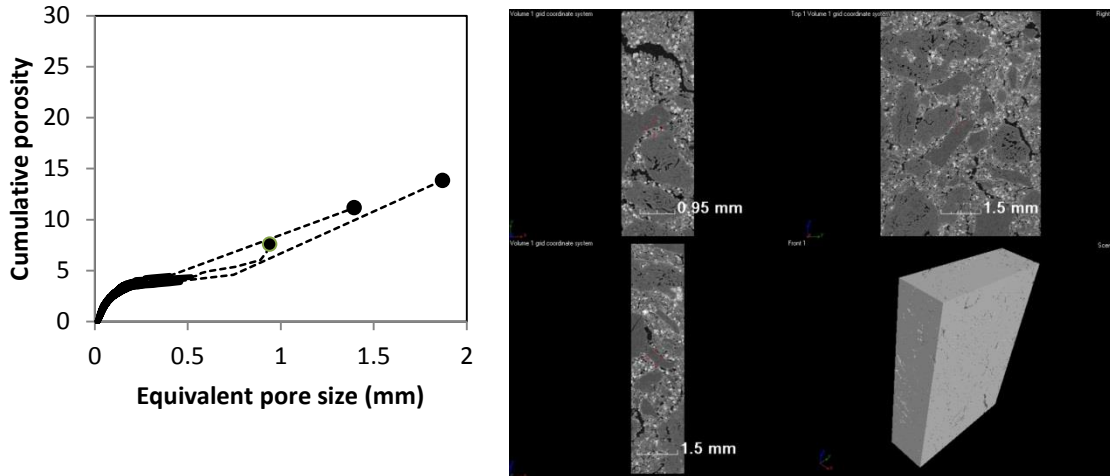


Figure 56: Pore size distribution of three samples of carbon block and an example of XRT micrographs defining the volume of material on which one of the measurements were based.

In Figure 57 the micrographs generated for the two refractory materials and pure graphite by XRT are compared to those generated by SEM BSE. The XRT samples were not mounted and the SEM EDS samples were mounted in iodoform-containing resin and polished.

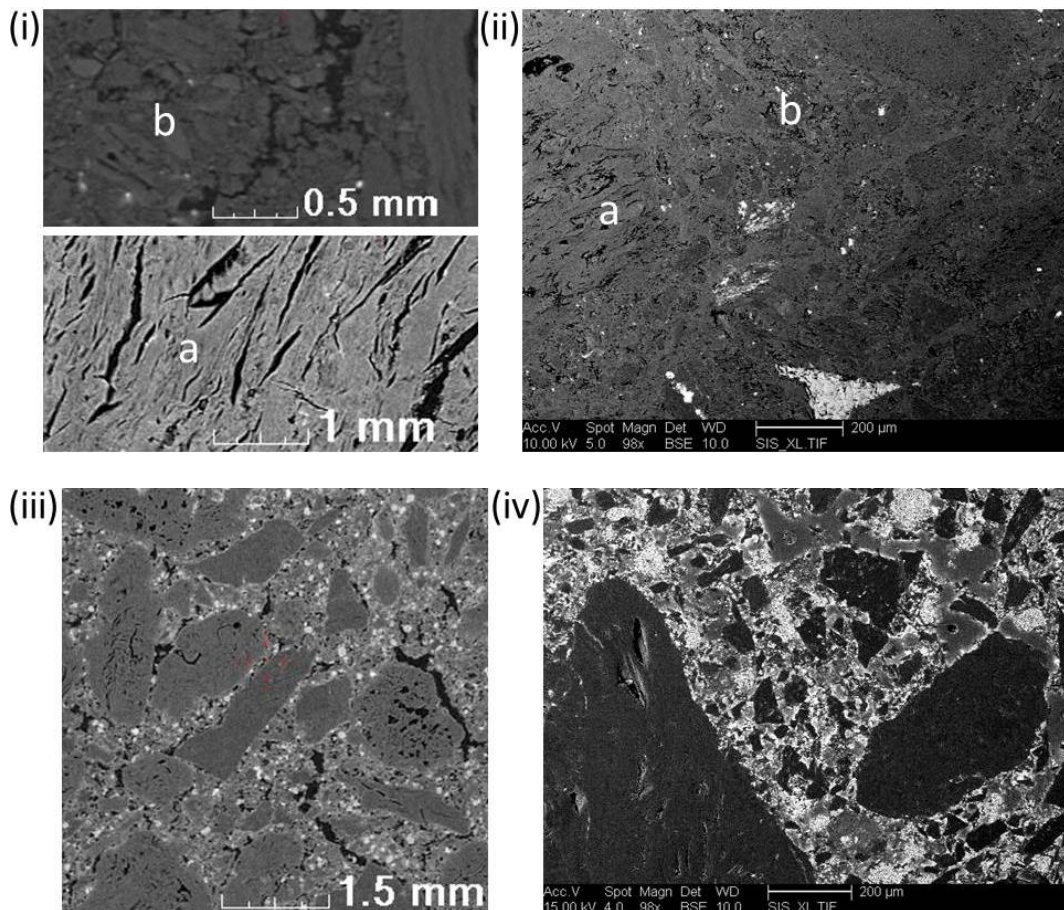


Figure 57: Micrographs obtained for pre-fired ramming paste with (i) XRT images and (ii) SEM BSE image at 10kV of (a) aggregate and (b) matrix; for carbon block with (iii) XRT image and (iv) SEM BSE image at 15kV. Scale bar indicates 200 μm in (ii) and 200 μm in (iv).

5.4 Discussion

The industrial slag consisted primarily of an amorphous slag phase but also contained moissanite (SiC), alabandite (MnS) and intermetallic phases (SiMn, Mn₅Si₃ and Mn₇C₃) – see Figure 42. The composition of the SiC phase was confirmed by comparing the measured EDS spectra with the EDS spectra predicted for SiC for a polished section coated with gold (Figure 45).

A secondary, apparently crystalline slag phase was identified by SEM BSE in some of the slag particles (Figure 43) and EDS (Table 35). The chemical composition of the secondary slag phase (taken from Table 36 but simplified to 20%Al₂O₃ – 10%MgO – 45%SiO₂ – 25%CaO) was projected onto the quaternary oxide phase diagram for the 20%Al₂O₃ – CaO – MgO – SiO₂ slag system in Figure 58. In Figure 58 the composition of the secondary slag phase fell into the anorthite primary phase field but cannot be pure anorthite (CaAl₂Si₂O₈) as it contained a significant proportion of MgO (in general, plagioclase minerals are not expected to have a MgO content this high [124]), nor was anorthite detected by X-ray diffraction.

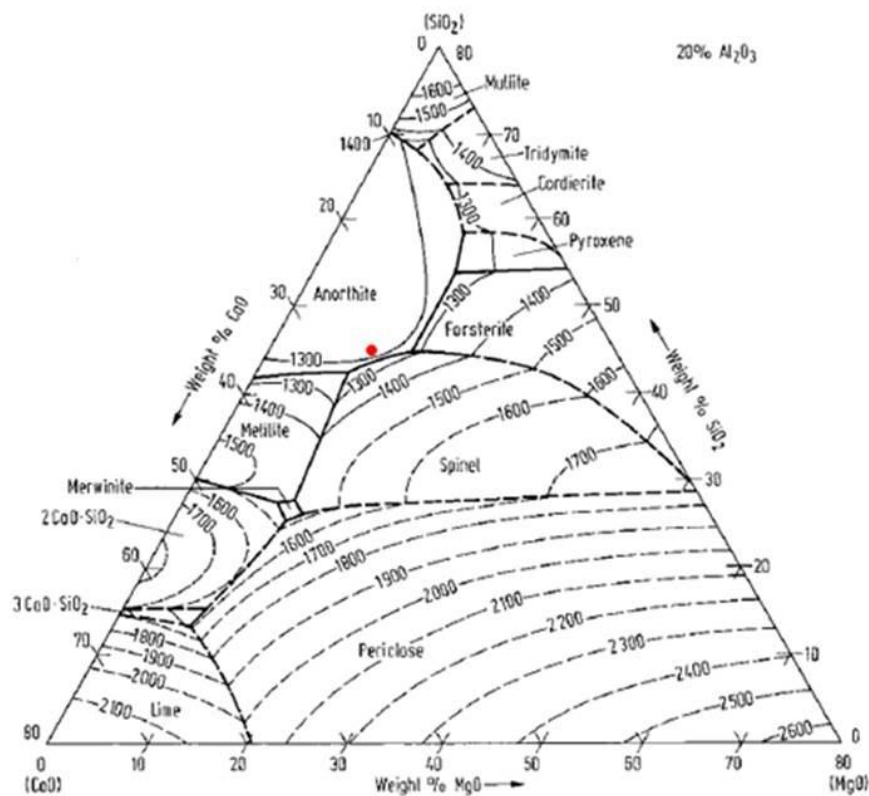


Figure 58: Quaternary oxide phase diagram for the 20%Al₂O₃ – CaO – MgO – SiO₂ slag system ([125]) with the composition of the secondary slag phase (simplified to 20%Al₂O₃ – 10%MgO – 45%SiO₂ – 25%CaO) indicated as a red dot.

Equilibrium phase distributions of both the amorphous slag phase and the secondary slag phase (compositions in Table 36) were calculated in FACTSage 6.4 in an attempt to identify the secondary slag phase. The results are presented in Figure 59. The first phase to precipitate upon steady state cooling in both instances was anorthite (CaAl₂Si₂O₈), followed by pyroxene (and olivine in the case of the secondary slag phase). Since anorthite was not found by X-ray diffraction, a calculation was also performed, with anorthite formation suppressed; the results in Figure 59 (iii) show that the dominant phase after solidification would then be pyroxene. Given the approximate correspondence between the composition of this secondary phase and that of pyroxene, and the correspondence

between the diffraction peaks of augite and diopside and the measured diffraction patterns, the secondary slag phase is probably a pyroxene.

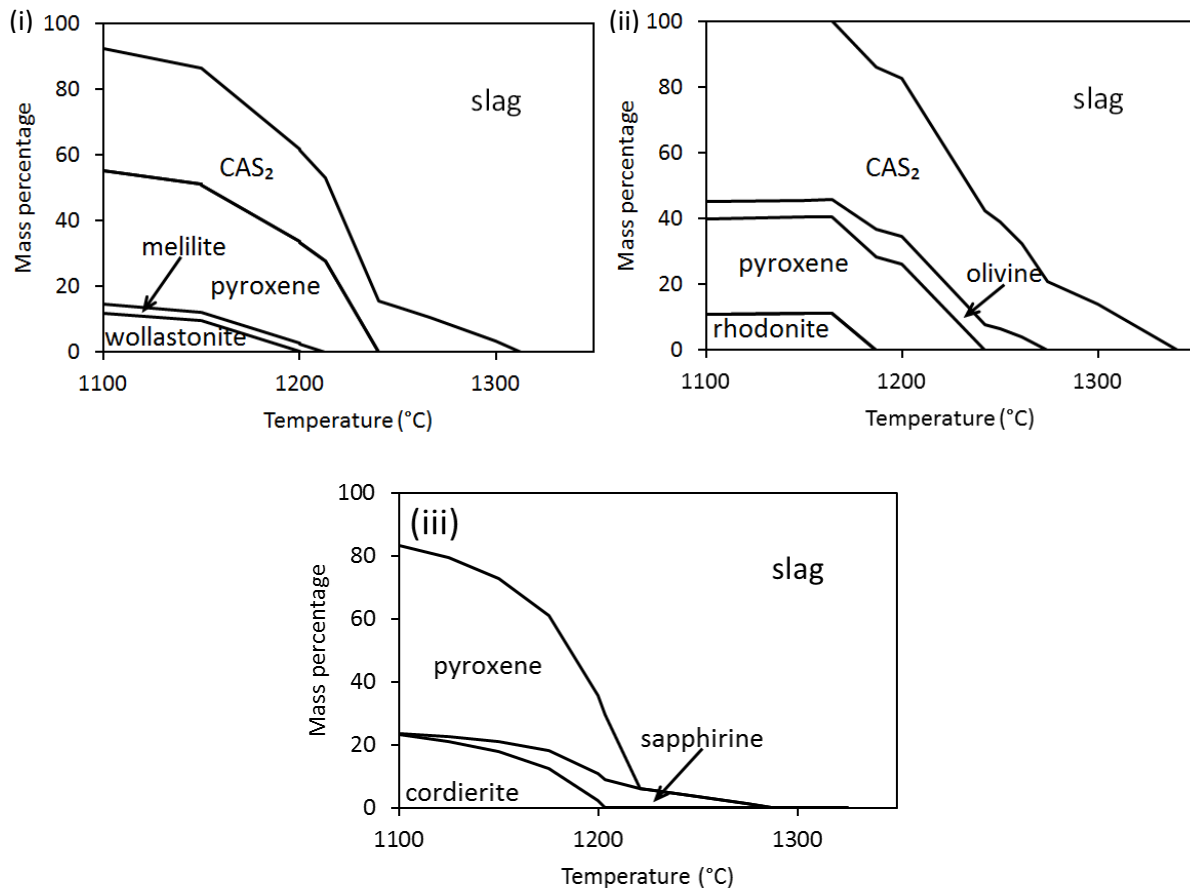


Figure 59: Equilibrium phase distribution (percentage by mass) of (i) the amorphous slag phase and (ii) the secondary slag phase based on the bulk chemical composition; calculated with FACTSage 6.4. In (iii) the predicted equilibrium phases are shown for the composition of the secondary slag phase, if anorthite formation is suppressed.

According to the calculations in FACTSage 6.4 (Figure 59) the slag would be fully liquid in the temperature range 1400 – 1600°C as the melting points of the slag phases were 1313°C and 1340°C respectively. The temperature range 1400 – 1600°C is important as it was the temperature range over which the laboratory-scale experiments were conducted.

The proximate analysis of the as-received carbon block indicated that the ash yield is similar to that of micropore brick (20%) and significantly higher than that of other carbon bricks ($\leq 12\%$) [76]. The ash yield of the ramming paste is typical of carbon refractories [76]. In the fired state the volatile matter released and moisture contents were similar. The calculated fixed carbon content of the ramming paste was higher than that of the carbon block due to the significantly lower ash yield from the ramming paste.

The crystalline phases identified in the carbon block were graphite (C), moissanite (SiC) and corundum (Al₂O₃). The graphite was present both as large aggregate particles and in the matrix or binder phase. The corundum was present as discrete particles in the matrix and SiC finely dispersed throughout the matrix; these were probably added to the bond matrix to generate micro-porosity or improve the wear resistance properties of the refractory material [34], [66]. The carbon itself was

primarily present as amorphous carbon with low graphite content. The crystallite size (L_c) was more than twice that of the ramming paste.

The crystalline phases identified in the pre-fired ramming paste sample were graphite (C), moissanite (SiC), quartz (SiO₂), cementite (Fe₃C) and mullite (3Al₂O₃2SiO₂). The graphite was present both as large aggregate particles and in the matrix or binder phase. None of the other components were added intentionally by the manufacturer and were therefore most probably products of calcination of the inorganic materials present in the anthracite. Slightly more than 50% of the carbon was present as graphite.

The equilibrium phase distribution of the carbon block and the pre-fired ramming paste were calculated in FACTSage 6.4 using the Equilib model. Mass balance calculations, based on the fixed carbon and ash contents reported in Table 38 and analyses of the ash (combustion product) in Table 39, were conducted to estimate the chemical composition of the carbon block and pre-fired ramming paste utilized in these calculations. Although presented as SiO₂ in the ash analysis, from the XRD results Si would rather be present as SiC in the carbon block (Figure 52) and as a combination of SiC and SiO₂ in the ramming paste (Figure 50) and was therefore taken as 100% Si for carbon block and approximated as 50:50% Si:SiO₂ (molar basis) for ramming paste (Table 42).

Table 42: Chemical composition (percentage by mass) of the carbon block and pre-fired ramming paste utilized to calculate the equilibrium phase distribution of both. The compositions were derived from the proximate and ash analyses in Table 38 and Table 39 and adjusted for Si and SiO₂ contents based on XRD analyses in Figure 50 and Figure 52.

	C	Si	SiO ₂	Al ₂ O ₃	TiO ₂	CaO	MgO	FeO	Total
Carbon block	85.55	3.91	-	9.71	0.05	0.10	0.05	0.63	100.00
Pre-fired ramming paste	94.54	0.86	1.83	2.01	0.10	0.08	0.08	0.50	100.00

For these FactSage calculations, the FToxid, FSstel and FACTPS databases were selected. The temperature range was 1400 – 1600°C with 100°C intervals. Default gas and solids were selected as pure species. Duplicates were suppressed with data from the FToxid database having preference to that of the FSstel database followed by the FACTPS database. As solution species liquid slag (SLAGA), orthopyroxene, Aorthopyroxene, LowClinopyroxene, A wollastonite, a'Ca₂SiO₄, aCa₂SiO₄, melilite, cordierite, liquid metal (LIQU), Aspinel, Amonoxide, Aclinopyroxene, Aolivine, mullite and corundum were selected as possible stable phases. Liquid slag was forced to remain a single phase, if present. The results reported are the mass percentage of each phase present – see Figure 60.

The equilibrium calculations predicted the formation of both metal and slag phases in both refractory materials in the temperature range under investigation. In the carbon block – Figure 60a – the slag and metal phases formed upon melting of the spinel, mullite and anorthite phases present at lower temperatures with very little gas formation. In the ramming paste – Figure 60b – the slag and metal phases were present from below 1400°C. The slag volume increased initially due to the dissolution of cordierite, but decreased significantly upon the formation of a metal phase at 1525°C and SiC at 1575°C due to the reduction of SiO₂.

The calculated equilibrium phase distributions when reacting 100g slag with 100g ramming paste and 100g slag with 100g carbon block (using the slag composition in Table 34 and refractory compositions in Table 42) are presented in Figure 61.

When exposing carbon block to slag the spinel, mullite and anorthite as well as the corundum phases present in the refractory would tend to dissolve in the slag, as shown by comparing Figure 61a to Figure 60a. Compared with equilibration of the refractory only, in contact with slag slightly more metal formed when slag reacted with carbon and / or SiC.

Similarly, when exposing ramming paste to slag the cordierite, mullite and corundum phases present in the refractory would tend to dissolve in the slag (see Figure 61b and Figure 60b), with slightly more metal formed for reaction with the slag, and also SiC formation by reduction (see significant gas formation above 1589°C).

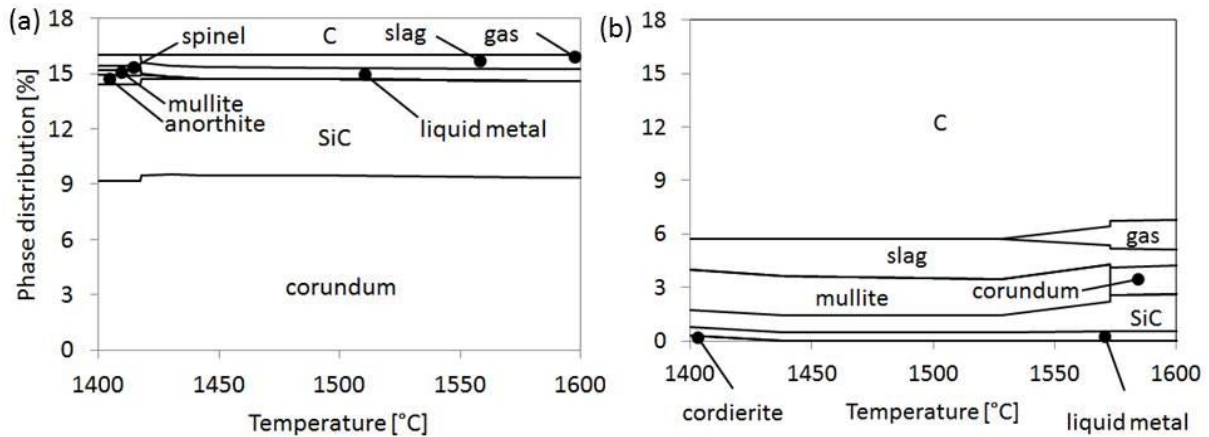


Figure 60: Equilibrium phase distribution (percentage by mass) of (a) the carbon block and (b) the pre-fired ramming paste based on the chemical compositions in Table 42; calculated with FACTSage 6.4.

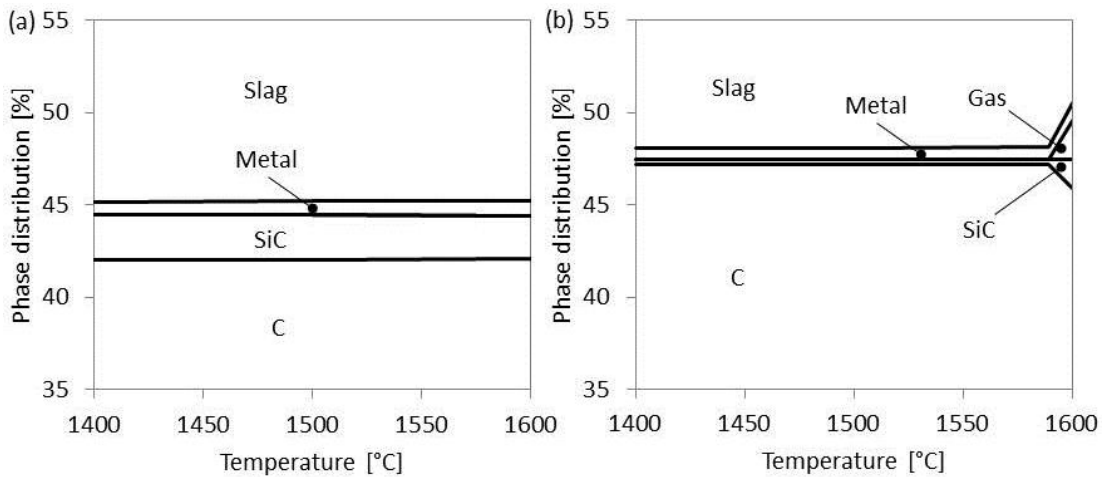


Figure 61: Equilibrium phase distribution when reacting 100g industrial slag with 100g of (a) carbon block and (b) 100g prebaked ramming paste at different temperatures. (Slag composition as given in Table 34 and refractory compositions as in Table 42).

The porosity of the carbon block is half that of the ramming paste and the porosity of the ramming paste matrix slightly higher than that of the ramming paste aggregate. For both the carbon block and the ramming paste, open porosity forms a significant part of the total porosity. For carbon block of the total porosity of 11% on average, 6 – 7% of the pores are open and connected (reported as one long pore) – see Figure 56. For ramming paste aggregate with total porosity of 17% on average, the number is 7 – 12% (Figure 54) and for ramming paste matrix with total porosity of 22% on average, the number is 19 – 21% (Figure 55).

5.5 Conclusion

The second research question posed was: *Is the choice in carbon-based refractory material important from a tap-hole refractory life perspective?*

Before investigating the reaction between an industrial slag and industrial carbon refractory materials, the materials have been characterized. As the reaction products expected from slag / refractory interactions were SiC and metal, the fact that the industrial slag sourced to conduct these experiments contained both had to be taken into account. The industrial SiMn slag consisted primarily of an amorphous slag phase, but also contained SiC, MnS and intermetallic phases including SiMn – present as large discrete particles as well as small droplets in the slag. A minor crystalline secondary slag phase was observed and tentatively identified as pyroxene. As the melting points of the amorphous slag phase and the secondary slag phase were predicted as 1313°C and 1340°C respectively, the slag would be fully liquid at the temperature range under investigation (1400°C – 1600°C).

Both refractory materials consisted of large carbon-based aggregate particles and a carbon binder phase containing smaller carbon-based aggregate particles. The carbon block had both Al₂O₃ and SiC particles added intentionally. The ramming paste contained inorganic phases too but these were not added intentionally and rather were calcination products formed during calcination of the anthracite. At the temperature range under investigation (1400°C – 1600°C) thermodynamic calculations predicted the presence of a slag and a metal phase upon melting of the inorganic phases present in both refractory materials. The porosity of the carbon block is half that of the ramming paste and the porosity of the ramming paste matrix slightly higher than that of the ramming paste aggregate.

Over the temperature range under investigation (1400°C – 1600°C) thermodynamic calculations predicted the dissolution of corundum in the slag when reacting carbon block with industrial slag. An increase in metal formation (compared with equilibration of the refractory only) was predicted for reaction of both carbon block and ramming paste with industrial slag. SiC formation in the ramming paste reaction was predicted for temperatures higher than 1589°C. The initial SiC concentration was decreased initially upon the carbon block reaction but as the temperature increased further SiC formation was predicted.

To test the thermodynamic predictions and study the influence of refractory properties two sets of laboratory-scale experiments were planned: Wettability tests and cup tests. Chapter 6 reports on the first of the two types of experiments: Wettability tests.

6 Importance of choice in refractory- Part B (wettability tests)

6.1 Introduction

Chapter 5 reported on the characterisation of commercially available carbon block and carbon-based cold ramming paste and industrial slag to be utilized in a study of the impact that the choice in carbon-based refractory material would have on tap-hole refractory life.

Chapter 6 reports on wettability tests conducted to study the importance of the choice in refractory material on tap-hole refractory life, and conclude with a review of the first and second research questions and an introduction to Chapter 7.

6.2 Method

The wettability tests were conducted with two goals in mind:

1. Confirm the potential for the chemical reaction to occur between the refractory materials and slag.
2. Study wettability of slag on refractory as it may affect infiltration.

The experimental conditions are summarised in Table 43.

Table 43: Experimental conditions of wettability tests.

	Slag	Refractories	Temperature [°C]	Atmosphere	Time [min]
1	Synthetic	Ramming paste matrix	1592	Argon	25
2	Industrial	Carbon block	1592	Argon	25
3	Industrial	Ramming paste matrix	1592	Argon	25
4	Industrial	Ramming paste aggregate	1592	Argon	25
5	Industrial	Ramming paste matrix	1592	CO	25
6	Industrial	Ramming paste aggregate	1592	CO	25
7	Industrial	Carbon block	1592	CO	25

The sessile drop test was utilised in the wettability study. See Figure 62 for sketch of experimental setup.

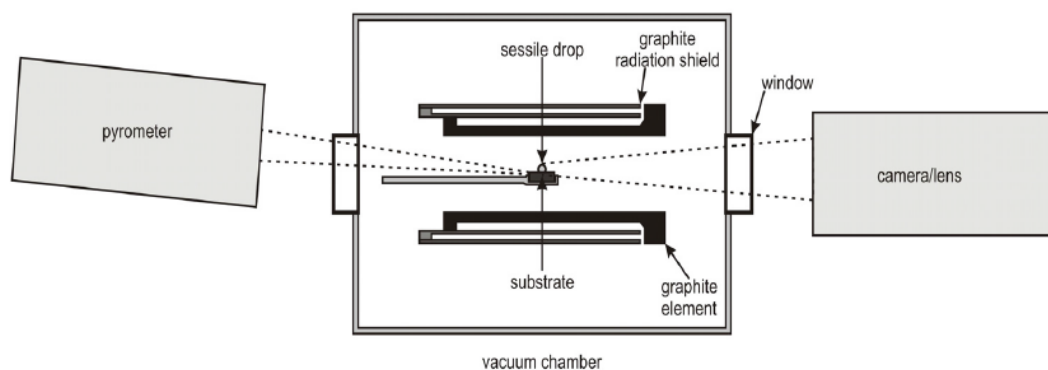


Figure 62: Sketch of the wettability furnace and experimental setup [39].

The experimental setup consisted of a graphite tube positioned horizontally inside a high-temperature furnace. All heated furnace parts, including the element and heat shields, were

constructed of graphite, allowing for flexibility in heating and cooling rates. The atmosphere could be regulated as either vacuum, inert gas (Ar) or reducing gas (CO).

The maximum temperature of the furnace was 2673 K (2400 °C). Temperature was measured using a KELLER PZ40 two-color pyrometer operating from 1173 K and focused on the edge of the graphite sample holder and a type C thermocouple installed inside the furnace just above the sample. A fire-wire digital video camera with a telecentric lens was utilized to record images of the sample.

A Cambridge Sensotec Rapidox 2100 (with accuracy from 10 – 17 ppm to 100 pct O₂) was employed to measure continually the partial pressure of oxygen in the gas outlet during the experiments. The furnace was designed to study the contact angle and the interaction between a small liquid sample and a substrate with the maximum size of 10 mm in diameter and 2 – 5 mm in height.

The powdered slag was pressed into small pellets using a press and die. To ensure that the liquid drop remained on top of the substrate without touching the edges, the typical slag sample volume was 0.013ml.

Scientific-grade argon gas (6.0), with 99.9999 pct Ar, was purified by an Alltec gas purifier combined with a Hydro Purge II type. This technology has the ability to remove moisture, oxygen and hydrocarbons. The content of water and oxygen in the outlet was stated to be < 1 ppb. Afterward, the argon gas ran through a furnace with Mg turnings at a temperature of 673 K (400 °C), which further reduced the oxygen content. The purified argon, at a flow rate of 500 ml/min, was utilized as the inlet gas to the vacuum chamber. The experiments were carried out at a pressure of 1 atmosphere. At the melting point of the slag, the oxygen activities ranged between 10⁻¹⁷ bar and 10⁻¹⁸ bar.

A detailed description of the experimental setup with photographs and equipment supplier details was supplied by Ciftja et al ([47]).

Validation of the temperature measurements were done using pure iron on a pure alumina substrate in an argon atmosphere. The melting point of pure iron is 1535°C. As pure iron was non-wetting on pure alumina, liquid iron formed a ball at 1535±1°C. When the liquid iron ball formed, the temperature readings on the type C thermocouple and the pyrometer were logged and the offset between the temperature readings and the melting point calculated. Assuming linearity, the actual temperature at the liquid / solid interface was controlled by controlling the temperature reading on the type C thermocouple.

The following experimental procedure applied:

- Draw vacuum
- Flush with UN1006 argon at a flow rate of 500 ml/min until pO₂ measurement on gas outlet reads less than 500ppm
- Heat furnace to 950°C at a rate of 300°C/h
- Then heat furnace to 1510°C at a rate of 50°C/h
- Then heat furnace to balling temperature at a rate of 5°C/h
- Terminate experiment on balling of iron which occurs within 1°C

The results are reported in Figure 63. At the melting point, the pyrometer reading had a -14°C offset and the type C thermocouple a +47°C offset. As the temperature readings increased linearly and in parallel with time, it was assumed that the offsets were the same at all temperatures. The

temperature measured with the type C thermocouple was logged automatically with the photographic images.

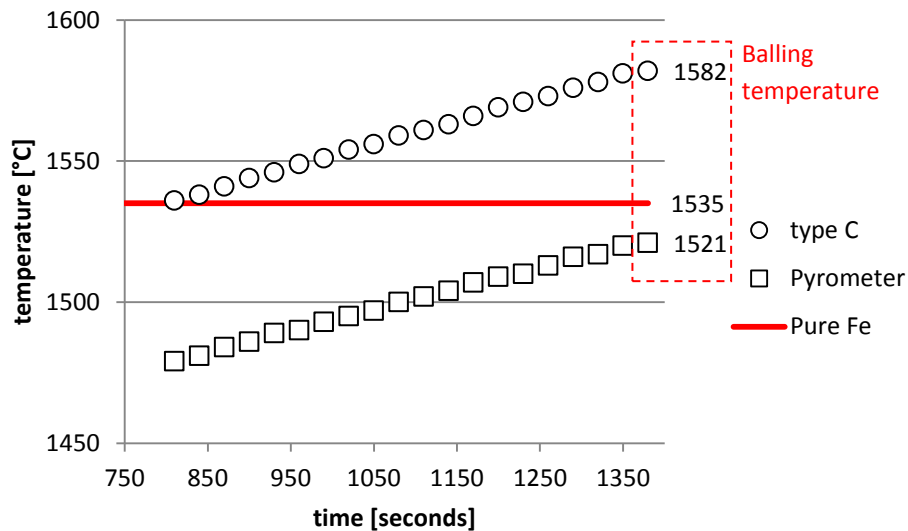


Figure 63: Results of temperature validation experiment indicating offset of pyrometer measurement 14°C below and of type-C thermocouple 47°C above melting point of pure iron (1535°C).

Polished sections were prepared of one each of the following experiments:

1. Synthetic slag on ramming paste matrix (defined in Figure 41) in Ar to study the interface for evidence of SiC and SiMn reaction products.
2. Industrial slag on graphite, carbon block, ramming paste matrix and ramming paste aggregate in Ar to study the refractory for evidence of infiltration.

To prepare the polished sections a method similar to the one described by Ciftja [47] was applied – see Figure 64. The samples were first mounted in resin and then cut in half. The cutting plane passed through the middle of the substrate and slag droplet. The observation plane was ground with SiC grinding paper and polished with diamond paste. Afterwards the samples were cleaned with soap and water, ethanol and hot air.

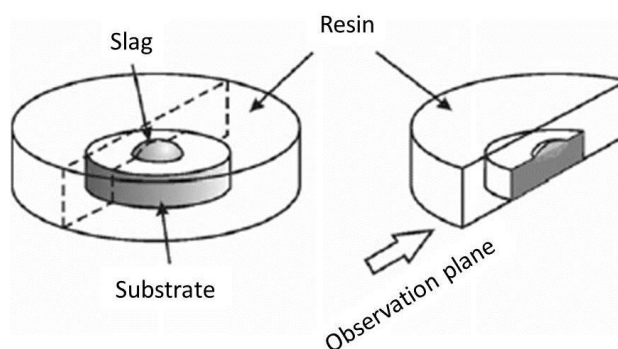


Figure 64: Sketch of sample preparation for wetting experiments analysis (after Ciftja et al., 2010).

The samples were studied using LOM and SEM EDS.

6.3 Results

For each experiment wetting angles (θ) were measured on images at:

1. 30 second intervals between the balling temperature of the slag and the holding temperature.
2. 5 minute intervals at the holding temperature with three measurements taken 10 seconds apart after each 5 minute interval.

For each image the wetting angles were measured on both sides. Measurements were done on images printed on paper using a ruler, pencil and protractor. First the baseline was drawn – line a-a in Figure 65a – followed by the two tangents b-b and c-c. Then the macroscopic contact angle (as defined in [56]) between a-a and b-b or a-a and c-c was measured using the protractor.

In most instances θ between a-a and b-b differed from θ between a-a and c-c. This was especially true in cases where a second phase (or droplet) formed that prevented the liquid from moving freely – see Figure 65b. Once a dataset was compiled a selection was made on whether the set of wetting angles measured between a-a and b-b or the set of wetting angles measured between a-a and c-c would be utilized for further analysis based on the dataset with the least secondary phase interference.

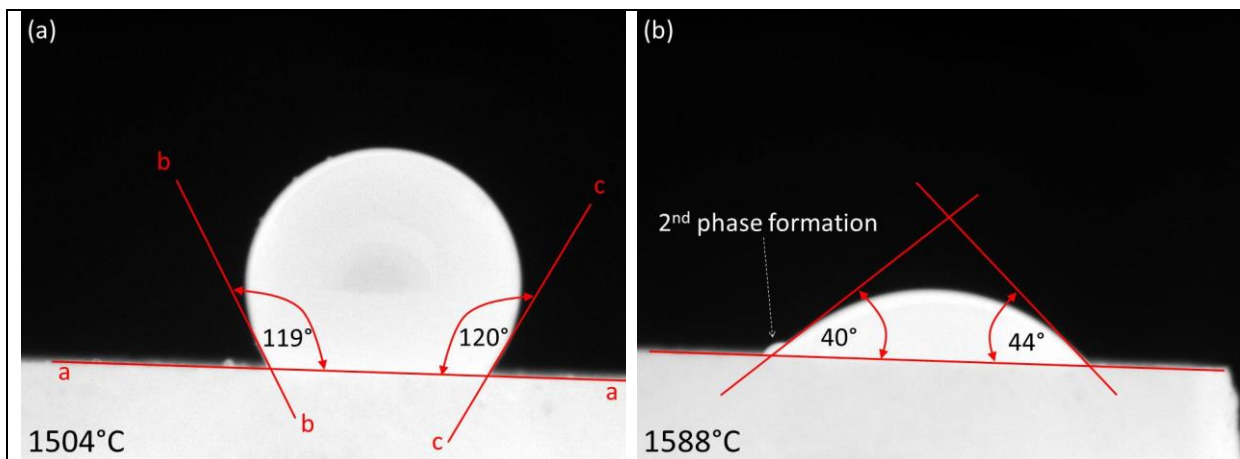


Figure 65: Wetting angle – θ – of synthetic slag on ramming paste matrix substrate in an argon atmosphere as measured in (a) non-wetting conditions and (b) wetting conditions.

Figure 66 contains a plot of a dataset of wetting angles as a function of time and temperature. The dataset was compiled for wetting angles measured between lines a-a and c-c for synthetic slag on ramming paste matrix substrate in an argon atmosphere.

To construct the plot, the temperature as a function of time was calculated based on the heating schedule. The wetting angles were then matched to a specific temperature during the heating period and to a specific time interval during the holding period. Temperature correction was taken into account.

To determine the random variation in the wetting angle measurements, two sets of data were prepared for the experiment where synthetic slag was melted on a ramming paste matrix substrate in an argon atmosphere. One set of data was prepared for non-wetting conditions and the images were selected from the balling temperature onwards. The other set of data was prepared for wetting conditions and the images were selected at the end of the experiment during the cooling down period.

Each set consisted of thirty images of which 20 were a time series taken at 1 second intervals and 10 were repeats of a single image, 5 the image as taken and 5 the same image flipped horizontally. Image numbers were randomised before measurements were conducted. The results are presented in Table 44.

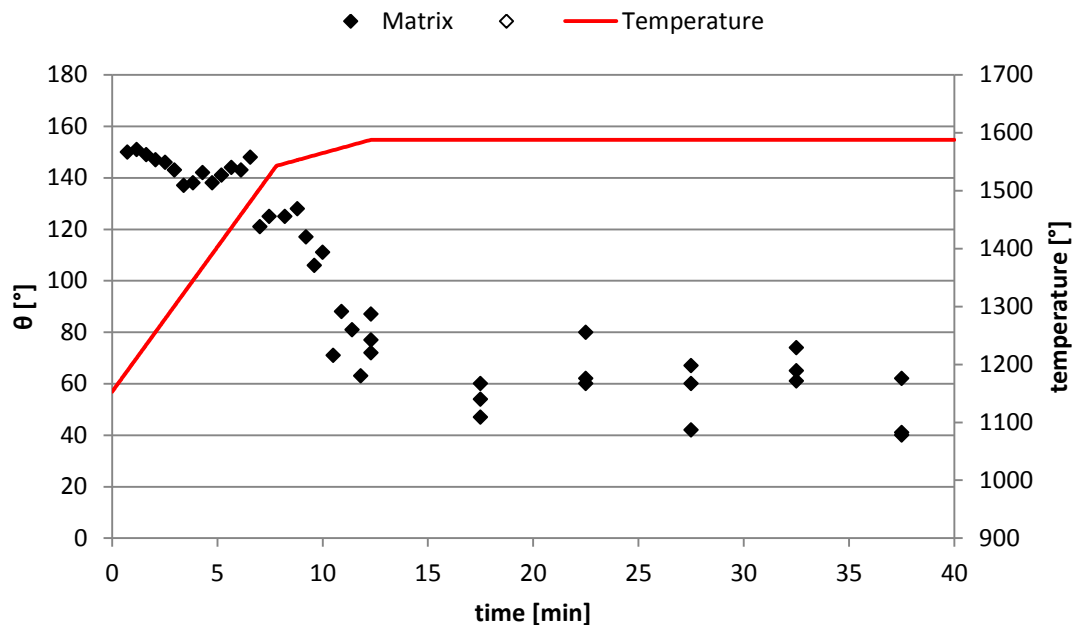


Figure 66: Wetting angle – θ – of synthetic slag on ramming paste matrix substrate in an argon atmosphere as a function of time and temperature. The holding temperature was 1588°C.

Table 44: Repeatability of wetting angle measurements on left-hand and right-hand side on time series of 20 consecutive images and 10 repeats of a single image taken under wetting and non-wetting conditions. The dataset was taken from the experiment conducted with synthetic slag on ramming paste matrix substrate in an argon atmosphere. The holding temperature was 1588°C.

	Wetting				Non-wetting			
	Time series		Repeat		Time series		Repeat	
	θ_L	θ_R	θ_L	θ_R	θ_L	θ_R	θ_L	θ_R
Average	36.8	34.2	35.4	33.5	144.6	145.2	145.5	145.8
STDev	4.2	2.2	2.7	2.7	1.6	2.2	2.0	1.8

To determine the repeatability of the experimental conditions, the wetting angle measurements (θ) of the two experiments conducted in duplicate were compared:

1. Industrial slag on ramming paste aggregate substrate in Ar-gas with holding temperature at 1588°C.
2. Industrial slag on ramming paste matrix substrate in Ar-gas with holding temperature at 1588°C.

Figure 67 is a plot of the wetting angles measured at the holding temperature (i.e. time 0 was when the actual holding temperature was reached) at the same time intervals for each set of experiments i.e. the X-axis is the wetting angle for the first set of experiments and the Y-axis the second set. The ideal condition is when the wetting angle measured in the first experiment is exactly the same as the wetting angle measured in the second experiment.

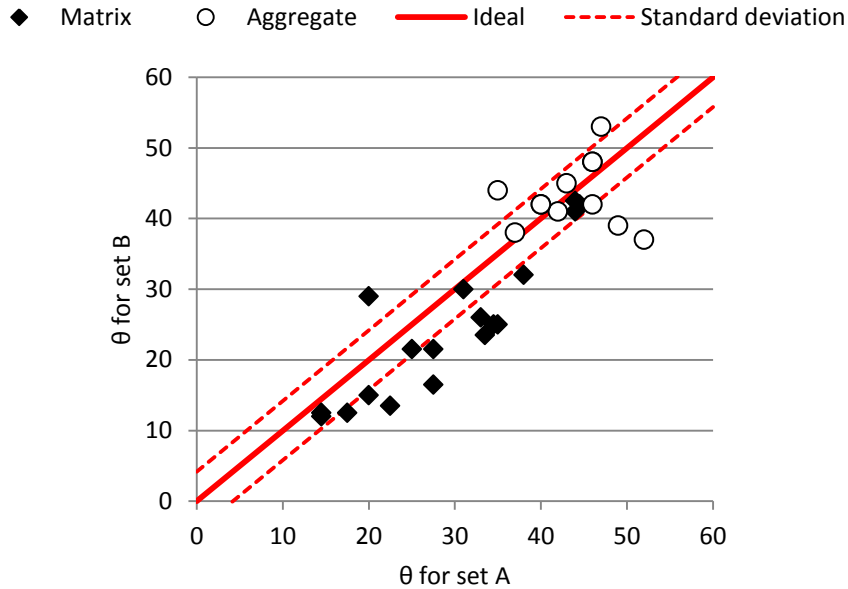


Figure 67: Comparison between wetting angles of two duplicate tests. The standard deviation boundaries are based on the largest value of standard deviation (θ) calculated under wetting conditions – see Table 44.

The balling temperature is the temperature at which the slag formed a sphere. Figure 68 shows the equilibrium phase chemical composition of the slag as a function of temperature as calculated in FACTSage 6.4. The bulk chemical composition of the synthetic slag in Table 27 was applied.

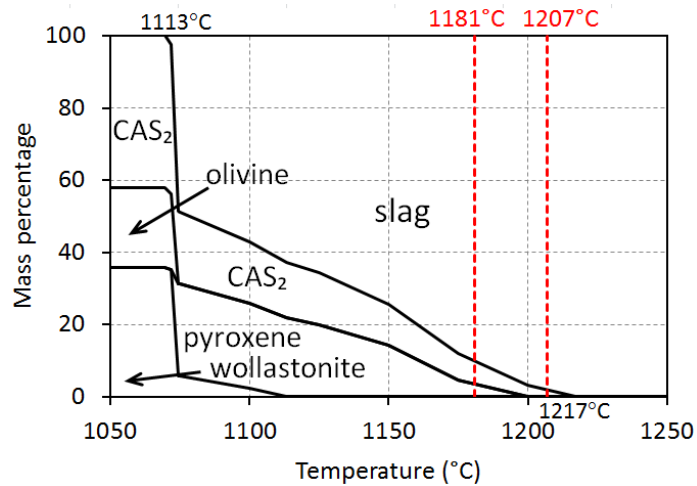
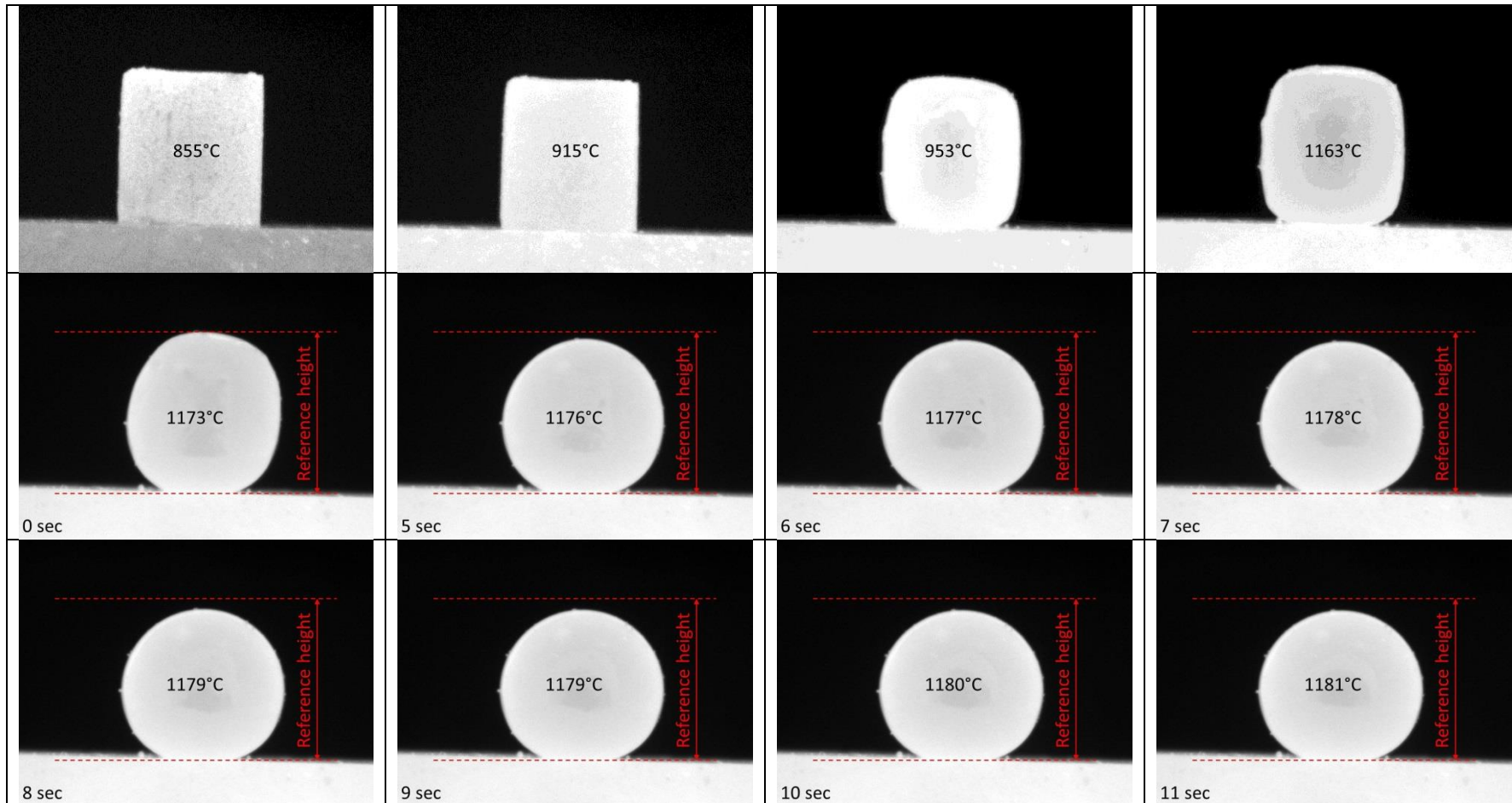


Figure 68: Balling (melting) temperatures of synthetic slag on different substrates in argon plotted on the equilibrium phase distribution of synthetic slag (percentage by mass) based on the chemical compositions in Table 27 determined in FACTSage 6.4.

Unlike with pure iron, melting of the slag occurred gradually. To illustrate the phenomenon of gradual melting, a selection of recorded images is shown in Table 45. These images were recorded for synthetic slag on a ramming paste matrix substrate in an argon atmosphere during the period where the heating rate of the sample was 300°C/h. The powdered slag (-106 μ) was initially pressed into a cylindrical pellet – see image at 855°C in Table 45 – and placed onto the refractory substrate.

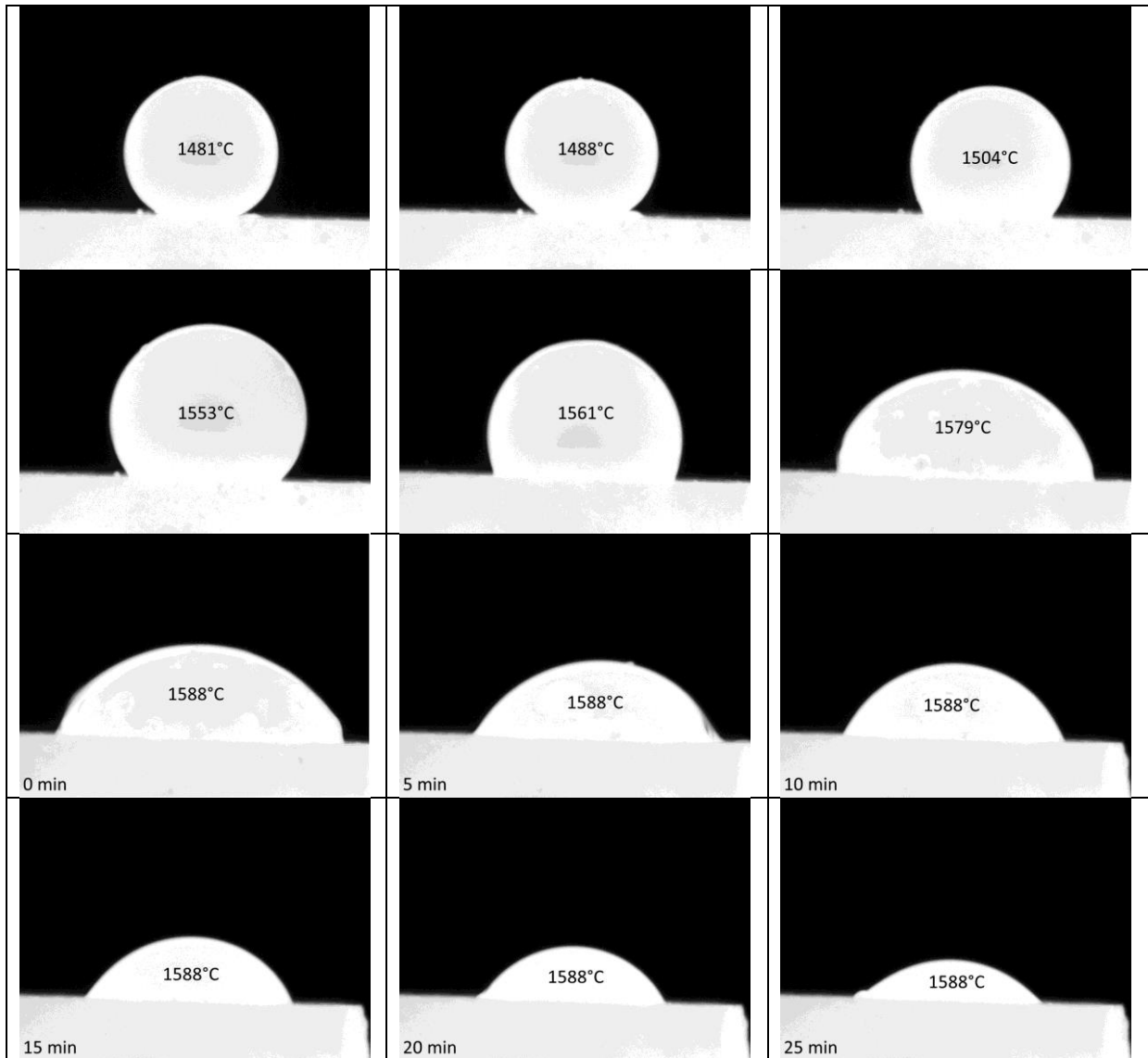
At 915°C the first signs of melting or sintering were noted at the right-hand corner of the interface between the slag pellet and refractory substrate. As the temperature increased all four corners of the sample rounded (see image at 953°C). Taken into account the position of the type C thermocouple - positioned above the sample - the measured temperature at which all four corners rounded correlated approximately with the calculated solidus temperature of the slag. Between 953 and 1163°C no significant changes in the shape of the sample were observed. From 1173°C onwards melting proceeded rapidly with the final ball forming within seconds at 1181°C. The images from 1173°C to 1181°C included a reference height which was utilized to determine to what extent the height of the slag sample decreased during the final stages of melting and reaction.

Table 45: Series of recorded images as a function of temperature and time for the synthetic slag on ramming paste matrix substrate in an argon atmosphere when the heating rate was 300°C. The holding temperature was 1588°C.



During the remainder of the heating period, the wetting angle changed from non-wetting ($>90^\circ$) to wetting ($<90^\circ$) and remained wetting for the duration of the holding period - see Figure 66. To illustrate the phenomenon a selection of recorded images is shown in Table 46, again for the same experiment i.e. synthetic slag on a ramming paste matrix substrate in an argon atmosphere.

Table 46: Series of recorded images as a function of temperature and time for the synthetic slag on ramming paste matrix substrate in an argon atmosphere. The holding temperature was 1588°C.



In Figure 69 the data points associated with some of these images are superimposed on the data from Figure 66. Open symbols represent images in Table 46 taken during the heat-up phase and red symbols, images taken at holding temperature at 5 minute intervals. As mentioned before, at each 5 minute interval the wetting angle was measured on three images taken 10 seconds apart. The red symbols with red borders represent the first of each of these three images.

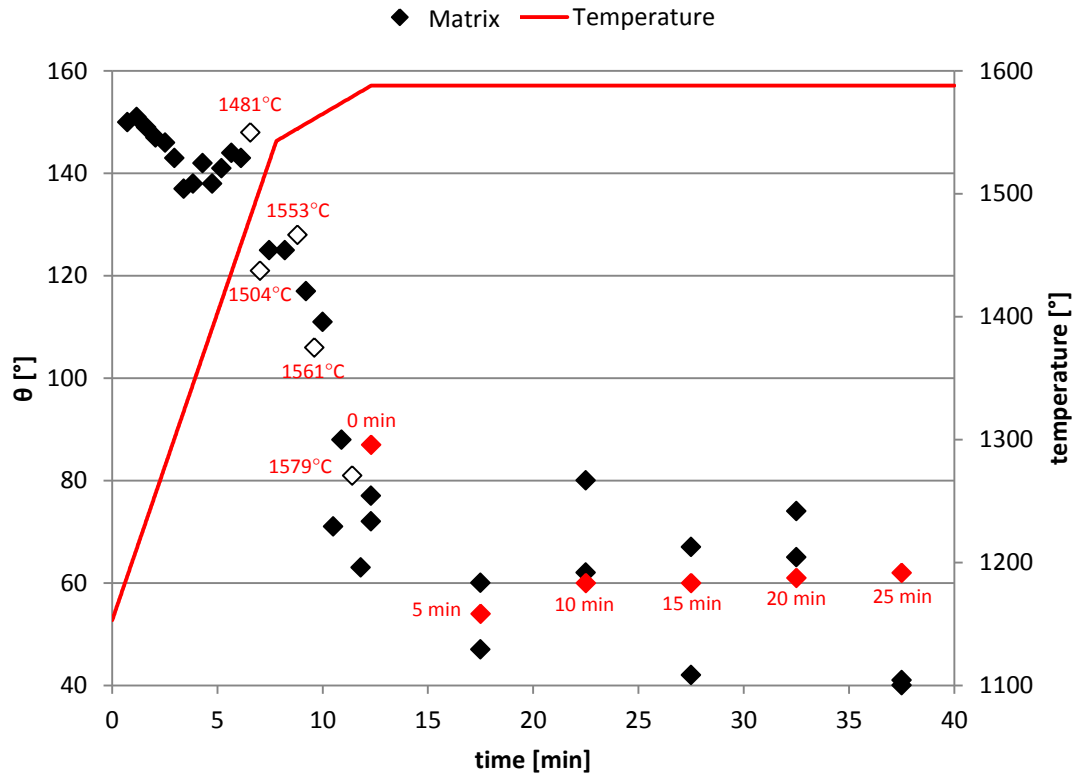


Figure 69: Wetting angle – θ – of synthetic slag on ramming paste matrix substrate in an argon atmosphere as a function of time and temperature. Open symbols represent images in Table 46 taken during heat-up phase and red symbols images taken at holding temperature at 5 minute intervals. The holding temperature was 1588°C.

Between the balling temperature of 1181°C and 1481°C – the remainder of the time period where the heating rate was 300°C/h – the wetting angle remained non-wetting ranging between 137° and 151°. As the temperature increased at a rate of 50°C/h, the wetting angle decreased reaching the change-over point of 90° at the start of the holding period. During the first 5 minutes of the holding period the wetting angle reduced further but remained wetting ranging between 40 and 80°.

The change in droplet size, which can be observed in Table 46, was either due to gas formation (increase in volume) or release (subsequent decrease in volume) or due to infiltration of the liquid into the refractory material, or both.

To quantify the change in droplet size, the assumption was made that the volume of the liquid droplet could be represented by a spherical cap [39], [56]. The volume of the spherical cap (V_{cap}) that remained above the refractory substrate was calculated using Equation 27 [126]. The parameters applied in Equation 27 are defined in Figure 70a for wetting conditions and Figure 70b for non-wetting conditions.

As no scale was available to convert measurements to actual values, the volume of the slag at balling temperature was selected as reference volume (V_{ref}) and all other measurements expressed in relation to this volume as the ratio V_x/V_{ref} .

Equation 27: Volume of the spherical cap [126]

$$V_{cap} = \frac{1}{6} \pi h (3a^2 + h^2)$$

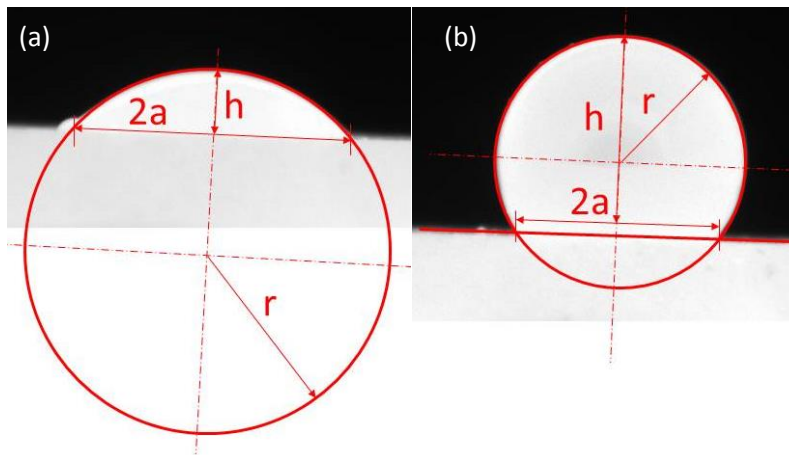


Figure 70: Definitions of parameters applied in volume calculations of droplets under (a) wetting and (b) non-wetting conditions.

Circles and straight lines were fitted to images in Microsoft PowerPoint and measurements conducted in ImageJ using the 'straight' tool and Analyse > Measure function. Calculations were done in Microsoft Excel.

To determine the repeatability of the volume measurements, two datasets were prepared for the experiment for synthetic slag on a ramming paste matrix substrate in an argon atmosphere. A set of samples prepared for non-wetting conditions was selected from the balling temperature onwards. The set of samples prepared for wetting conditions was selected from the images taken at the end of the experiment during the cooling down period.

Each set consisted of thirty images of which 20 were consecutive (1 second time interval) and 10 were repeats of a single image, 5 as taken and 5 the same image flipped horizontally (mirror image). Image numbers were randomised and measurements conducted. The results are presented in Table 47.

Table 47: Repeatability of volume ratio on time series of 20 consecutive images and 10 repeats of a single image taken under wetting and non-wetting conditions. The dataset was taken from the experiment conducted with synthetic slag on ramming paste matrix substrate in an argon atmosphere. The holding temperature was 1588°C.

	Wetting		Non-wetting	
	Consecutive	Single	Consecutive	Single
Average	1.01	1.04	1.01	1.01
STDev	0.03	0.04	0.01	0.02

The volume ratio was calculated for the dataset in Table 46. The results are presented in Figure 71 (as numerical values stated next to the corresponding contact angle); $V_x/V_{ref} < 1$ represents a reduction in volume and $V_x/V_{ref} > 1$ an increase in volume. The largest volume change occurred during the transition period. During the holding period, a decrease in volume occurs without any significant change in wetting angle.

Changes in volume were also associated with large variations in wetting angle observed during the holding period. The phenomenon is illustrated in Table 48 with images taken 10 seconds apart, 15 minutes into the holding period. The diameter of the base of the spherical cap (2a) remained

constant but as the gas formed the height of the spherical cap (h) increased resulting in an increase in volume and with an associated change in wetting angle.

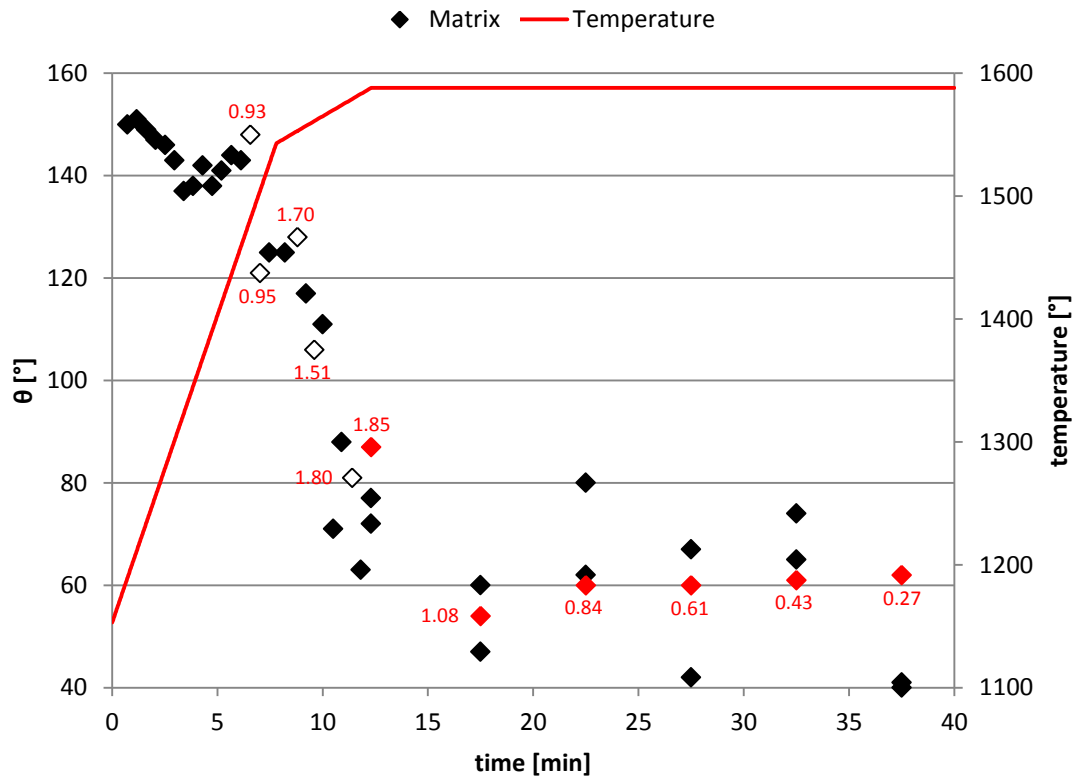
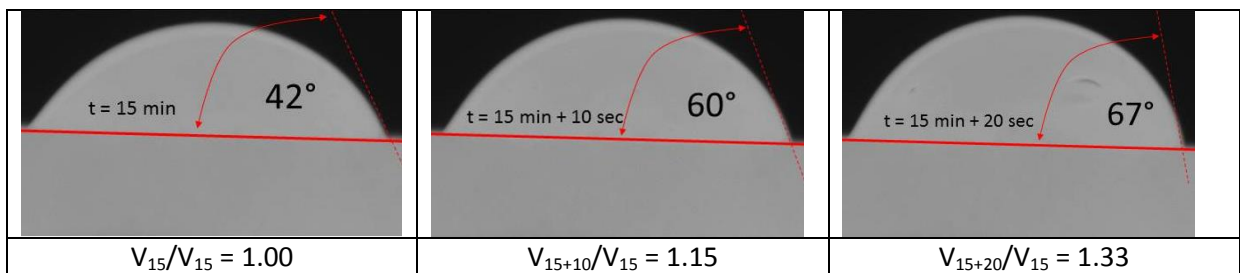


Figure 71: V_x/V_{ref} of images in Table 46 (numerical values) superimposed on the measured contact angles (as plotted in Figure 69), for the synthetic slag on a ramming paste matrix substrate in an argon atmosphere with the holding temperature at 1588°C.

Table 48: Dependency of wetting angle on change in volume caused by gas formation at 15 minutes into the holding period for the synthetic slag on ramming paste matrix substrate in an argon atmosphere. The holding temperature was 1588°C. Images were taken 10 seconds apart.



In order to quantify the effect at a higher time resolution - considering 1 second intervals between images – the volume ratio was calculated for periods of 30 seconds each at 5, 15 and 25 minutes into the holding period. The results are presented in Figure 72.

Between time intervals, the average volume size decreased significantly with increase in time, an indication of the extent to which the slag infiltrated the refractory material. The average size of the volume ratio was 1.01 at 5 minutes, 0.68 at 15 minutes and 0.30 at 25 minutes. The range of the

volume ratio too decreased with increase in time with the range being 0.79 – 1.34 ($\Delta 0.55$) at 5 minutes, 0.50 – 0.89 ($\Delta 0.39$) at 15 minutes and 0.28 – 0.32 ($\Delta 0.04$) at 25 minutes, an indication of the decrease in gas bubble formation rate.

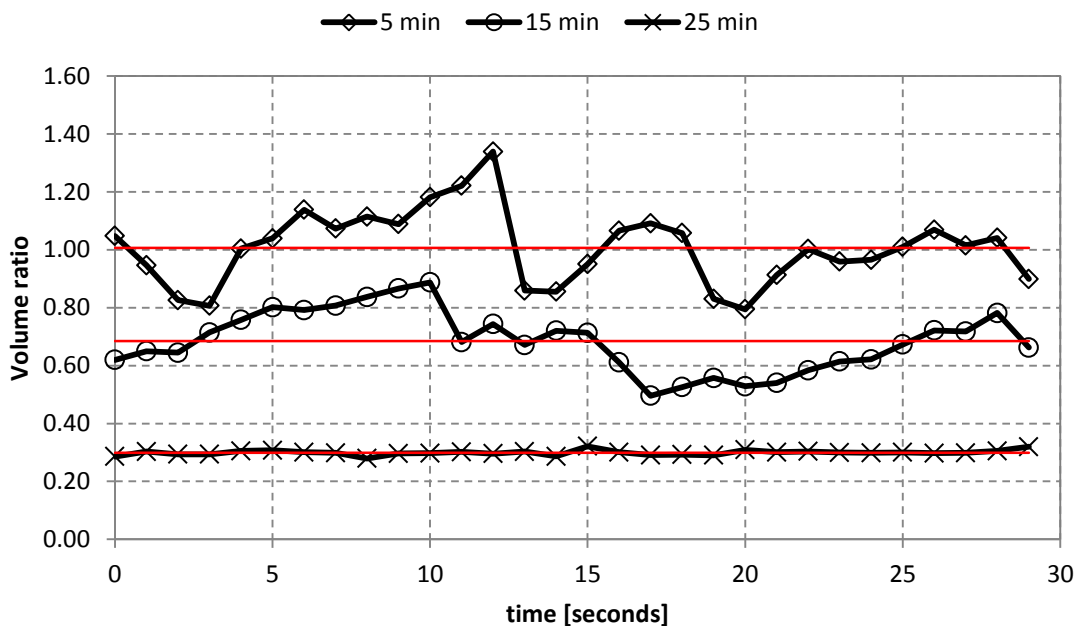
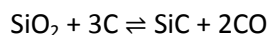


Figure 72: Calculated volume ratio (V_x/V_{ref}) of synthetic slag on ramming paste matrix substrate in an argon atmosphere at 5, 15 and 25 minutes into the holding period. Calculations were done at 1 second intervals for 30 seconds at each holding period. Red lines represent calculated average volume ratio over each 30 second time period. The holding temperature was 1588°C.

It is proposed that the source of the gas formed in the experiment was the reduction product (primarily CO-gas) of slag reacting with refractory material, as discussed in Chapter 3 and Chapter 4, and that this reaction was the main cause for wetting of the carbon refractory by the slag (reactive wetting).

In line with the proposed role of reaction, SEM investigation of the sample revealed SiC formation (reduction according to Equation 28) – see Figure 73 and Figure 74 – but not of metal formation.

Equation 28: Formation of SiC through SiO₂ reduction



The idea that the reduction reaction was responsible for the gas formation and wetting behaviour of the slag towards the refractory was further illustrated by wettability experiments conducted with industrial slag on different substrates (carbon block, ramming paste aggregate and ramming paste matrix) in a 1-atm CO atmosphere. The assumption was that the CO atmosphere would tend to suppress gas evolution (Equation 28) according to Le Chatelier’s principle, if the source of the gas formed in the experiment were the reduction product (primarily CO-gas) of slag reacting with refractory material. If reaction were suppressed, wetting conditions would remain non-wetting if the reaction were the main cause of wetting of the refractories by the slag. The results of experimental tests of this idea are presented in Figure 75.

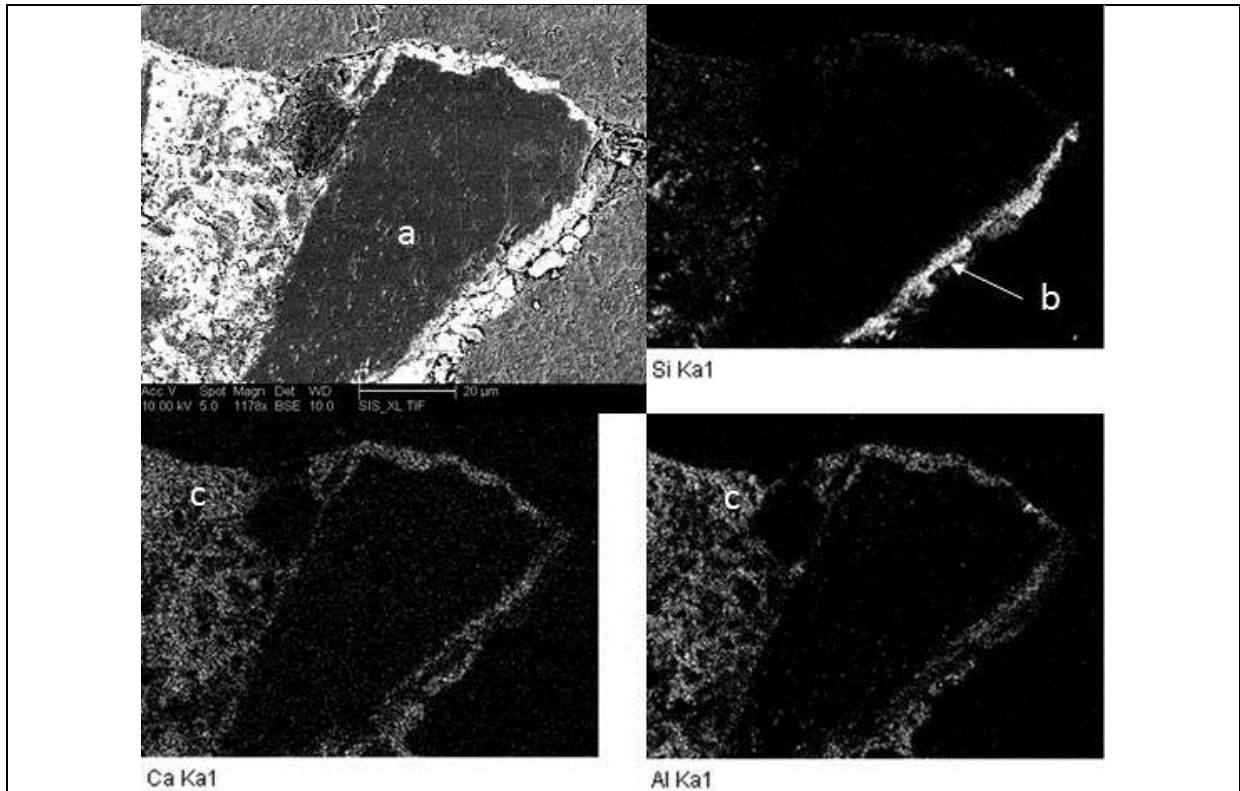


Figure 73: SEM BSE micrograph and EDS elemental maps for Si, Ca and Al determined at 15kV for synthetic slag on ramming paste matrix substrate in an argon atmosphere with (a) refractory aggregate, (b) reaction product and (c) refractory matrix infiltrated by slag. The holding temperature was 1588°C.

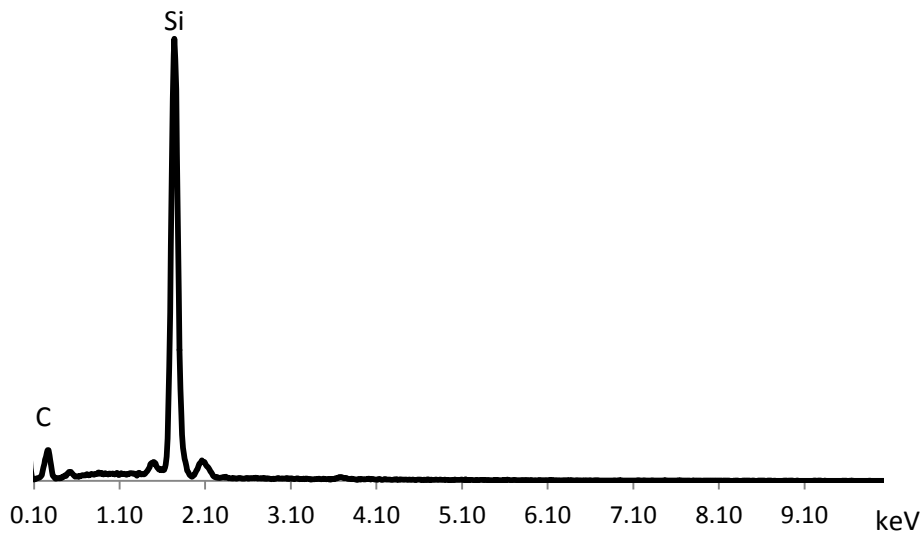


Figure 74: Measured EDS spectrum (15kV) of Si-rich layer in Figure 73. The Si-rich layer formed at the interface between synthetic slag and an aggregate particle present in the ramming paste matrix. The experiment was conducted with synthetic slag on ramming paste matrix substrate in an argon atmosphere. The holding temperature was 1588°C.

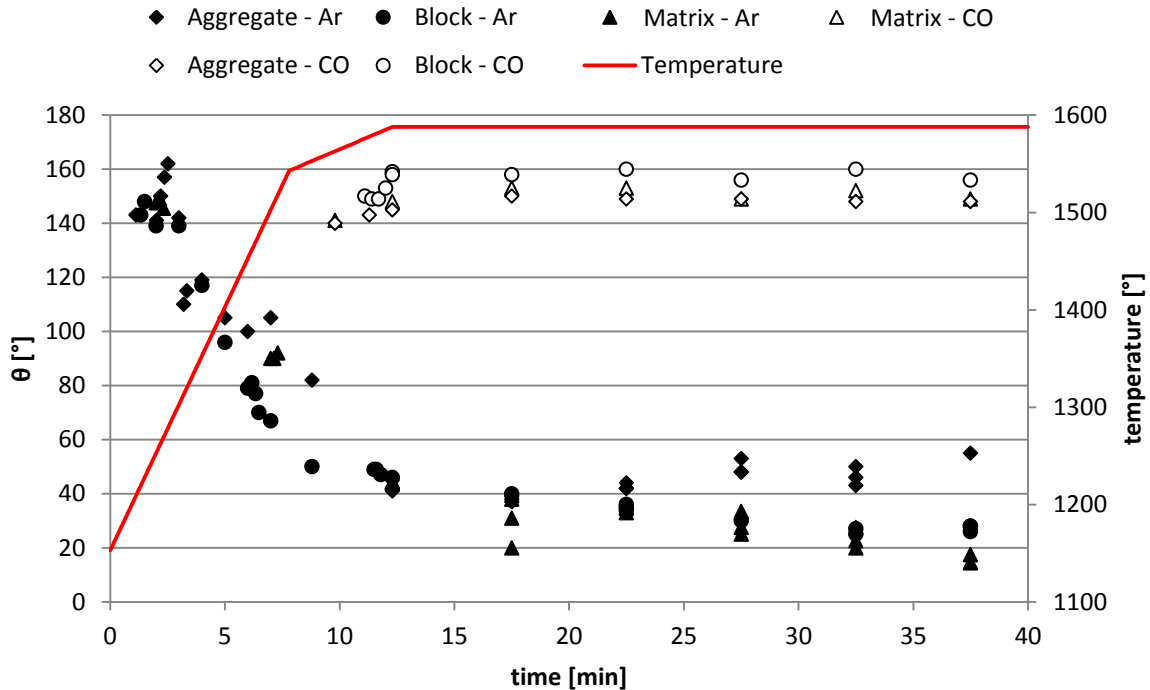


Figure 75: Wetting angle – θ – as functions of time, for industrial slag on different substrates (carbon block, ramming paste aggregate and ramming paste matrix substrates) in either Ar or CO atmospheres. The holding temperature was 1588°C.

From Figure 75, the three experiments conducted in an Ar-gas atmosphere all followed the same trend (similar to that of the synthetic slag on ramming paste matrix) even though the refractory substrates differed significantly in terms of composition and porosity. Initially the slag was non-wetting towards the refractory substrate but as the temperature increased the wetting angle decreased significantly, maintaining fairly constant wetting conditions during the holding period.

The experiments conducted in the CO-gas atmosphere also followed the same trend, but one that was significantly different from that of the experiments conducted in the Ar-gas atmosphere:

1. The balling temperatures of the slag in the experiments conducted in CO-gas were significantly higher than that of the experiments conducted in Ar-gas. (The balling temperature is indicated by the temperature at the time when the first measured contact angle is plotted.)
2. The conditions remained non-wetting for the duration of all the experiments conducted in CO-gas.

Figure 76 contains the equilibrium phase distribution of the slag as a function of temperature as calculated with FACTSage 6.4. The bulk chemical composition of the industrial slag in Table 34 was applied.

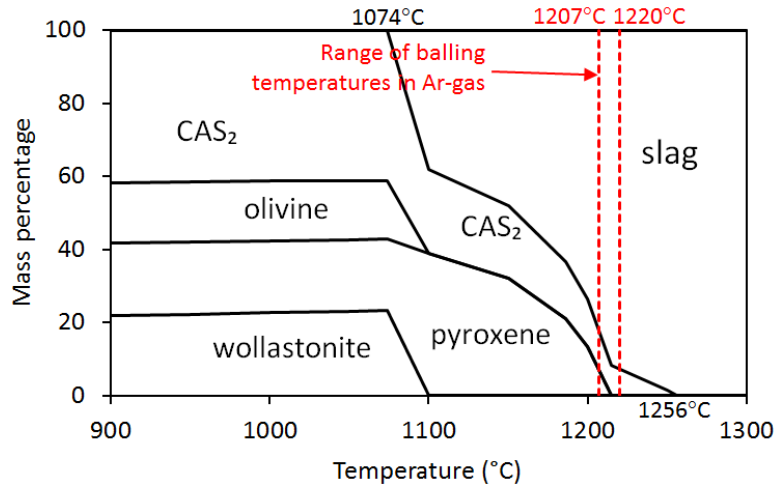


Figure 76: Range of balling (melting) temperatures of industrial slag for wettability tests conducted in argon gas on different types of refractory substrates plot, superimposed on the equilibrium phase distribution of industrial slag (percentage by mass), calculated for the chemical compositions in Table 34 using FACTSage 6.4. The balling temperature of the slag in CO-gas (not indicated on graph) ranged between 1563°C and 1576°C.

Differences in slag volume during wetting tests were examined at a higher time resolution (1 second intervals between images) for periods of 30 seconds each at 5, 15 and 25 minutes into the holding period for industrial slag on ramming paste matrix substrates in Ar-gas or CO-gas. The resulting volume ratios are presented as functions of time in Figure 77a for Ar-gas and Figure 77b for CO-gas.

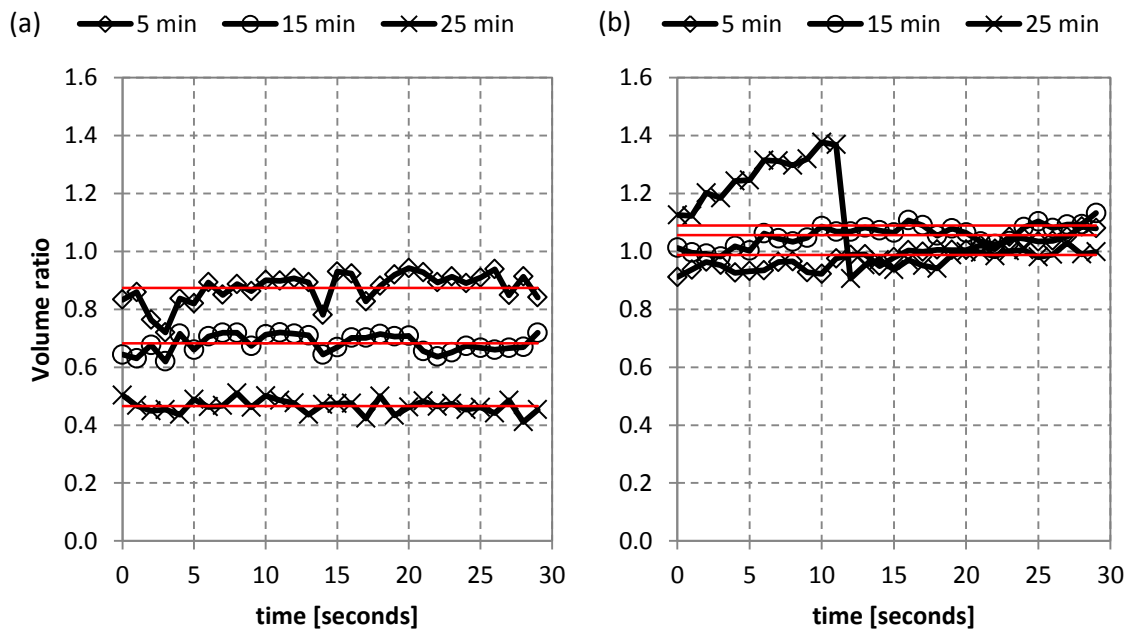


Figure 77: Calculated volume ratio of industrial slag droplet on ramming paste matrix substrate in (a) an Ar-gas atmosphere and (b) a CO-gas atmosphere at 5, 15 and 25 minutes into the holding period. Calculations were done at 1 second intervals for 30 seconds at each holding period. Red lines represent calculated average volume ratio over each 30-second periods.

As with the synthetic slag on ramming paste matrix in Ar-gas, the average volume ratio decreased significantly with time between holding periods, for reaction of industrial slag with ramming matrix in Ar: The average volume ratio was 0.87 at 5 minutes, 0.68 at 15 minutes and 0.47 at 25 minutes. The range of fluctuations in the volume ratio over each 30-second period also decreased with time; the range was 0.72 – 0.94 (width of range 0.22) at 5 minutes, 0.62 – 0.72 (width of range 0.10) at 15 minutes and 0.41 – 0.51 (width range 0.10) at 25 minutes.

In contrast, in CO-gas the average volume ratio changed far less between holding periods. The average volume ratio was 0.99 at 5 minutes, 1.06 at 15 minutes and 1.09 at 25 minutes. However, the range of volume fluctuations was no smaller than in Ar, and – at least for the run examined – remained approximately constant with time; the range was 0.91 – 1.09 (width of range 0.17) at 5 minutes, and 0.98 – 1.13 (width of range 0.15) at 15 minutes; after 25 minutes a gas bubble collapse occurred during the 30-second period studied, increasing the range to 0.91 – 1.38 (width of range 0.47).

It is considered that the extent of infiltration was a consequence of the wetting behaviour caused by chemical reaction. The maximum infiltration depth per experiment is reported in Table 49; the micrographs on which the infiltration depth measurements were made are presented in Figure 78 to Figure 80.

Table 49: Summary of the maximum depth – measured in Figure 78 to Figure 80 – to which industrial slag infiltrated into the refractory samples. The holding temperature was 1592°C and atmosphere argon gas.

Solid phase	Infiltration depth [mm]
Carbon block	2.7
Ramming paste aggregate	0.4
Ramming paste matrix	1.0

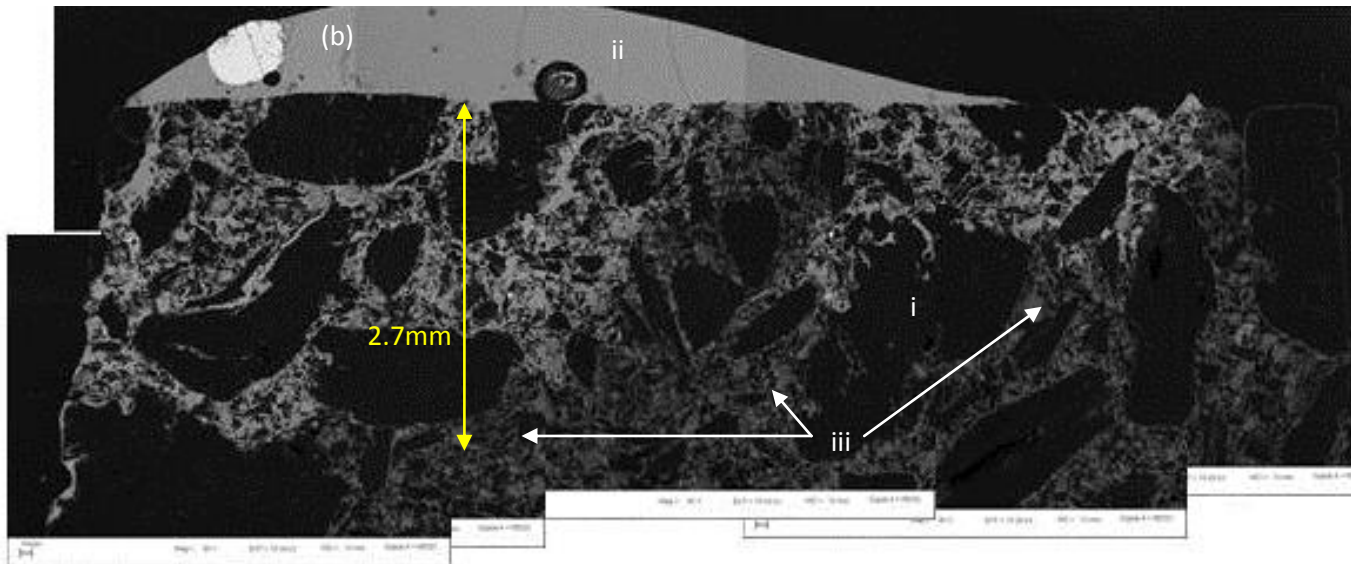
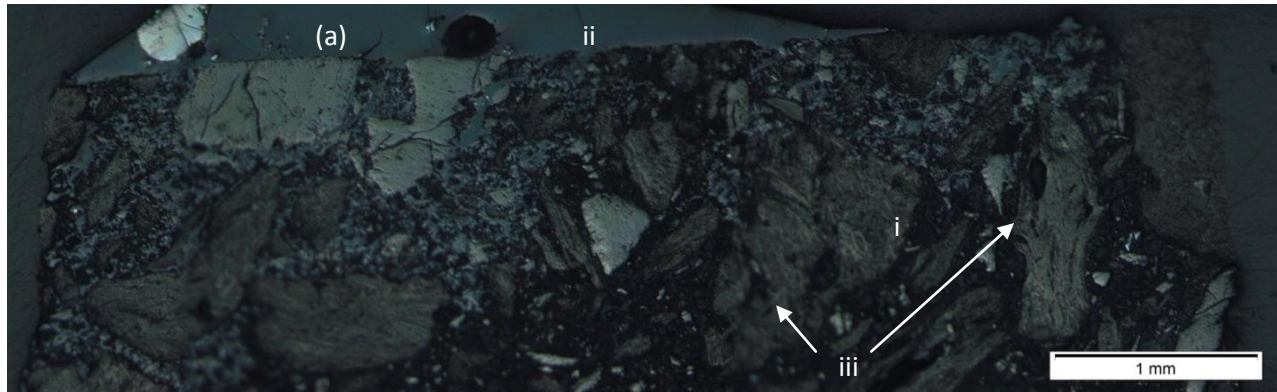


Figure 78: Stitched (a) LOM and (b) SEM BSE micrographs of (i) carbon block exposed to (ii) industrial slag at 1592°C in an argon atmosphere with (iii) infiltration of the slag into the carbon block. Scale bars indicate 1mm on (a) and 100 µm on (b). Maximum infiltration depth reported in Table 49 indicated by yellow line on (b).

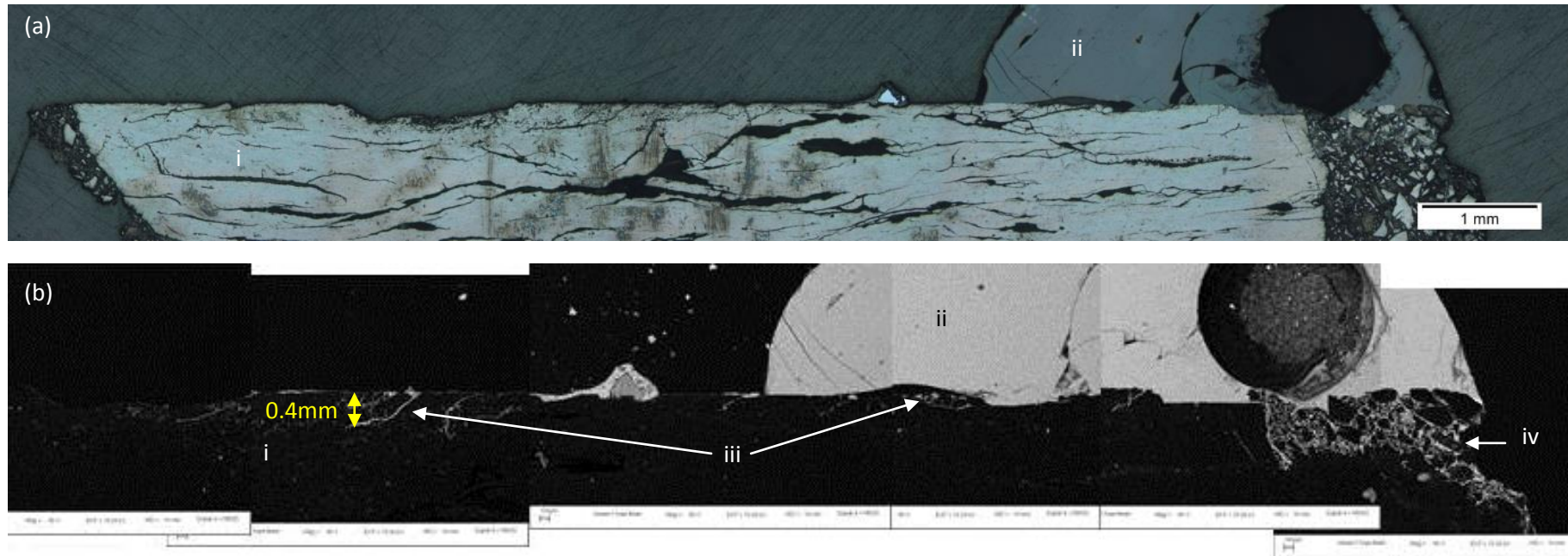


Figure 79: Stacked (a) LOM and (b) SEM BSE micrographs of (i) ramming paste aggregate exposed to (ii) industrial slag at 1592°C in an argon atmosphere with infiltration of slag into the (iii) ramming paste aggregate and (iv) ramming paste matrix. Scale bars indicate 1mm on (a) and 100 μm on (b). Maximum infiltration depth reported in Table 49 indicated by yellow line on (b).

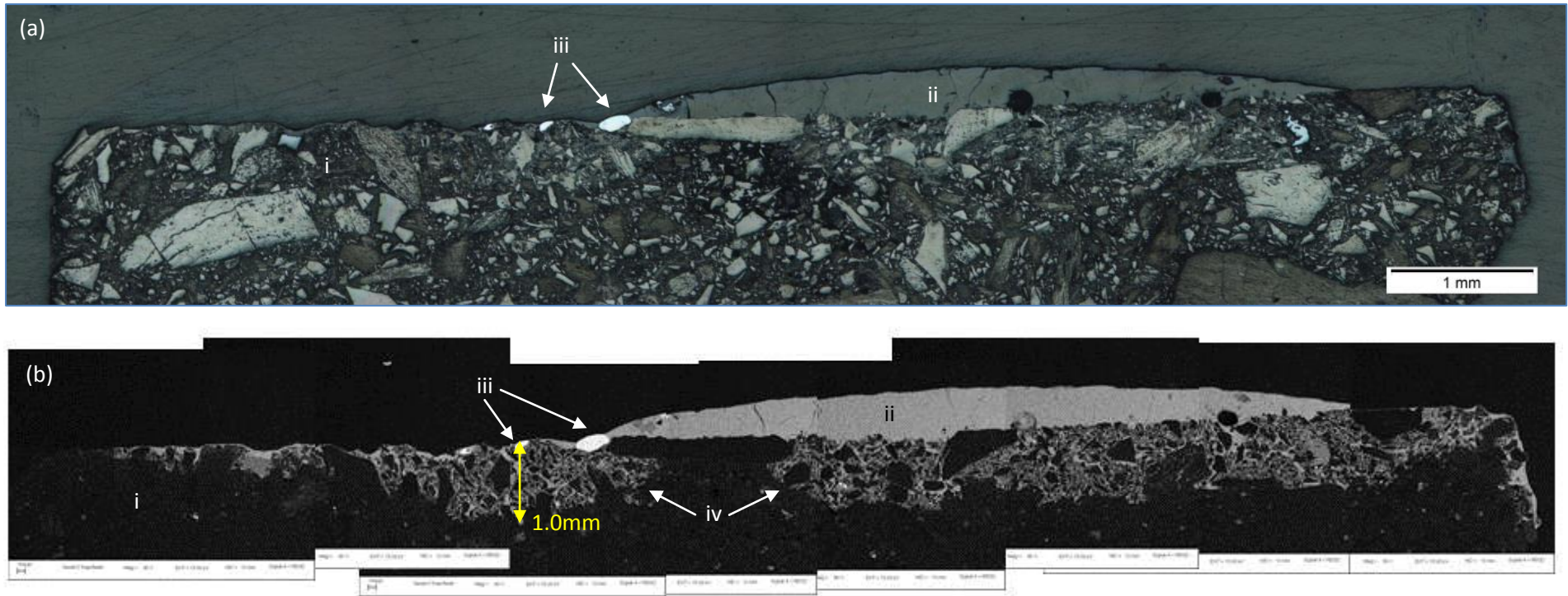


Figure 80: Stacked (a) LOM and (b) SEM BSE micrographs of (i) ramming paste matrix exposed to (ii) industrial slag at 1592°C in an argon atmosphere with (iii) metal droplets and (iv) infiltration of slag into the ramming paste matrix. Scale bars indicate 1mm in (a) and 100 µm in (b). Maximum infiltration depth reported in Table 49 indicated by yellow line in (b).

6.4 Discussion

To confirm, on a microscopic level, the potential for chemical reaction to occur in the system where the reaction products were potentially SiC and metal, synthetic slag was utilized as liquid medium, rather than industrial slag which already contained SiC and metal (as illustrated in Figure 42).

According to thermodynamic calculations the solidus temperature of the synthetic slag was 1070°C and the liquidus temperature 1217°C - Figure 68. The balling temperatures of the synthetic slag ranged between 1181°C and 1207°C, correlating well with the calculated slag liquidus temperature.

Initially, after melting, the liquid synthetic slag did not wet the ramming paste matrix - Figure 66. As the temperature increased to the holding temperature, the wetting angle changed from non-wetting (approximately 150°) to wetting (approximately 60°) and remained wetting for the duration of the experiment - Figure 69. The volume ratio of slag reduced from 1.0 at the balling temperature to 0.27 towards the end of the experiment - Figure 71 – showing significant slag infiltration into the substrate.

During the change from non-wetting to wetting, significant slag droplet volume fluctuations occurred with the volume ratio ranging between 0.95 and 1.85 (Figure 71). These volume fluctuations are attributed to gas (CO) evolution from the occurrence of one or both of the chemical reaction(s) identified in Chapter 3 and Chapter 4: The reduction of SiO₂ in the slag to form SiC and the formation of metal through the reduction of SiO₂ and MnO in the slag. Evidence of SiC formation was found – see Figure 73 and Figure 74 – but not of metal.

The idea that chemical reaction with the substrate occurred and contributed to wetting was further supported by experiments conducted with industrial slag as liquid medium and two different atmospheres: 100%Ar-gas or 100%CO-gas. As solid substrates carbon block, ramming paste aggregate and ramming paste matrix were utilised. In Figure 75 the experiments conducted in Ar-gas were all wetting at the holding temperature of 1588°C and the experiments conducted in CO-gas were all non-wetting. The initial idea was that all three potential reduction reactions listed in Table 32 would be suppressed (according to Le Chatelier's principle) in the presence of CO-gas, and would be promoted by the absence of CO-gas.

Although the experiments conducted demonstrated that chemical reaction between slag and refractory in CO-gas atmosphere was much less than in Ar-gas (supported by both volume changes and wetting angle measurements), the simple view of the presence of CO-gas suppressing all reactions is not supported by the experimental observations. Under argon, gas evolution was observed, and it seems reasonable to assume that the gas that formed was CO. This means that reaction between slag and carbon could nucleate CO bubbles at the reaction temperature; nucleation would require a CO pressure slightly above the ambient pressure of 1 atm (in line with the equilibrium calculations). While such a bubble was growing, the atmosphere at the reaction interface would have been 1 atm CO, no different from the atmosphere supplied externally in experiments performed under CO. Indeed, in both cases (for experiments performed under Ar and under CO) volume fluctuations indicating CO evolution occurred. It hence appears that maintaining a CO atmosphere did not suppress reduction of SiO₂, but rather changed the site of the reaction – from the slag-substrate interface (under Ar), to the slag-gas interface (under CO). This suggestion is supported by the absence of infiltration (and observation of non-wetting behaviour) in experiments under CO (indicating an absence of reactive wetting of the substrate), and by observation of deposited carbon on the slag surface for experiments under CO (as shown below, see discussion around Equation 29) – demonstrating that the CO atmosphere was a source of elemental carbon (which would have been able to react with the slag).

The idea that the chemical reaction was responsible for the increased wetting of the refractory substrates is further supported by the observation that nonreactive slags are generally non-wetting towards graphite in an argon atmosphere [63]. For ramming paste one would therefore expect the slag to behave in a non-wetting fashion in the absence of reactions; in fact, wetting was observed in the experiments (Figure 75).

Because the refractory materials are not pure carbon, but also contain phases which are wetted by slag – such as alumina and silicon carbide in the carbon block – it is necessary to evaluate whether the presence of these phases could have caused wetting even in the absence of chemical reactions. To estimate these effects, the Cassey-Baxter law for wetting of a heterogeneous surface – Equation 7 – was applied; the input data and result are presented in Table 50. The phase distribution of the carbon block was estimated from the proximate analysis in Table 38, assuming that of the 20% of the ash-yielding components half was corundum and half SiC. To a first approximation, these were taken to correspond to volume fractions of 0.1 each (a slight overestimate, since the densities of alumina and SiC are larger than that of graphite). The wetting angle of slag on each phase was sourced from literature [48], [63]. The literature values are for an atmosphere of argon gas (as in the experiments), but the slag compositions - Table 51 - and temperatures varied. The calculated equilibrium contact angle of slag on the mixture (95°) is therefore only a first estimate, but does support the suggestion that, in the absence of chemical reaction, carbon block would not to be wetted by the slag. Experimental observation of wetting (Figure 75) supports the suggestion that reaction occurred.

Table 50: Calculated equilibrium contact angle (θ_c) for slag on carbon block based on published [48], [63] wettability data for slags on different substrates and the carbon block phase distribution estimated from Table 38.

Solid substrate	Slag	Holding temperature [K]	$\theta_{\text{slag on substrate}}$		Reference	ϕ_s	Reference
			°	radians			
Graphite	A	1673	110	1.920	Figure 8 in [63]	0.8	
SiC	B	1873	20	0.349	Figure 8 in [48]	0.1	Table 38
Corundum	A	1473	10	0.175	Figure 6 in [63]	0.1	Table 38
$\cos \theta_c$				-0.081			
θ_c			95	1.652			

Table 51: Published [48], [63] compositions of slags utilized to measure wettability of graphite and corundum (A) and SiC (B).

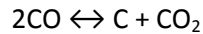
Slag	CaO	SiO ₂	MnO	TiO ₂	FeO	Total	Reference
A	55	45	-	-	-	100	[63]
B	-	38.7	44.3	11.4	5.6	100	[48]

According to thermodynamic calculations the solidus temperature of the industrial slag was 903°C and the liquidus temperature 1256°C - Figure 76. The balling temperatures of the industrial slag – for experiments conducted in Ar-gas – ranged between 1207°C and 1220°C again correlating well with the calculated liquidus temperature of the slag. The balling temperature in CO-gas ranged between 1563°C and 1576°C, significantly higher temperatures than the liquidus temperature of the slag.

One potential explanation for the significantly higher balling temperature could be carbon depositing from the CO-gas [69] according to Equation 29 hindering slag agglomeration. In refractory

materials the presence of Fe / FeO [69] and Mn-bearing spinels [128] acts as catalyst for carbon formation according to Equation 29; it hence seems reasonable to assume that carbon deposition could have occurred on the surface of the slag, which is rich in manganese oxide. It also seems reasonable to assume that such deposited carbon could have hindered slag agglomeration (balling): In mould fluxes (for continuous casting) carbon is added intentionally to control the melting rate by hindering slag agglomeration [129], [130].

Equation 29: Deposition of carbon from CO-gas [69]



To test this idea, the carbon content at the surface of milled industrial slag (not exposed to a CO atmosphere) was compared to that on an industrial slag ball formed on carbon block substrate in the wettability experiment conducted in CO-gas. SEM EDS analysis technique was applied. Area analysis of each sample was conducted at 5kV in triplicate (using the low acceleration voltage to emphasise the K_{α} peak of carbon). For SEM-EDS, the samples were mounted next to each other on a stub and coated with gold (20 – 30nm). To monitor beam stability Si was utilized as quant optimisation element. Examples of EDS spectra are presented in Figure 81, demonstrating a significant increase in the surface carbon content of the slag from the wettability test, and supporting the proposed mechanism by which the CO atmosphere suppressed reaction of slag with, and wetting of, the refractory.

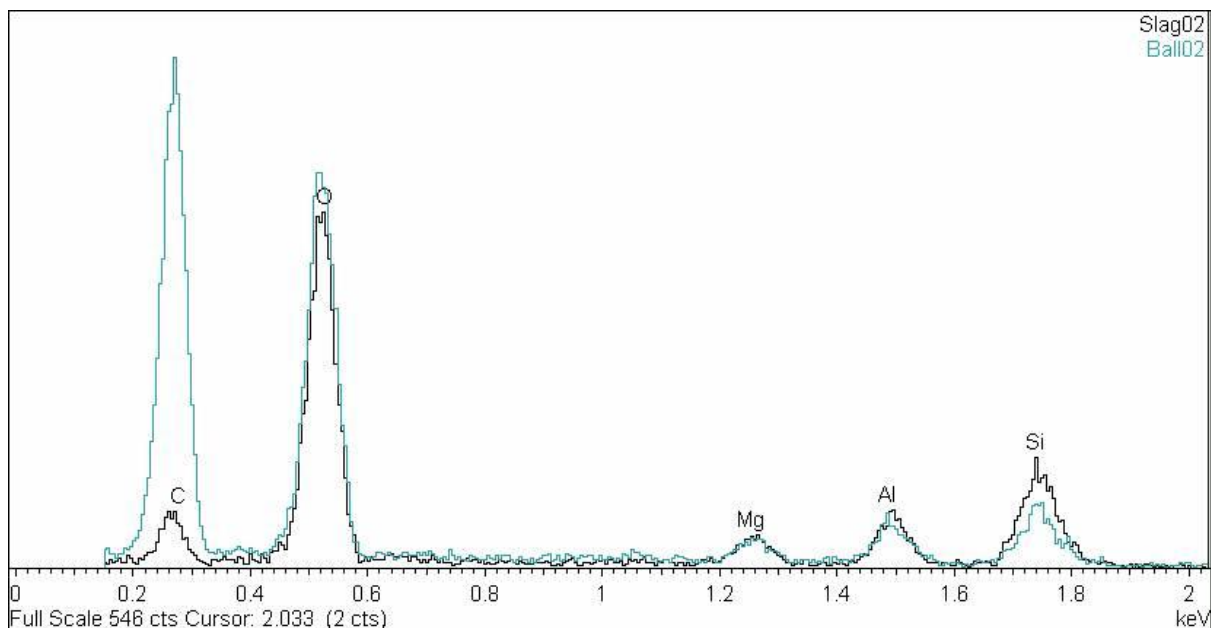


Figure 81: Measured EDS spectra (area analysis at 5kV) of powdered industrial slag (Slag02) and industrial slag ball formed in wettability study performed in CO-gas (Ball02). Note the much larger C peak in the latter case.

Since both infiltration of slag into the refractory and wetting of the refractory by the slag appear to be driven by slag-refractory reaction, it appears reasonable to expect a relationship between infiltration depth and wetting. Ciftja et al [47] found such a relationship when studying the wettability of molten solar grade silicon on different grades of dense graphite; see Figure 82a for data from that study showing the correlation between final wetting angle and infiltration depth. However, in the present study – see Figure 82b – no clear correlation was found: Even with a higher wetting angle than on ramming paste matrix, slag penetrated significantly deeper into the carbon block.

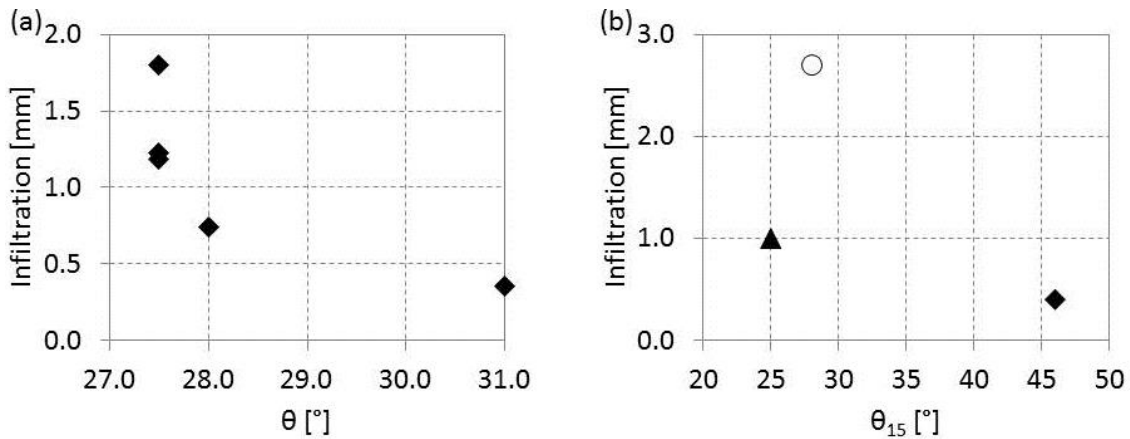


Figure 82: Correlation between wetting angle and maximum infiltration depth as measured by (a) Ciftja et al [47] for molten solar grade silicon on different grades of graphite and (b) for the study presented here for industrial slag on commercial refractories in Ar-gas atmosphere 15 minutes into the holding time at 1588°C. In (b) solid diamond represents ramming paste aggregate, solid triangle represents ramming paste matrix and open circle represents carbon block. For infiltration depths in (b) refer to Table 49 and for wetting angles to Figure 75.

Potential explanations for this behaviour include differences between the different carbon-based refractories with respect to porosity, average pore size and in the amounts of slag taken up by the refractory (as indicated by the decreased change in slag droplet volume).

In Figure 83 possible relationships between maximum infiltration depth and the following variables are tested: (a) percentage total porosity (Table 41), (b) average open equivalent pore size (Figure 54 to Figure 56) and (c) final volume ratio (of the slag droplet). Based on these plots an apparent correlation was found, where the infiltration depth increased with increase in average open equivalent pore size as measured by XRT. Ciftja et al [47] did find a similar correlation for infiltration of solar grade silicon into different grades of graphite (with porosity measured by MIP).

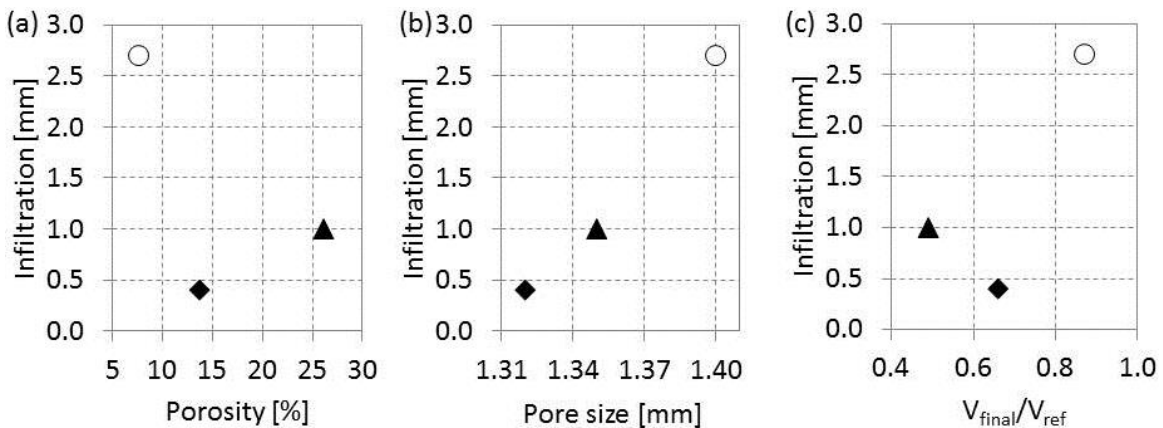


Figure 83: Correlation between maximum infiltration depth - Figure 75 - and (a) total porosity - Table 41 -, (b) average open equivalent pore size - Figure 54 to Figure 56 - and (c) final volume ratio. Solid diamond represents ramming paste aggregate, solid triangle represents ramming paste matrix and open circle represents carbon block. Data presented for wetting angle at 15 minutes into the holding time at 1588°C for industrial slag on commercial refractories in Ar-gas atmosphere.

6.5 Conclusion

The first research question posed was: *When exposing carbon-based refractory material (ramming paste and carbon block) to SiMn slag or metal in the tap-hole, is chemical reaction between refractory and slag or refractory and metal a potential wear mechanism?*

The results of the wettability tests confirm the conclusions in Chapter 3 and Chapter 4: Chemical reaction between carbon-based refractory material and slag (and metal) is possible at tapping temperatures. In the wettability tests reduction of SiO_2 in the slag by carbon in the refractory to form SiC as reaction product was demonstrated, but no evidence was found of the formation of metal.

The second research question posed was: *Is the choice in carbon-based refractory material important from a tap-hole refractory life perspective?*

From a measured wetting angle perspective the choice in refractory material was insignificant with all materials being wetted by slag at the holding temperature. From literature it was expected that the slag would be non-wetting towards the refractory in the absence of chemical reaction, but all experiments conducted in Ar-gas showed wetting. The slag was non-wetting towards all materials in CO-gas. These results support the idea that the chemical reaction between the slag and the refractory is the main origin of wetting, with little effect of differences in the carbon-based refractory material.

From an infiltration (and porosity) perspective the choice in refractory material was significant with carbon block being more deeply infiltrated by slag than ramming paste aggregate or matrix. Deeper infiltration would lead to a larger slag / refractory surface area and therefore more potential for the chemical reactions to occur. Based on this observation, one might expect the carbon block to have a higher wear rate than the ramming paste; this contradicts plant observations.

As wettability studies were conducted on very small samples of slag and refractory components, cup tests were conducted to study slag / refractory interactions. The purpose of these tests was to further investigate the potential for chemical reactions to occur and the potential for slag infiltration in the refractory. Chapter 7 therefore reports on the second of the two types of laboratory-scale experiments: Cup tests.

7 Importance of choice in refractory- Part C (cup tests)

7.1 Introduction

As reported in Chapter 6, wettability tests confirmed that chemical reaction occurs between industrial slag and both ramming paste and carbon block refractories. Results indicated that these chemical reactions are the main origin of wetting, with little effect of differences in the carbon-based refractory material. Results also indicated a possible effect of the type of refractory material on infiltration, with carbon block being infiltrated deeper than ramming paste.

In the wettability tests the sample sizes were very small with slag volume rather than type of refractory material potentially influencing the infiltration results. In order to verify the observations made in the wettability tests, larger scale laboratory cup tests were conducted. These tests utilised larger slag sample sizes which should allow for the study of infiltration without any limitations posed by insufficient slag availability. The tests also allow for the study of wettability between industrial slag and carbon block or ramming paste on a larger scale and further verification of the potential for chemical reaction between slag and refractory.

Chapter 7 reports on the results of these tests. The sourcing, preparation and characterisation of the industrial slag and characterisation of the commercial carbon-based refractory materials applied in the laboratory-scale cup tests were described in Chapter 5. Chapter 7 concludes with a review of the first and second research questions, an introduction to the third research question and an introduction to Chapter 8.

7.2 Method

The cup test experiments were a continuation of work conducted by a Norwegian exchange student at the University of Pretoria in 2011 [116] where it was found that industrial SiMn slag reacted with ramming paste in cup tests conducted in the temperature range 1400 – 1600°C, with evidence found of SiC formation [116]. The earlier experiments [116] had been conducted in a vertical tube furnace. For the experiments presented here, an induction furnace setup was utilised - Figure 84.

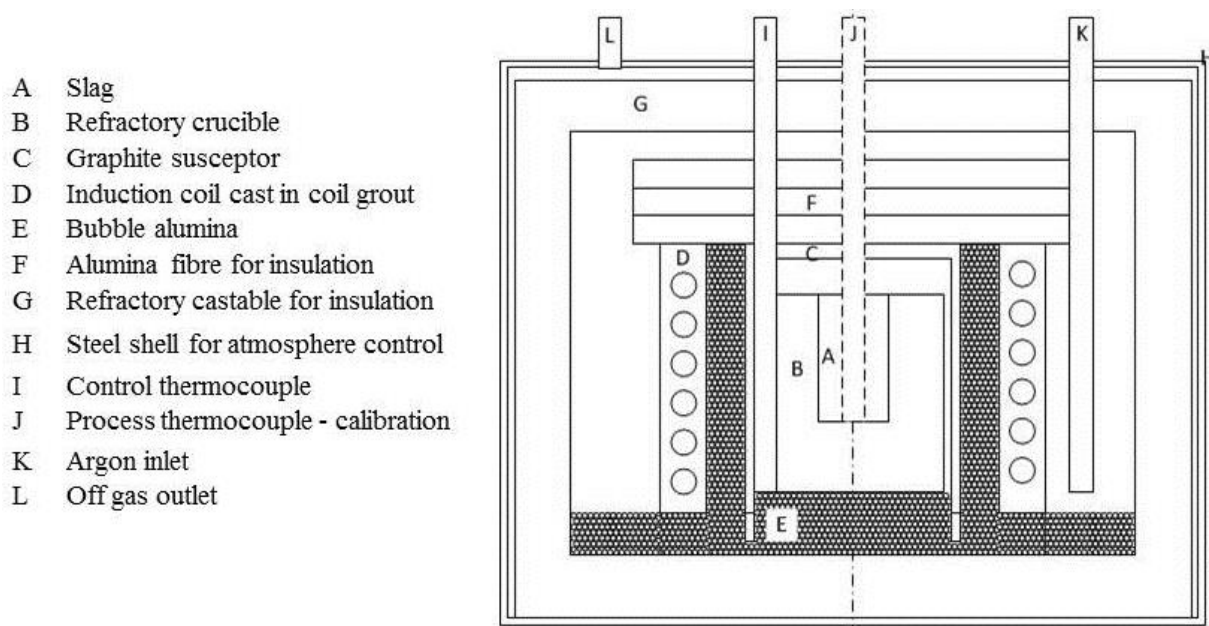


Figure 84: Experimental apparatus utilised in cup tests.

The carbon block was machined into crucibles with OD (outer diameter) 65 mm, ID (inner diameter) 25 mm, EH (external height) 70 mm and IH (internal height) 45 mm – see Figure 85. Cold ramming paste crucibles required an outer shell machined from graphite with OD 65 mm, ID 55 mm, EH 70 mm and IH 60 mm. Ramming paste was rammed by hand around a spacer creating a cavity with ID 25 mm and IH 45 mm. Rammed crucibles were placed in steel cans with a layer of carbon powder, covered with refractory paper and carbon powder, heated in a muffle furnace to 950°C at a rate of 40°C per hour and baked for 30 minutes. The furnace was switched off and cooled to room temperature. The ID of each crucible was measured using callipers.

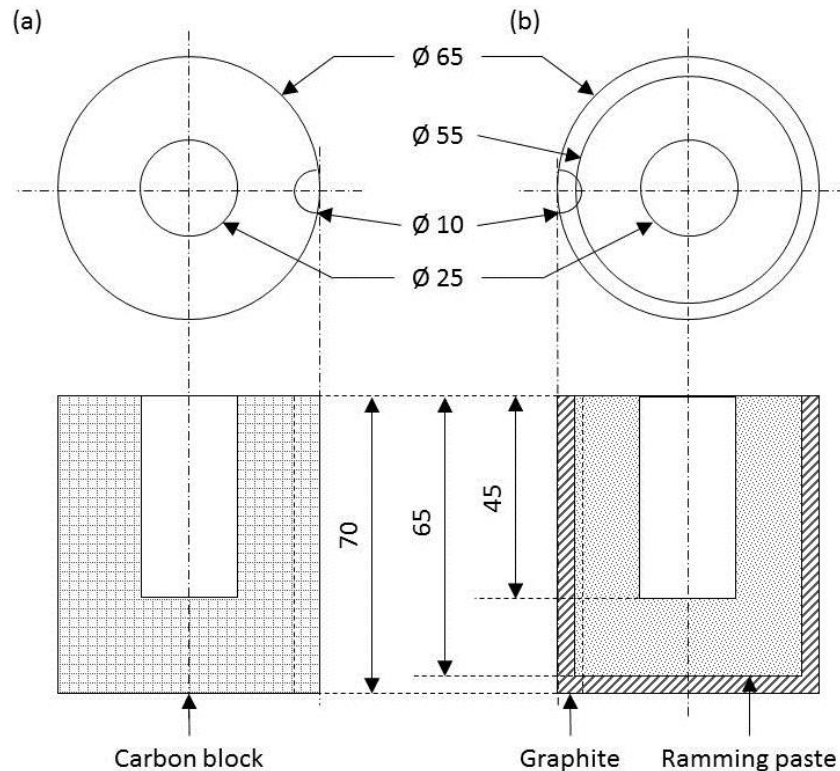


Figure 85: Design of crucibles utilised in cup test experiments with (a) carbon block crucible and (b) ramming paste crucible with graphite shell - all measurements in mm.

A crucible with its cavity filled to the top with slag (40 – 45g) was placed in a high-frequency induction furnace, heated to 1400°C, 1500°C or 1600°C in 1 hour, held at temperature for 4 hours and cooled in the furnace to room temperature. The experiments were conducted in argon which was purified by flowing the argon through a column containing zirconium turnings at 300°C. Once the furnace was sealed, the chamber was flushed with argon at a flow rate of 1.8 l/min for 40 minutes. Once the temperature ramp-up started the argon flow rate was reduced to 0.7 l/min. The chamber volume was 0.074 m³. Argon was added to prevent the graphite crucible from oxidising and act as carrier gas for any CO-rich process gas formed during slag / refractory interaction. The slag / refractory interface studied in the post mortem was not affected by the argon.

Cooled samples were removed from the furnace and filled with resin to keep the process material in position. Once the resin cured, the samples were sliced in half. One half was utilized for sampling and preparation of polished sections and the other for wear profile measurements. After testing in contact with slag (crucible tests), no significant change in the internal diameter of any of the samples could be determined by visual inspection or measurement using the calliper method applied by Mølneås [116]. Both chemical wear and infiltration had to be studied at microscopic level and therefore polished sections were studied by LOM, SEM, FEGSEM and EDS.

7.3 Results

For comparative purposes photographs of the sectioned samples are presented in Table 52.

Table 52: Sectioned cup test samples where (a) industrial SiMn slag was held for 4 hours in cups made of (b) industrial grade ramming paste, rammed into (c) graphite crucibles and then prebaked, or (d) carbon block at three different holding temperatures. To ensure slag remain in place during cutting, cups were filled with (e) resin which was allowed to cure prior to sectioning.

	Ramming paste	Carbon block
1400°C		
1500°C		
1600°C		

Due to the smooth surface finish of the carbon block the wetting angle could be measured in a macro-scale as illustrated in Figure 86.

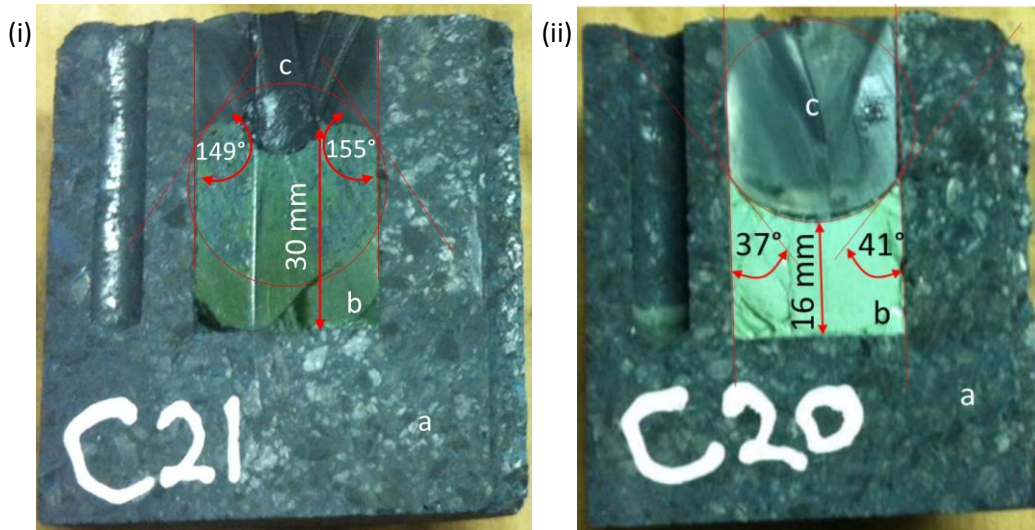


Figure 86: Sectioned (a) carbon block crucible exposed to (b) industrial slag at (i) 1500°C and (ii) 1600°C for 4 hours in an argon atmosphere. The cavity was filled with (c) resin after cooling to keep slag intact during cutting. Wetting angles were measured as described in Chapter 6.

The depth of infiltration in each refractory material, tested at different temperatures, was determined from stitched LOM images, examples of which can be seen in Figure 87 and Figure 88 (i). Results are reported in Table 53. The depth of infiltration was not uniform over the whole slag-crucible contact region (as is evident in Figure 87 and Figure 88) and the results in Table 53 are for the maximum depth observed in the samples analysed. In both materials infiltration occurred mainly in the matrix.

Table 53: Maximum depth of infiltration (mm) of industrial slag into refractory as measured on stitched LOM images.

Temperature	Carbon block	Ramming paste
1600°C	4.0	3.7
1500°C	0.5	0.8
1400°C	-	-

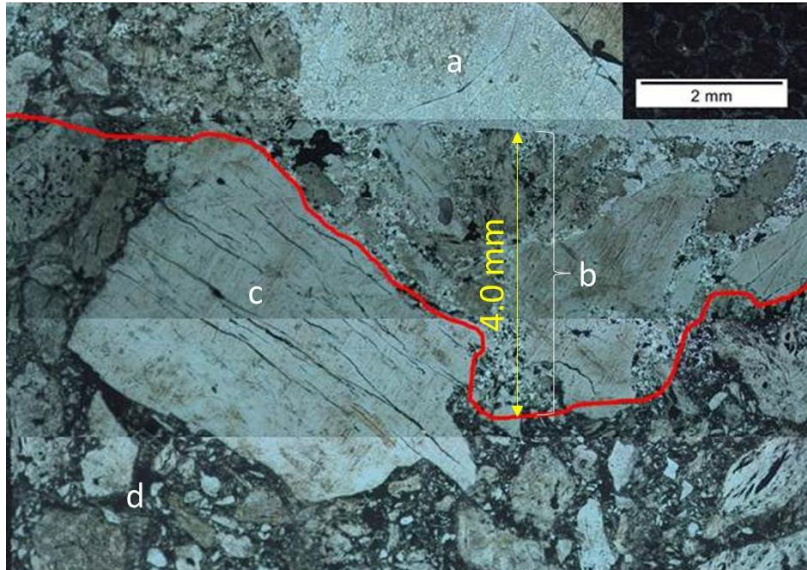


Figure 87: Stitched LOM-image of carbon block reacted with industrial SiMn slag at 1600°C for 4 hours. The red line is the boundary indicating the extent of infiltration of slag into the refractory with (a) slag, (b) reaction zone, (c) aggregate and (d) unreacted refractory. Yellow arrow indicates depth of infiltration. Scale bar indicates 2mm.

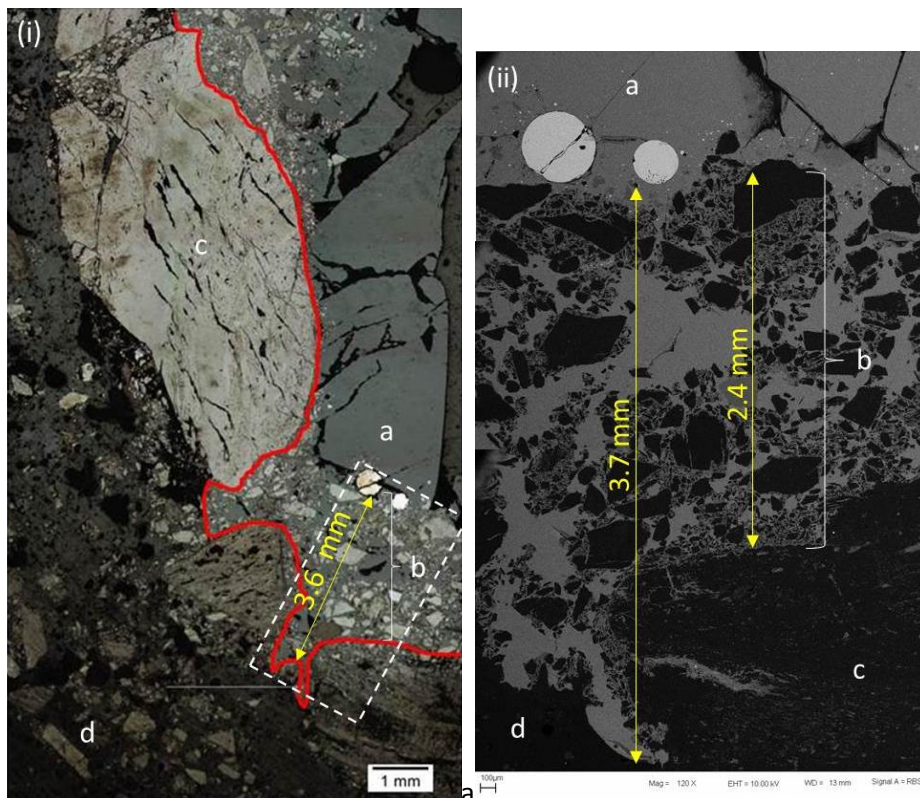


Figure 88: (i) LOM and (ii) SEM BSE image of ramming paste in contact with industrial slag at 1600°C for 4 hours with (a) slag, (b) reaction zone, (c) aggregate and (d) unreacted refractory. Yellow lines indicate depths of infiltration. The position of (ii) is indicated in the rectangle in (i). Scale bars indicate (i) 1mm and (ii) 100 micron.

SEM backscattered electron images of the carbon block exposed to industrial slag at 1600°C are presented in Figure 89 and Figure 90 to illustrate the phase changes that occurred.

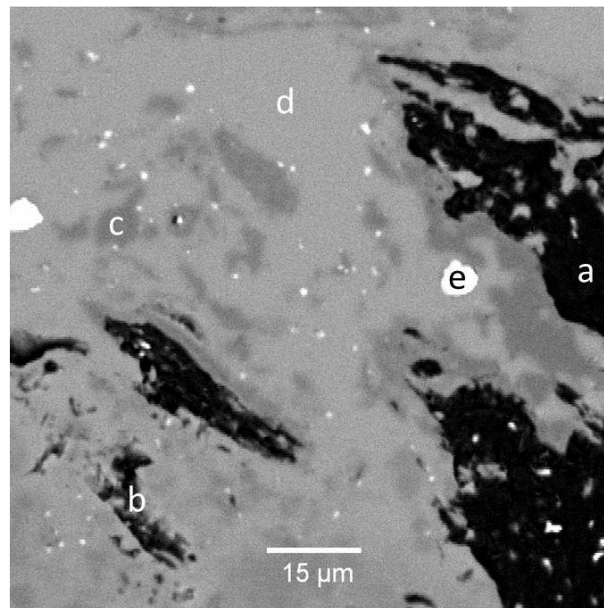


Figure 89: SEM backscattered electron image of slag-refractory interface for carbon block exposed to industrial slag at 1600°C for 4 hours in a crucible test with (a) aggregate, (b) matrix, (c) SiC, (d) slag and (e) metal. Scale bar indicate 15 micron.

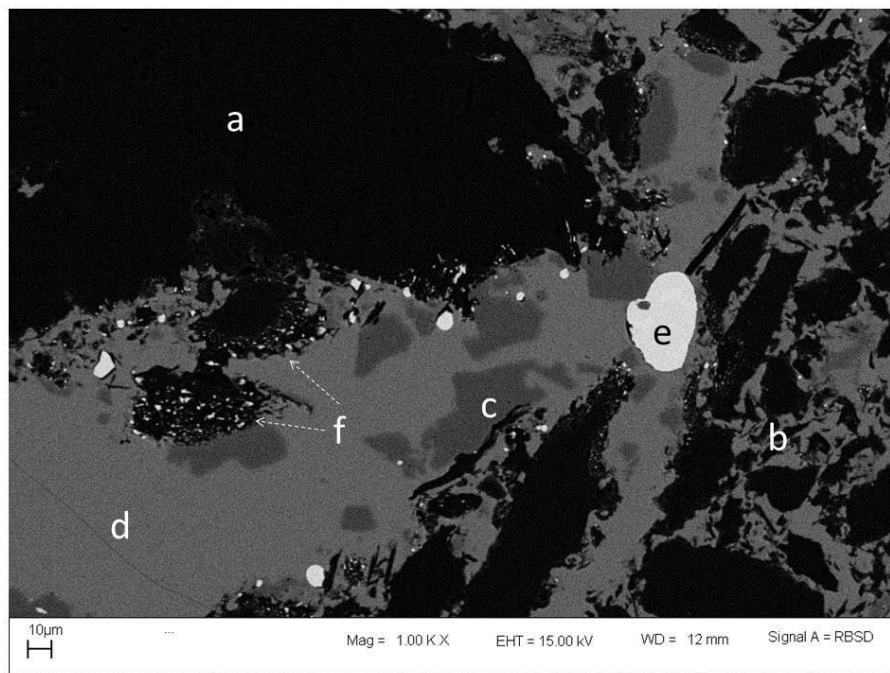


Figure 90: SEM Backscattered electron image of ramming paste exposed to industrial slag at 1600°C for 4 hours in a crucible test with (a) aggregate, (b) remnants of matrix, (c) SiC, (d) slag, (e) metal and (f) reaction zones. Scale bar indicate 10 micron.

As discussed in Chapter 5 the phases identified in the as-received sample were carbon aggregate, carbon matrix, SiC and corundum (Figure 48 and Figure 52). All of these phases remained to some extent after reaction, with the exception of corundum (which dissolved in the slag). In addition,

solidified slag containing metal droplets were present after the cup tests and silicon carbide was evident in the slag near the unreacted aggregate (Figure 89). It is not clear whether these are products of reaction, or simply pre-existing silicon carbide from slag or refractory. Similar features were observed in ramming paste after cup tests (Figure 90) of ramming paste after exposure to industrial slag at 1600°C. As discussed in Chapter 5 the phases identified in the as-received pre-fired ramming paste were carbon aggregate, carbon matrix, moissanite (SiC), quartz, cementite and mullite (Figure 48 and Figure 50). The phases identified in the post-mortem sample were slag, SiC, metal, carbon matrix and carbon aggregate with a distinct reaction zone.

7.4 Discussion

In the cup tests, wetting of both carbon block and ramming paste refractories was observed at 1600°C but not at 1400°C or 1500°C (compare the slag / refractory / gas interface for each experiment in Table 52 to the definitions of wettability in Figure 13a or Figure 14c). Equilibrium calculations (refer Figure 21 and Figure 61) indicate that 1600°C is just above the minimum temperature required for chemical reaction between slag and carbon. This implies that at 1600°C wettability of the refractory by slag will be that of a reactive system and at 1400°C or 1500°C that of a non-reactive system (for definitions of reactive and non-reactive systems see paragraph 2.2.4).

Wetting angles ($\approx 150^\circ$) measured for carbon block exposed to industrial slag for 4 hours at 1500°C in the cup test – Figure 86a – were higher than the 110° reported by Shen et al [63] for slag produced by welding flux on graphite at 1400°C (Table 50 and Table 51), but still non-wetting.

The wetting angles ($\approx 40^\circ$) measured for carbon block exposed to industrial slag for 4 hours at 1600°C in the cup test – Figure 86b – were very similar to the wetting angles ($\approx 50^\circ$) measured after 25 minutes at 1592°C in the wettability tests (Figure 75). The results in Figure 86 therefore support the idea of reactive wetting occurring at 1600°C and non-wetting at 1500°C.

A similar observation can be made from the infiltration results (Table 53): The strong effect of temperature is evident with substantial infiltration only occurring at the highest test temperature (1600°C), with the absence of any obvious effect of material type evident. Observation of significant infiltration at 1600°C hence also supports the suggestion that wettability and therefore infiltration of the refractory by the slag is dependent on chemical reaction between the slag and carbon refractory.

While the depth of infiltration decreased significantly with decrease in temperature, the maximum depth of infiltration at each temperature was similar for the two materials (Table 53). This observation differs from the wettability results where the maximum depth of infiltration in the carbon block was 2.7 times that of the ramming paste (Table 49). The results support the idea that limited slag volume affected the extent of infiltration in the wettability tests.

At 1600°C, for both the carbon block and ramming paste, the depth of infiltration varied significantly across the sample surface both in the wettability tests and the cup tests. However, in both material types it was evident that slag infiltration occurred mainly in the matrix (defined in Figure 41); compare Figure 78 – Figure 80, Figure 87 and Figure 88.

The infiltration of the matrix rather than the aggregate by the slag is probably because most of the porosity is associated with the matrix, with the total porosity of the matrix being 22.2% by volume compared to 17.1% by volume for the aggregate as reported in Table 41 (also compare porosity results for ramming paste aggregate and matrix Figure 54 and Figure 55). More pores will result in a larger surface area available for reaction with slag, resulting in increased wetting, resulting in increased infiltration. The dependence of maximum infiltration at 1600°C on porosity and pore size

for ramming paste and carbon block was demonstrated in Figure 91. Total porosity of ramming paste based on volume average of aggregate and matrix and pore size on weighted average. Mass ratio of 20/80 matrix/aggregate and bulk density of 1.8 g/cm^3 was assumed.

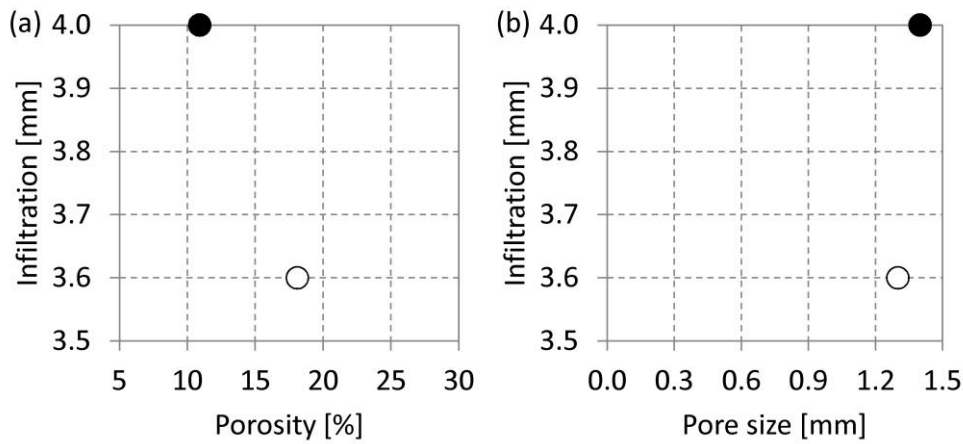


Figure 91: Correlation between maximum infiltration depth - Table 53 - and (a) total porosity - Table 41 - and (b) average open equivalent pore size - Figure 54 to Figure 56. Solid circle represents ramming paste and open circle represents carbon block. Total porosity of ramming paste based on volume average of aggregate and matrix and pore size on weighted average. Mass ratio of 20/80 matrix/aggregate and bulk density of 1.8 g/cm^3 was assumed.

Infiltration of the matrix rather than the aggregate by slag could also be due to differences in wettability caused by differences in chemical reactivity between slag and the carbon present in the matrix or aggregate.

Carbon in ramming paste and carbon block is present both as graphite and as microcrystalline or amorphous carbon as indicated by the widening of the graphite peaks in the XRD patterns for both materials in Figure 92. The size of the graphite crystallites (L_c) derived from these same peaks is significantly larger in carbon block than in ramming paste – see Table 40.

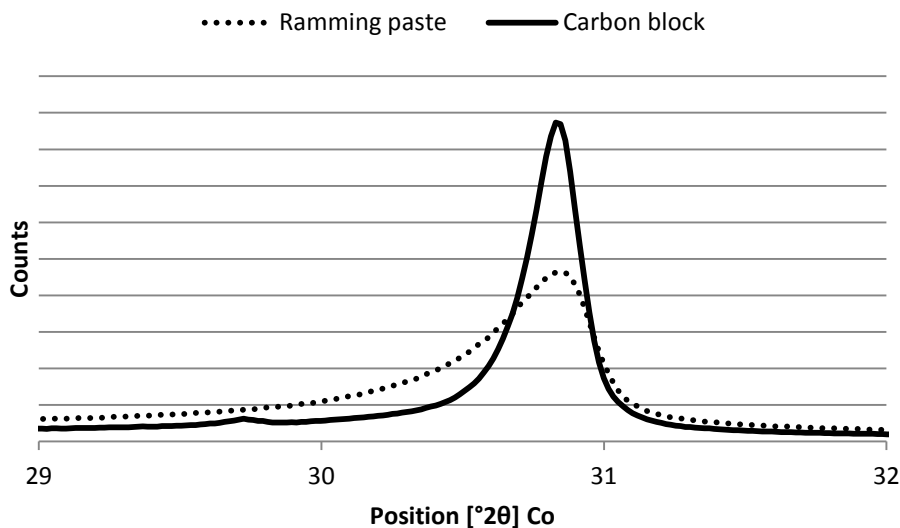


Figure 92: High resolution XRD patterns – derived from Figure 51 and Figure 53 – of the ramming paste and carbon block refractory samples at the graphite peak.

XRD results therefore confirm that carbon is present as both graphite and amorphous carbon in both carbon block and ramming paste and that the graphite crystallites in carbon block are larger than in ramming paste, but does not indicate whether the graphite is present in the aggregate, the matrix or both.

Based on the production methods for carbon block and ramming paste summarised in 2.2.2, the graphite is more likely to be present in the electrically calcined anthracite aggregate than in the binder phase found in the matrix. The carbonisation temperature for carbon block (800 – 1400°C) and baking temperature for ramming paste (950°C) are too low for graphitisation of the carbon present in the binder phase.

SEM backscattered images of both ramming paste (Figure 93) and carbon block (Figure 94) indicate that the binder phase reacted extensively with the slag rather than the carbon aggregate. This is in agreement with observations made in blast furnace ironmaking where alkali and zinc attack the binder phase first [72] and molten iron preferentially dissolves the (coal tar pitch-based) binder phase [78].

First indications therefore are that the slag:refractory reaction would involve preferential reaction of the complex carbon structure rather than the crystalline graphite structure. Follow-up investigation studying the reaction kinetics of the binder phase vs. the aggregate would be useful.

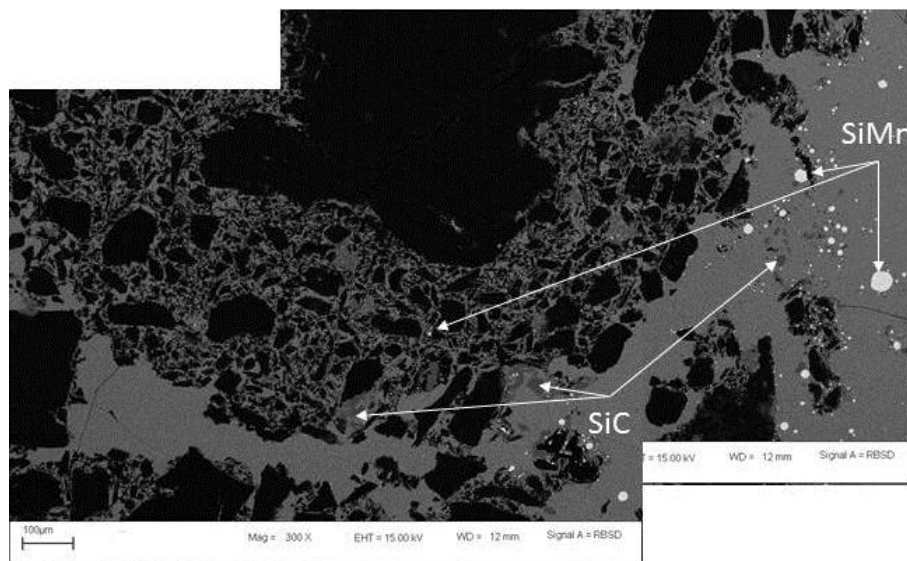


Figure 93: SEM BSE of ramming paste exposed to industrial slag at 1600°C for four hours. Micrographs were taken from the side of the crucible and indicate the presence of both SiC and SiMn reaction products. Scale bar indicate 100 micron.

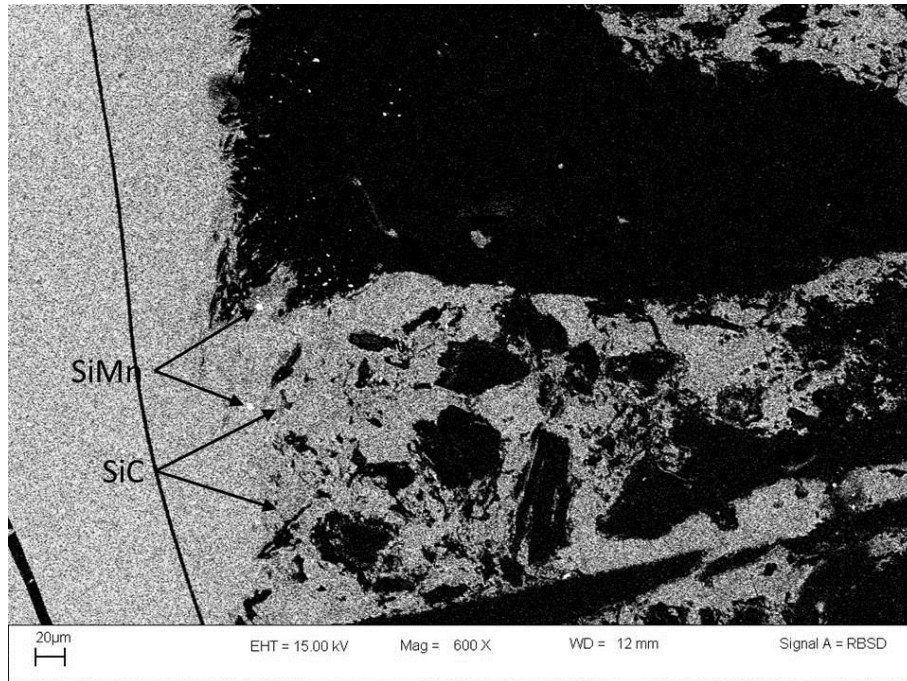


Figure 94: SEM BSE of carbon block exposed to industrial slag at 1600°C for four hours. Scale bar indicate 20 micron.

The discussions above conclude that chemical reaction is an essential requirement for both wettability and infiltration of slag into the refractory. To test whether such reactions occurred, the refractory material exposed to the cup test was studied in detail. Scanning electron microscopy and micro-analysis were utilized to investigate whether reaction products could be detected. A significant complication is that both likely reaction products – silicon carbide and metal – were present in the as-received industrial slags (before contact with the carbon refractories – see Figure 42, Figure 45 and Figure 47), and the ramming paste and carbon block also contained silicon carbide before reaction (Figure 50 and Figure 52 respectively). As the SiC was added to the matrix of the carbon block on purpose (Figure 49) and not to ramming paste [99] the slag:ramming paste sample was studied in detail for evidence of both SiC and SiMn formation.

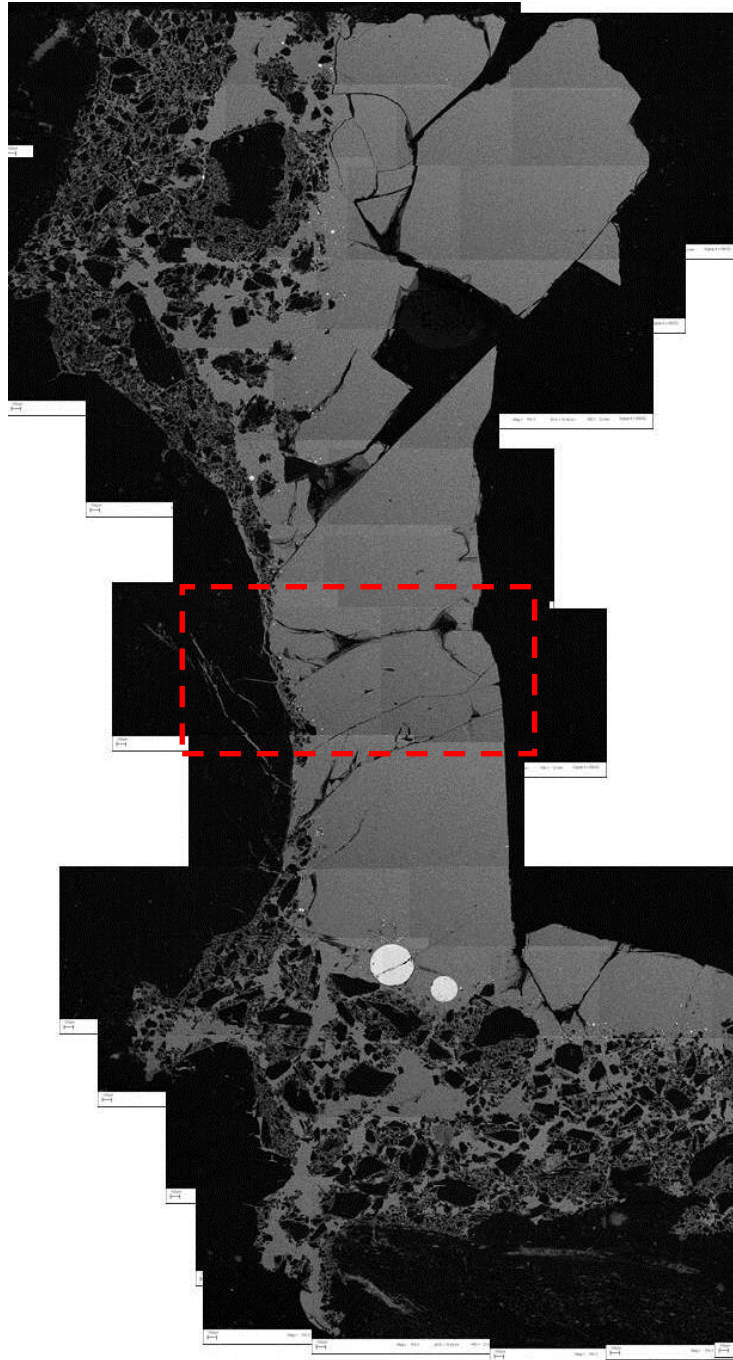


Figure 95: Collage of SEM BSE micrographs indicating the presence of small metal droplets (bright spots), smaller than 25 micron, both on the side of the crucible and at the bottom for the cup test where ramming paste exposed to industrial slag at 1600°C for four hours. The area in the red rectangle in enlarged in Figure 96. Scale bar indicates 100 micron.

After the cup test at 1600°C, metal droplets were evident in the slag close to the ramming paste refractory both on the sides and bottom of the crucible as can be observed in Figure 95. The metal droplet concentration was much higher than in the bulk of the slag – see Figure 96.

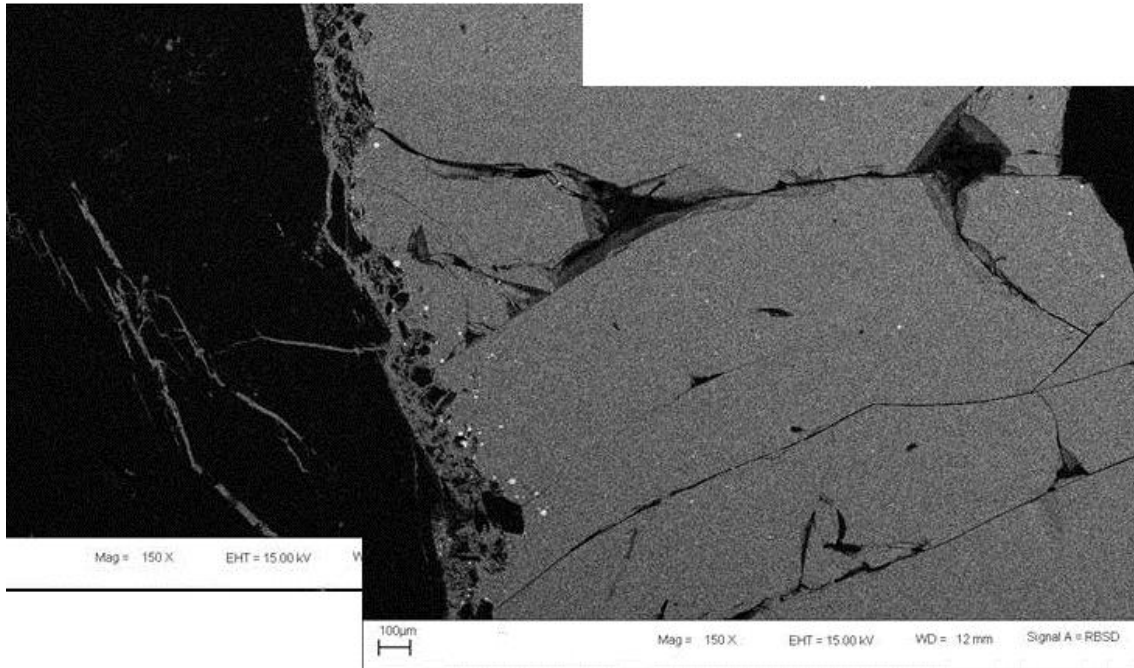


Figure 96: SEM BSE micrographs indicating the presence of small metal droplets (bright spots) concentrated near the ramming paste refractory as opposed to the bulk of the industrial slag on the sidewall of the crucible for the cup test where ramming paste exposed to industrial slag at 1600°C for four hours. Scale bar indicates 100 micron.

After the cup tests at 1600°C, SiC particles were evident in the slag close to the ramming paste refractory both on the sides and bottom of the crucible - Figure 97.

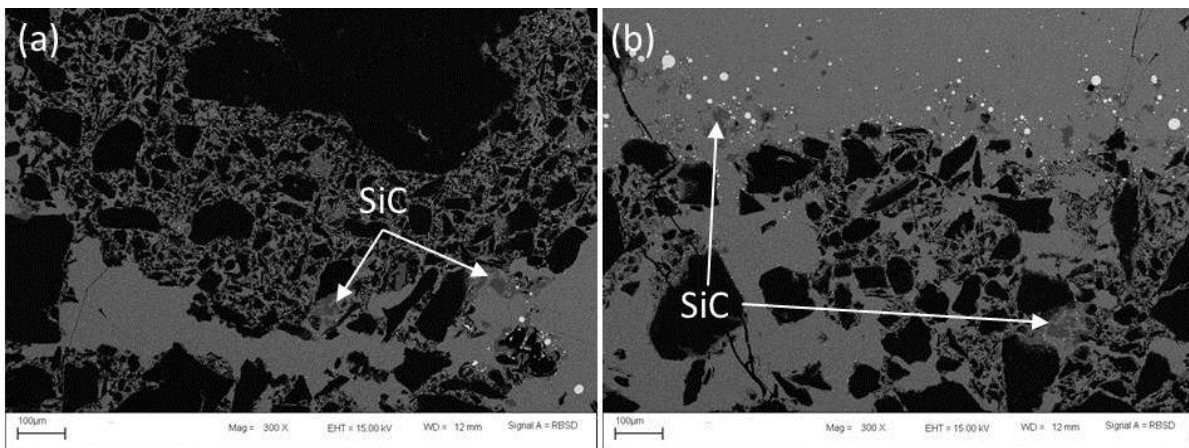


Figure 97: SEM BSE micrographs indicating the presence of SiC (dark grey phase) concentrated in the slag:refractory reaction zone both on the (a) side and at the (b) bottom of the crucible for ramming paste exposed to industrial slag at 1600°C for four hours. Scale bar indicates 100 micron.

In an attempt to test whether the metal droplets at the slag / refractory interface could have originated from the industrial slag or might have formed as reaction product, the metal droplets from the test with ramming paste in contact with industrial slag at 1600°C for 4 hours were studied in more detail: Droplet sizes were estimated by microscopy (size affects droplet settling rate), and compositions were measured by microanalysis (since the Si:Mn ratio of metal formed by slag:refractory reaction is expected to be different from that of the bulk ferroalloy). Converting the chemical composition (percentage by mass) of metal analyses in Table 15 to molar ratios results in a

predicted Si:Mn ratio of 0.58 for the published [1] metal composition, 0.53 for the published [1] metal composition equilibrated at 1600° and 0.44 for metal that formed when reacting published [1] SiMn slag with graphite. Therefore should metal droplets form due to slag:refractory reaction, the Si:Mn molar ratio is expected to be lower than that of metal originating from the tapped slag.

The total depth of the slag in the cup tests was approximately 16 mm (see Figure 86). To compare this depth with the distance that metal droplets could settle in SiMn slag at 1600°C in 4 hours, the terminal velocity was calculated according to the Hadamard-Rybczynski expression [131] in Equation 30 with variables defined (with numerical values) in Table 54. The Hadamard-Rybczynski expression applies to gravitational movement of fluid spheres through another fluid; flow within the fluid sphere changes the flotation (or sinking) rate from that calculated with the Stokes equation (which applies to solid spheres). The Hadamard-Rybczynski expression has been used previously to calculate settling rates of metal or matte droplets, for example in the work of Warczok and Utigard [132].

Equation 30: Hadamard-Rybczynski expression [131]

$$u_T = \frac{gr^2(\rho_{metal} - \rho_{slag})}{3\mu_{slag}}$$

Table 54: Definition of variables applied in Equation 30 and values applied in calculations.

Variable	Description	Unit	Value	Reference
u_T	terminal velocity	m/s	-	-
g	gravity constant	m/s^2	9.81	[50]
r	radius of droplet	m	-	Figure 98 and Figure 99
ρ_{metal}	density of metal	kg/m^3	4412	See estimate in Appendix C
ρ_{slag}	density of slag	kg/m^3	2774	[82] – SiMn Slag A
μ_{slag}	slag viscosity	kg/ms	0.74	[82] – SiMn Slag A

The apparent metal droplet sizes were determined for SEM-EDS micrographs in Figure 98 and Figure 99 using ImageJ [133]. The true droplet diameters are larger than the section sizes (because of the random way in which the polishing plane intersected droplets), but the observed diameters give a first indication of possible droplet sizes.

The terminal velocity (u_T) and settling distance (Δz) for 4 hours were calculated for these droplet diameters ($d_{droplet}$); see Table 55 for the results. From the results in Table 55 all particles with diameters larger than approximately 25 micron would have settled the full depth of the slag (16 mm) during 4 hours, to accumulate at slag / refractory interface at bottom of the crucible.

Table 55: Terminal velocity (u_T) and settling distance after 4 hours (Δz) for different metal droplet diameters ($d_{droplet}$) in slag at 1600°C. Settling distance was derived from terminal velocity estimated with the Hadamard-Rybczynski expression (Equation 30) and variables defined in Table 54.

$d_{droplet}$	micron	1.0	10.0	24.5	287.0	480.0
u_T	m/s	1.8E-09	1.8E-07	1.1E-06	1.5E-04	4.3E-04
Δz	mm	0.027	2.7	16.0	2193	6135

Droplets smaller than 10 microns would only have settled from a fraction of the slag depth. Such small droplets were found both near the bottom of the crucible, and near the crucible wall; see

Figure 95. Figure 95 and Figure 96 indicate that small droplets are much more prevalent close to the crucible wall than in the bulk of the slag, indicating that these formed by chemical reaction.

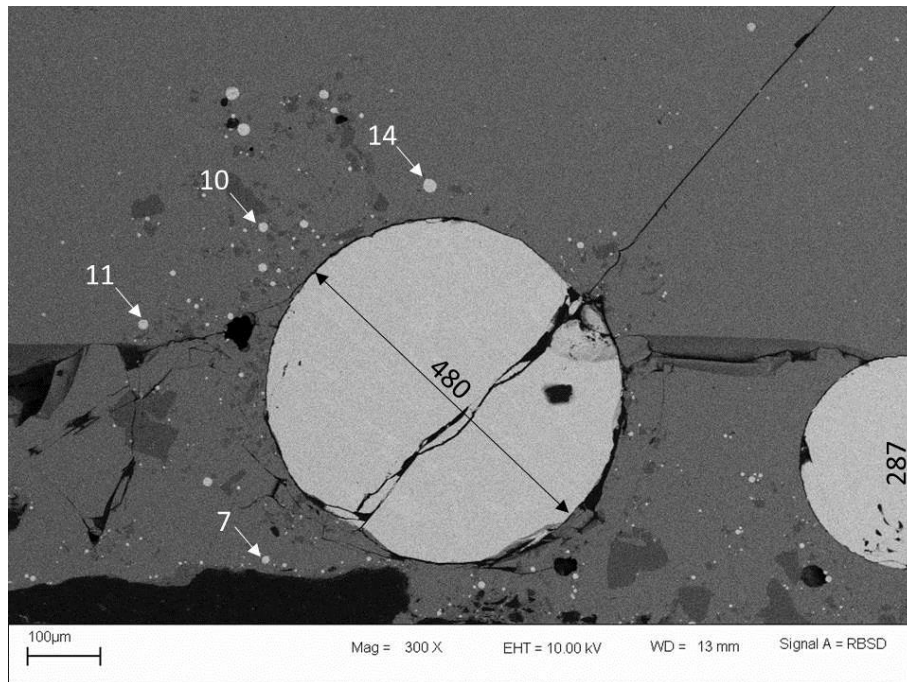


Figure 98: SEM BSE images of ramming paste after contact with industrial slag at 1600°C for 4 hours (region shown is slag near the lower interface with the refractory) indicating diameters of several metal droplets; 300 times magnification. The numbers on the micrograph indicate the apparent metal droplet diameters in micron. Scale bar indicates 100 micron.

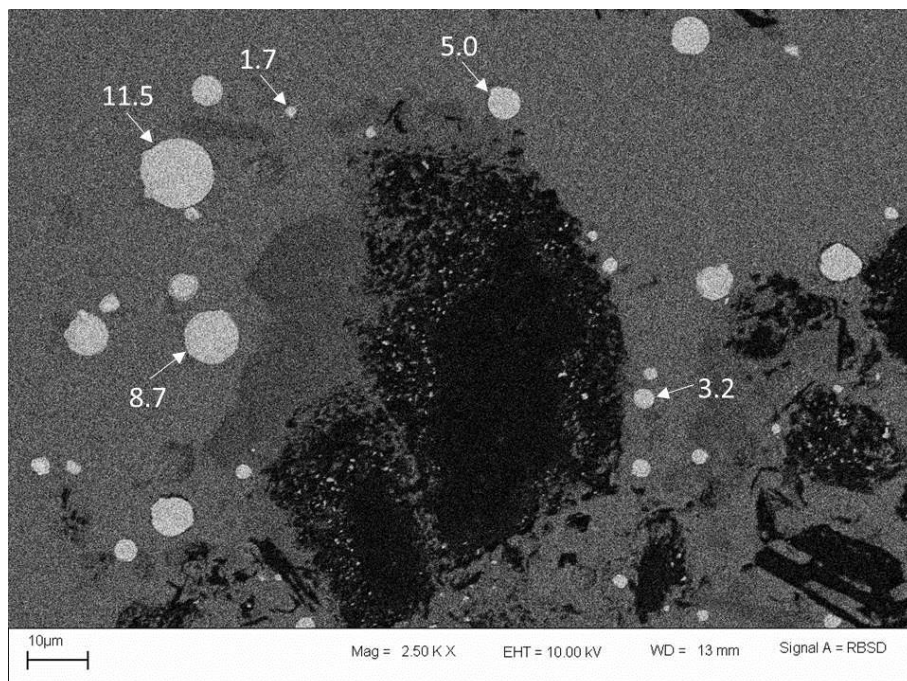


Figure 99: SEM BSE images of ramming paste after contact with industrial slag at 1600°C for 4 hours (region shown is slag near the lower interface with the refractory) indicating diameters of several

metal droplets; 2500 times magnification. The numbers on the micrograph indicate the apparent metal droplet diameters in micron. Scale bar indicates 10 micron.

To quantify the prevalence of metal droplets image analysis was conducted in ImageJ [133] on the micrograph in Figure 100. Two sections were identified: one at the slag:refractory interface (Figure 100a) and the other in the bulk slag (Figure 100b). The percentage area covered by metal droplets in each image was 0.93% and 0.29% respectively, showing that droplets are much more prevalent close to the refractory.

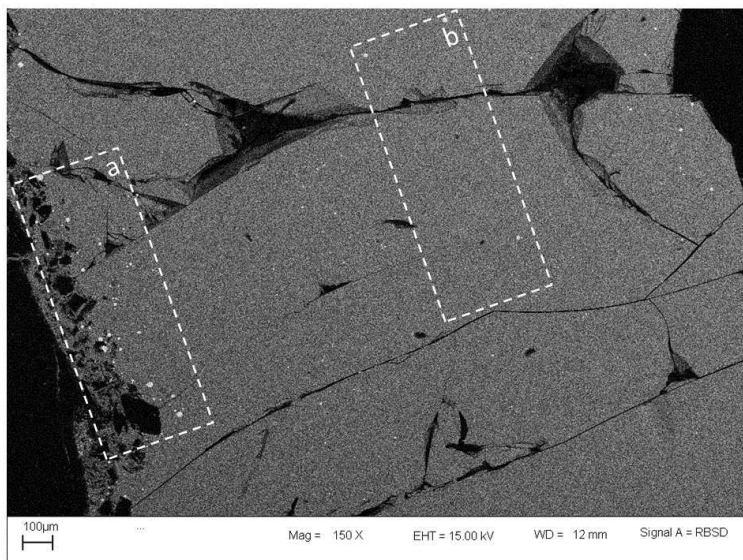


Figure 100: Two sections in the SEM BSE micrograph from Figure 96 indicating the areas on which image analyses were conducted to quantify the presence of small metal droplets (bright spots) (a) concentrated near the refractory as opposed to the (b) bulk of the slag. Scale bar indicates 100 micron.

As mentioned earlier, the elemental analysis of the droplets could also give an indication of whether the droplets formed during the cup tests, or were pre-existing droplets. The Si:Mn molar ratio for metal present in the slag is expected to be 0.58 or 0.53 when equilibrated, and for metal formed during slag:refractory reaction 0.44.

Since the large droplets were likely present before the cup tests, possible trends of composition with size were investigated. Droplets were categorised as (see Figure 101):

1. Large droplets;
2. Droplets in the apparent size range 5 – 10 micron present in the bulk slag;
3. Droplets in the apparent size range 5 – 10 micron near the interface between slag and reaction zone; and
4. Droplets along the rim of an aggregate particle.

Corresponding chemical compositions are reported in Table 56.

The compositions of droplets were determined as point analyses by SEM EDS at 10kV on ten droplets per droplet category (except for the two large droplets a and b). To verify that analyses were not influenced by slag, Ca was utilized as slag indicator. All analyses containing more than 1%Ca were deleted from the dataset where-after the analysis per droplet was normalised and the averages and standard deviations calculated. The average Si:Mn molar ratio was calculated.

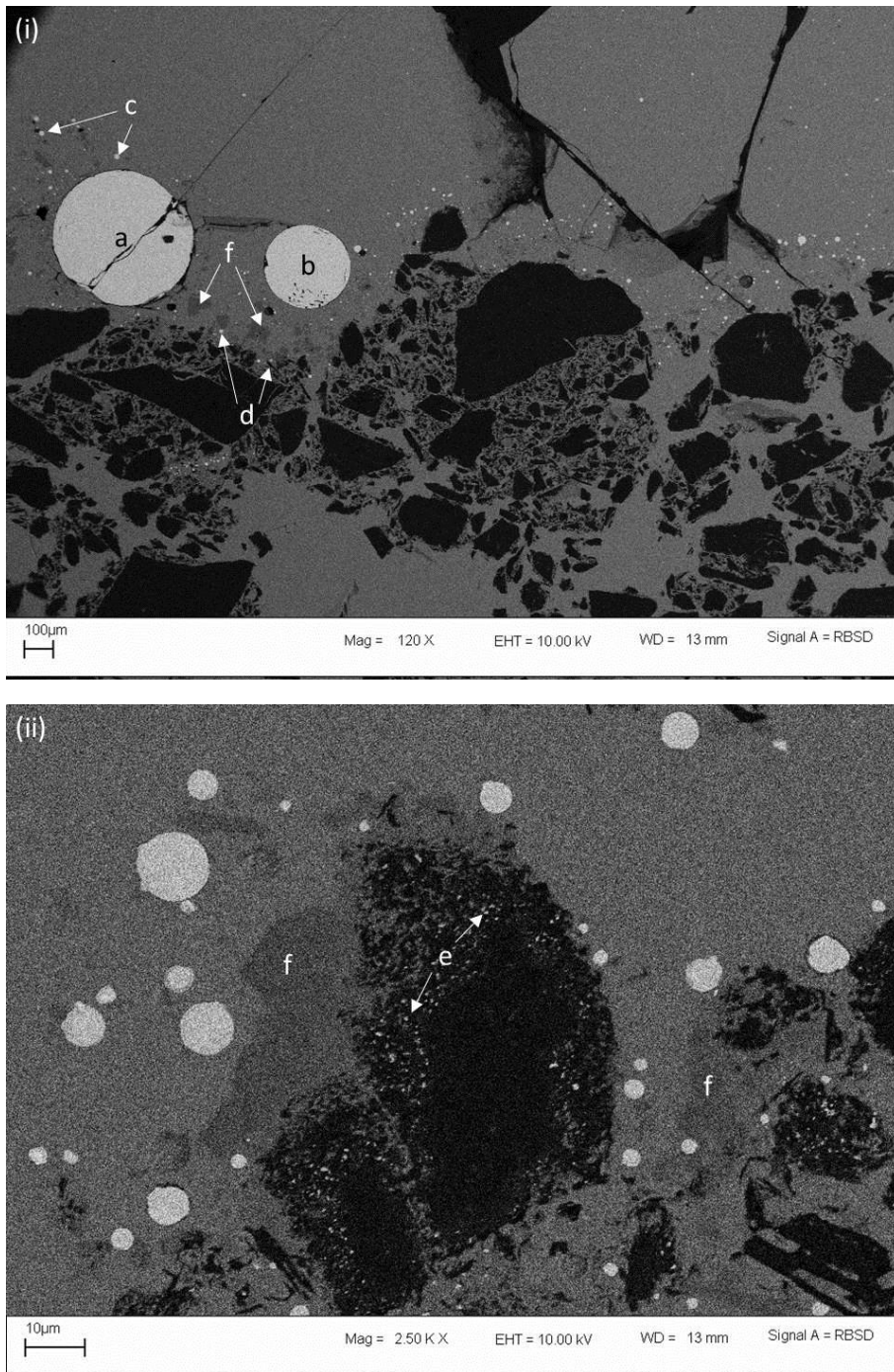


Figure 101: SEM BSE images of for ramming paste after contact with industrial slag at 1600°C for 4 hours, showing metal droplets size categories: (a,b) large, (c) apparent diameter of 5 – 10 micron in slag, (d) apparent diameter of 5 – 10 micron at interface between slag and reaction zone and (e) along rim of aggregate particle. Also indicated is (f) SiC. Scale bars indicate (i) 100 micron and (ii) 10 micron.

Table 56: Composition of metal droplets (percentage by mass; carbon not analyzed) in ramming paste in contact with industrial slag at 1600°C for 4 hours. Types of metal droplet were identified in Figure 101. Composition based on SEM-EDS point analysis conducted at 10 kV on ten droplets each per category except for the two large droplets (a and b). Ca was utilized as slag-indicator and all analysis containing more than 1%Ca were deleted from dataset. Analysis per droplet (percentage by mass) was normalised and the averages and standard deviations calculated. Normalised composition per droplet was converted to number of moles in 100g and Si:Mn ratio calculated. Average and 95% confidence limits of Si:Mn ratio per droplet category were calculated.

Category		Average				Standard deviation			Si:Mn molar ratio (average, with 95% confidence limits)
		%Si	%Mn	%Fe	%Total	%Si	%Mn	%Fe	
a	Large	21.8	71.8	6.4	100.0	-	-	-	0.59
b	Large	14.7	76.6	8.7	100.0	-	-	-	0.38
c	5 – 10 micron in slag	19.4	76.6	4.0	100.0	4.4	6.7	2.7	0.51±0.29
d	5 – 10 micron at interface between slag and reaction zone	17.3	79.2	3.5	100.0	5.9	8.3	3.0	0.44±0.38
e	Rim of aggregate particle	34.7	61.3	4.0	100.0	14.9	13.6	7.2	1.23±1.50

The metal droplets analysed along the rim of an aggregate particle appeared to have a higher Si content (but similar Mn:Fe ratios), but with a wide confidence interval. The higher Si-content could either be attributed to the presence of reduced Si in the metal or due to SiC being analysed with the metal droplet. Because the droplets along the aggregate particles were so small (apparent size estimated as < 0.2 micron from micrograph in Figure 99), the electron interaction volume could have extended beyond the metal to adjacent phases (such as silicon carbide).

To test this possibility, the depth of the X-ray range was calculated as 0.145 micron applying the Anderson-Hasler expression (see Equation 31; variables defined in Table 57). It is therefore possible to include Si from SiC present in the rim when analysing metal droplets formed in the rim.

Equation 31: Anderson-Hasler expression [134]

$$R_x = \frac{0.064}{\rho} (E_0^{1.68} - E_c^{1.68})$$

Table 57: Definition of variables applied in Equation 31 and values applied in calculations.

Variable	Description	Unit	Value	Reference
R_x	Depth of X-ray production	μm	-	-
E_0	Instantaneous beam energy	kV	10	-
E_c	Critical ionization energy of the shell (a function of the element analysed)	kV	0	Will calculate maximum depth
ρ	density of metal	g/cm^3	4.4	See estimate in Appendix B

The results Table 56 show that the Si:Mn ratio of the largest metal droplet and the average of those in the slag approached the Si:Mn ratio for tapped metal; the average Si:Mn ratio of the second largest metal droplet and those at the slag:refractory interface approximated the predicted Si:Mn ratio for metal formed during slag:refractory reaction. However, the uncertainty in the ratios is too large for any conclusion about the provenance of the droplets based on their composition.

7.5 Conclusion

The first research question posed was: *When exposing carbon-based refractory material (ramming paste and carbon block) to SiMn slag or metal in the tap-hole, is chemical reaction between refractory and slag or refractory and metal a potential wear mechanism?*

The results of the cup tests confirmed that chemical reaction between carbon-based refractory material and slag (and metal) was possible at tapping temperatures derived through wettability and infiltration results which pointed to the need for chemical reaction to explain observations and study of reaction products found. As for the experiments conducted in Chapter 4 and Chapter 6 evidence was found for the reduction of SiO_2 in the slag by carbon in the refractory to form SiC. Evidence of the reduction of SiO_2 and MnO by refractory to form SiMn was also found.

The second research question posed was: *Is the choice in carbon-based refractory material important from a tap-hole refractory life perspective?*

The results of the cup tests did not agree with the observation made in the wettability tests – Chapter 6 – that the choice in refractory material might influence the extent of infiltration of slag into the refractory material. In the cup tests, where the slag volume did not limit the extent of infiltration, the extent of infiltration was the same for carbon block and ramming paste. As with the

wettability tests infiltration of slag occurred in the matrix rather than the aggregate in both the carbon block and the ramming paste samples. The wetting angles for slag on carbon block at a larger scale were similar to the angles measured in the small-scale wettability tests.

From the perspective of chemical wear and infiltration, the choice of carbon-based refractory material – whether ramming paste or carbon block – is not important: the carbon in both materials reacted with slag to form reaction products and slag infiltrated both materials to the same extent. The differences in refractory life observed on the plant should therefore be attributed to other wear mechanisms.

In Chapter 8 the third and final research question will be addressed: *What are the implications for the life of the tap-hole in a SiMn furnace?* The question will be answered along the lines of a digout of an industrial scale SiMn furnace.

8 Implications for the life of the tap-hole in a SiMn furnace

8.1 Introduction

In Chapter 3 and Chapter 4, and Chapter 6 and Chapter 7, the potential for chemical reaction between refractory and slag or refractory and metal as wear mechanism in the tap-hole was demonstrated through thermodynamic modelling and laboratory-scale experiments. Evidence was found of the formation of both SiC and SiMn as reaction products.

From the wettability results obtained in Chapter 6 the choice in refractory materials seemed to be significant in terms of infiltration but not in terms of wettability or chemical reaction. In the larger-scale cup tests, conducted in Chapter 7, no difference between the materials in terms of infiltration could be identified either.

To address the third research question – *what are the implications for the life of the tap-hole in a SiMn furnace?* – the tap-hole wear profile of an industrial scale furnace was studied during excavation. As part of the introduction to Chapter 8 the lining design and life cycle and expected wear profile will be discussed. Chapter 8 reports on observations made during the excavation and thermodynamic calculations to improve the understanding of the wear profile observed. Chapter 8 concludes with an introduction to Chapter 9.

8.2 Background

The SiMn furnace under investigation had a power rating of 48 MVA and was excavated in April 2013 after being in operation for 10 years. Gous et al [14] reported on the methodology followed and main observations made during the excavations. The purpose of the study presented here was to report on the tap-hole wear profile in more detail and to report on a thermodynamic study conducted to understand the potential for chemical reaction as wear mechanism in the tap-hole area.

The SAF was of circular design with an open roof and outer diameter of 12 m. The furnace containment system consisted of a refractory lining installed in a steel shell. The refractory design from the hearth to the top of the sidewall is indicated in Figure 102. The compositions of the refractory materials of interest are presented in Table 58.

In the hearth, fireclay (an aluminosilicate aggregate with alumina cement binder) was cast onto the steel shell to level the floor. Five layers of super-duty fireclay bricks were installed as back lining, with high-grade carbon ramming as working lining. In the lower sidewall, a single layer of super-duty fireclay brick was installed as back lining with high-grade carbon ramming as working lining. As safety lining, a low-grade carbon ramming was emplaced between the steel shell and the back lining. In the upper sidewall, the lining design was similar to the lower sidewall but with the super-duty fireclay brick layer forming both the working lining and the back lining, i.e. no high-grade carbon ramming installed. The two, single-level tap-holes were built with SiC bricks supported by super-duty fireclay bricks.

The original lining was installed in April 2003. In September 2007 the refractory was partially demolished and rebuilt, including both tap-holes. Tap-hole A was partially repaired in March 2012 (the front two rows of SiC carbide bricks were replaced), but no repairs were done on tap-hole B. Finally, the complete lining was demolished and rebuilt in April 2013. From the time of the partial reline in September 2007, 7520 taps were made through tap-hole A and 1880 through tap-hole B. During the final excavation, tap-hole B was studied in detail.

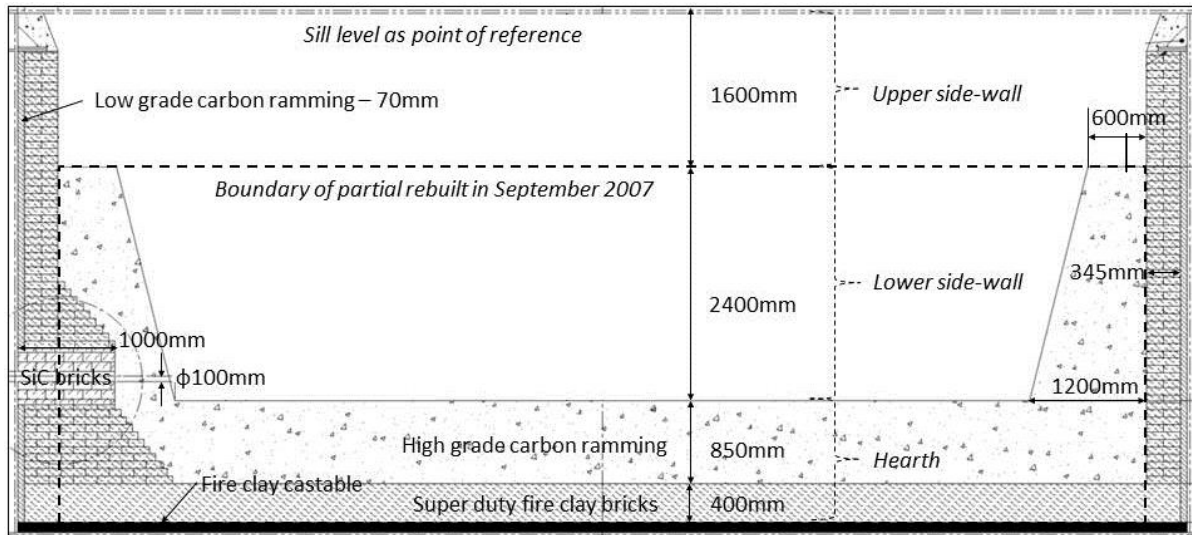


Figure 102: SiMn lining design – drawing to scale.

Table 58: Composition and thermal conductivity of refractory materials as obtained from supplier datasheets except where indicated differently.

Material	Raw materials	Thermal conductivity	Composition (weight %)						
			SiO ₂	Al ₂ O ₃	Fe ₂ O ₃	TiO ₂	CaO	MgO	Alks
Fireclay – brick	-	1.2 W/mK at 1000°C	53.6	42.0	1.5	1.6	0.15	0.3	0.85
			Al ₂ O ₃	Anthracite	Clay	Graphite	Resin	Tar	
Carbon ramming – high-grade	Carbon	11 W/mK at 1000°C	1-5	50-70	1-5	15-25	6-12	2-7	
			SiC	Si ₃ N ₄	Fe ₂ O ₃	Al ₂ O ₃	CaO		
SiC – brick	Silicon carbide (nitride-bonded)	15-20 W/mK at 1200°C [135]	75	23.4	0.3	0.3	0.2		
			Al ₂ O ₃	SiO ₂	TiO ₂	Fe ₂ O ₃			
Tap-hole clay	Silica and alumina (resin-bonded)	1.3 W/mK at 1000°C	19	79	0.5	0.8			

Owing to the single-level tap-hole design, slag and metal were tapped simultaneously at three-hour intervals. Tapping duration varied between 30 and 45 minutes. The tap-hole was typically opened with a drill and closed with a mudgun pushing clay into the tap-hole – see Table 58 for the clay composition. In cases where problems were experienced with keeping the tap-hole open, oxygen lancing was applied.

High steel shell temperatures (above 300°C and below 480°C) measured at the tap-hole area using thermal imaging techniques (Figure 103) were the major factor leading to the switch-out of the furnace for a total reline.

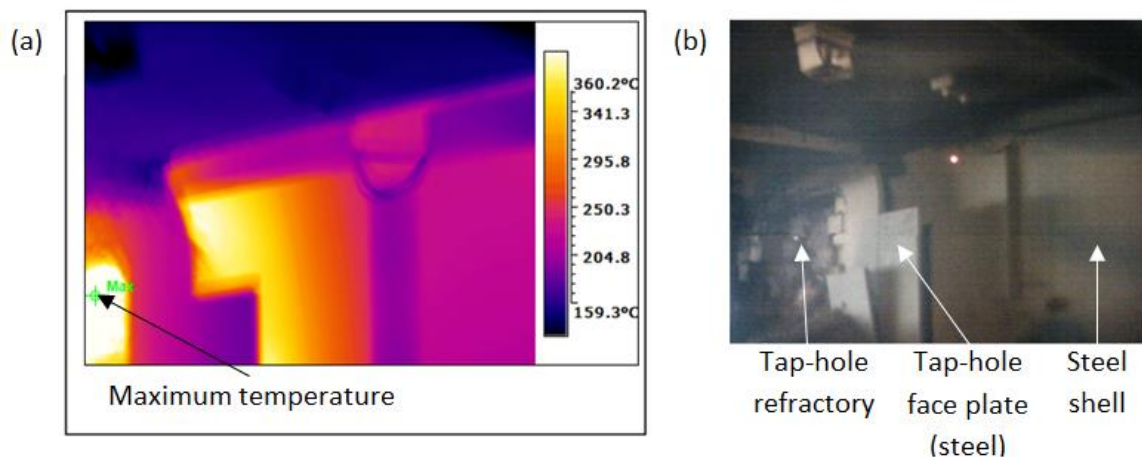


Figure 103: Tap-hole area of SiMn furnace with (a) thermal image and (b) visible-light photograph of section of steel shell on which thermal image was based. The maximum temperature of 480°C (indicated) was measured at the tap-hole itself.

A typical tap size was 22 t of alloy and 17.6 t of slag. The tapping temperatures, as measured at the tap-hole, varied between 1420 and 1520°C. Slag and metal were sampled at each tap. The slag sample was taken with a metal rod in the launder and the metal sample in the metal ladle with 'lollipop-sample dipstick'. Slag and metal compositions were determined by powdered X-ray fluorescence (XRF) analysis. Carbon content of metal samples was determined by combustion analysis (LECO).

For the purpose of thermodynamic and kinetic calculations, the chemical compositions of slag and metal were normalized per tap for the six-component slag system (MnO, SiO₂, MgO, CaO, FeO, and Al₂O₃) and four-component metal system (Mn, C, Si, and Fe). The average and standard deviation of the normalized results calculated for a 4-month period (November 2012 to February 2013) are reported in Table 59 and Table 60. To correct the slag composition for entrained metal, it was assumed that all FeO in the slag was associated with entrained metal droplets with average composition shown in Table 60. Mass balance calculations were conducted to correct the slag composition for FeO, SiO₂, and MnO, as reported in Table 59.

Since the formation of SiC as a product of the reaction between slag or metal and carbon-based refractory material at tapping temperatures was demonstrated in laboratory-scale studies [116], [136] and the reported tapping temperatures of 1420 to 1520°C were significantly lower than the tapping temperatures reported for SiMn elsewhere [1], it was expected that SiC tap-blocks would not show any significant chemical wear when placed in contact with SiMn metal or slag (however, see the note later in this chapter regarding the likely difference between the measured tapping temperatures and the actual temperature inside the furnace).

Another aspect contributing to the expected reduced wear of the tap-hole was the use of reconstructive tap-hole clay (Table 58). The purpose of reconstructive tap-hole clay is not only to plug the tap-hole at the end of the tap, but also to reconstruct the sidewall by forming a 'mushroom' of clay protecting the sidewall from slag and metal wear [24], [27]–[29]. Evidence of a mushroom in the furnace was therefore expected.

Oxygen lancing was frequently applied in opening the tap-hole or to keep it open, potentially contributing to increased wear of the tap-hole.

The condition of the tap-hole area was therefore of keen interest to the team involved in the investigation.

Table 59: Average and standard deviation of as-received slag analyses and slag composition corrected for metal inclusions.

	MnO	SiO ₂	MgO	CaO	FeO	Al ₂ O ₃	Total
Average (as-received)	13.3	46.0	6.0	25.3	0.5	5.9	97.0
Average (normalised)	13.7	47.4	6.2	26.1	0.5	6.1	100.0
Standard deviation	1.8	0.8	0.4	1.0	0.3	0.7	-
Corrected	11.9	48.3	6.4	27.1	0.0	6.3	-

Table 60: As-received metal composition.

	Mn	C	Si	Fe	Total	Mn:Fe
Average (as-received)	66.2	1.8	17.0	14.8	99.8	
Average (normalised)	66.3	1.8	17.1	14.8	100.0	4.6
Standard deviation	0.5	0.2	0.8	0.6	-	

8.3 Method

The top 2 m of the burden below sill level was dug out from the top of the furnace by manual labour. Thereafter the furnace was dug out from the side, excavating a circular sector of 120° between electrode 3 and electrode 1 (Gous *et al.*, 2014). The centreline of electrode 1 was positioned in the middle of the centrelines of tap-hole A and tap-hole B which were positioned 60° apart. For the macro-scale investigation, photographs were taken of the refractory *in-situ*, using a CANON EOS 30D camera installed on a tripod and triggered by remote trigger. The camera settings for aperture and shutter speed were adjusted manually based on the light meter readings on the camera. Lighting was provided by free-standing floodlights, and no flash was utilized. The refractory thickness was measured with a tape measure and / or laser measurement device. The original design drawing was marked up with the measured wear profile (Figure 104). For more details on the methodology followed during the excavation the reader is referred to the paper by Gous *et al.* [14].

8.4 Results

In Figure 104 the dimensions of the worn lining are superimposed onto the refractory design drawing presented in Figure 102. The dimensions of the red-line drawing were obtained on a vertical plane passing through the centre of the tap-hole.

As can be seen in Figure 104 and the series of photographs in Figure 105 to Figure 110, wear of the tap-hole area was extensive. As indicated in Figure 104, more than 50% of the SiC brick was worn away, with most of the wear occurring at the hot face of the sidewall. Wear of the SiC brick was more extensive above the tap-hole than below. Furthermore, the carbon ramming above the SiC brick was worn all the way to the top of the carbon. In plan view (not indicated), the wear pattern was in the form of a channel 500 mm wide, with fairly straight sidewalls rather than funnel-shaped as is typical of the wear pattern in open bath furnaces. The SiC brick and the carbon ramming paste in the hearth in front of the tap-hole were worn away both below and above the tap-hole.

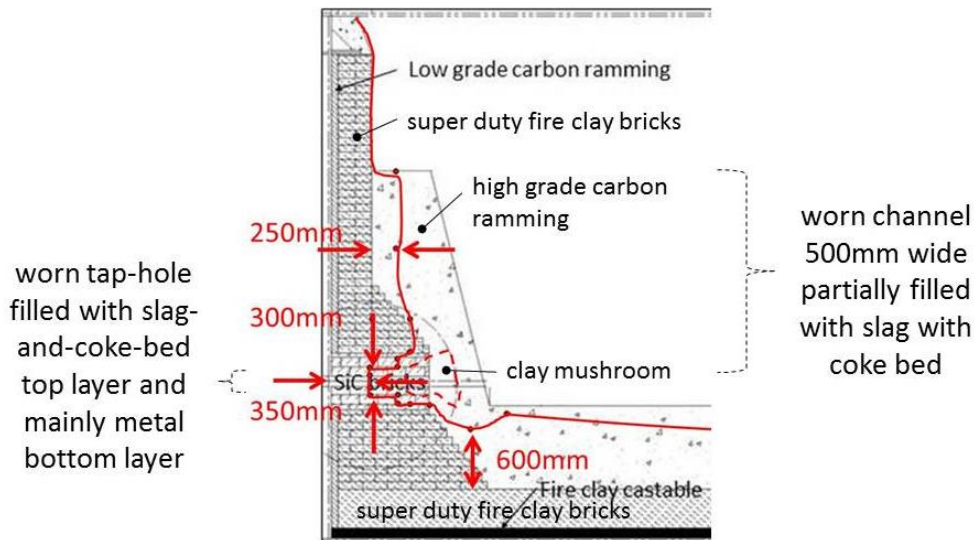


Figure 104: Refractory design drawing with red line indicating the refractory hot face as determined during excavation – drawing to scale.

Figure 105 shows a side view of the tap-hole region (compare Figure 104) with the high-grade carbon ramming and SiC tap-hole extension (c) removed on the left-hand side exposing the super-duty fireclay brick installed as back lining (a). On the right-hand side, the high-grade carbon ramming (b) was left intact. The 500 mm wide slot worn into the high-grade carbon ramming and SiC all the way from the tap-hole to the top of the ramming crucible is clearly visible (d). The slot was partially filled with a slag / burden layer (d) that extended into the upper part of the worn tap-hole. The lower part of the tap-hole was filled with mixed material containing metal (e). A clay mushroom, which formed when clay forced through the tap-hole spread radially when coming in contact with burden, was observed (f). Instead of the clay rebuilding the tap-hole by forming a new interface between the refractory and slag / metal, the slag and metal channelled around the clay mushroom before exiting the furnace through the worn tap-hole. Note that the mushroom was not in contact with the tap-hole, as would be expected of a reconstructive tap-hole clay [24], [27]–[29].

Figure 106 and Figure 107 show the tap-hole area in close-up, making it easier to distinguish the different zones, comprising super-duty fire-clay brick back lining (a), high-grade carbon ramming crucible (b), SiC bricks utilized to build the tap-hole (c), slag with burden and / or coke bed material present either in the worn channel (vertical section or upper (d)) or in the worn tap-hole (horizontal section or lower (d)), mixed material containing metal (e), and tap-hole clay mushroom (f).

Figure 108 and Figure 109 show the interior of the tap-hole, illustrating the extent to which the SiC brick in the tap-hole has worn away.

Figure 110 shows the tap-hole in perspective, with operating personnel standing on the steel shell / fireclay castable of the furnace hearth. This photograph was taken at the stage of furnace excavation as the photograph in Figure 109.

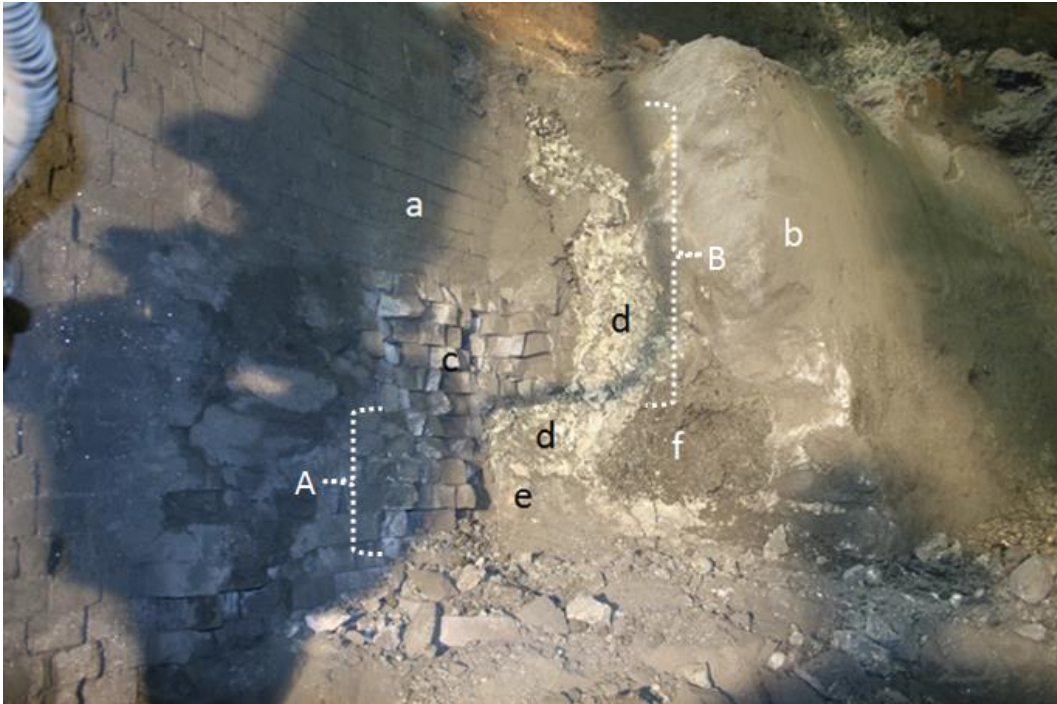


Figure 105: View of tap-hole region with (a) super duty fire-clay bricks, (b) high grade carbon ramming, (c) SiC bricks, (d) slag with burden and / or coke bed material, (e) mixed material containing metal and (f) tap clay mushroom. (A) indicates the worn tap-hole filled with a slag-and-coked bed top layer and (mainly metal bottom layer and (B) the worn channel 500 wide and partially filled with slag with coke bed. The tap-hole (Figure 109) is to the left of (e) and lower (d).

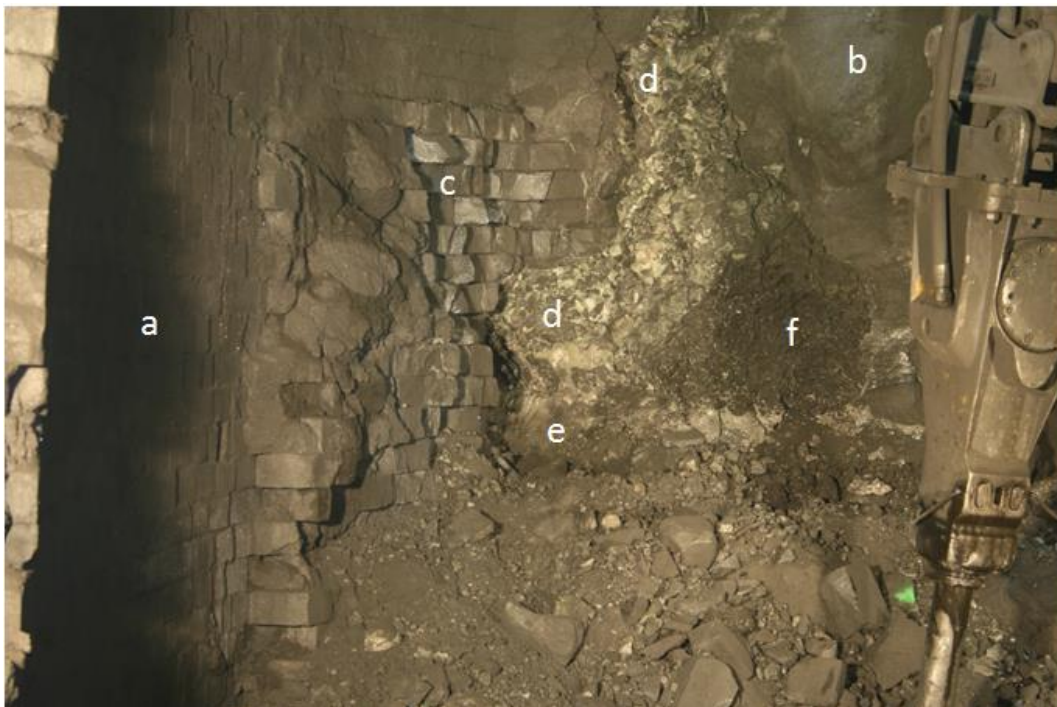


Figure 106: Closer view of tap-hole B with (a) super duty fire-clay bricks, (b) high grade carbon ramming, (c) SiC bricks, (d) slag with burden and / or coke bed material, (e) mixed material containing metal and (f) tap clay mushroom.

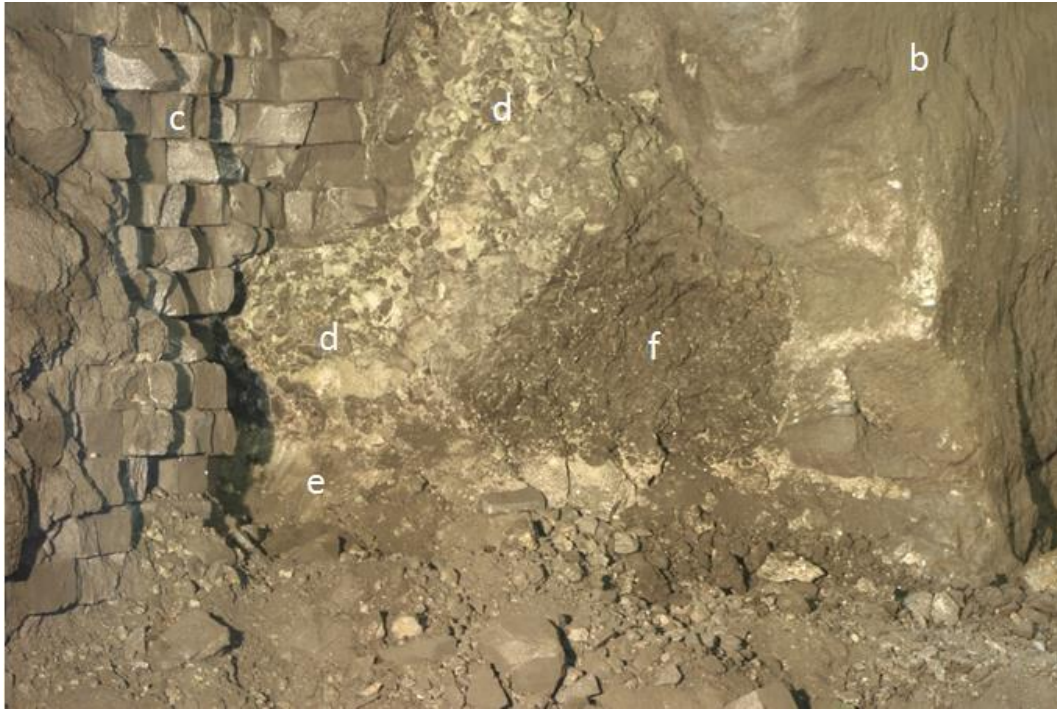


Figure 107: Closer view of zones in front of tap-hole B with (b) high grade carbon ramming, (c) SiC bricks, (d) slag with burden and / or coke bed material, (e) mixed material containing metal and (f) tap clay mushroom.

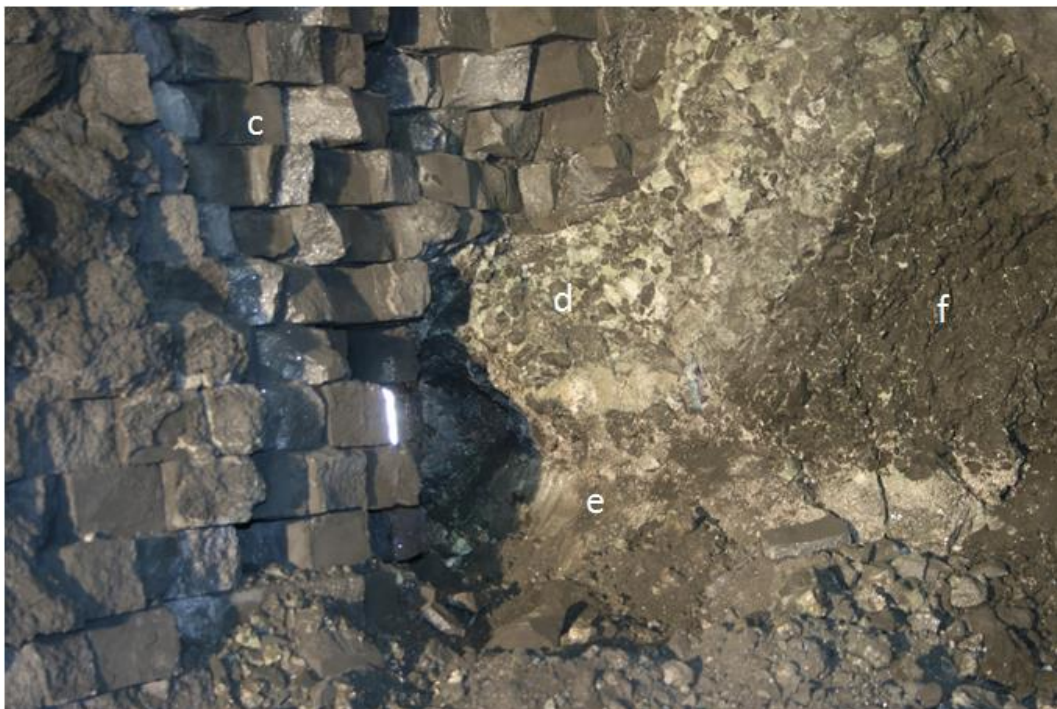


Figure 108: Going into tap-hole B with (c) SiC bricks, (d) slag with burden and / or coke bed material, (e) mixed material containing metal and (f) tap clay mushroom infiltrated with slag.



Figure 109: Tap-hole B with (c) SiC bricks, (d) slag with burden and / or coke bed material and (e) mixed material containing metal.



Figure 110: Tap-hole B put into perspective. The operating personnel are standing on (g) the steel shell / fireclay castable of the furnace hearth sampling the metal layer at the interface between the (i) high grade carbon ramming and (j) burden. Also note the (h) five layers of super duty fireclay bricks in the hearth.

8.5 Discussions

The three main observations made during the excavation were as follows:

1. Contrary to expectations based on laboratory test work and the low reported tapping temperature, the SiC brick in the tap-hole itself wore extensively. From laboratory-scale experiments it was expected that the C-based refractory material would wear, but not the SiC-based refractory material, as it was found that SiC formed as a product of the reaction between SiMn slag and C-based refractory material at tapping temperatures [116], [136].
2. Above the tap-hole, not only did the SiC brick extension wear but so did the high-grade carbon ramming. Wear took place in a channel 500 mm wide and extended to the top of the carbon ramming. Again, wear of the SiC was not expected, but should the C-based refractory material have come into contact with slag at tapping temperatures, reaction between slag and carbon would have been possible [116], [136]. The fact that the channel extended to the top of the C-based refractory material was unexpected. The channel may have been worn by gas formed during lancing or evolved from the clay as reported for FeNi smelters [25].
3. A clay mushroom did form, but rather than being attached to the SiC brick reconstructing the tap-hole, it was detached from the SiC brick, and metal and slag channelled around it.

8.5.1 Potential for chemical reaction between slag or metal and refractory

In order to investigate the potential for chemical reaction (corrosion) between slag or metal and refractory as a mechanism contributing to the wear observed in the tap-hole area, thermodynamic calculations were conducted in FACTSage 6.4 [117]. The Equilib model was utilized, and depending on the type of calculation the FToxid and / or FSstel and FACTPS databases were selected. Default gas, liquids, and solids were selected as pure species with duplicates suppressed with the order of preference being the FToxid, FSstel, and then the FACTPS databases. As solution species, only liquid slag (SLAGA) and liquid metal (LIQU) were selected where applicable.

In all calculations the temperature range was 1500 – 1700°C at 25°C intervals and at 1 atmosphere pressure, although the ambient pressure at the plant is typically 0.85 atmosphere [137]. The temperature range was selected based on the following criteria:

1. The process temperature required for the production of SiMn with 17.0% Si in equilibrium with slag with a silica activity of 0.2 (typical of SiMn production) is calculated as 1600°C [1]
2. Actual tap temperatures measured at the plant ranged between 1420 and 1520°C. A difference between tapping temperature and process temperature of 50 – 100°C is typical of plant operations [1]
3. The actual temperature experienced by the hot face refractories would therefore have been 1600°C or more
4. A first indication of the effect of lancing on tap-hole wear was to be obtained (albeit not a detailed investigation).

To obtain an initial understanding of the system under investigation, the equilibrium phase distributions of both slag and the metal were calculated. The composition and databases associated are stated in Table 61 for slag and Table 62 for metal. Initial conditions were not specified. For the slag calculations, 0.00001 g of argon was added to enable the calculation to converge.

Table 61: Material compositions applied in free energy minimization calculations where slag is reacted with either C- or SiC-based refractory material (mass percentages).

Composition [g]	Slag						Refractory	
	MnO	SiO ₂	CaO	MgO	Al ₂ O ₃	FeO	C	SiC
As-received	13.7	47.4	26.1	6.2	6.1	0.5	100	100
Corrected	11.9	48.2	27.1	6.4	6.3	0	100	100

Table 62: Material compositions (mass percentages) applied in free energy minimization calculations where metal is reacted with either C- or SiC-based refractory material.

Amount [g]	Metal				Refractory	
	Mn	C	Si	Fe	C	SiC
	66.3	1.8	17.1	14.8	100	100

The predicted equilibrium phase distributions, for both as-received slag *not* corrected for metal entrainment and slag corrected for metal entrainment, are presented in Figure 111. In both instances the slag would be fully liquid at the temperatures under investigation (1500 – 1700°C) with the calculated melting point at 1260°C and 1274°C respectively. As the composition of liquid slag phase was not changed by the presence of a second phase, the slag composition in Table 61 could therefore be utilized ‘as is’ in thermodynamic calculations to study the potential of chemical reactions between slag and refractory.

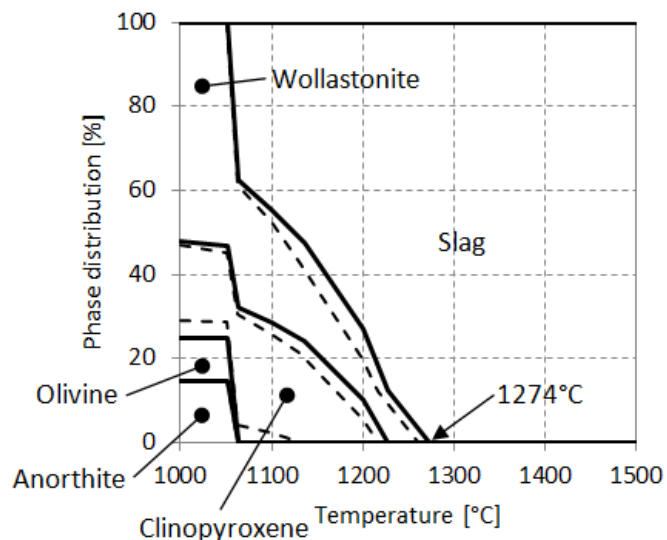


Figure 111: Equilibrium phase distribution of industrial slag based on compositions in Table 61 with solid lines presenting slag corrected for metal entrainment and dotted lines not.

The predicted equilibrium phase distribution of the as-received metal and chemical composition of the metal phase as a function of temperature are presented in Figure 112. At temperatures below 1625°C the metal is saturated in SiC, as seen by the precipitation of SiC as a separate phase and the lower Si and C contents of the liquid metal phase. As the temperature increases, the solubility of the SiC in the metal increases to the point (above 1625°C) where the metal becomes unsaturated in SiC.

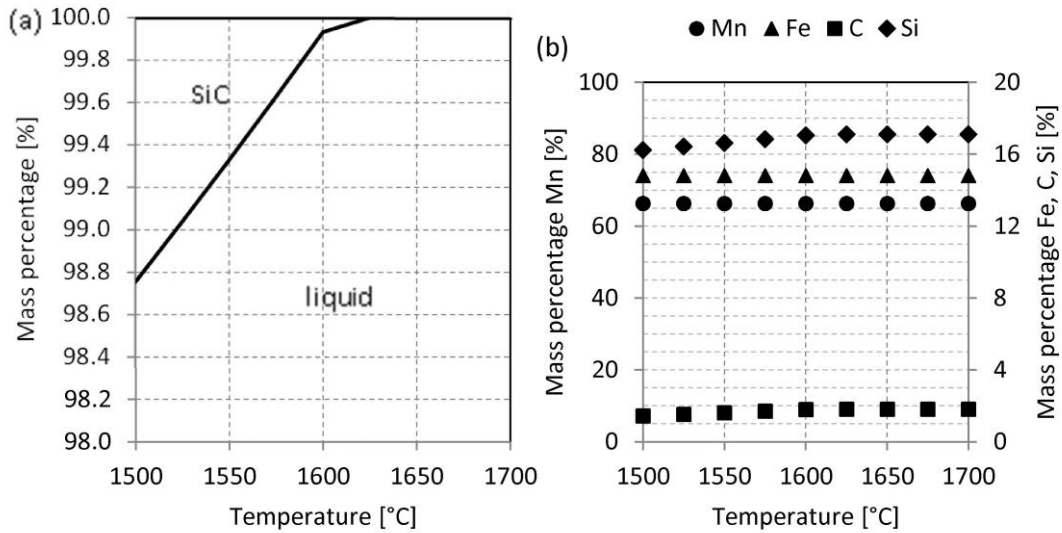


Figure 112: Predicted (a) phase distribution of as-received metal and (b) chemical composition of liquid metal phase as a function of temperature.

This is in agreement with the C solubility diagram for Si-Mn-Fe alloys presented in Figure 113 and constructed from thermodynamic calculations conducted in FACTSage 6.4 [117]. Once the temperature has increased to such an extent that the metal is unsaturated in SiC, the metal will dissolve any SiC it comes into contact with, except for limitations posed by reaction kinetics [120].

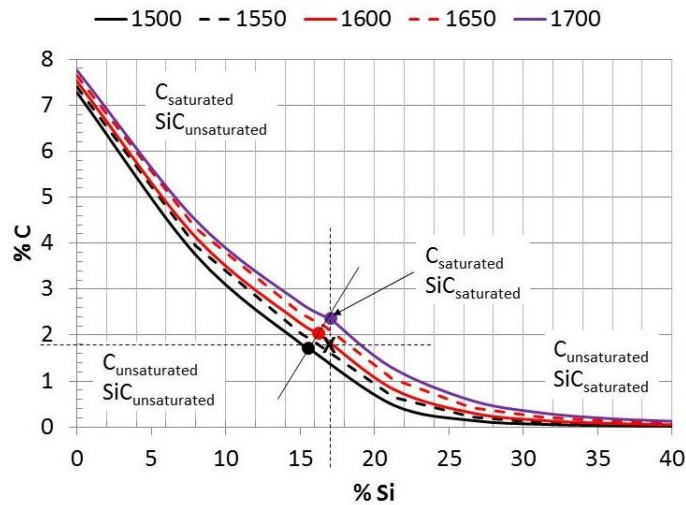


Figure 113: Calculated carbon solubility in Mn-Si-Fe alloys with fixed Mn:Fe ratio of 4.5 at 1500–1700°C. The black cross indicates the composition of the alloy given in Table 62.

The possibility of reaction was assessed by calculating the equilibrium phase distribution of the reaction products for the reaction of equal masses of slag and refractory as a function of temperature. Equal masses of slag and refractory were assumed for convenience; in reality, the refractories are exposed to large volumes of process materials (slag, metal) that are continuously being replenished by fluid flow past the hot face and due to new process material being continuously produced. This means that the effective ratio of process material to refractory material is usually very large, which may affect refractory consumption. Estimates of the actual quantity of slag participating in the reactions (based on mass transfer) are presented later. As the slag was fully liquid in the temperature range under investigation, the composition in Table 61 could be utilized in

calculations. For the metal, the composition in Table 62 was utilized. The fact that the metal was already saturated in SiC (and unsaturated in C) was taken into account when interpreting the results of the thermodynamic calculations. The refractory was assumed to consist of 100% C or 100% SiC.

The predicted equilibrium phase distributions when slag reacts with SiC or C refractories are presented in Figure 114, and chemical distribution of the slag, metal, and gas phases in Figure 115. The difference in phase distribution of slag not corrected for metal and slag corrected for metal was insignificant. The remainder of the discussion will focus on slag corrected for metal only. This means that the elements actively participating in slag / refractory interaction were considered as being Mn, Si, O, and C (Fe excluded).

The reaction products for SiC-based refractory reacting with slag are metal and gas phases (Figure 114a). Metal formation is significant throughout the temperature range under investigation (1500°C to 1700°C). Metal formation increases with increasing temperature from 1575°C, which is the temperature at which gas formation also becomes significant. The formation of SiMn metal (Figure 114a) is associated with a decrease in the MnO content of the slag (Figure 115a), a decrease in SiC (Figure 114a), and formation of a CO-rich gas phase (Figure 115c). Wear of the SiC-based refractory therefore appears to have been due to the formation of a metal phase – through both the reduction of MnO and the subsequent dissolution of SiC into the metal phase formed – and formation of a CO-rich gas phase.

The reaction products for C-based refractory reacting with slag are metal, gas and SiC (Figure 114b). Metal formation commences at 1525°C and SiC formation at 1575°C, with gas formation being significant from 1550°C. The formation of SiMn metal (Figure 114b) and SiC is associated with decreases in both MnO and SiO₂ contents of the slag (Figure 115a), a decrease in C (Figure 114b), and formation of a CO-rich gas phase (Figure 115c). Wear of the C-based refractory therefore appears to have been due to the formation of metal phase (through both the reduction of MnO and SiO₂ and through subsequent dissolution of C into the metal phase formed), formation of a SiC-phase through reduction of SiO₂ and formation of a CO-rich gas phase.

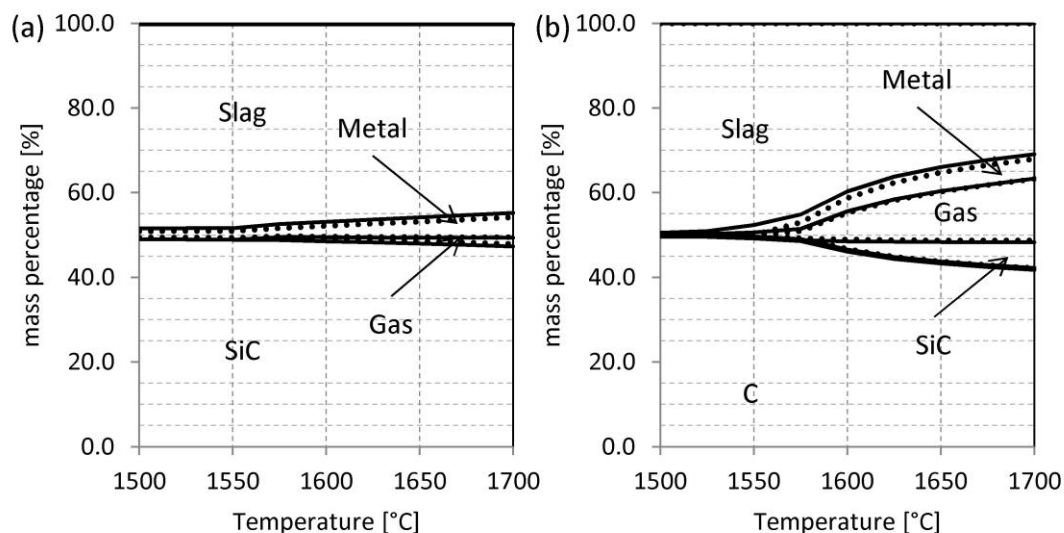


Figure 114: Predicted phase distribution of 100g slag reacted with 100g of (a) SiC- and (b) C-based refractory material as a function of temperature. Solid lines represent the borders for phase distribution calculated from the as-received slag analysis and dotted lines calculated from the corrected slag analysis.

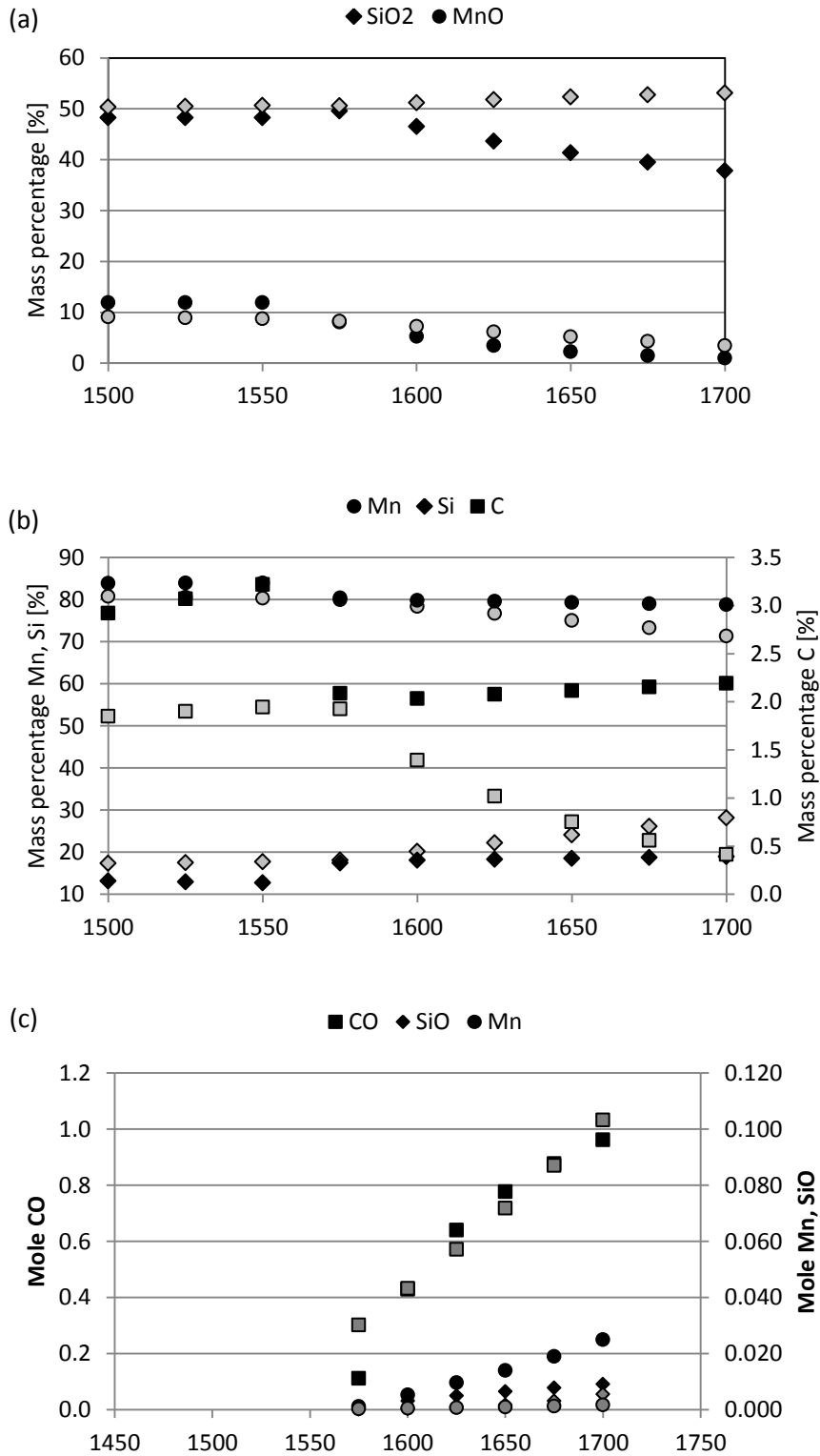


Figure 115: Predicted chemical composition of (a) slag, (b) metal and (c) gas phases that form when reacting 100g slag with 100g of SiC- (grey symbols) or C- (black symbols) based refractory material as functions of temperature.

8.5.2 Refractory consumption

The predicted refractory consumption (X) is plotted as kilograms of refractory consumed (W_{ref}) per ton of slag or metal in Figure 116. Consumption was calculated as in Equation 32.

Equation 32: Refractory consumption calculation #1

$$X = \frac{W_{ref}}{100} \times 1000$$

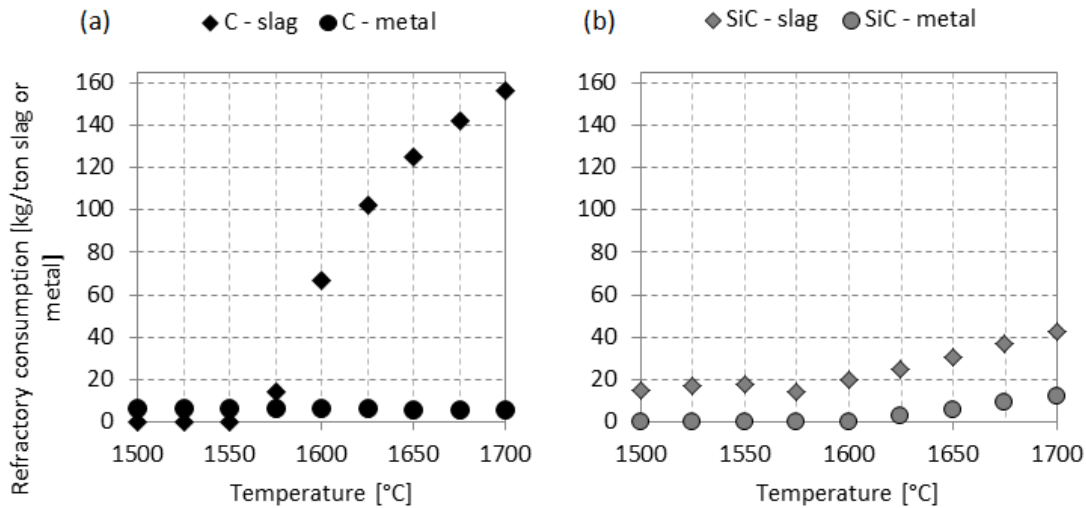


Figure 116: Calculated equilibrium consumption of (a) carbon and (b) SiC through reaction with either slag or metal, where the mass of slag or metal is equal to that of the refractory. Equilibrium calculations were conducted with FACTSage.

The highest wear predicted was for carbon-based refractory reacting with slag at temperatures exceeding 1675°C, followed by SiC-based refractory reacting with slag. This is expected, as slag reactions involve both chemical reaction and dissolution as discussed above, whereas metal reaction involves only dissolution. Dissolution of SiC into metal (Figure 116b) occurs only once the metal becomes unsaturated in SiC (Figure 112a and Figure 113), whereas the metal is already unsaturated in C (Figure 113), with carbon potentially dissolving in metal throughout the temperature range (Figure 116a).

When C-based refractory reacts with slag, if the SiC reaction product were to form an *in-situ* refractory layer at the slag / refractory interface, the potential for refractory wear by chemical reaction would be reduced [18]. However, experimental work has shown that SiC detaches from the refractory rather than forming an *in-situ* protective layer [116], [136].

To put the results in Figure 116 into perspective, the actual refractory consumption was calculated (Equation 33) over the lifetime of tap-hole B.

Equation 33: Refractory consumption calculation #2

$$X = \frac{T_{ref}}{T_s} \times 1000$$

The results are reported in Table 63. The mass of refractory worn was calculated from the wear profile in Figure 104. The total amount of slag tapped through the tap-hole was calculated from production figures (see Table 64).

Table 63: Actual mass of C and SiC refractory worn as calculated from the wear profile in Figure 104.

High carbon ramming				SiC			
Assume vertical rectangle	H	2.4	m	Assume vertical rectangle	H	0.5	m
	W	0.5	m		W	0.5	m
	D	0.9	m		D	0.7	m
Volume		1.08	m ³	Volume		0.2	m ³
Density		1.8	t/m ³	Density		2.6	t/m ³
Mass		1.944	t	Mass		0.433	t
Total mass					T _{ref}	2.377	t

Table 64: Total amount of slag tapped through the tap-hole estimated from actual production figures.

Symbol	Description	Equation	Value	Unit
R	Slag / alloy ratio		0.8	
	Size of a tap			
A	Alloy		22	ton
S	Slag	$R \times A$	17.6	ton
n	Number of taps		1880	
T _s	Total amount of slag	$n \times S$	33088	ton

From Table 63 and Table 64 the actual refractory consumption relative to the total amount of slag tapped through the tap-hole was calculated. The result obtained – 0.07 kg refractory per ton of slag – was far lower (by a factor of ten thousand) than the predicted equilibrium consumption (around 70 kg refractory per ton of slag, depending on temperature) (see Figure 116).

A likely explanation for the significant difference is that not all slag that was tapped through the tap-hole participated in chemical wear. According to the principles of fluid dynamics, velocity and diffusion boundary layers develop near the wall inside a circular pipe (tap-hole) due to the effects of viscosity. The boundary layers influence the heat and mass transfer in the pipe. In the case of slag / refractory interaction in the tap-hole, only SiO₂ and MnO that diffuse through the boundary layer would react with the refractory at the slag / refractory interface.

The amount of slag participating in the reaction was estimated from the mass transfer coefficient for laminar flow inside a circular pipe, taking account of entrance effects [138] (see Table 65). The transition from laminar to turbulent flow takes place at a Reynolds number (Re) of around 2300, therefore the flow in the tap-hole was taken to be laminar, for slag tapping (see Re in Table 65).

The rate at which slag is transported across the boundary layer to react with the interior surface of the tap-hole is simply given by the product of the mass transfer coefficient (k_c), the inner area of the tap-hole, and the slag density; the proportion of slag reacting is then given by Equation 34.

Equation 34: Slag available for reaction per ton of slag tapped.

$$M_R = \frac{k_c \times \pi \times D_T \times L \times \rho \times t \times 60}{M}$$

Table 65: Calculation of mass transfer coefficient for silica for laminar flow inside a circular pipe.

Symbol	Description	Equation	Value	Unit	References
t	Duration of tap	-	30	min	-
M	Size of tap	-	17.6	tons	Table 64
m	Slag mass flow rate	$\frac{M}{t} \times 60$	35.2	t/h	-
ρ	Slag density	-	2774	kg/m ³	[82]
\dot{m}	Volumetric slag flow rate	$\frac{m \times 1000}{\rho \times 3600}$	0.003525	m ³ /s	-
D _T	Inner diameter of the pipe	-	0.1	m	-
U _m	Average velocity over the cross-section of the pipe	$\frac{\dot{m}}{\pi} \times \frac{D_T^2}{4}$	0.448791	m/s	[138]
μ	Slag viscosity	-	0.74	kg/ms	[82]
Re	Reynolds number	$\frac{\rho D_T U_m}{\mu}$	168	-	[138]
D	Effective binary diffusivity of silica in slag	-	10 ⁻¹¹		[139]
Sc	Schmidt number	D/(μ/ρ)	2.67 x 10 ⁷	-	[138]
L	Length of the pipe	-	1	m	-
Gz	Graetz number for mass transfer	$\frac{\pi}{4} \times \frac{D_T}{L} \times Re \times Sc$	3.52 x 10 ⁸	-	[138]
Sh	Sherwood number	1.65 x Gz ^{1/3}	1166	-	[138]
k _c	Mass transfer coefficient of silica	$\frac{Sh \times D}{D_T}$	1.2 x 10 ⁻⁷	m/s	[138]

The calculation (see details in Appendix C) indicates that the mass of slag reacting is approximately 0.01 kg per ton of slag tapped. Based on the estimate of 70 kg of refractory consumed per ton of slag tapped (see Figure 116), the predicted refractory wear is 0.0007 kg per ton of slag tapped, two orders of magnitude smaller than the observed wear. The conclusion is thus that mass transfer effects in the tap-hole significantly limit the extent of reaction. It should be noted that wear by metal was not considered in this calculation; the mass transfer coefficient for metal (with lower viscosity and higher diffusivity) would be much higher than for slag.

8.6 Conclusions

The third research question posed was: *What are the implications for the life of the tap-hole in a SiMn furnace?*

One of the reasons for the excavation and relining of the 48 MV SiMn furnace was the high shell temperatures (300 – 480°C) in the vicinity of the tap-hole. Prior to the excavation, the SiC brick utilized as tap-hole refractory (which should not react with slag) and the reconstructive tap-hole clay utilized to form a mushroom attached to the refractory were expected to protect the tap-hole from wear. However, the use of oxygen lancing should contribute to wear.

During the furnace excavation, it was found that the tap-hole area was one of two high refractory wear areas; the other was the furnace hearth. It was found that the SiC brick in the tap-hole itself wore extensively. Above the tap-hole, not only did the SiC brick extension wear but so did the high-grade carbon ramming, with wear taking place unexpectedly in a channel 500 mm wide and

extending to the top of the carbon ramming. A clay mushroom did form, but rather than being attached to the SiC brick reconstructing the tap-hole, it was detached from the SiC brick with metal and slag channelling around it.

Thermodynamic calculations predicted wear of both C- and SiC-based refractory through chemical reaction with slag and dissolution in metal. The SiC-based refractory wore when metal and CO-rich gas phases formed through the reduction of MnO in the slag and by the subsequent dissolution of SiC to form a SiMn alloy saturated in C and SiC. The C-based refractory wore when metal, SiC, and CO-rich gas phases formed through the reduction of MnO and SiO₂ in the slag and by the subsequent dissolution of SiC and C to form a SiMn alloy saturated in C and SiC. The metal tapped from the furnace was typically saturated in SiC but not in C, therefore C-based refractory would dissolve in the metal and SiC-based refractory at temperatures where the metal becomes unsaturated in SiC. The potential for chemical wear was therefore highest for C-based refractory material.

Furthermore, mass transfer calculations indicated that not all the slag tapped from the furnace was available for participation in chemical reactions responsible for wear. Comparison with estimated wear rates indicates that slag mass transfer was too slow to account for the observed wear. Although chemical reaction between slag and refractory is a potential mechanism responsible for refractory wear in the tap-hole, it appears not to be the only wear mechanism.

Further work to investigate flow conditions in the tap-hole region, and their possible effects on wear, would be useful, as would investigations into the effect of lancing and tap-hole clay studies.

In Chapter 9 the three research questions and arguments will be revised and recommendations made for future investigations.

9 Final conclusions and recommendations for future research

The goal of the study presented here was to determine to what extent chemical reaction between slag and refractory materials would be responsible for tap-hole refractory wear. The study was structured to address three research questions:

Question 1: When exposing carbon-based refractory material (ramming paste and carbon block) to SiMn slag or metal in the tap-hole, is chemical reaction between refractory and slag or refractory and metal a potential wear mechanism?

Question 2: Is the choice in carbon-based refractory material important from a tap-hole refractory life perspective?

Question 3: Having obtained answers to Question 1 and Question 2, what are the implications for the life of the tap-hole in a SiMn furnace?

These three questions were addressed by combining thermodynamic calculations, different laboratory scale experiments and the excavation of a tap-hole from an industrial scale furnace.

The answer to question 1 – *when exposing carbon-based refractory material (ramming paste and carbon block) to SiMn slag or metal in the tap-hole, is chemical reaction between refractory and slag or refractory and metal a potential wear mechanism?* – is yes.

Thermodynamic calculations indicated that the reactions most likely responsible for wear in the tap-hole were the reduction of SiO_2 to produce SiC or alloyed Si, and of MnO producing alloyed Mn and the dissolution of carbon in metal up to the point of dual saturation – in both carbon and SiC.

The formation of SiC as reaction product was demonstrated in three types of laboratory-scale experiments in which (1) graphite was exposed to synthetic slag in a cup test, (2) ramming paste matrix was exposed to synthetic slag in wettability tests and (3) ramming paste was exposed to industrial slag in cup tests.

The formation of SiMn as reaction product was validated provisionally in the experiments where graphite was exposed to synthetic slag and appeared to occur in a cup test where ramming paste was exposed to industrial slag.

Based on published [63] data, slag should be non-wetting towards carbon block and ramming paste. This was not found: both synthetic and industrial slag wetted both types of refractory materials. Chemical reactions in reactive systems could cause non-wetting conditions to change to wetting conditions. The potential for chemical reaction between refractory and slag being the cause of the wetting behaviour was further confirmed by slag being non-wetting on all three substrates in CO-gas atmospheres which appeared to suppress the chemical reaction between the refractory substrate and slag.

The answer to question 2 – *is the choice in carbon-based refractory material important from a tap-hole refractory life perspective?* – is no, when limited to the study of slag / refractory interactions presented in this study.

To address the question industrial grade carbon-based refractory material and industrial SiMn slag were sourced, prepared and characterised.

As the reaction products expected from slag / refractory interactions were SiC and SiMn, the fact that the industrial slag sourced to conduct these experiments contained both had to be taken into

account. The industrial SiMn slag consisted primarily of an amorphous slag phase, but also contained SiC, MnS and intermetallic phases including SiMn. The slag was fully liquid at the temperature range under investigation (1400°C – 1600°C).

Both refractory materials consisted of large carbon-based aggregate particles and a carbon binder phase containing smaller carbon-based aggregate particles. The carbon block had both Al₂O₃ and SiC particles added intentionally. The ramming paste contained inorganic phases too but these were not added intentionally and rather were calcination products formed during calcination of the anthracite. At the temperature range under investigation (1400°C – 1600°C) thermodynamic calculations predicted the presence of minor slag and metal phases upon melting of the inorganic phases present in both refractory materials. The porosity of the carbon block was half that of the ramming paste and the porosity of the ramming paste matrix slightly higher than that of the ramming paste aggregate.

As with the pure species, thermodynamic calculations predicted the potential for reduction of SiO₂ to form SiC and alloyed Si, and reduction of MnO to produce alloyed Mn, when reacting the industrial slag with industrial grade refractory materials. Both phases were observed in wettability tests and cup tests exposing refractory to industrial slag. The SiC formed did not attach to the carbon forming a protective layer but rather detached into the slag phase potentially due to the wettability of SiC towards slags. The carbon in both materials appeared to have reacted with slag to form SiC and SiMn (although the presence of SiC and metal in unreacted slag causes some ambiguity) with the binder phase being attacked preferentially to the aggregate. From a chemical reaction perspective a difference between the two types of refractory materials could therefore not be found.

Another aspect studied was the extent of infiltration of slag into the refractory; increased infiltration would lead to increased surface area available for slag / refractory interaction. In wettability tests the carbon block was infiltrated more deeply by slag than ramming paste aggregate or matrix, but in cup tests where the amount of slag was significantly higher, no difference was found. In cup tests, the extent of infiltration was the same for both materials as was the infiltration path: slag filled the open pores in the matrix rather than filling aggregate particles. Slag appears to infiltrate both materials to the same extent.

It was concluded that, for the two types of carbon-based refractory materials under investigation, the choice of material would not influence chemical wear based on the results obtained from the experimental methods (wettability test and crucible tests) utilized. The differences in refractory life observed on the plant should therefore be attributed to wear mechanisms other than purely the chemical wear observed by these two methods.

Question 3 – *what are the implications for the life of the tap-hole in a SiMn furnace?* – was addressed in the context of an excavation of an industrial scale furnace where the tap-hole was based on a combination of SiC bricks and carbon ramming paste.

According to thermodynamic calculations the predicted extent of chemical wear by slag was larger for carbon-based refractory materials (than for SiC). If the SiC reaction product were to form an *in situ* refractory layer at the slag / refractory interface, the potential for refractory wear by chemical reaction would therefore be reduced – but the laboratory experiments did not show adherence of the SiC product to the carbon refractory.

Preliminary consideration of mass transfer in the tap-hole indicated that, although chemical reaction between slag and refractory is a potential mechanism responsible for refractory wear in the tap-hole, it is not the only wear mechanism applicable.

In the study presented here, thermodynamic calculations focussed on the formation of SiC from SiO₂ irrespective of reaction paths. The experimental work that followed studied the slag/graphite reaction, not metal/graphite reaction; that would be interesting future work.

The carbon block and ramming paste examined in this study contained a significant proportion of inorganic components. The potential for these components to partially dissolve in slag and contribute to wear would also be interesting future work.

As a next step in understanding the difference in wear observe between carbon block and ramming paste the potential for erosion caused by slag or metal and solid material abrading refractory [19], [88] in combination with chemical reaction should be investigated. Laboratory-scale techniques available to investigate erosion in neutral gas atmospheres are rotary finger tests [66], [114].

Furthermore understanding the influence of mass and heat transfer on the temperature of the refractory at the slag / refractory interface would improve understanding of the potential for chemical reaction to contribute to the wear in the tap-hole.

As oxygen lancing of the tap-hole – initially to open it and during tap to keep it open – is applied on most industrial scale furnaces the effect of lancing on tap-hole wear should be further investigated. Lancing has the potential to change both chemistry and temperature in the tap-hole and to influence the material flow. Excessive lancing is expected to be highly detrimental to tap-hole life.

10 References

- [1] S. E. Olsen, M. Tangstad, and T. Lindstad, *Production of manganese ferroalloys*. Trondheim, Norway: Tapir Academic Press, 2007, pp. 1–247.
- [2] “Manganese (Mn),” *Encyclopædia Britannica Online Academic Edition*, 2012. [Online]. Available: www.britannica.com/EBchecked/topic/361875/manganese. [Accessed: 22-Apr-2013].
- [3] R. Reisfeld, “Optical properties of rare earth and transition element doped glasses,” in *Encyclopedia of Materials - Science and Technology*, Elsevier, 2001, pp. 6472 – 6477.
- [4] “Pottery,” *Encyclopædia Britannica Online Academic Edition*, 2012. [Online]. Available: www.britannica.com/EBchecked/topic/472867/pottery. [Accessed: 22-Apr-2013].
- [5] B. Clegg, “Chemistry in its element - potassium permanganate.” [Online]. Available: http://www.rsc.org/chemistryworld/podcast/CIIEcompounds/transcripts/potassium_permanganate.asp. [Accessed: 19-Apr-2013].
- [6] J. H. Downing, “Manganese Processing,” *Encyclopædia Britannica Online Academic Edition*, 2012. [Online]. Available: <http://www.britannica.com/EBchecked/topic/361933/manganese-processing>. [Accessed: 22-Apr-2013].
- [7] ASTM Standards A99-03, “Standard Specification for Ferromanganese.” ASTM International, West Conshohocken, PA, 2003, pp. 1–3, 2009.
- [8] ASTM Standards A483 / A483M - 10, “Standard Specification for Silicomanganese.” ASTM International, West Conshohocken, PA, 2003, pp. 1–2, 2010.
- [9] W. T. Lankford, N. L. Samways, R. F. Craven, and H. E. McGannon, “The physical chemistry of iron and steelmaking,” in *Making, shaping and treating of steel*, 10th ed., Association of Iron and Steel Engineers, 1985, pp. 407–409.
- [10] International Manganese Institute, “IMnI 2010 Mn Public Report,” 2010. [Online]. Available: www.manganese.org. [Accessed: 13-Mar-2012].
- [11] World Steel Association, “Annual crude steel production 2000 - 2009,” 2009. [Online]. Available: www.worldsteel.org. [Accessed: 25-Mar-2012].
- [12] World Steel Association, “Annual crude steel production 2010,” 2010. [Online]. Available: www.worldsteel.org. [Accessed: 25-Mar-2012].
- [13] F. Habashi, *Handbook of extractive metallurgy*, vol. 1. Wiley-VCH, 1997.
- [14] J. P. Gous, J. H. Zietsman, J. D. Steenkamp, and J. J. Sutherland, “Excavation of a 48 MVA silicomanganese submerged-arc SiMn furnace in South Africa – Part I:

- Methodology and Observations,” in *5th International Symposium on High-Temperature Metallurgical Processing*, 2014, pp. 255–269.
- [15] J. P. Gous, “Personal communication.” 2014.
- [16] J. D. Steenkamp and J. Basson, “The manganese ferroalloys industry in southern Africa,” *J. South. African Inst. Min. Metall.*, vol. 113, pp. 667–676, 2013.
- [17] H. Brun, “Development of Refractory Linings for Electric Reduction Furnaces Producing Mn Alloys at Elkem A/S-PEA Plant, Porsgrunn, Norway.,” *J. Inst. Refract. Eng.*, no. Spring, pp. 12–23, 1982.
- [18] W. E. Lee and R. E. Moore, “Evolution of in Situ Refractories in the 20th Century,” *J. Am. Ceram. Soc.*, vol. 81, no. 6, pp. 1385–1410, 1998.
- [19] P. L. Duncanson and J. D. Toth, “The truths and myths of freeze lining technology for submerged arc furnaces,” in *INFACON X: Transformation through technology*, 2004, vol. Cape Town., pp. 488–499.
- [20] P. Hloben, *Refractory materials - Major industrial applications*. Bryanston, South Africa: REXXON Corporation, 2000.
- [21] J. P. Holman, *Heat Transfer*, vol. 9th. McGraw-Hill, 2002, p. 665.
- [22] J. D. Steenkamp, P. Chris, and M. Tangstad, “Thermal conductivity of manganese bearing slags - an introduction,” in *Poster presented at Fray international symposium*, 2011.
- [23] A. M. Hearn, A. J. Dzermejko, and P. H. Lamont, “‘Freeze’ lining concepts for improving submerged arc furnace lining life and performance,” in *8th International Ferroalloys Congress*, 1998, pp. 401–426.
- [24] L. R. Nelson and R. Hundermark, “‘The tap-hole’ – key to furnace performance,” in *Furnace Tapping Conference 2014*, 2014, pp. 1–32.
- [25] L. Thomson, “Monitoring, repair and safety practices for electric furnace matte tapping,” in *Furnace Tapping Conference 2014*, 2014, pp. 87–96.
- [26] M. Tangstad, “Question and answer session, School on Manganese Ferroalloy production.” Muldersdrift, South Africa, 2012.
- [27] S. R. Dash, “Development of improved tap hole clay for blast furnace tap hole,” National Institute of Technology, Rourkela, 2009.
- [28] Y. Ko, C. Ho, and H. Kuo, “The Thermal Behavior Analysis in Tap-Hole Area,” *China Steel Tech. Rep.*, no. 21, pp. 13–20, 2008.

- [29] T. Inada, A. Kasai, K. Nakano, S. Komatsu, and A. Ogawa, “Dissection Investigation of Blast Furnace Hearth—Kokura No. 2 Blast Furnace (2nd Campaign),” *ISIJ Int.*, vol. 49, no. 4, pp. 470–478, 2009.
- [30] Anonymous, “Personal communication with plant personnel (site or company name not to be disclosed).” 2010.
- [31] A. G. Matyas, R. C. Francki, K. M. Donaldson, and B. Wasmund, “Application of new technology in the design of high-power electric smelting furnaces,” *CIM Bull.*, vol. 86, no. 972, pp. 92–99, 1993.
- [32] M. Tangstad, “Ferromanganese research in Norway,” *Presentation at the Pretoria branch of the SAIMM - 5 May 2010*, 2010. [Online]. Available: <http://saimm.co.za/about-saimm/branchessaimm/58-saimm-pretoria/159-ferromanganese-research-in-norway>. [Accessed: 10-Apr-2014].
- [33] E. M. M. Ewais, “Carbon Based Refractories,” *J. Ceram. Soc. Japan*, vol. 112, no. 10, pp. 517–532, 2004.
- [34] K. Piel and A. Schnittker, “Carbon and graphite bricks / blocks,” in *Handbook of Refractory Materials: Design / Properties / Testings*, 4th ed., Vulkan-Verlag Essen, 2012, pp. 48 – 51.
- [35] C. Wu and V. Sahajwalla, “Dissolution Rates of Coals and Graphite in Fe-C-S Melts in Direct Ironmaking : Influence of Melt Carbon and Sulfur on Carbon Dissolution,” *Metall. Mater. Trans. B*, vol. 31B, no. April, pp. 243–251, 2000.
- [36] J. H. Chesters, *Refractories production and properties*. London, UK: The iron and steel institute, 1973, p. 553.
- [37] P. C. Pistorius, “Reductant selection in ferro-alloy production: The case for the importance of dissolution in the metal,” *J. South African Inst. Min. Metall.*, vol. January/Fe, pp. 33–36, 2002.
- [38] ASTM Standards D5187-10, “Standard test method for determination of crystallite size (Lc) of calcined petroleum coke by X-Ray diffraction,” *Annual Book of ASTM Standards*, no. C. ASTM International, West Conshohocken, PA, 2003, pp. 1–4, 2010.
- [39] J. Safarian, L. Kolbeinsen, S. Gaal, and G. Tranell, “The effect of graphite properties on the rate of MnO reduction from high carbon ferromanganese slag,” in *Infacon XI: Innovation in Ferroalloy Industry*, 2007, no. 1, pp. 321–334.
- [40] J. Safarian and L. Kolbeinsen, “Kinetic of Carbothermic Reduction of MnO from High-carbon Ferromanganese Slag by Graphite Materials,” *ISIJ Int.*, vol. 48, no. 4, pp. 395–404, 2008.
- [41] J. Safarian, G. Tranell, L. Kolbeinsen, M. Tangstad, S. Gaal, and J. Kaczorowski, “Reduction Kinetics of MnO from High-Carbon Ferromanganese Slags by

- Carbonaceous Materials in Ar and CO Atmospheres,” *Metall. Mater. Trans. B*, vol. 39, no. 5, pp. 702–712, Sep. 2008.
- [42] J. Safarian, L. Kolbeinsen, M. Tangstad, and G. Tranell, “Kinetics and Mechanism of the Simultaneous Carbothermic Reduction of FeO and MnO from High-Carbon Ferromanganese Slag,” *Metall. Mater. Trans. B*, vol. 40, no. 6, pp. 929–939, Sep. 2009.
- [43] J. Safarian and M. Tangstad, “Slag-carbon reactivity,” in *Infacon XII: Sustainable future*, 2010, pp. 327–338.
- [44] H. Sun, M. Y. Lone, S. Ganguly, and O. Ostrovski, “Wettability and reduction of MnO in slag by carbonaceous materials,” *ISIJ Int.*, vol. 50, no. 5, pp. 639–646, 2010.
- [45] C. Wu and V. Sahajwalla, “Dissolution rates of coals and graphite in Fe-C-S melts in direct ironmaking: dependence of carbon dissolution rate on carbon structure,” *Metall. Mater. Trans. B*, vol. 31B, pp. 215–216, 2000.
- [46] V. Sahajwalla and R. Khanna, “A Monte Carlo simulation study of dissolution of graphite in iron-carbon melts,” *Metall. Mater. Trans. B Process Metall. Mater. Process. Sci.*, vol. 31, no. 6, pp. 1517–1525, 2000.
- [47] A. Ciftja, T. A. Engh, and M. Tangstad, “Wetting properties of molten silicon with graphite materials,” *Metall. Mater. Trans. B*, vol. 41A, no. December, pp. 3183–3195, 2010.
- [48] J. Safarian and M. Tangstad, “Wettability of Silicon Carbide by CaO-SiO₂ Slags,” *Metall. Mater. Trans. B*, vol. 40, no. 6, pp. 920–928, Sep. 2009.
- [49] J. C. Kotz and K. F. Purcell, *Chemistry & chemical reactivity*, 2nd ed. Philadelphia: Saunders College Publishing, 1991, pp. 524–526.
- [50] F. W. Sears, M. W. Zemansky, and H. D. Young, *University Physics*, 7th ed. 1987: Addison Wesley World Student Series, 1987, pp. 313–317.
- [51] B. E. Poling, G. H. Thomson, D. G. Friend, R. L. Rowley, and W. V. Wilding, *Perry’s chemical engineers handbook*, 8th ed. New York, USA: McGraw-Hill, 2008, pp. 2–513 – 2–515.
- [52] B. J. Keene, “Surface tension of slag systems,” in *Slag Atlas*, 2nd ed., Duesseldorf, Germany: Verlag Stahleisen GmbH, 1995, pp. 403–405.
- [53] B. J. Keene, “Contact angle and work of adhesion between ferrous melts and non-metallic solids,” in *Slag Atlas*, 2nd ed., Duesseldorf, Germany: Verlag Stahleisen GmbH, 1995, pp. 513–517.
- [54] D. Young, “An essay on the cohesion of fluids,” *Philos. Trans. R. Soc. London*, pp. 65–87, 1804.

- [55] C. Wu and V. Sahajwalla, "Influence of Melt Carbon and Sulfur on the Wetting of Solid Graphite by Fe-C-S Melts," *Metall. Mater. Trans. B*, vol. 29, no. April, 1998.
- [56] N. Eustathopoulos, M. G. Nicholas, and B. Drevet, *Wettability at high temperatures*. Amsterdam: Pergamon press, 1999, pp. 1–420.
- [57] J. Bico, C. Marzolin, and D. Quere, "Pearl drops," *Europhys. Lett.*, vol. 47, no. 2, pp. 220–226, 1999.
- [58] I. A. Aksay, C. E. Hoge, and J. A. Pask, "Wetting under chemical equilibrium and nonequilibrium conditions," *J. Phys. Chem.*, vol. 78, no. 12, pp. 1178 – 1183, 1974.
- [59] X. B. Zhou and J. T. M. De Hosson, "Reactive wetting of liquid metals on ceramic substrates," *Acta mater.*, vol. 44, no. 2, pp. 421 – 426, 1996.
- [60] G. Routschka and H. Barthel, "Introduction," in *Pocket Manual , Refractory Materials, Basics - Structures - Properties*, 2nd ed., G. Routschka, Ed. Essen, Germany: Vulkan-Verlag, 2004, pp. 1–16.
- [61] H. Barthel, "Carbon-containing magnesia and magnesia-carbon bricks," in *Pocket Manual , Refractory Materials, Basics - Structures - Properties*, 2nd ed., G. Routschka, Ed. Essen, Germany: Vulkan-Verlag, 2004, pp. 158–173.
- [62] P. Bartha and H. Barthel, "Magnesia bricks," in *Pocket Manual , Refractory Materials, Basics - Structures - Properties*, 2nd ed., G. Routschka, Ed. Essen, Germany: Vulkan-Verlag, 2004, pp. 146–158.
- [63] P. Shen, H. Fujii, and K. Nogi, "Wettability of some refractory materials by molten SiO₂–MnO–TiO₂–FeOx slag," *Mater. Chem. Phys.*, vol. 114, pp. 681–686, 2009.
- [64] M. Nitta, "Investigation of used carbon blocks for blast furnace hearth and development of carbon blocks with high thermal conductivity and high corrosion resistance," *Nippon Steel Tech. Reports*, vol. 94, no. July, pp. 122–126, 2006.
- [65] S. A. Podkopaev, L. N. Ruzhevskaya, and I. V. Rybyanets, "Carbon and carbon-containing refractory materials for blast-furnaces at the Chelyabinsk electrode plant," *Refract. Ind. Ceram.*, vol. 45, no. 5, pp. 317–319, 2004.
- [66] J. Tomala and S. Basista, "MICROPOROUS CARBON FURNACE LINING," in *Infacon XI: Innovation in Ferroalloy Industry*, 2007, pp. 722–727.
- [67] F. Prins, "Personal communication: Elkem Carbon Furnace Lining Materials." 2011.
- [68] P. Hayes, *Process principles in minerals and materials production*, vol. Third. Brisbane, Australia: Hayes publishing company, 2003, pp. 1–734.
- [69] D. H. Hubble, "Steel plant refractories," in *The making, shaping and treating of steel - Ironmaking volume*, 11th ed., D. H. Wakelin, Ed. Pittsburgh: The AISE Steel Foundation, 1999, pp. 161–228.

- [70] M. Nitta, H. Nakamura, and A. ISHII, “Development of carbon blocks for blast furnace hearths,” *Nippon Steel Tech. Rep.*, vol. 98, pp. 49–54, 2008.
- [71] F. Prins, “Personal communication: Elkem carbon ramming pastes.” 2011.
- [72] A. J. Dzermejko, “Carbonaceous refractories,” in *Refractories Handbook*, 1st ed., C. Schacht, Ed. CRC Press, 2004, pp. 217–230.
- [73] L. Shoko, J. Beukes, and C. Strydom, “Determining the baking isotherm temperature of Söderberg electrodes and associated structural changes,” *Miner. Eng.*, vol. 49, pp. 33–39, 2013.
- [74] J. D. Steenkamp, J. P. Gous, P. C. Pistorius, M. Tangstad, and J. H. Zietsman, “Wear analysis of a taphole from a SiMn production furnace J.,” in *Furnace Tapping Conference 2014*, 2014, pp. 51–64.
- [75] K. Goto, K. Kohno, M. Nitta, S. Hanagiri, and Y. Tsutsui, “Development of refractory technology,” *Nippon Steel Tech. Rep.*, vol. 101, no. November, pp. 111–114, 2012.
- [76] Anonymous, “NMATM HotPressedTM carbon brick, UMPTM micropore block and UCBTM Block.” Graftech International, p. 3, 2008.
- [77] S. A. Podkopaev, “Carbon-based refractories for the lining of blast furnaces,” *Refract. Ind. Ceram.*, vol. 45, no. 4, pp. 235–238, 2004.
- [78] S. Fujihara, S. Tamura, M. Ikeda, and M. Nakai, “High duty carbon blocks,” *Nippon Steel Tech. Rep.*, vol. 41, no. April, 1989.
- [79] G. Routschka, *Pocket manual - Refractory Materials*, 2nd ed., vol. 2nd. Essen, Germany: Vulkan-Verlag, 2004, pp. 1–512.
- [80] K. Verscheure, A. K. Kylo, A. Filzwieser, B. Blanpain, and P. Wollants, “Furnace cooling technology in pyrometallurgical processes,” in *Sohn International Symposium: Advanced processing of metals and materials*, 2006, vol. 4 - New, i, pp. 139–154.
- [81] N. Voermann, F. Ham, J. Merry, R. Veenstra, and K. Hutchinson, “Furnace Cooling Design for Modern High-Intensity Pyrometallurgical Processes,” in *Copper 99 – Cobre 99 International Conference*, 1999.
- [82] J. Muller and J. Steenkamp, “An evaluation of thermochemical property models for CaO-MnO-SiO₂-Al₂O₃-MgO slag,” *J. Manuf. Sci. Prod.*, vol. 13, no. 4, pp. 251–262, 2013.
- [83] J. R. Welty, C. E. Wicks, R. E. Wilson, and G. L. Rorrer, *Fundamentals of Momentum, Heat, and Mass Transfer*, vol. 3. John Wiley & Sons, 2008, p. 729.
- [84] J. D. Steenkamp, M. Tangstad, and P. C. Pistorius, “Thermal conductivity of solidified manganese-bearing slags — A preliminary investigation,” in *Southern African Pyrometallurgy 2011*, 2011, no. March, pp. 327–344.

- [85] P. G. Whiteley, “Developments in critical areas of blast furnace linings,” *Steel times Int.*, vol. November, pp. 30–32, 1990.
- [86] K. Gritsishin and Y. Mudron, “The refractory lining of blast furnaces and modernization of their cooling system,” *Metallurgist*, vol. 50, no. 7–8, pp. 351–360, 2006.
- [87] A. J. Dzermejko, D. F. Baret, and D. H. Hubble, “Ironmaking refractory systems,” in *Making, shaping and treating of steel - Ironmaking volume*, 11th ed., D. H. Wakelin, Ed. Pittsburgh: The AISE Steel Foundation, 1999, pp. 229–258.
- [88] J. D. Hancock, *Practical refractories*. Vereeniging, South Africa: Cannon & Hancock cc, 2006.
- [89] C. Coetzee, P. L. Duncanson, and P. Sylven, “Campaign extensions for ferroalloy furnaces with improved tap hole repair system,” in *Infacon XII: Sustainable future*, 2010, pp. 857–866.
- [90] K. Sugita, “Historical overview of refractory technology in the steel industry,” *Nippon Steel Tech. Rep.*, vol. 98, no. July, pp. 8–17, 2008.
- [91] K. Hiragushi, C. Horio, H. Yamanaka, M. Ikeda, Y. Shinohara, K. Sawano, and T. Matsui, “Those days of our fight against heat,” *Nippon Steel Tech. Rep.*, vol. 98, no. July, pp. 2–7, 2008.
- [92] S. V Glebov, “Carbon refractories for blast furnaces in the USA,” *Foreign Sci. Technol.*, pp. 187–192, 1964.
- [93] A. E. Paren’kov, F. L. Skuridin, and A. N. Pyrikov, “Composite refractories for the most loaded areas of blast furnaces,” *Refract. Ind. Ceram.*, vol. 50, no. 1, pp. 13–16, 2009.
- [94] K. Kawaoka, A. Tsuda, Y. Matsuoka, K. Nishioka, K. Anan, K. Kakiuchi, H. Takeshita, and H. Takasaki, “Latest blast furnace relining technology at Nippon Steel,” *Nippon Steel Tech. Rep.*, vol. 94, no. July, pp. 127–132, 2006.
- [95] A. K. Kylo, “Water Cooled Refractories,” in *John Floyd International Symposium on Sustainable Developments in Metals Processing*, 2005, pp. 341–350.
- [96] K. Narita, T. Onoye, Y. Satoh, M. Mayimoto, K. Taniguchi, S. Kamatani, T. Sato, and S. Fukihara, “Effects of alkalis and zinc on the wear of blast furnace refractories and the tuyere displacement,” *Trans. ISIJ*, vol. 21, pp. 839–845, 1981.
- [97] L. H. Van Vlack, “Chemical and mineralogical changes in stack and hearth refractories of a blast furnace,” *J. Am. Ceram. Soc.*, vol. 31, no. 8, pp. 220–235, 1948.
- [98] S. N. Silva, F. Vernilli, S. M. Justus, O. R. Marques, A. Mazine, J. B. Baldo, E. Longo, and J. A. Varela, “Wear mechanism for blast furnace hearth refractory lining,” *Ironmak. Steelmak.*, vol. 32, no. 6, pp. 459–467, 2005.

- [99] L. Lindstad, "Personal communication." 2013.
- [100] X. Chen, Y. Li, S. Jin, L. Zhao, and S. Ge, "Effect of temperature on the properties and microstructures of carbon refractories for blast furnace," *Metall. Mater. Trans. A*, vol. 40, no. July, pp. 1675–1683, 2009.
- [101] Y. Li, X. Chen, S. Sang, and L. Zhao, "Effect of multiwalled carbon nanotubes on the thermal conductivity and porosity characteristics of blast furnace carbon refractories," *Metall. Mater. Trans. A*, vol. 41, no. September, pp. 2383–2388, 2010.
- [102] X. Chen, Y. Li, S. Sang, L. Zhao, S. Jin, and S. Li, "Properties and microstructures of blast furnace carbon refractories with Al additions," *Ironmak. Steelmak.*, vol. 37, no. 6, pp. 398–406, 2010.
- [103] Y. Li, X. Chen, S. Sang, S. Jin, L. Zhao, and S. Ge, "Microstructures and Properties of Carbon Refractories for Blast Furnaces with SiO₂ and Al Additions," *Metall. Mater. Trans. A*, vol. 41, pp. 2085–2092, 2010.
- [104] S. Baxendale, "Testing of refractory materials," in *Refractories Handbook*, 1st ed., C. A. Schacht, Ed. CRC Press, 2004, pp. 435–474.
- [105] G. H. Jeffery, J. Basset, J. Mendham, and R. C. Denney, *Vogel's textbook of quantitative chemical analysis*, 5th ed. New York, USA: Longman Scientific and Technical, 1989, pp. 1–877.
- [106] ASTM Standards D3176 – 09, "Ultimate analysis of coal and coke." ASTM International, West Conshohocken, PA, 2003, pp. 1–4, 2009.
- [107] ASTM Standards D5373 – 14, "Determination of carbon, hydrogen and nitrogen in analysis samples of coal and carbon in analysis samples of coal and coke." ASTM International, West Conshohocken, PA, 2003, pp. 1–11, 2014.
- [108] A. standards D4239, "Sulfur in the analysis sample of coal and coke using high-temperature tube furnace combustion." ASTM International, West Conshohocken, PA, 2003, pp. 1–6, 2014.
- [109] M. T. Weller, *Oxford Chemistry Primers: Inorganic materials chemistry*. Oxford: Oxford University Press, 1994, pp. 1–94.
- [110] ASTM Standards D3172 – 07a, "Proximate analysis of coal and coke." ASTM International, West Conshohocken, PA, 2003, pp. 1–2, 2007.
- [111] ASTM Standards D3173-11, "Moisture in the Analysis Sample of Coal and Coke." ASTM International, West Conshohocken, PA, 2003.
- [112] ASTM Standards D3175-11, "Volatile Matter in the Analysis Sample of Coal and Coke." ASTM International, West Conshohocken, PA, 2003.

- [113] ASTM Standards D3174-12, “Ash in the Analysis Sample of Coal and Coke from Coal.” ASTM International, West Conshohocken, PA, 2003.
- [114] M. Dunkl, “Corrosion tests - A very important investigation method for the selection of refractories for glass tanks,” *Glas. Sci. Technol. Int. J. Ger. Soc. Glas. Technol.*, vol. 67, no. 12, pp. 325–334, 1994.
- [115] K. Goto, B. B. Argent, and W. E. Lee, “Corrosion of MgO–MgAl₂O₄ Spinel Refractory Bricks by Calcium Aluminosilicate Slag,” *J. Am. Ceram. Soc.*, vol. 80, no. 2, pp. 461–471, 1997.
- [116] H. Mølnås, “Compatibility Study of Carbon-Based Refractory Materials utilized in Silicomanganese Production Furnaces,” Norwegian University of Science and Technology, 2011.
- [117] C. Bale, P. Chartrand, S. Degterov, and G. Eriksson, “FactSage thermochemical software and databases,” *Calphad*, vol. 26, pp. 189–228, 2002.
- [118] D. R. Gaskell, *Introduction to the Thermodynamics of Materials*, 5th ed. CRC Press, 2008, pp. 1–618.
- [119] H. Li and A. Morris, “Evaluation of unified interaction parameter model parameters for calculating activities of ferromanganese alloys: Mn-Fe-C, Mn-Fe-Si, Mn-C-Si and Mn-Fe-C-Si systems,” *Metall. Mater. Trans. B*, vol. 28B, pp. 553–562, 1997.
- [120] J. Einan, “Formation of Silicon Carbide and Graphite in the Silicomanganese Process,” Norwegian University of Science and Technology, 2012.
- [121] J. W. Hoffman and F. C. De Beer, “Characteristics of the Micro-Focus X-ray Tomography Facility (MIXRAD) at Necsa in South Africa,” in *18th World Conference on Nondestructive Testing*.
- [122] C. O. Gomez, D. W. Strickler, and L. G. Austin, “An iodized mounting medium for coal particles,” *J. Electron Microsc. Tech.*, vol. 1, pp. 285–287, 1984.
- [123] W. E. Straszheim, K. A. Younkin, R. T. Greer, and R. Markuszewski, “Mounting materials for automated image analysis of coal using backscattered electron imaging,” *Scanning Microsc.*, vol. 2, no. 3, pp. 1257–1264, 1988.
- [124] I. N. Bindeman, A. M. Davis, and M. J. Drake, “Ion microprobe study of plagioclase-basalt partition experiments at natural concentration levels of trace elements,” *Geochim. Cosmochim. Acta*, vol. 62, no. 7, pp. 1175–1193, 1998.
- [125] M. Kowalski, P. J. Spencer, and D. Neuschuetz, “Phase diagrams,” in *Slag Atlas*, 2nd ed., Duesseldorf, Germany: Verlag Stahleisen GmbH, 1995, pp. 21 – 214.
- [126] E. W. Weisstein, “Spherical Cap,” *MathWorld--A Wolfram Web Resource*. [Online]. Available: <http://mathworld.wolfram.com/SphericalCap.html>. [Accessed: 11-Mar-2014].

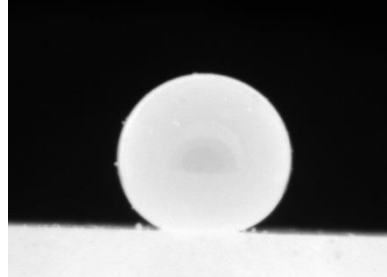
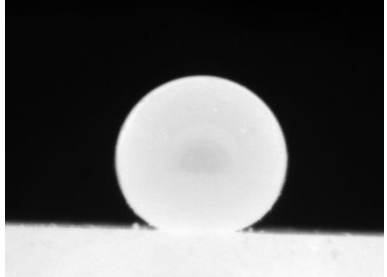
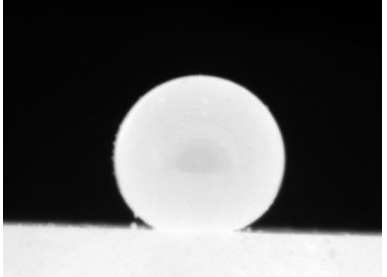
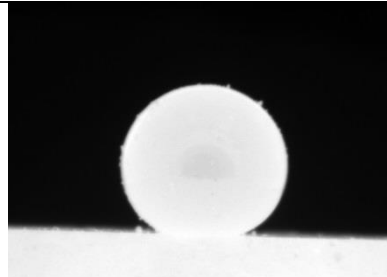
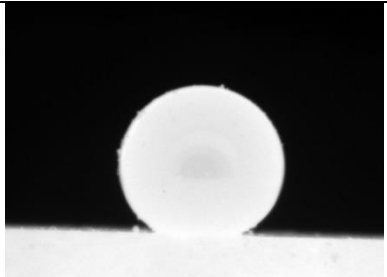
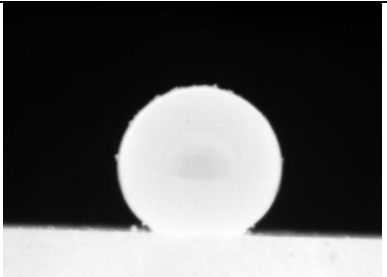
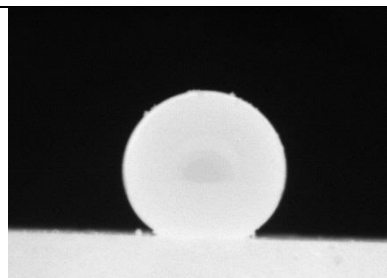
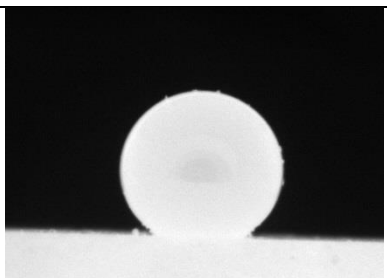
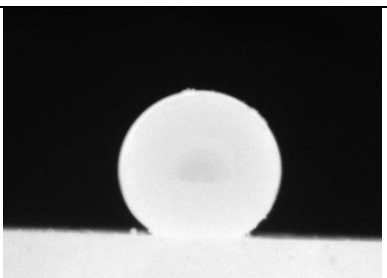
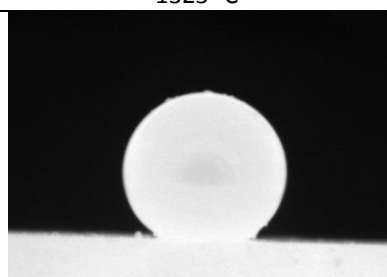
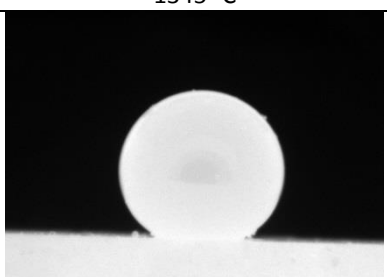
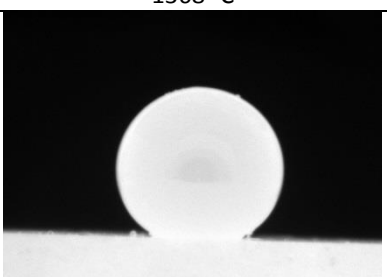
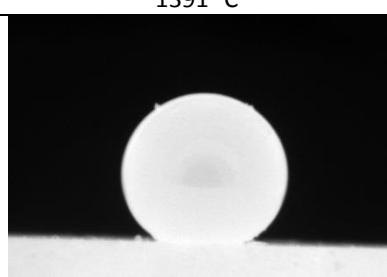
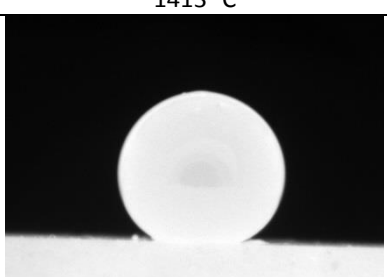
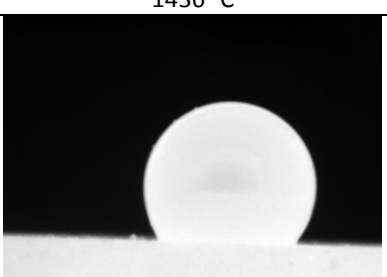
- [127] G. Parry and O. Ostrovski, "Wettability of solid metals by molten MnO-SiO₂ slag," *Metall. Mater. Trans. B Process Metall. Mater. Process. Sci.*, vol. 39, no. 5, pp. 669–680, 2008.
- [128] G. C. Allen and J. A. Jutson, "Carbon deposition on iron-manganese-chromium spinels," *J. Mater. Chem.*, vol. 1, no. 1, pp. 73–78, 1991.
- [129] K. C. Mills, A. B. Fox, Z. Li, and R. P. Thackray, "Performance and properties of mould fluxes," *Ironmak. Steelmak.*, vol. 32, no. 1, pp. 26–34, 2005.
- [130] E. Wei, Y. Yang, C. Feng, I. Sommerville, and A. McLean, "Effect of carbon properties on melting behaviour of mold fluxes for continuous casting of steels," *Int. J. Iron Steel Res.*, vol. 13, no. 2, pp. 22–26, 2006.
- [131] R. Clift, J. R. Grace, and M. E. Weber, *Bubbles, drops and particles*. New York, USA: Academic Press, 1978, pp. 30–47.
- [132] A. Warczok and T. A. Utigard, "Settling of copper drops in molten slags," *Metall. Mater. Trans. B Process Metall. Mater. Process. Sci.*, vol. 26, no. 6, pp. 1165–1173, 1995.
- [133] W. S. Rasband, "ImageJ," *U. S. National Institutes of Health, Bethesda, Maryland, USA*. [Online]. Available: <http://imagej.nih.gov/ij/>. [Accessed: 16-Jan-2014].
- [134] J. Goldstein, D. Newbury, D. Joy, C. Lyman, P. Echlin, E. Lifshin, L. Sawyer, and J. Michael, *Scanning electron microscopy and X-Ray microanalysis*, 3rd ed. Springer, 2003.
- [135] A. Fickel, "Silicon-carbide minerals," in *Pocket Manual , Refractory Materials, Basics - Structures - Properties*, 2nd ed., G. Routschka, Ed. Essen, Germany: Vulkan-Verlag, 2004, pp. 84–89.
- [136] J. Steenkamp, M. Tangstad, P. Pistorius, H. Mølnås, and J. Muller, "Corrosion of taphole carbon refractory by CaO-MnO-SiO₂-Al₂O₃-MgO slag from a SiMn production furnace," in *INFACON XIII*, 2013, pp. 669–676.
- [137] Anonymous, "Real time wind and weather report eMalahleni (9 January 2014 to 15 January 2014)," 2014. [Online]. Available: www.windfinder.com. [Accessed: 16-Jan-2014].
- [138] K. Asano, "Heat and mass transfer in a laminar flow inside a circular pipe," in *Mass transfer: From Fundamentals to Modern Industrial Applications*, Weinheim: WILEY-VCH Verlag GmbH & Co, 2006, pp. 89–100.
- [139] Y. Liang, "Models and experiments for multicomponent chemical diffusion in molten silicates," University of Chicago, 1994.
- [140] C. Dumay and A. W. Cramb, "Density and interfacial tension of liquid Fe-Si alloys," *Metall. Mater. Trans. B*, vol. 26B, no. February, pp. 173–176, 1995.

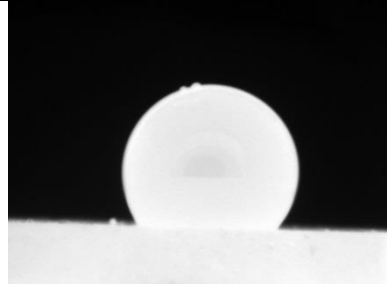
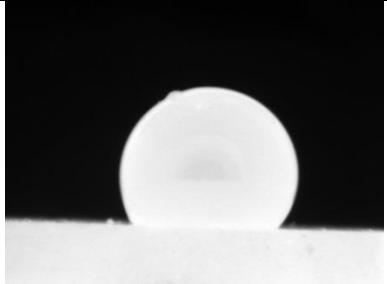
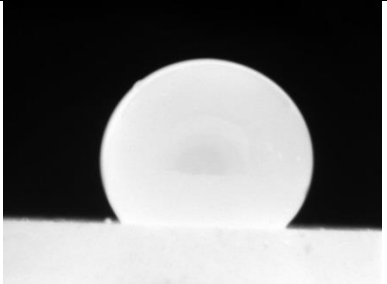
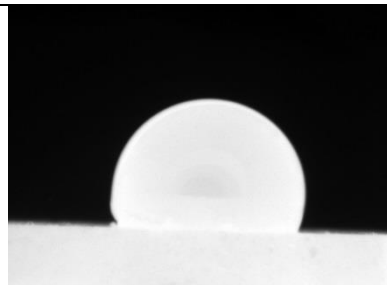
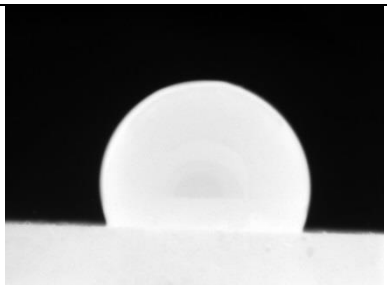
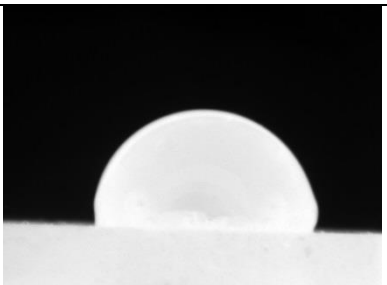
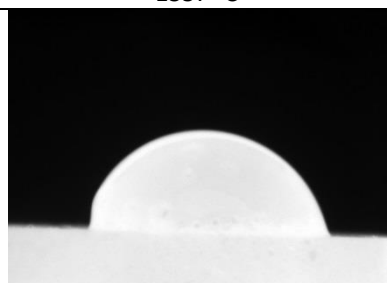
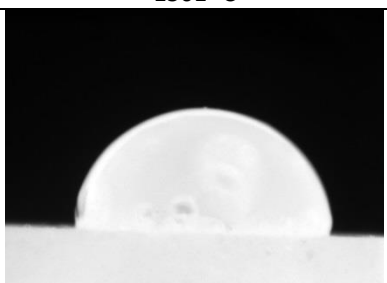

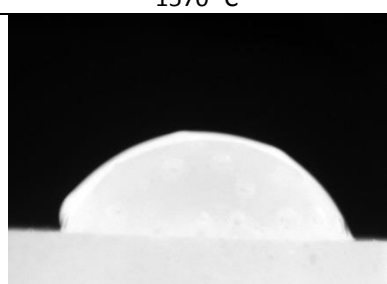
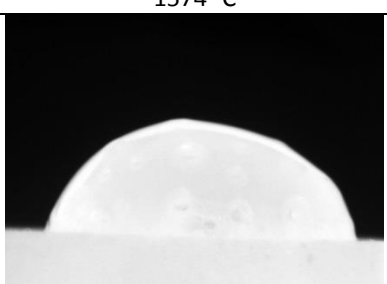
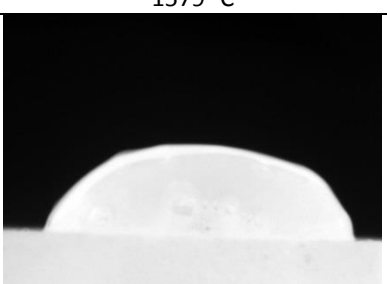
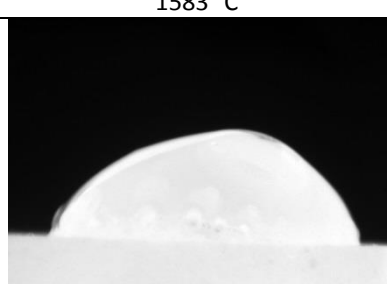
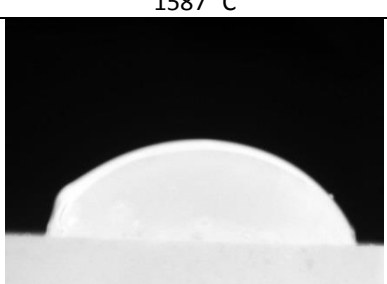
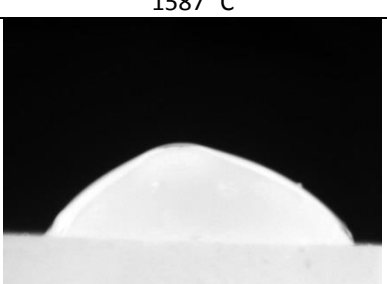
- [141] N. K. Dzhemilev, S. I. Popel, and B. V. Tsarevskii, "The density and surface tension isotherms of manganese-silicon melts," *Sov. powder Metall. Met. Ceram.*, vol. 4, no. 10, pp. 838–840, 1965.
- [142] A. F. Crawley, "Density of liquid metals and alloys," *Int. Metall. Rev.*, vol. 19, pp. 32–48, 1974.
- [143] P. M. Nasch and S. G. Steinemann, "Density and thermal expansion of molten Manganese, Iron, Nickel, Copper, Aluminum and Tin by means of the gamma-ray attenuation technique," *Phys. Chem. Liq. An Int. J.*, vol. 29, pp. 43–58, 1995.
- [144] I. Jimbo and A. W. Cramb, "The density of liquid iron-carbon alloys," *Metall. Mater. Trans. B*, vol. 24B, no. February, pp. 5–10, 1993.

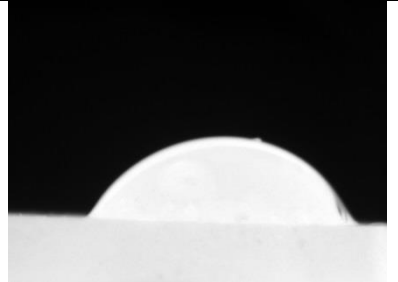
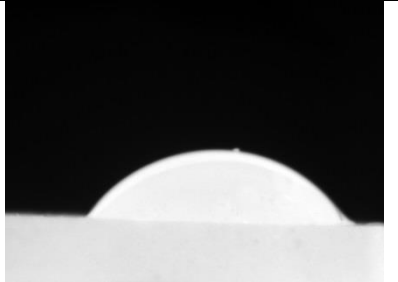
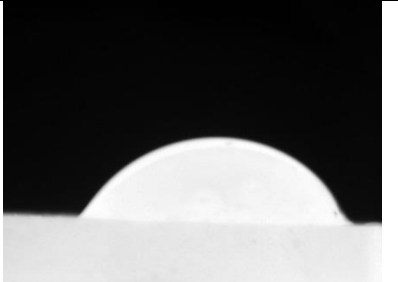
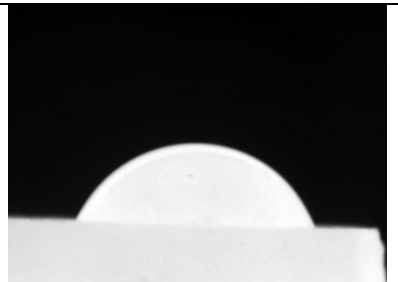
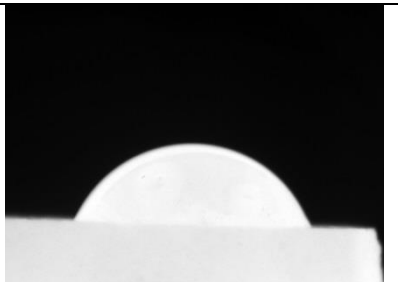
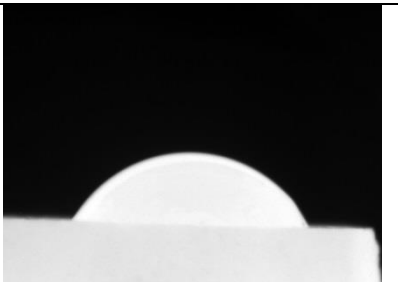
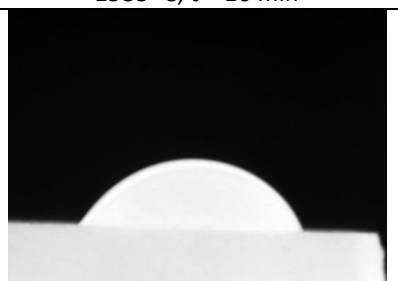
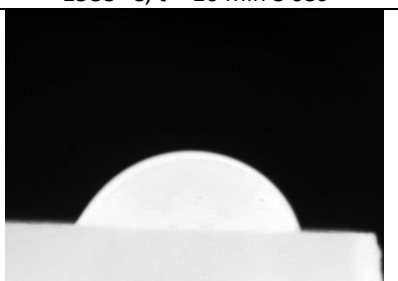
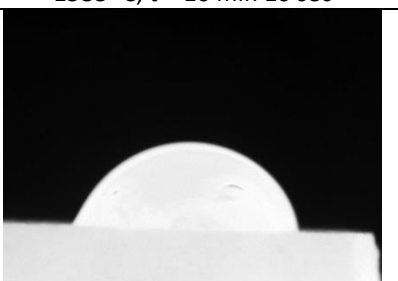
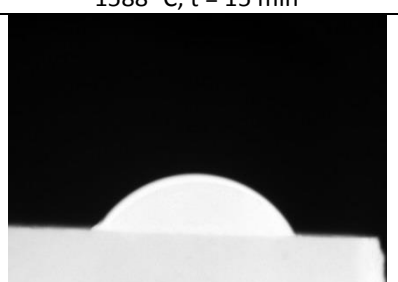
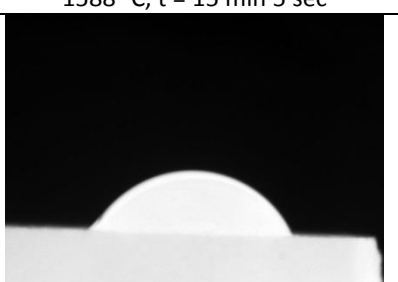
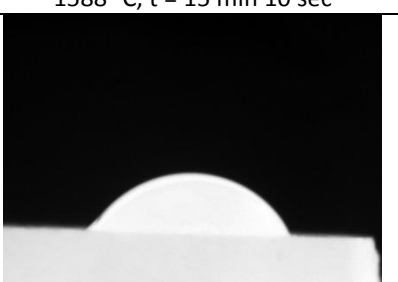
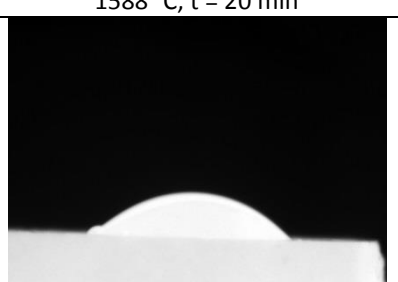
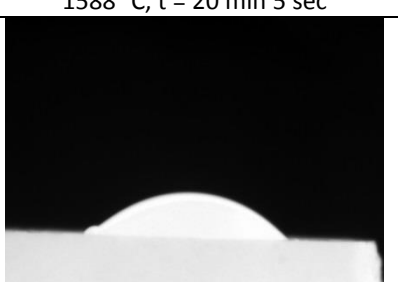
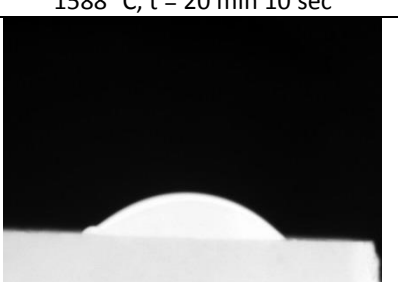
11 Appendix A: Summary of wettability results

11.1 Synthetic slag on ramming paste matrix in Ar-gas

Table 66: Synthetic slag on ramming paste matrix substrate in an argon atmosphere held at 1588°C.

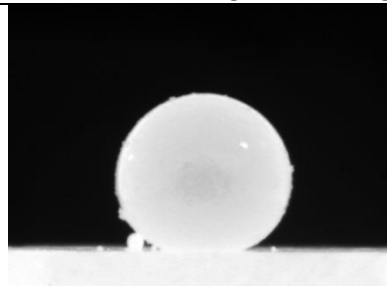
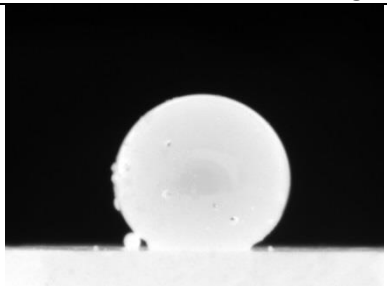
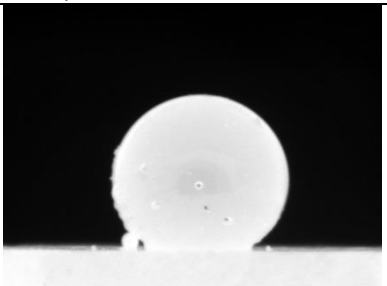
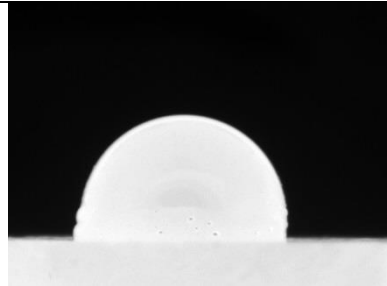
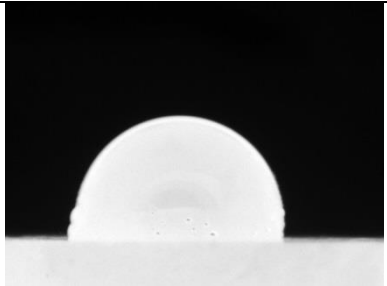
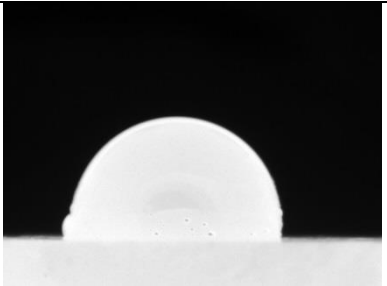
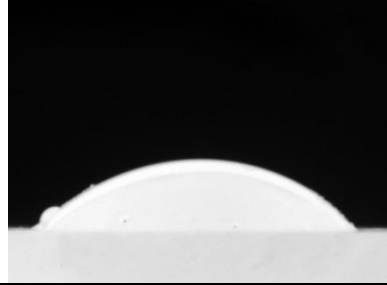
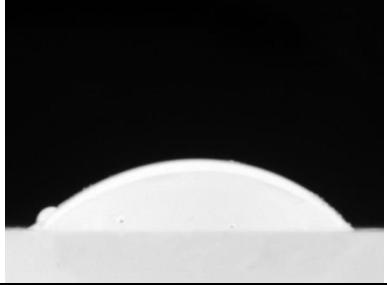
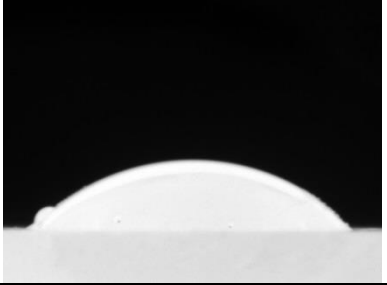
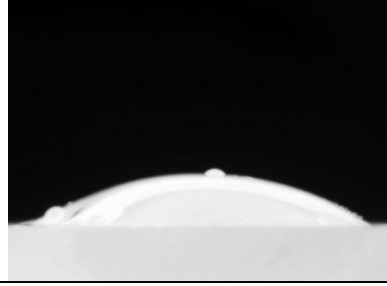
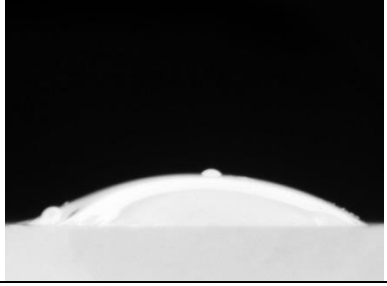
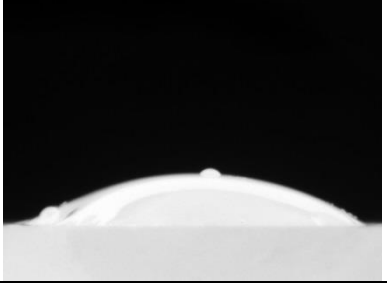
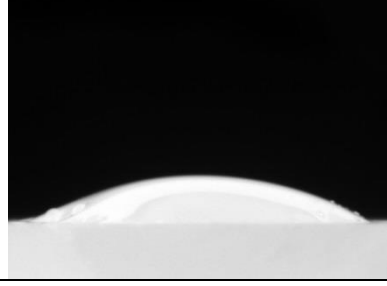
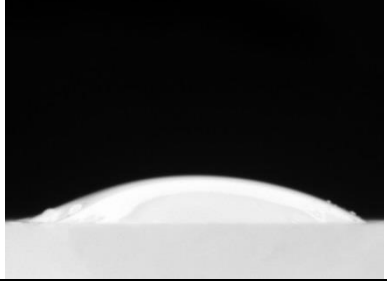
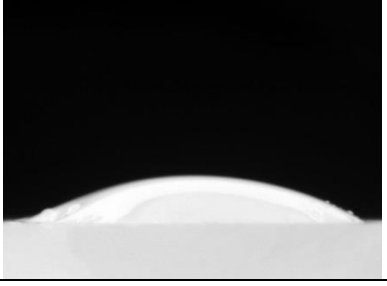
Synthetic slag on ramming paste matrix substrate in an argon atmosphere held at 1588°C		
		
1189 °C	1211 °C	1234 °C
		
1256 °C	1279 °C	1301 °C
		
1323 °C	1345 °C	1368 °C
		
1391 °C	1413 °C	1436 °C
		

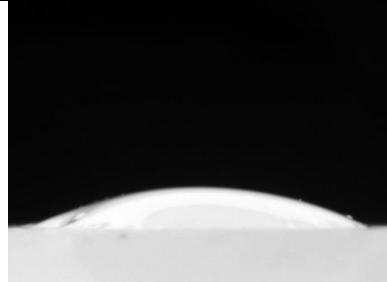
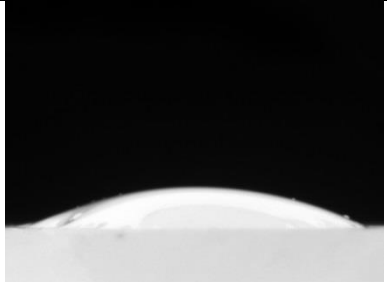
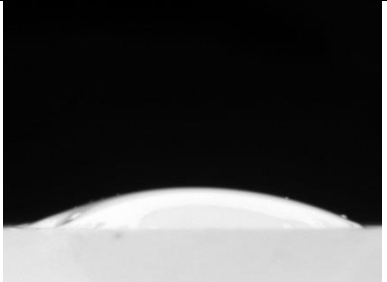
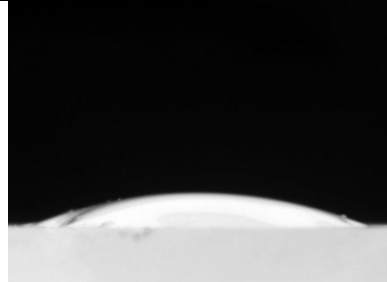
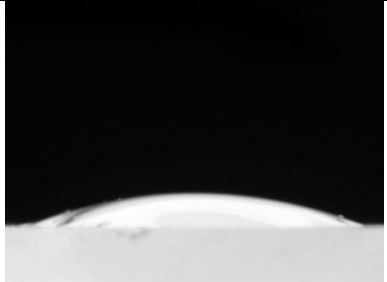
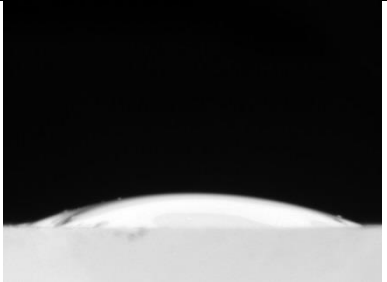
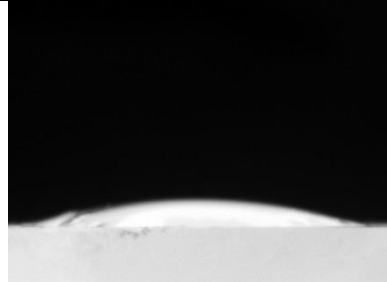
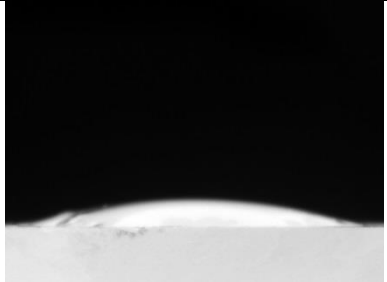
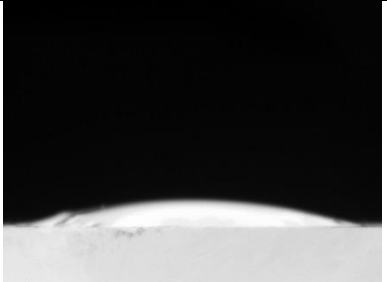
Synthetic slag on ramming paste matrix substrate in an argon atmosphere held at 1588°C		
1459 °C	1481 °C	1504 °C
		
1526 °C	1547 °C	1553 °C
		
1557 °C	1561 °C	1565 °C
		
1570 °C	1574 °C	1579 °C
		
1583 °C	1587 °C	1587 °C
		
1588 °C, t = 0 min	1588 °C, t = 0 min 5 sec	1588 °C, t = 0 min 10 sec

Synthetic slag on ramming paste matrix substrate in an argon atmosphere held at 1588°C		
		
1588 °C, t = 5 min	1588 °C, t = 5 min 5 sec	1588 °C, t = 5 min 10 sec
		
1588 °C, t = 10 min	1588 °C, t = 10 min 5 sec	1588 °C, t = 10 min 10 sec
		
1588 °C, t = 15 min	1588 °C, t = 15 min 5 sec	1588 °C, t = 15 min 10 sec
		
1588 °C, t = 20 min	1588 °C, t = 20 min 5 sec	1588 °C, t = 20 min 10 sec
		
1588 °C, t = 25 min	1588 °C, t = 25 min 5 sec	1588 °C, t = 25 min 10 sec

11.2 Industrial slag on ramming paste matrix in Ar-gas

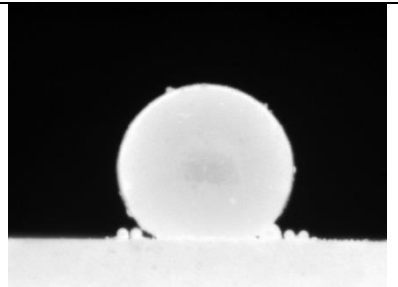
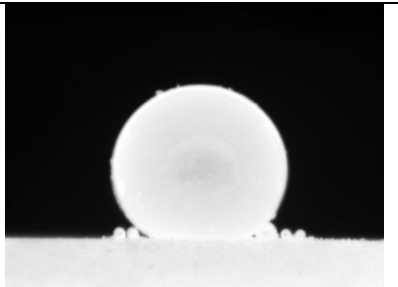
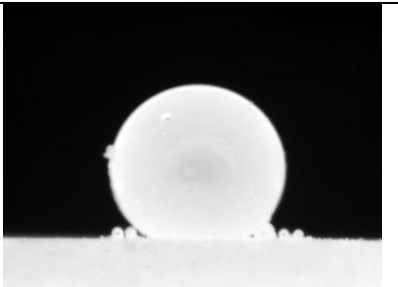
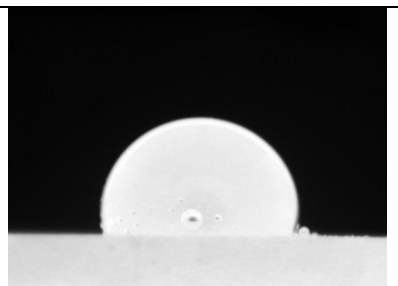
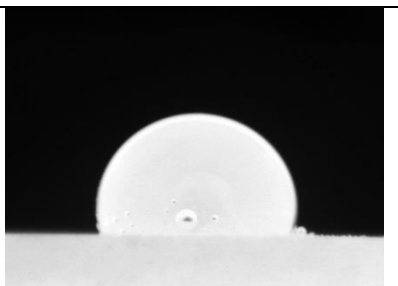
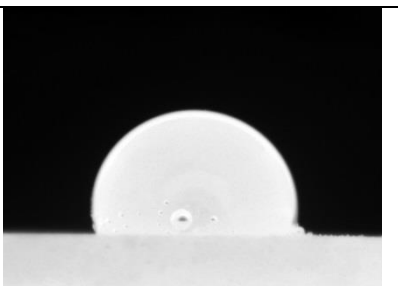
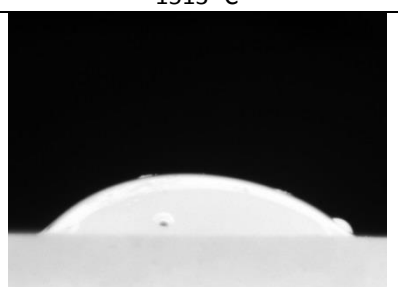
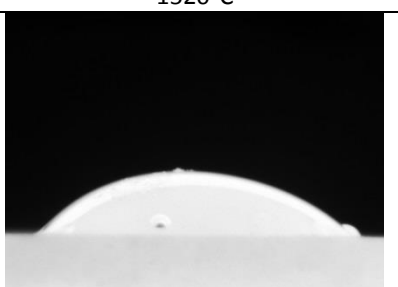
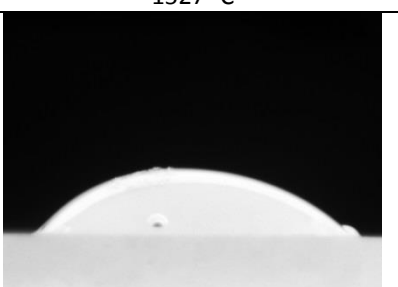
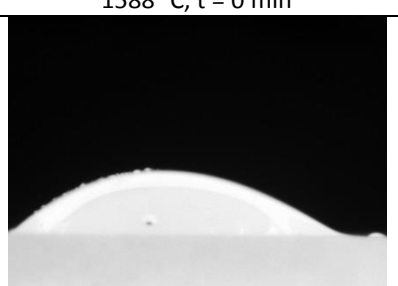
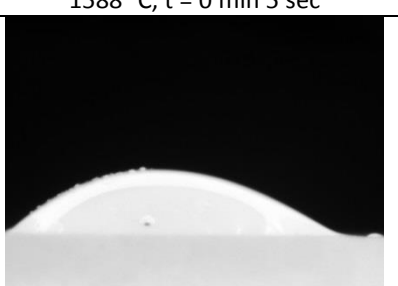
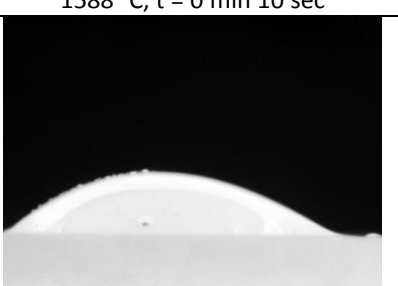
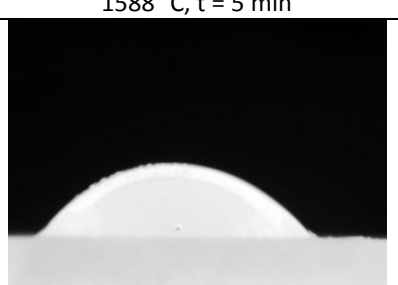
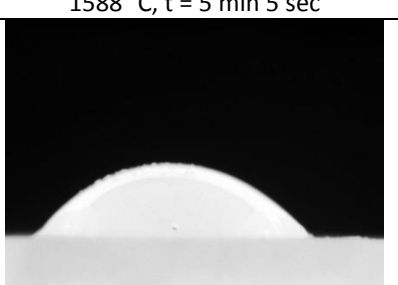
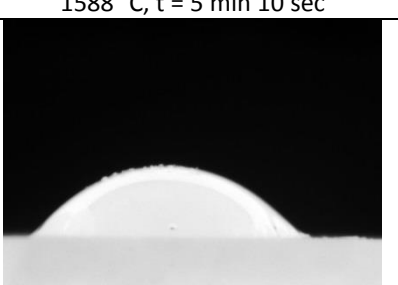
Table 67: Industrial slag on ramming paste matrix substrate in an argon atmosphere held at 1588°C.

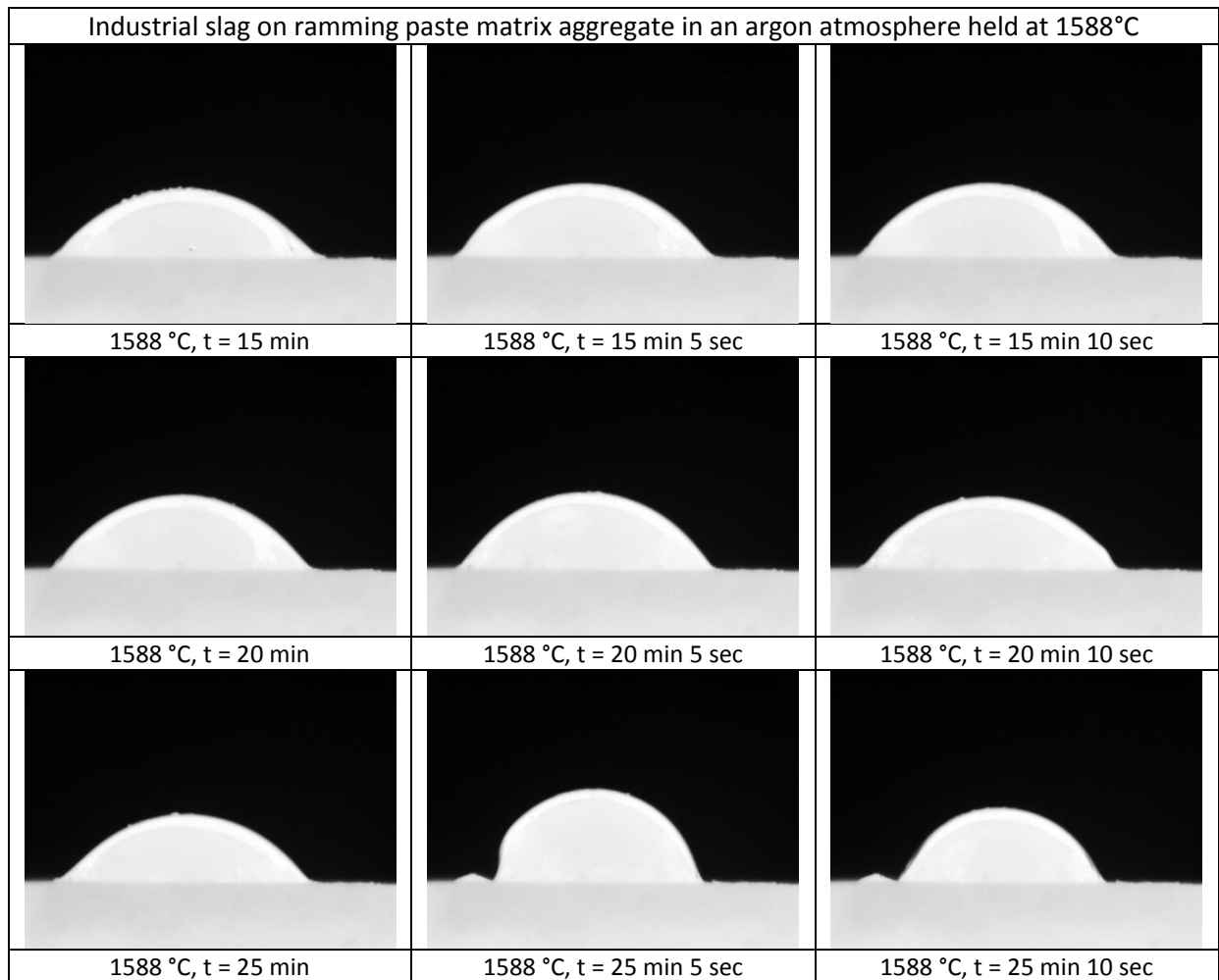
Industrial slag on ramming paste matrix substrate in an argon atmosphere held at 1588°C		
		
1215 °C	1253 °C	1269 °C
		
1503 °C	1510 °C	1518 °C
		
1588 °C, t = 0 min	1588 °C, t = 0 min 5 sec	1588 °C, t = 0 min 10 sec
		
1588 °C, t = 5 min	1588 °C, t = 5 min 5 sec	1588 °C, t = 5 min 10 sec
		
1588 °C, t = 10 min	1588 °C, t = 10 min 5 sec	1588 °C, t = 10 min 10 sec

Industrial slag on ramming paste matrix substrate in an argon atmosphere held at 1588°C		
		
1588 °C, t = 15 min	1588 °C, t = 15 min 5 sec	1588 °C, t = 15 min 10 sec
		
1588 °C, t = 20 min	1588 °C, t = 20 min 5 sec	1588 °C, t = 20 min 10 sec
		
1588 °C, t = 25 min	1588 °C, t = 25 min 5 sec	1588 °C, t = 25 min 10 sec

11.3 Industrial slag on ramming paste aggregate in Ar-gas

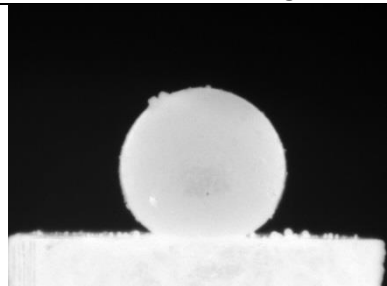
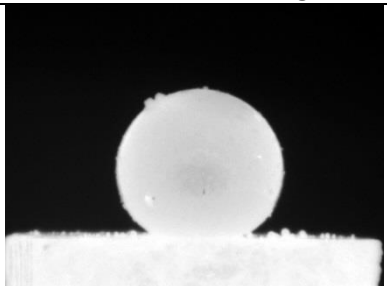
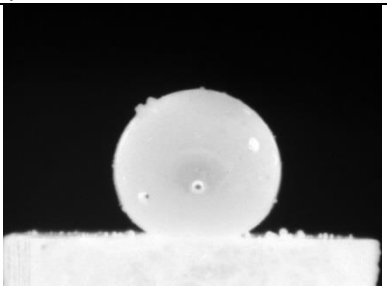
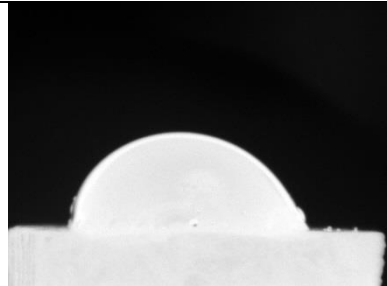
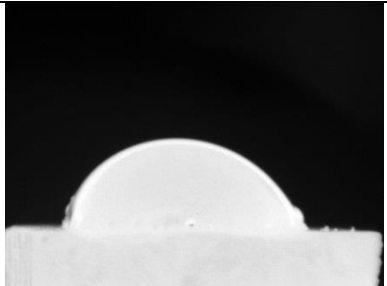
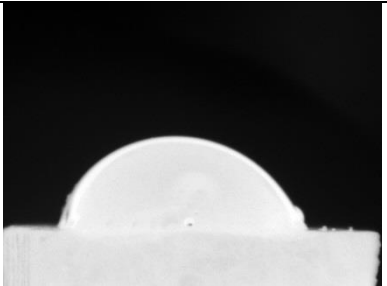
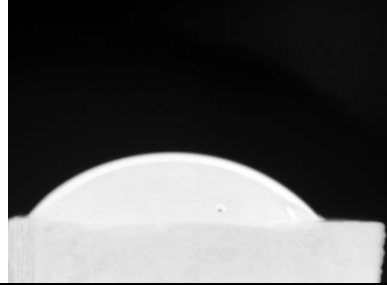
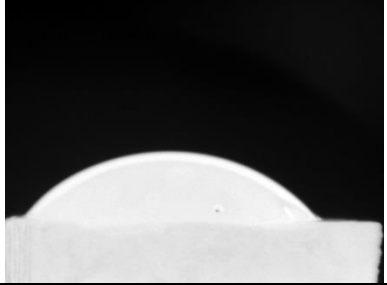
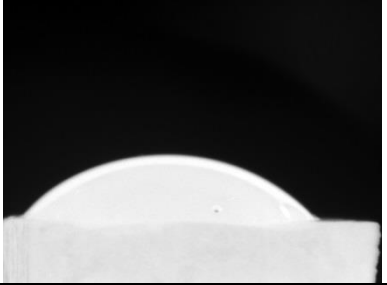
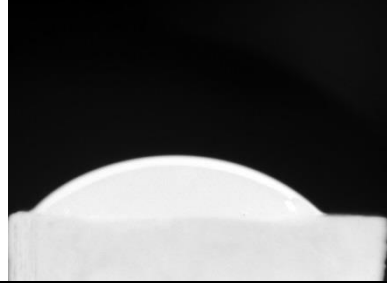
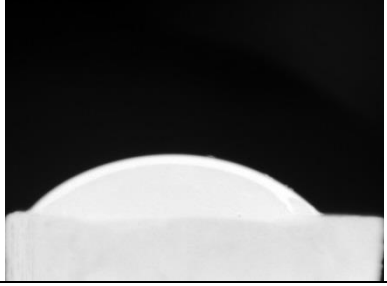
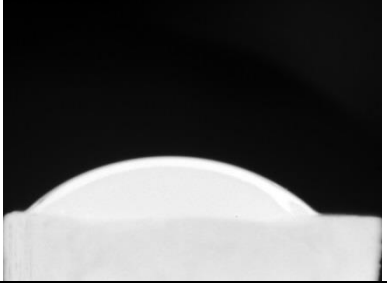
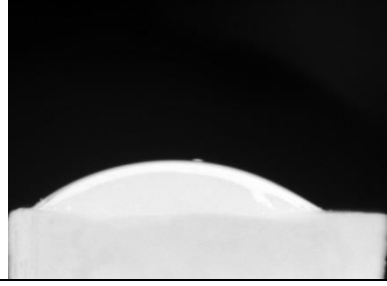
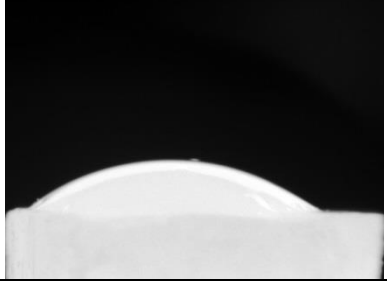
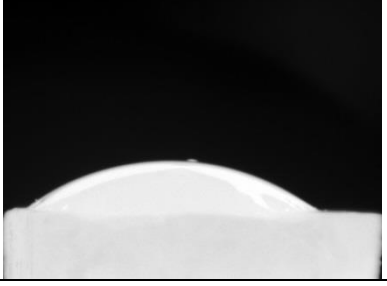
Table 68: Industrial slag on ramming paste aggregate substrate in an argon atmosphere held at 1588°C.

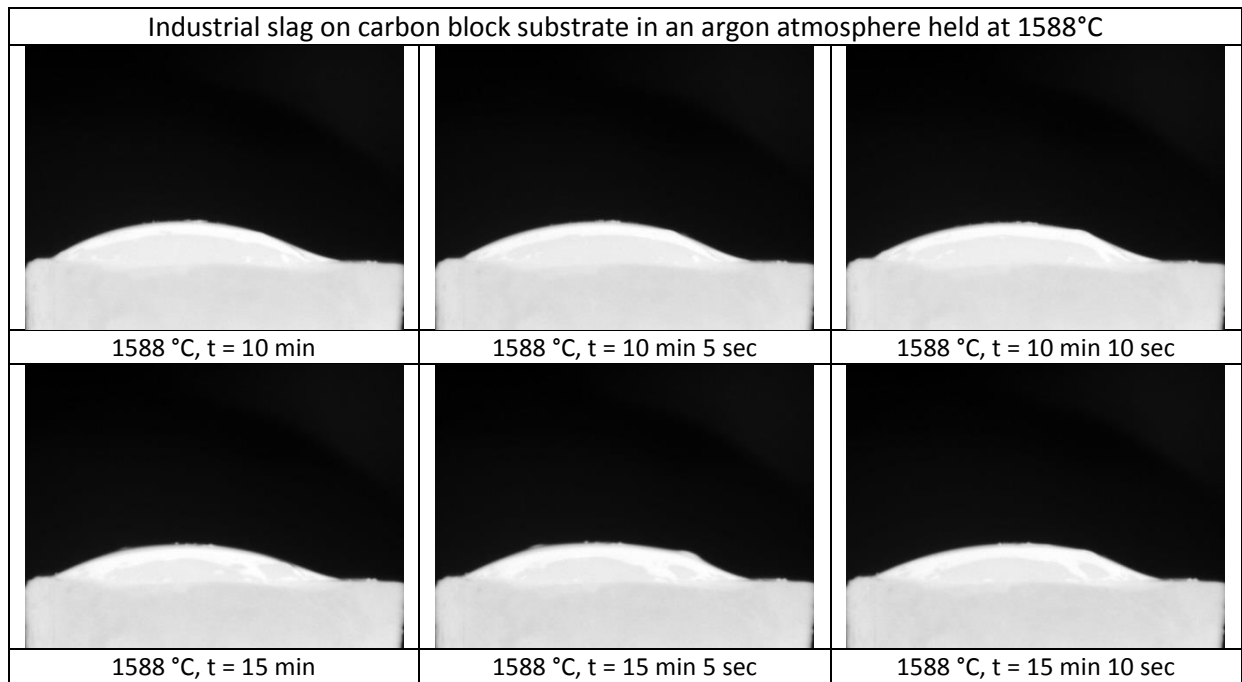
Industrial slag on ramming paste matrix aggregate in an argon atmosphere held at 1588°C		
		
1211 °C	1263 °C	1279 °C
		
1513 °C	1520 °C	1527 °C
		
1588 °C, t = 0 min	1588 °C, t = 0 min 5 sec	1588 °C, t = 0 min 10 sec
		
1588 °C, t = 5 min	1588 °C, t = 5 min 5 sec	1588 °C, t = 5 min 10 sec
		
1588 °C, t = 10 min	1588 °C, t = 10 min 5 sec	1588 °C, t = 10 min 10 sec



11.4 Industrial slag on carbon block in Ar-gas

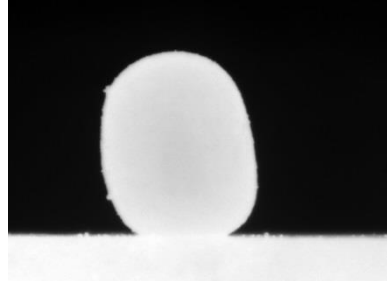
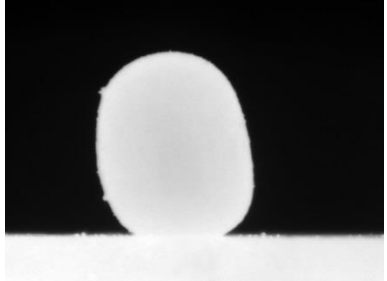
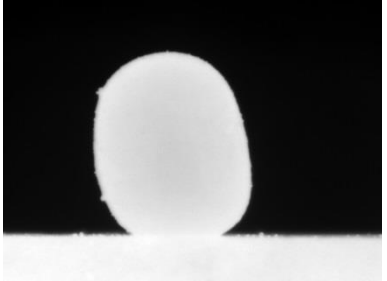
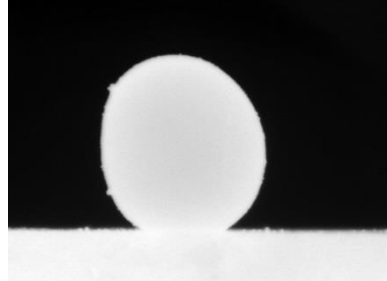
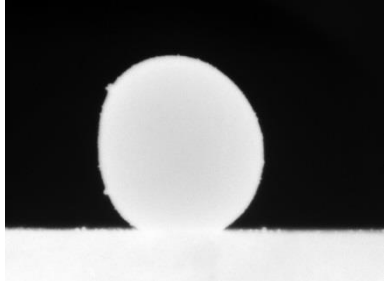
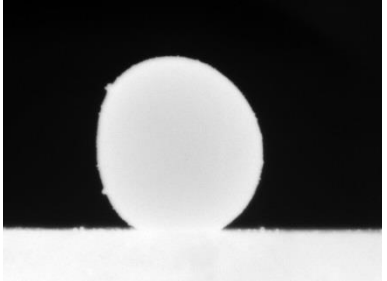
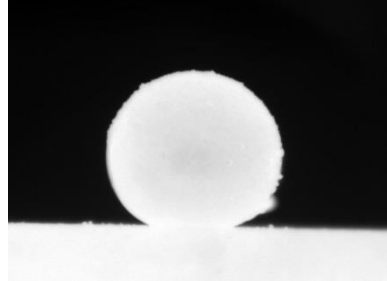
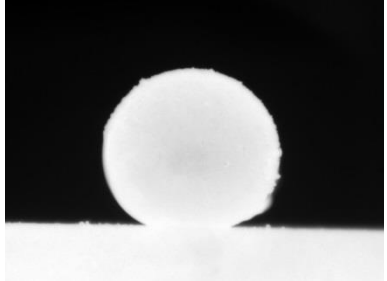
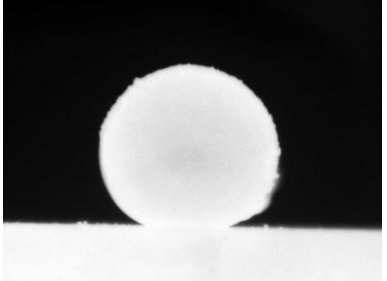
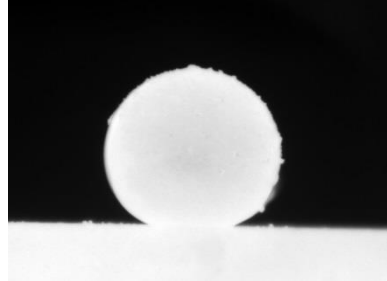
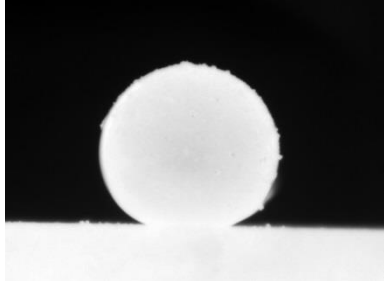
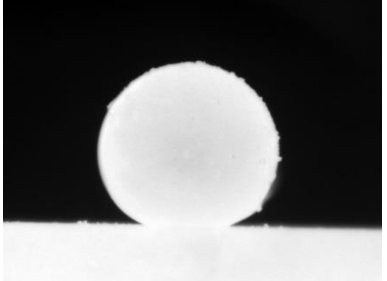
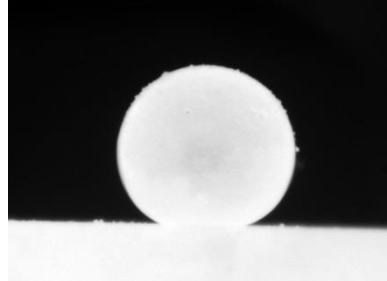
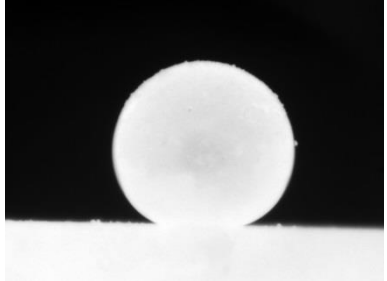
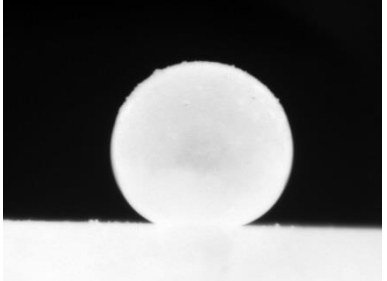
Table 69: Industrial slag on carbon block substrate in an argon atmosphere held at 1588°C.

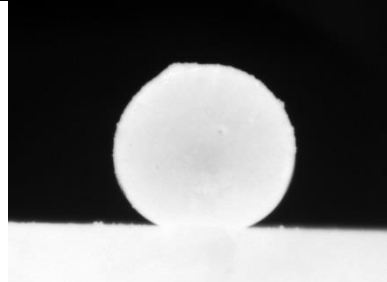
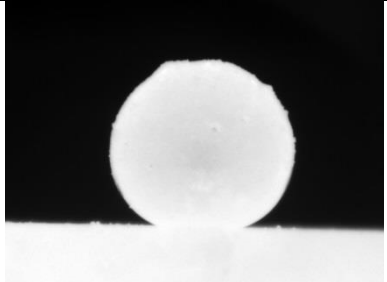
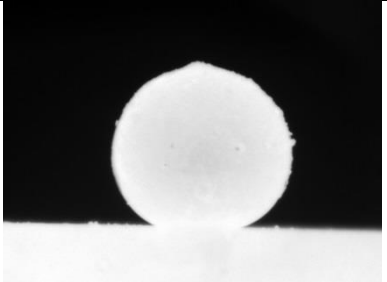
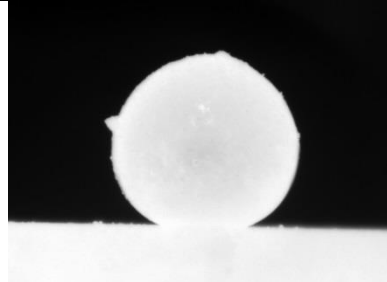
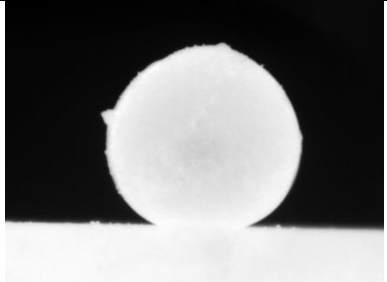
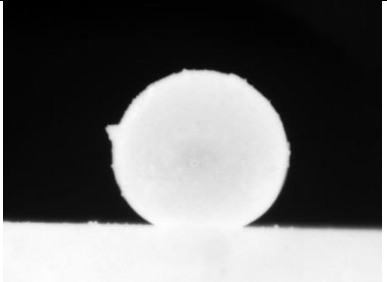
Industrial slag on carbon block substrate in an argon atmosphere held at 1588°C		
		
1220 °C	1222 °C	1228 °C
		
1462 °C	1470 °C	1477 °C
		
1580 °C	1581 °C	1583 °C
		
1588 °C, t = 0 min	1588 °C, t = 0 min 5 sec	1588 °C, t = 0 min 10 sec
		
1588 °C, t = 5 min	1588 °C, t = 5 min 5 sec	1588 °C, t = 5 min 10 sec



11.5 Industrial slag on ramming paste matrix in CO-gas

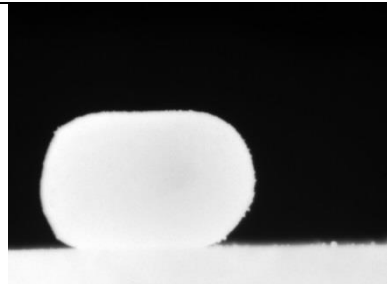
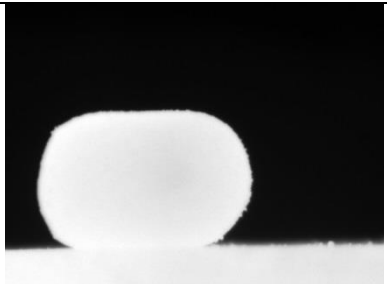
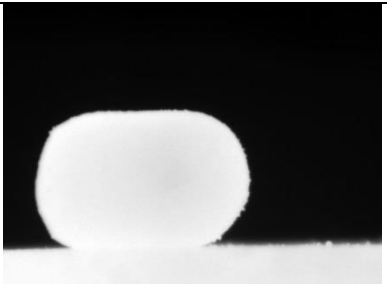
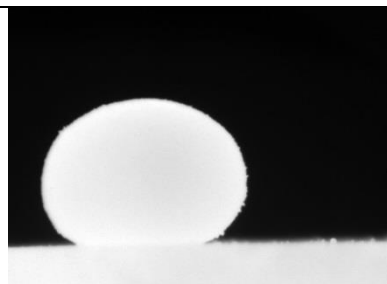
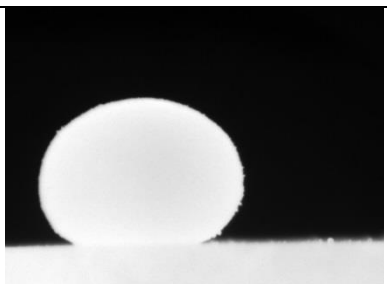
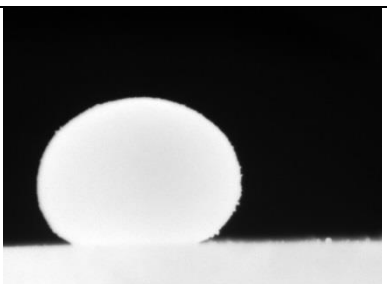
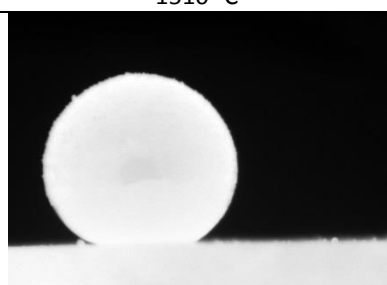
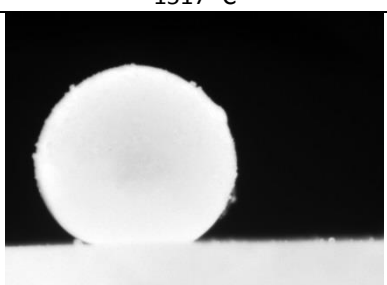
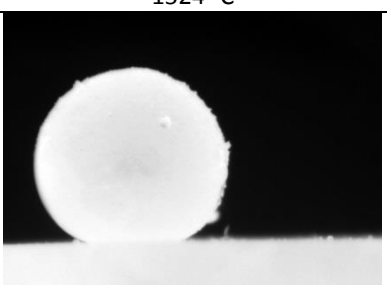
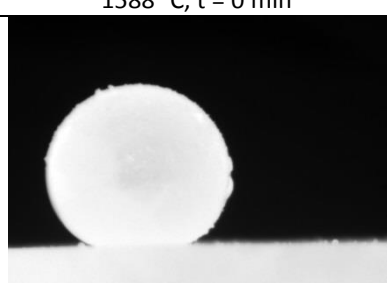
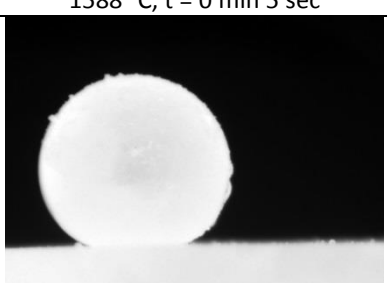
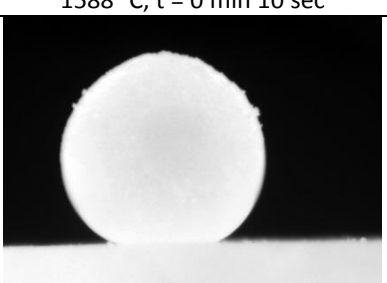
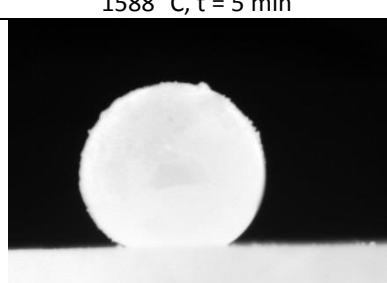
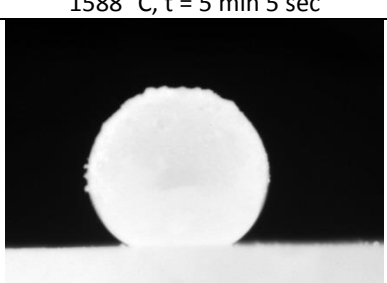
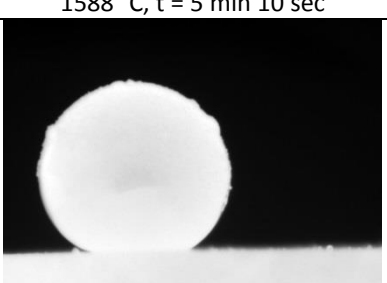
Table 70: Industrial slag on ramming paste matrix substrate in a CO-gas atmosphere held at 1588°C.

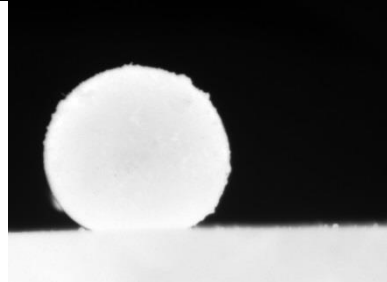
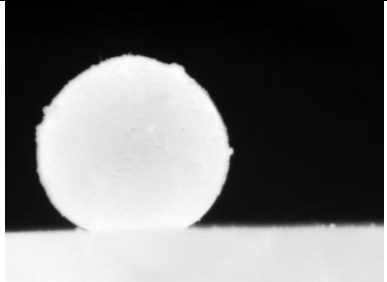
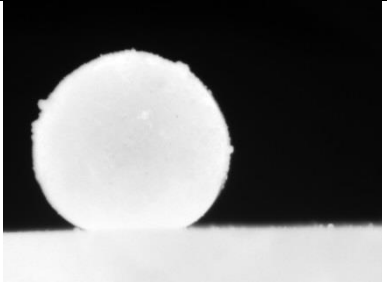
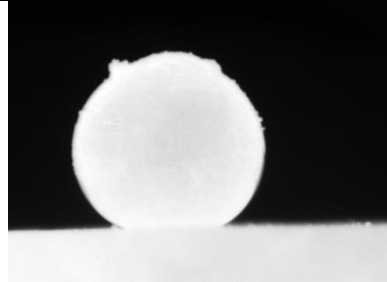
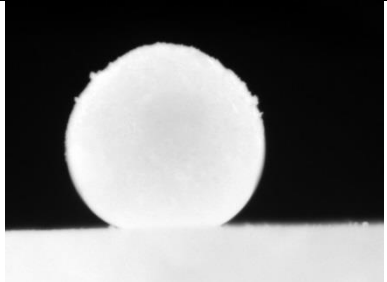
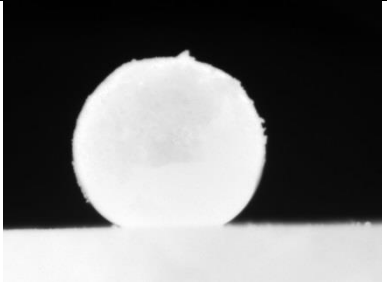
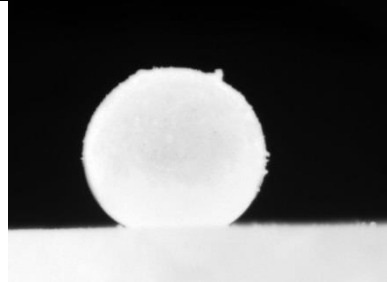
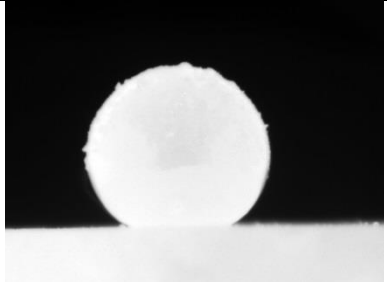
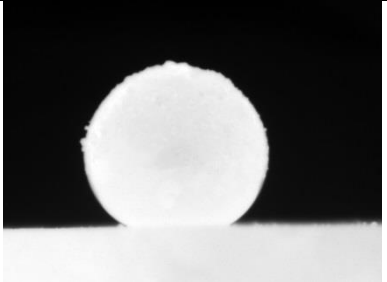
Industrial slag on ramming paste matrix substrate in a CO-gas atmosphere held at 1588°C		
		
1246 °C	1253 °C	1261 °C
		
1495 °C	1502 °C	1510 °C
		
1588 °C, t = 0 min	1588 °C, t = 0 min 5 sec	1588 °C, t = 0 min 10 sec
		
1588 °C, t = 5 min	1588 °C, t = 5 min 5 sec	1588 °C, t = 5 min 10 sec
		
1588 °C, t = 10 min	1588 °C, t = 10 min 5 sec	1588 °C, t = 10 min 10 sec

Industrial slag on ramming paste matrix substrate in a CO-gas atmosphere held at 1588°C		
		
1588 °C, t = 15 min	1588 °C, t = 15 min 5 sec	1588 °C, t = 15 min 10 sec
		
1588 °C, t = 20 min	1588 °C, t = 20 min 5 sec	1588 °C, t = 20 min 10 sec

11.6 Industrial slag on ramming paste aggregate in CO-gas

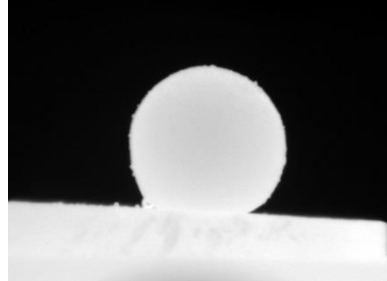
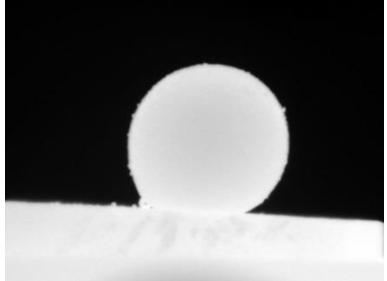
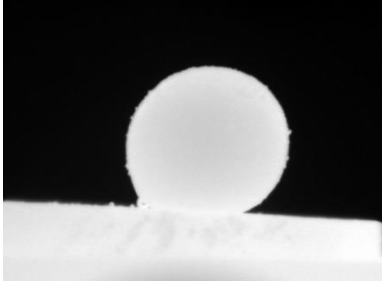
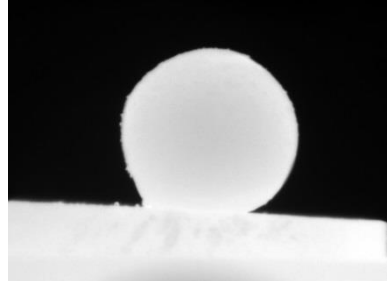
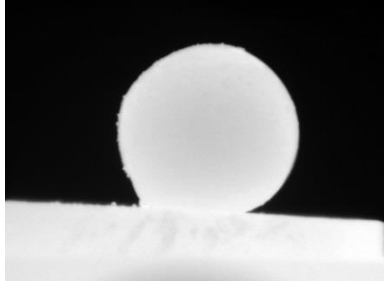
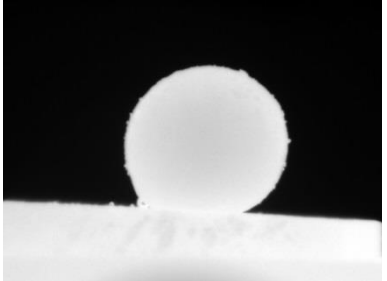
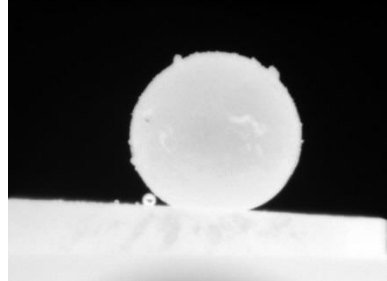
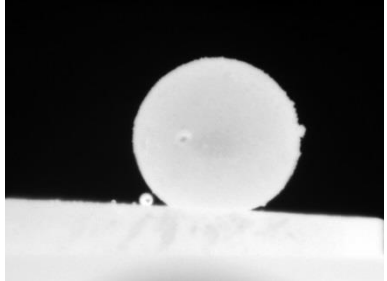
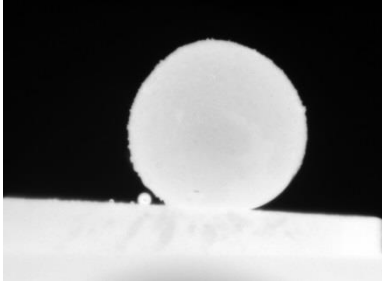
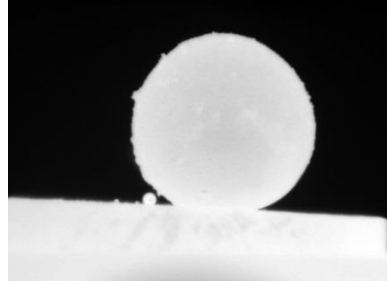
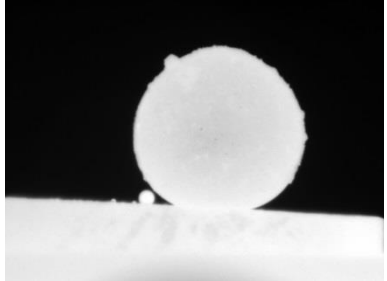
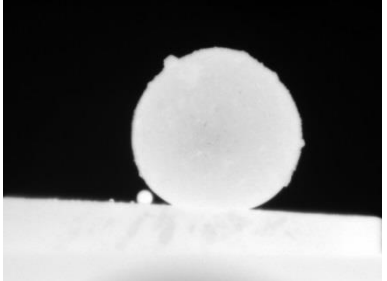
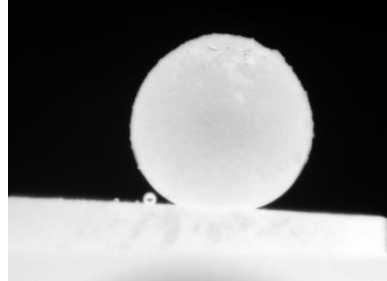
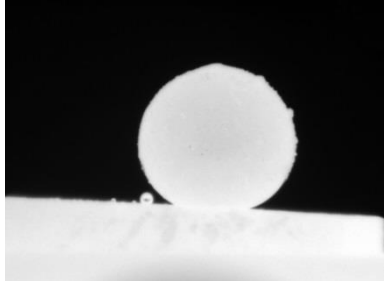
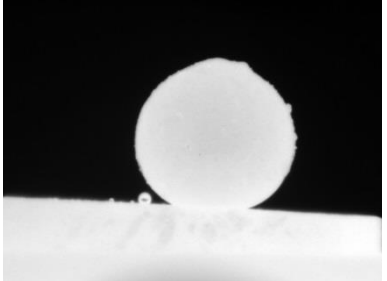
Table 71: Industrial slag on ramming paste aggregate substrate in a CO-gas atmosphere held at 1588°C.

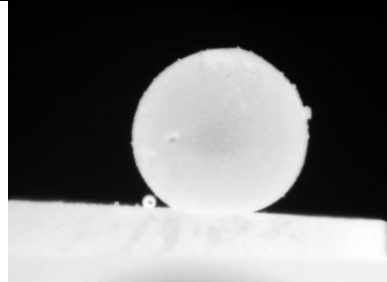
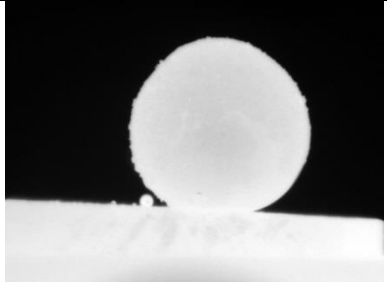
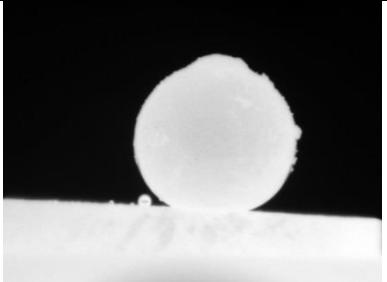
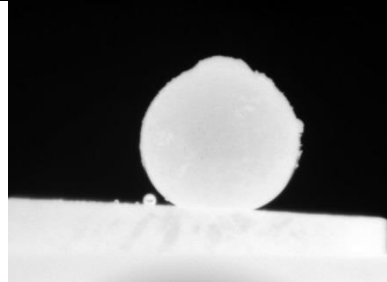
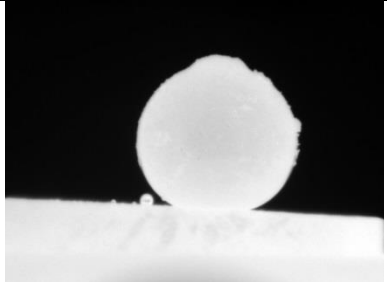
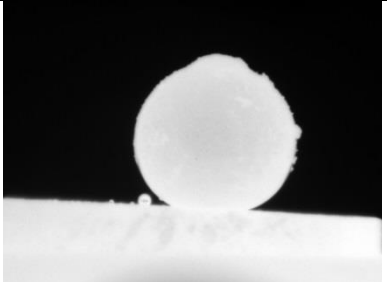
Industrial slag on ramming paste matrix aggregate in a CO-gas atmosphere held at 1588°C		
		
1260 °C	1267 °C	1274 °C
		
1510 °C	1517 °C	1524 °C
		
1588 °C, t = 0 min	1588 °C, t = 0 min 5 sec	1588 °C, t = 0 min 10 sec
		
1588 °C, t = 5 min	1588 °C, t = 5 min 5 sec	1588 °C, t = 5 min 10 sec
		
1588 °C, t = 10 min	1588 °C, t = 10 min 5 sec	1588 °C, t = 10 min 10 sec

Industrial slag on ramming paste matrix aggregate in a CO-gas atmosphere held at 1588°C		
		
1588 °C, t = 15 min	1588 °C, t = 15 min 5 sec	1588 °C, t = 15 min 10 sec
		
1588 °C, t = 20 min	1588 °C, t = 20 min 5 sec	1588 °C, t = 20 min 10 sec
		
1588 °C, t = 25 min	1588 °C, t = 25 min 5 sec	1588 °C, t = 25 min 10 sec

11.7 Industrial slag on carbon block in CO-gas

Table 72: Industrial slag on carbon block substrate in a CO-gas atmosphere held at 1588°C.

Industrial slag on carbon block substrate in a CO-gas atmosphere held at 1588°C		
		
1579 °C	1582 °C	1585 °C
		
1588 °C, t = 0 min	1588 °C, t = 0 min 5 sec	1588 °C, t = 0 min 10 sec
		
1588 °C, t = 5 min	1588 °C, t = 5 min 5 sec	1588 °C, t = 5 min 10 sec
		
1588 °C, t = 10 min	1588 °C, t = 10 min 5 sec	1588 °C, t = 10 min 10 sec
		
1588 °C, t = 15 min	1588 °C, t = 15 min 5 sec	1588 °C, t = 15 min 10 sec

Industrial slag on carbon block substrate in a CO-gas atmosphere held at 1588°C		
		
1588 °C, t = 20 min	1588 °C, t = 20 min 5 sec	1588 °C, t = 20 min 10 sec
		
1588 °C, t = 25 min	1588 °C, t = 25 min 5 sec	1588 °C, t = 25 min 10 sec

12 Appendix B: Density calculations for liquid metal phase

The estimate of the density of the liquid metal phase was based on the assumptions that:

1. The total volume of the alloy is simply the sum of the volumes of pure Mn, Fe and Si. This assumption is not entirely true as the molar volume of FeSi and SiMn alloys shows a strong negative deviation (of up to 15%) from the ideal as indicated in Figure 117 [140]–[142];

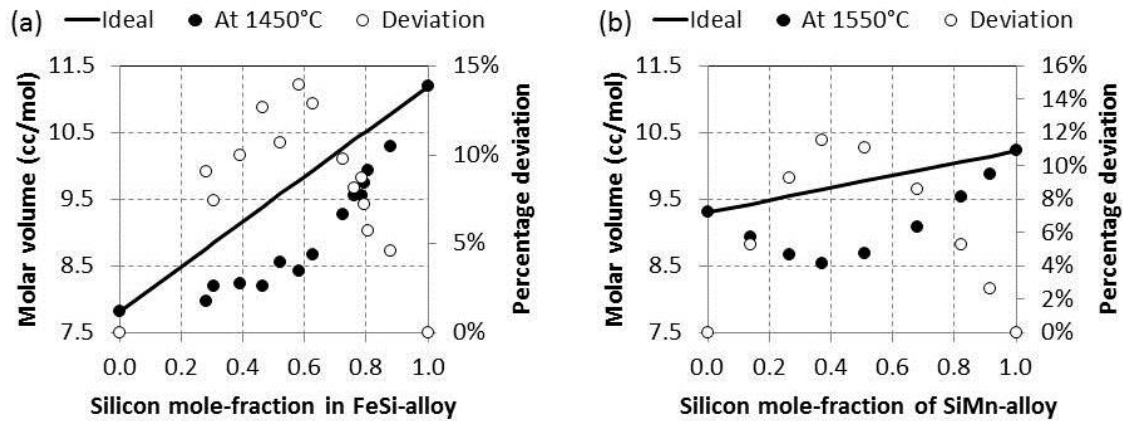


Figure 117: Molar volume of (a) FeSi-alloy measured at 1450°C and (b) SiMn-alloy measured at 1550°C, with ideal relationship shown.

2. The density calculated as such is adjusted for carbon by assuming that the density decrease due to the presence of 2%C in the alloy is the same as the factor by which the density of Fe-2%C is lower than that of pure liquid Fe;
3. Composition of metal stated in Table 73.

Table 73: Metal composition applied in calculation of density of metal (ρ_{metal}).

	Mass %				
	Mn	Si	Fe	C	Total
4-component	68.0	20.0	10.0	2.0	100
3-component	69.4	20.4	10.2	0.0	100

The density of each pure metal component was calculated according to Equation 35.

Equation 35: density of pure liquid metal as a function of temperature ($\rho(T)$) [142], [143]

$$\rho(T) = a + b (T - T_{mp})$$

Table 74: Definition of variables applied in Equation 35 and densities calculated at 1600°C.

Variable	Description	Unit	Mn	Fe	Reference	Si	Reference
T_{mp}	Melting point	K	1525	1809	[142]	1683	[142]
a	Density at melting point	kg/m ³	5.95	6.98	[143]	2.524	[142]
b	Change in density with change in temperature	kg/(m ³ .K)	-10.53 x 10 ⁻⁴	-5.72 x 10 ⁻⁴	[143]	-3.487 x 10 ⁻⁴	[142]

The density of the 3-component metal is calculated as shown in Table 75.

Table 75: Density of the 3-component metal.

Variable	Description	Unit	Mn	Si	Fe	Metal
m	mass	ton	69.4	20.4	10.2	100
ρ (1873)	Density at 1600°C	ton/m ³	5.58	2.46	6.94	4.504
V	volume	m ³	12.43	8.30	1.47	22.2

The decrease in density due to the presence of carbon (Table 76) was calculated by applying Equation 36 where the density of liquid Fe-C alloys as a function of carbon content (percentage by mass) and temperature (K) derived by [144] from experimental data in the ranges 0%C - 4%C and 1250°C - 1550°C.

Equation 36: Density of liquid Fe-C alloys as a function of carbon content and temperature [144]

$$\rho = (7.10 - 0.0732\%C) - (8.28 - 0.874\%C) \times 10^{-4}(T - 1823)$$

Table 76: Density of liquid Fe-C alloys as a function of carbon content calculated according to Equation 36.

T (K)	[%C]	ρ (g/cm ³)
1823	0	7.10
1823	2	6.95
Density decrease due to 2%C (ratio)		0.98 (dimensionless)

The resulting density of the 4-component metal was then calculated as 4412 kg/m³ (4.504 x 0.98) assuming that the ratio would be the same at 1550°C and 1600°C. The assumption appears reasonable as the calculated ratio was the same at 1500°C and 1450°C.

13 Appendix C: Calculation of mass transfer coefficient for silica for laminar flow inside a circular pipe

The amount of slag participating in the reaction was estimated from fluid dynamics by calculating the mass transfer coefficient for laminar flow inside a circular pipe [138] – see Table 65. The transition from laminar to turbulent flow takes place at around $Re = 2300$ therefore the flow in the pipe was taken to be laminar – see Re in Table 65.

The flux of silica (J) was calculated according to Equation 37 with C_B the concentration of SiO_2 in the bulk of the slag and C_W the concentration of SiO_2 at the slag/refractory interface.

Equation 37: Flux calculation.

$$J = \frac{k_c}{C_B - C_W}$$

The difference in concentration ($C_B - C_W$) should be the difference between the actual SiO_2 concentration and the equilibrium SiO_2 concentration for slag-SiC-CO equilibrium, but was here taken to be the same as the bulk concentration (that is, the equilibrium concentration was taken to be zero) to give an upper-bound estimate of the amount of slag that can react with the carbon refractory.

The concentration of SiO_2 in the slag was calculated from the corrected slag composition as indicated in Table 77.

Table 77: Calculating the concentration of SiO_2 in the slag.

Symbol	Description	Equation	Value	Unit	References
% SiO_2	Mass percent SiO_2 in slag	-	48.3	-	Table 59
ρ	Slag density	-	2774	kg/m ³	[82]
M_{SiO_2}	Molar mass of SiO_2	-	0.0600848	kgmol	-
C_{BSiO_2}	Concentration of SiO_2 in the bulk of the slag	$\frac{\rho \times SiO_2/100}{M_{SiO_2}}$	22331	mol/m ³	-

The rate of SiO_2 transfer (kg/h) was calculated from Equation 38. For the conditions listed in Table 64 and Table 77 the rate of SiO_2 transfer was calculated as 0.177 kg/h.

Equation 38: Rate of SiO_2 transfer through boundary layer (kg/h).

$$Rate_{SiO_2} = C_{BSiO_2} \times k_c \times \pi \times D_T \times L \times 3600 \times M_{SiO_2}$$

The kilogram slag available for reaction (M_R) per ton of slag tapped was calculated from Equation 34 which on substitution for the conditions listed in Table 64 and Table 77 resulted in M_R calculated to be 0.01 kg slag per ton of slag tapped.

Equation 39: Amount of slag available for tap per ton of slag tapped.

$$M_R = \frac{k_C \times \pi \times D_T \times L \times \rho \times t/60}{M}$$